UNIVERSITÉ DU QUÉBEC À MONTRÉAL

ON THE IMPACTS OF THE GGW ON THE AFRICAN CLIMATE AND NORTH ATLANTIC TROPICAL CYCLONES

THESIS

PRESENTED

AS PARTIAL REQUIREMENT

TO THE DOCTORATE IN EARTH AND ATMOSPHERIC SCIENCE

BY

ROBERTO INGROSSO

MARCH 2025

UNIVERSITÉ DU QUÉBEC À MONTRÉAL

IMPACTS DE LA GRANDE MURAILLE VERTE SUR LE CLIMAT AFRICAIN ET LES CYCLONES TROPICAUX DE L'OCÉAN ATLANTIQUE NORD

THÈSE

PRÉSENTÉE

COMME EXIGENCE PARTIELLE

DU DOCTORAT EN SCIENCES DE LA TERRE ET DE L'ATMOSPHÈRE

PAR

ROBERTO INGROSSO

MARS 2025

ACKNOWLEDGMENTS

I am grateful to Francesco and Mathieu for all their precious help during this long process. It was a pleasure to learn from and work with them. I also want to thank Katja Winger for her patience to help and guide me in running GEM and with all the technical queries, Prof. Suzana Camargo for sharing her incredible wisdom on tropical cyclones dynamics, David Carozza for his fundamental support in the knowledge of the UQAM-TCW model and Lenin Del Rio Amador for his suggestions and collaboration. Finally, I am thankful with the AXA XL team and in particular with Ioana Dima-West and Alec Vessey, for their precious feedback during our monthly meetings.

The simulations have been run by using the servers from Digital Research Alliance servers and Calcul Quebec. This research has been supported by the Natural Sciences and Engineering Research Council of Canada (NSERC grant no. RGPIN-2018-04981) and NOVA - FRQNT-NSERC program (ALLRP 577112-22 and 2023-NOVA-324826).

Chapter 3 was funded by a Mitacs Accelerate Grant as part as a research partnership with AXA XL (London, UK).

CONTENTS

LIST OF FIGURES

LIST OF TABLES

RÉSUMÉ

Lancée en 2007 par l'Union Africaine, l'initiative de la Grande Muraille Verte (GMV) vise à restaurer 100 millions d'hectares de terres actuellement dégradées et à freiner l'expansion du désert du Sahara sur le Sahel. Le concept initial de « mur d'arbres » a évolué en une mosaïque d'actions diverses guidées par une approche intégrée de gestion des écosystèmes. Cette nouvelle perspective cherche à créer davantage d'opportunités économiques et à assurer la sécurité alimentaire des communautés locales, renforçant ainsi la résilience climatique dans une région où le changement climatique présente des risques significatifs pour des millions de vies humaines.

Les impacts climatiques potentiels du récent plan de la Grande Muraille Verte (GMV) sur l'Afrique du Nord et des régions éloignées n'ont pas encore été suffisamment évalués, ce qui rend difficile la prévision d'effets climatiques inattendus qui pourraient compromettre la stabilité politique en Afrique du Nord et entraver les objectifs de l'initiative. Par conséquent, l'objectif de ce travail de doctorat est d'examiner les impacts de la GMV sur la mousson ouest-africaine, le climat de l'Afrique du Nord et l'activité des cyclones tropicaux de l'Océan Atlantique Nord.

Tout d'abord, nous avons réalisé des simulations climatiques considérant quatre scénarios différents de la Grande Muraille Verte (GMV) avec des densités de végétation variables, en utilisant un modèle climatique régional à haute résolution pour deux scénarios avec une forte augmentation et une forte diminution de la concentration des gaz à effet de serre. L'impact climatique de ces scénarios de la GMV sur l'Afrique du Nord a été évalué en termes de changements dans les conditions climatiques moyennes et extrêmes. Ensuite, pour évaluer les effets potentiels de la GMV sur l'activité des cyclones tropicaux de l'Atlantique (ATC), nous avons utilisé deux approches distinctes. La première approche consiste à détecter et à suivre les cyclones tropicaux en utilisant des facteurs environnementaux à grande échelle dérivés de nos simulations. Cependant, l'approche de détection des cyclones tropicaux avec en algorithme de trajectoire échoue souvent à capturer un nombre suffisant de cyclones, en particulier les grandes tempêtes, et les critères utilisés dans ces algorithmes peuvent influencer la précision de la détection. Cette limitation nous a conduits à adopter une deuxième approche basée sur la modélisation synthétique, qui nous permet de générer un grand nombre de trajectoires et renforce la robustesse de notre analyse. À cette fin, nous avons utilisé le modèle hybride global récent UQAM-TCW et proposé trois mises à jour du modèle (UQAM-TCW2). Des résultats préliminaires concernant les changements futurs de l'activité des cyclones tropicaux et des risques sous un scénario à fortes émissions de gaz à effet de serre (RCP8.5) sont fournis pour l'Atlantique Nord sans la GMV. Cette approche permet d'évaluer à l'avenir comment la GMV pourrait impacter l'activité des ATC.

En ce qui concerne les changements climatiques en Afrique du Nord, les résultats montrent une augmentation des précipitations s'étendant bien au-delà de la région de la Grande Muraille Verte (GMV), ainsi qu'une réduction de la durée des périodes de sécheresse et une augmentation du nombre de jours de pluie dans les scénarios avec une densité de végétation plus élevée. Bien que les températures estivales diminuent, une augmentation des journées extrêmement chaudes et des valeurs élevées de l'indice de chaleur est prévue pendant la saison précédent la mousson dans tous les scénarios étudiés de la GMV. Ainsi, bien que la GMV puisse aider à réduire l'aridité au Sahel, elle pourrait aussi considérablement accroître l'intensité de la chaleur ressentie par la population locale.

Notre analyse n'indique pas un impact significatif de la GMV sur l'activité des cyclones dans tout le bassin atlantique. "ne augmentation significative de la densité de genèse des cyclones tropicaux est observée sur

la partie orientale de la principale région de développement, accompagnée d'une diminution sur l'Océan Atlantique centre-ouest entre 25°N et 35°N. Ce schéma en dipôle apparaît de manière cohérente dans toutes les expériences GGW avec des densités de végétation moyennes à extrêmes. De plus, une augmentation de la genèse des TC est notée au large des côtes est des États-Unis. L'intensification des ondes d'est africaines est liée à l'augmentation de la genèse des cyclones tropicaux dans l'est de la principale région de développement, tandis que les changements dans les facteurs atmosphériques à grande échelle expliquent l'augmentation au large des côtes américaines.

Les résultats préliminaires des trois versions du modèle UQAM-TCW2 indiquent un changement contrasté dans la fréquence des cyclones tropicaux dans l'Atlantique Nord sous le scénario RCP8.5 sans la GMV. Une augmentation de la proportion des grandes tempêtes et un renforcement de l'intensité des cyclones tropicaux dans tous les bassins sont également observés. Le risque associé a le passage de cyclones tropicaux sur le continent augmente le long de la côte est de l'Amérique du Nord et dans le centre et le sud du Mexique, en raison d'une combinaison de taux du passage de cyclones tropicaux sur le continent plus élevés et de changements dans l'exposition. En revanche, certaines régions du Mexique devraient voir une diminution du risque, principalement en raison d'un nombre réduit des passages de cyclones tropicaux sur le continent de cyclones.

ABSTRACT

Launched in 2007 by the African Union, the Great Green Wall (GGW) initiative aims to restore 100 million hectares of currently degraded land and hold back the expansion of the Sahara Desert over the Sahel. The original concept of "a wall of trees" has evolved into a mosaic of diverse actions guided by an integrated ecosystem management approach. This new perspective seeks to create more economic opportunities and ensure food security for local communities, enhancing climate resilience in a region where climate change poses significant risks to millions of human lives.

The potential climate impacts of the recent GGW plan on northern Africa and distant regions have not yet been adequately assessed, making it challenging to anticipate unexpected climate effects that could jeopardize political stability in northern Africa and hinder the initiative's objectives. Consequently, the aim of this PhD thesis is to investigate the impacts of the GGW on the West African Monsoon, the climate of northern Africa, and Atlantic Tropical Cyclone (ATC) activity.

First, we conducted climate model simulations using four different GGW scenarios with varying vegetation densities, using a high-resolution atmospheric regional climate model under two (high and low) future greenhouse gases concentration pathways. The climatic impact of these GGW scenarios on northern Africa was evaluated in terms of changes in both mean and extreme climate conditions. Next, to assess the potential effects of the GGW on ATC activity, we employed two distinct approaches. The first approach involves TC detection and tracking using large-scale environmental factors derived from our simulations. However, TC tracking algorithms often fail to capture an adequate number of TCs, particularly major storms, and the criteria used in these algorithms can influence detection accuracy. This limitation led us to adopt a second approach based on synthetic modeling, which allows us to generate a large number of tracks and enhances the robustness of our analysis. To this end, we utilized the recent hybrid global UQAM-TCW model and proposed three different updates of the model (UQAM-TCW2). Preliminary results of future change in TC activity and risk under a high emission greenhouse gas concentration scenario (RCP8.5) are provided for the North Atlantic without GGW. This approach enables future evaluations of how the GGW may impact ATC activity.

Regarding changes in northern Africa climate, the findings indicate an increase in rainfall extending well beyond the GGW region, along with a reduction in drought lengths and an increase in rainy days in scenarios with higher vegetation density. While summer temperatures decrease, more extreme hot days and elevated heat index values are projected during the pre-monsoon season across all GGW scenarios. Although the GGW could help reduce aridity in the Sahel, it may also significantly increase heat intensity experienced by the local population.

TC tracking results do not show any significant impact of the GGW on TC activity in terms of TC frequency, intensity, speed over the whole Atlantic basin. A significant increase in TC genesis density is observed over the eastern part of the Main Development Region (MDR), accompanied by a decrease over the central-western Atlantic between 25°N and 35°N. This dipole pattern appears consistently across all GGW experiments with medium-to-extreme vegetation densities. Additionally, an increase in TC genesis is noted off the eastern U.S. coasts. The rise in AEW intensity is linked to the increase in TC genesis across the eastern MDR, while changes in large-scale atmospheric factors account for the increase off the U.S. coasts.

Preliminary results from three versions of UQAM-TCW2 indicate contrasting change in TC frequency across the models in the North Atlantic ocean under RCP8.5 without GGW. A rise in the proportion of major storms and a boost in TC intensity in all basins are also observed. The overall risk increases along the eastern coast of North America and in central and southern Mexico, driven by a combination of higher landfall rates and changes in exposure. Conversely, some regions of Mexico are expected to see a decline in risk, primarily due to fewer landfalls.

INTRODUCTION

0.1 The Great Green Wall

The Sahel is a region on the southern border of the Sahara Desert, defined between 100 and 400 mm/yr isohyets (PAGGW, 2018; Saley et al., 2019). It has been considered one of the most important regional climate change hotspots throughout this century using the Standard Euclidean Distance (Diffenbaugh and Giorgi, 2012; Turco et al., 2015). A climatic hotspot is defined as a «region which displays the largest variations in multiple statistics (mean, variability, and extremes) of climate variables» (Giorgi, 2006). The Sahel region was hit by severe droughts during the 70s and 80s, that combined with an increase in population (Sinclair and Fryxell, 1985), led to prolonged famines in the region. In order to fight potential future droughts and land degradation, a range of stakeholders, including national governments, international organizations, such as the United Nations Convention to Combat Desertification (UNCCD), the Food and Agriculture Organization of the United Nations (FAO), the World Bank and also the business sector and the local population, came up with a fascinating and complex project: the Great Green Wall (GGW, Fig.0.1). The GGW is based on the ecological restoration of about to 7,000-kilometre-long stretch of degraded land from Senegal in West Africa to Djibouti in the east, with the objective of changing its hydrological cycle, increasing local rainfall.

The proposal of a green belt between the Sahara and the Sahel dates back to the early 20th century. In 1935 the British forester, E.P. Stebbing, suggested the creation of two forest belts over the Sahara and the Sahel in order to reduce southward movement of sand and man-made soil erosion (Stebbing, 1935). Views of the encroaching of the southern boundary of the Sahara favored by human misuse and population increase were common in the 1930s. Deforestation and overgrazing along with the use of fire in agricultural and pastoral settings were identified as the biggest problems leading to desertification in the Sahel. The concept of desertification began to emerge during this period (Lavauden, 1927), along with its proposed counter-solution of forced afforestation or regreening. The desertification concept is closely linked to the notion of expanding deserts and human responsibility for deforestation, overgrazing, and arid land degradation. These ideas spread widely in the following decades, remaining prevalent to these days, particularly in political contexts. In recent decades, increasing criticism of this simplistic view has emerged, with experts highlighting a growing disconnect between the traditional idea of desertification and the scientific understanding of land degradation (Andersson et al., 2011). New evidence overcame the supposed fragility of dryland ecosystems as vegetation is quick to expand in response to increased rainfall. The standard notion of desertification has been refuted (Behnke and Mortimore, 2016) based on environmental monitoring, aerial and satellite

imagery, ecological modeling, and local knowledge combined with field observations (Scoones, 2018). However, it still persists in plans promoted by international aid agencies and governments. These plans are based on large-scale projects with top-down planning, including human resettlement and large-scale irrigation, aiming to transform the nature of the region (Toulmin and Brock, 2016). An example of the persistence of the idea of encroachment of Sahara can be found in the 2007 report «Sudan Post-Conflict Environmental Assessment» produced by the United Nations Environment Programme (UNEP), where the Stebbing's work is still cited as almost unique reference. In the Sahel, new studies based on net primary production (NPP) have shown that vegetation closely follows rainfall patterns, recovering rapidly from droughts and contradicting fears of widespread desertification (Prince et al., 1998). This research suggests that desert expansion is more closely linked to latitudinal rainfall variability than to local anthropogenic activities (Tucker et al., 1991). Re-greening of the Sahel has emerged in the last decades thanks to satellite observations (Herrmann et al., 2005; Dardel et al., 2014).

However, during the 80s, Thomas Sankara, Burkina Faso's president, renewed this idea to combat desertification in his own country (Reenberg, 2012), but only in 2005, Olusegun Obasanjo, the president of Nigeria, presented the GGW proposal to the 7th summit of the leaders and Heads of State of the Community of Sahel-Saharan States. In 2007, the GGW was officially adopted by the 11 founding members at the conference of Heads of State and Government of the African Union.

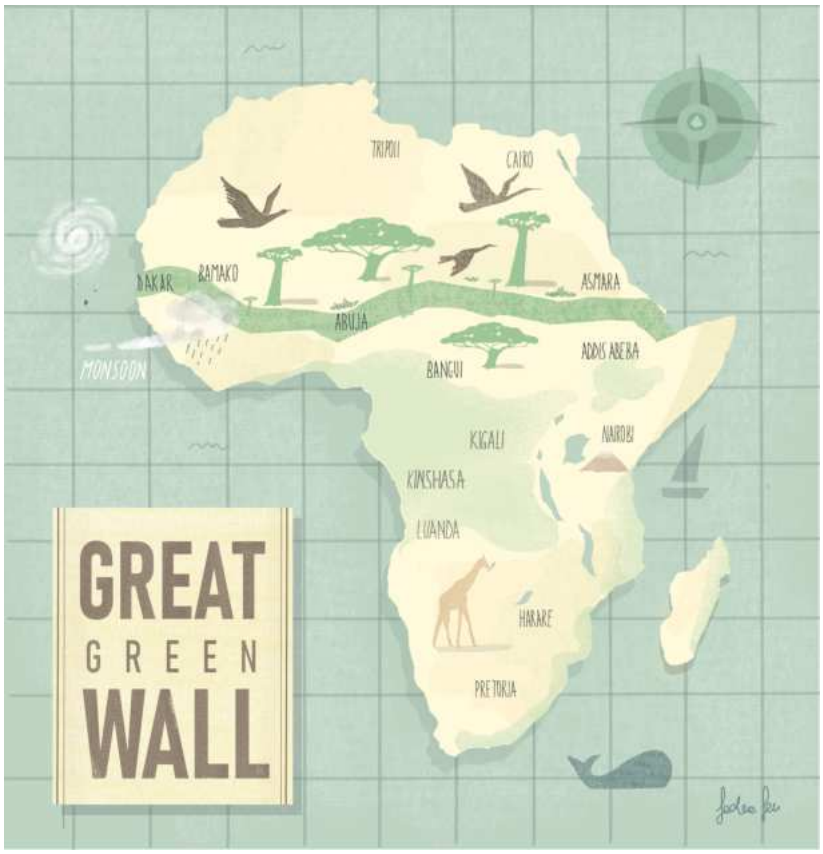

Figure 0.1: Illustration of the Great Green Wall. Courtesy of Federica Ferri.

Evidence of widespread afforestation as a failing strategy has emerged in the last decades. Converting bare land into forests can significantly impair ecosystem functions (Holl and Brancalion, 2020), markedly reduce biodiversity by harming native ecosystems and species (Veldman et al. 2019), and even create «underground deserts» (Tölgyesi et al., 2020). Multiple local or sub-regional initiatives such as soil and water conservation measures or local afforestation based on the idea to improve Sahelian resilience society have demonstrated to be more efficient (Sendzimir et al., 2011; West et al., 2014).

The initial project of a *wall of trees* has been replaced by a more feasible initiative, an integrated ecosystem management approach, which consists of «a mosaic, comprised of diverse, landscape-scale actions that are designed to provide long-term solutions for improving environmental and socio-economic conditions in the zone» (Goffner et al. (2019), Fig.0.2). The reforestation activities of variable shape, size, and function are (or should be) decided between the stakeholders mentioned above. Some projects have a specific use, such as *Acacia Senegal* reforestation for gum Arabic production, some have diverse species planted to generate

multiple economic, ecological and social benefits to local communities. The current initiative seems to put efforts towards small-scale farming and support for local community initiatives based on locally-generated practices for managing soil and water in a dryland farm setting such as the *zai* planting pit, a traditional Sahelian practice to conserve moisture and preserve soils across the region (Reij et al., 1996). The GGW aims to strengthen the resilience of the local communities and natural systems, the protection of rural heritage and the improvement of the living conditions of the local population. The ability to strictly involve the local populations is the base of the success of this project.

The general interest to the GGW has recently grown up in the scientific community (Nature, 2020; Science, 2020; Nature, 2022), and among the media and general public (Morrison, 2016; Nationalgeographic, 2024). As a consequence, during the One Planet Summit in January 2021, world leaders announced the launch of the GGW Accelerator, with the funding of further USD 14.3 billion to help reaching the 100-million-hectare target (OnePlanetSummit, 2025).

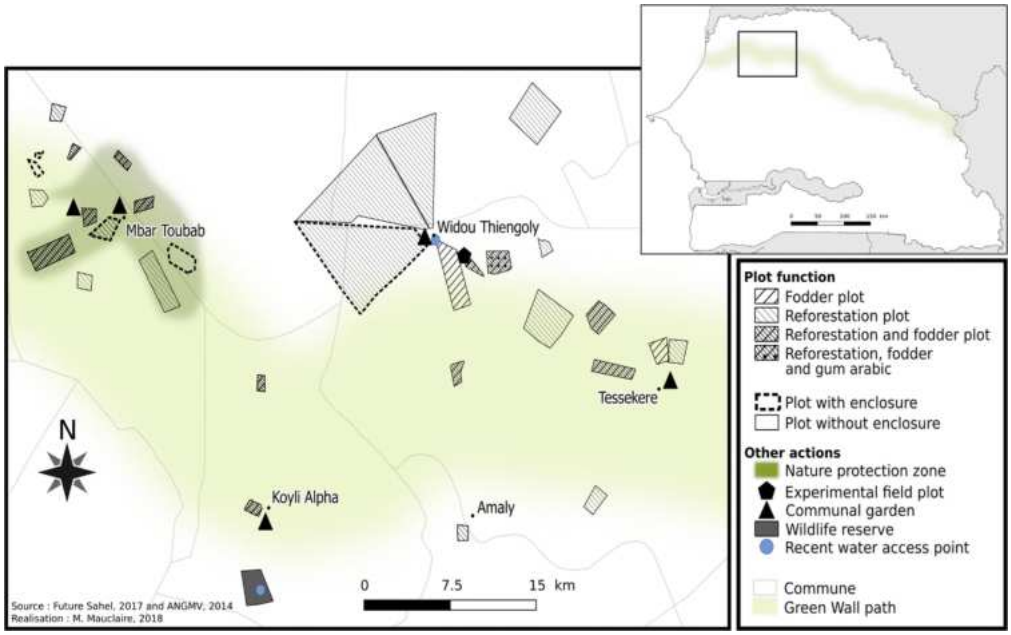

Figure 0.2: Mosaic landscape in GGW actions Example of a mosaic landscape in Northern Senegal. Different actions such as reforestation, plantation of Acacia Senegal for gum Arabic, communal gardens, natural reserves, water access point and experimental field plot characterized the new GGW concept. From Goffner et al. 2019.

0.2 Main scientific question: Could the GGW impact on Northern Africa climate and Atlantic Tropical Cyclone activity?

With growing evidence highlighting the role of land use change (LUC) as a significant human-induced forcing, particularly at regional and local scales (Findell et al., 2009; Davin et al., 2020), it becomes essential to quantify the potential bio-geophysical impact of a large-scale initiative such as the Great Green Wall. Sahel precipitation is closely linked to the West African Monsoon (WAM), a coupled atmosphere-ocean-land system characterized by rainfall during the summer and a winter drought over the continent. WAM is part of the global monsoon system that regulates the moisture and heat budget of the atmosphere in low latitudes and the agricultural production in densely populated areas depending on agriculture. Furthermore, a clear relationship has also been found in several studies between these regional weather systems and the Atlantic Tropical Cyclone (ATCs) activity. Given the lack of comprehensive studies in the scientific literature on the potential climatic impacts of the GGW project, the main scientific question behind this doctoral work is how this potential massive greening initiative over Sahel could impact northern African climate and ATC activity. In the next sections, we describe the main dynamics related to WAM and the TCs, then we provide a review of the current scientific literature on the regional impact of reforestation in northern-Africa and connections between WAM and TC. We also introduce two different approaches to study the TC activity based on TC detection and tracking in high resolution climate models and on producing big datasets of synthetic tracks by means of statistical/dynamical TC models.

0.3 The West African Monsoon

The main general picture of WAM was developed by British and French colonial meteorologists working in West Africa in the 1950s and 1960s (Nicholson, 2009). According to this traditional idea, WAM is characterized by a surface convergence between the south-westerly flow from the ocean (monsoon) and the north-easterly flow from the desert (Harmattan winds). This convergence line is called the Inter-Tropical Front (ITF, Hamilton et al. (1945)) or the surface Inter-Tropical Convergence Zone (ITCZ) and moves northward, at about 20°N, during the northern Hemisphere summer and southward, at about 8°N, during the winter. The ITCZ slopes towards the equator with the height and the depth of the moist layer sharply increase southward, leading to heavier precipitation 500 km south of the surface convergence. Hamilton et al. (1945) defined four different weather zones (Fig.0.3), from A to D, with zones C and D, which are present only in the summer, characterized by the peak of monsoon precipitation and wind speed, respectively. Zones A and B are the regions divided by the ITF. Zone A extends a few hundred km northward of

the ITF with a cloudless sky, whereas zone B extends southward of the ITF for about 150-250 km and could exceptionally be hit by isolated convective thunderstorms in the afternoon or evening.

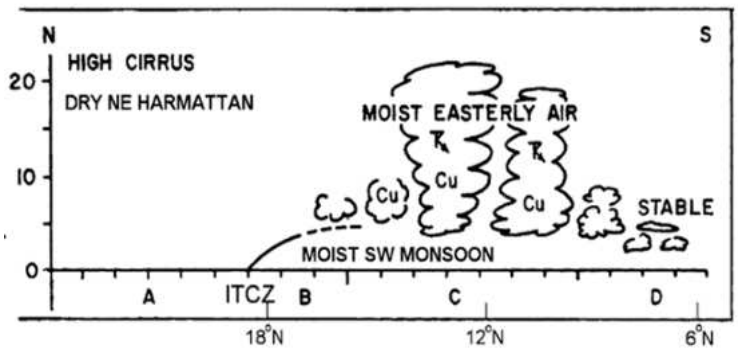

Figure 0.3: Illustration of the WAM. Classic picture of WAM and weather zones (A-D) of West Africa. Zones A-B are drier regions, divided by the ITF, the surface convergence between the south-westerly flow from the ocean (monsoon) and the north-easterly flow from the desert (Harmattan winds). The cloudiness and precipitation maxima are located equator-ward, 500 km south of the surface convergence, over the zones C and D. Revised by Nicholson 2009.

Most recent studies (Grist and Nicholson, 2001; Gu and Adler, 2004; Nicholson et al., 2013) diminished the importance of the ITCZ and showed a more complex picture, highlighting the role of different regional features: two distinct jet streams, the African Easterly Jet (AEJ) and the Tropical Easterly Jet (TEJ), the African Easterly Waves (AEWs), and the Saharan Heat Low (SHL), a low pressure system, which appears over the Western Sahara in the boreal summer (Fig.0.4). The AEJ is an easterly mid-tropospheric jet, baroclinically induced and maintained by thermal contrasts between the Atlantic Ocean and the hot Sahara and humidity contrasts between the moist convection to the south and dry convection to the north, with a maximum wind speed of around 12.5 m/s at 600-700 mb and 15°N (Thorncroft and Blackburn, 1999).

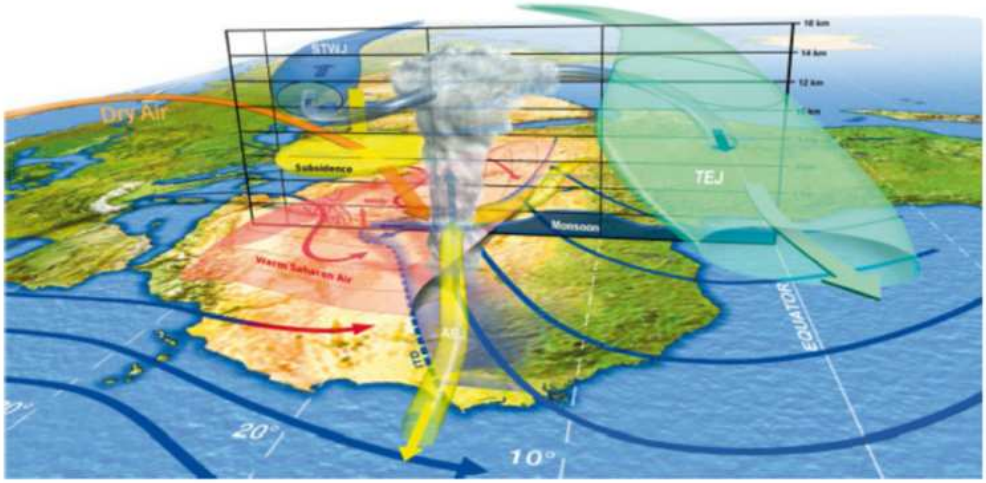

Figure 0.4: Three-dimensional schematic view of the WAM.. ITD, inter-tropical discontinuity; TEJ, tropical easterly jet; STWJ, subtropical westerly jet; AEJ, African easterly jet. The oscillation of the AEJ yellow tube figures an African easterly wave. From Lafore et al. (2011).

Horizontal and vertical shears, which characterize this region, are important factors for the growth of easterly waves (Burpee, 1972; Paradis et al., 1995), that move from east to west over the Sahel region and are largest in the mid-levels of the atmosphere. Early observational studies estimated AEW wavelengths at 2000 km (Carlson, 1969) or between 3000 km and 4000 km (Burpee, 1972, 1974). Paradis et al. (1995) found a length of the AEWs waves at 3300 km and a propagation speed at 7.8 m/s. At synoptical scale, the AEWs represent the primary precursors for ATCs (Russell et al., 2017), propagating westward toward the Atlantic Ocean. Several studies found that about 50-60% of tropical cyclones (Simpson et al., 1969; Frank, 1970; Avila et al., 2000; Chen et al., 2008) and 83% of most intense TCs (Landsea, 1993) are originated from AEWs.

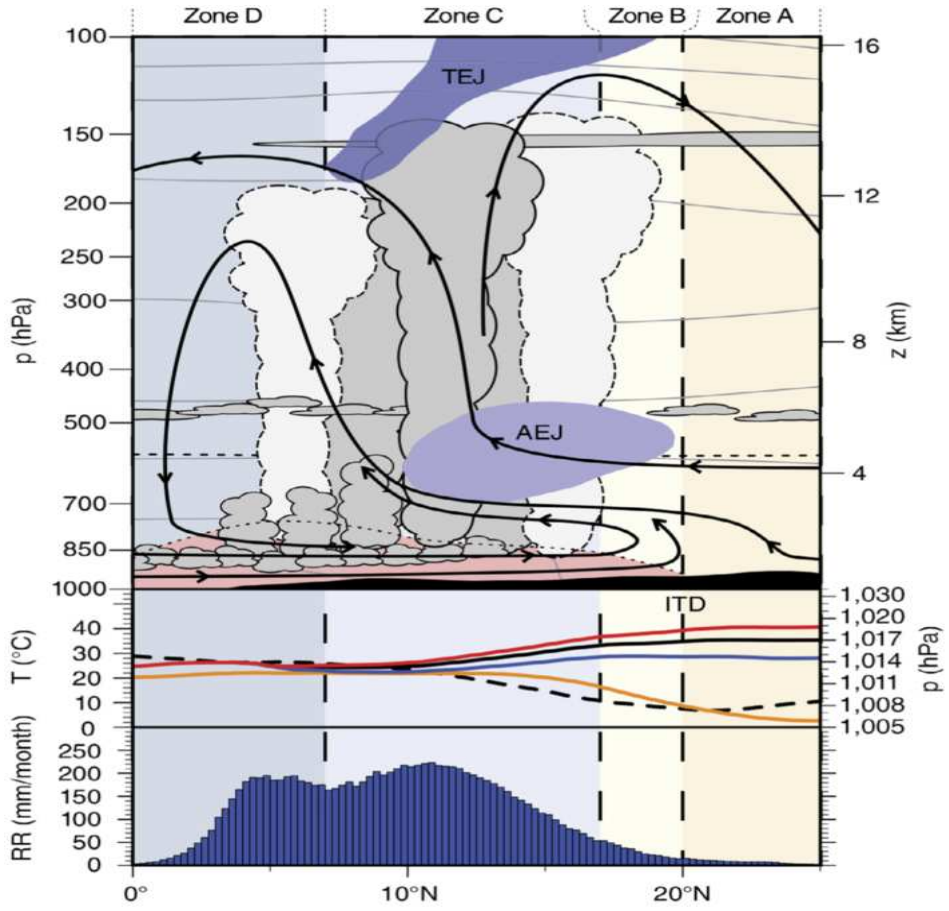

Figure 0.5: Schematic cross-section of the atmosphere between 10°W and 10°E in July. Top panel shows are the positions of the ITD (or ITF), the African easterly jet [AEJ], the tropical easterly jet [TEJ], the monsoon layer (pink shaded area) streamlines (black arrows), streamlines, clouds. Mid panel shows the freezing level (0°C isotherm), isentropes (Θ), minimum (Tn), maximum (Tx) and mean (T) and dew point (Td) temperatures, atmospheric pressures (p). Bottom panel shows the mean monthly rainfall (RR). Zones A-D represent the weather zones of the WAM. From Biasutti (2019), revised by Parker and Diop-Kane (2016).

In summer, the strong baroclinicity and the gradient of humidity enhance convergence and the associated upper-level anticyclonic and divergent flow, which feeds the TEJ, an upper-tropospheric jet at 200-300 mb. The TEJ may also play an important role by promoting ascent in the lower troposphere on the cyclonic side of the AEJ, where the disturbances develop. Generally, a stronger TEJ and a weaker and northernmost AEJ are associated with an intensification and a northward migration of the WAM, with heavier rain in the Sahel region. However, these zonal components are not the only regional features of the WAM system. At the

surface, the southerly flow from the ocean penetrates well north of the region characterized by the peak of precipitation (zone C, Fig.0.5), sucked out by SHL to the south-east of its core. A northerly return flow of Saharan dry air at about 600 mb (the northeasterly Harmattan winds to the west of the low pressure) reaches the rain band. A significant negative potential vorticity anomaly is associated with SHL and the low static stability air in the deep well-mixed boundary layer. It characterizes the anticyclonic side of the AEJ and the sign-reversal that supports AEWs growth (Thorncroft and Blackburn, 1999). The direct circulations that develop in association with the heat low also play an important role regarding the transport of moisture in the WAM. Heat low circulations encourage poleward movement of moist air at low-levels and equatorward movement of dry air at mid-levels and are thus expected to play a vital role in the seasonal evolution of the WAM.

0.4 Tropical cyclones

Tropical cyclones (TCs) are *rapidly rotating storms that begin over tropical oceans*, *varying in speed*, *size*, *and intensity* (`https://wmo.int/topics/tropical-cyclone`). These tropical low-pressure systems are driven by turbulent transfer of energy from the surface of the ocean - which is generally warmer than the surrounding air - to the space by radiative cooling. TCs with maximum winds of 17 ms^{-1} are known as tropical depressions, whereas when they reach a wind speed higher than 18 ms^{-1}, they are called tropical storms. TCs with maximum winds 33 ms^{-1} or greater are called hurricanes in the North Atlantic and eastern North Pacific basins, typhoons in the western North Pacific, and just tropical cyclones elsewhere. These storms are relatively rare with medians of 80/85 TCs per year at global scale depending on the dataset (Schreck et al., 2014) and with only 12 of them making landfall globally with wind speeds greater than 33 ms^{-1} (Weinkle et al., 2012).

Tropical cyclone formation has been much studied, starting since the 1960s and 1970s. Gray (1979) indicated empirical necessary conditions for TC genesis, clarifying that TC frequency is not just related to sea surface temperature (SST) values but rather to various climatological parameters, which represent large scale environmental factors useful for TC formation. These so-called ingredients for TC formation are low-level vorticity, Coriolis parameter, vertical wind shear between lower and upper troposphere, ocean thermal energy (sea temperature above 26°C to a depth of 60 m), the difference in equivalent potential temperature between the surface and upper troposphere (conditional instability) and midlevel relative humidity. The product of the last three parameters indicates a thermal potential while the product of low-level vorticity,

Coriolis parameter, vertical wind shear specifies a dynamic potential.

0.4.1 Thermal potential

Ocean energy plays a crucial role in the formation and maintenance of tropical cyclones (TCs). TCs draw substantial amounts of sensible and latent heat energy through sea-air fluxes. The commonly accepted threshold for SST to supply sufficient latent heat energy for storm development is 26.5°C (Leipper and Volgenau, 1972). Nevertheless, approximately 7% of TCs - generally across subtropics - occur over sea surfaces that are cooler than this 26.5°C threshold (Dare and Mcbride, 2011). McTaggart-Cowan et al. (2015) suggested complementing this SST threshold with an additional criterion for subtropics storms: a maximum difference of 22.5°C between the tropopause level and the 850-hPa equivalent potential temperature (the temperature of a parcel would have if it were raised to 0 mb with pseudo adiabatic expansion, condensing all moisture from the parcel, and then lowered to 1000 mb with a dry-adiabatic compression). Vecchi et al. (2008) questioned the existence of a direct relationship between absolute SST and hurricane activity. They argued that warming in remote ocean basins also tends to stabilize the atmosphere by warming the upper troposphere, thereby inhibiting TC activity. Their study highlighted that it is the SST in the tropical Atlantic relative to the tropical mean SST - rather than the absolute SST - that modulates Atlantic hurricane activity. Understanding whether relative SST or absolute SST plays a dominant role is crucial, as it has important implications for attributing past changes in TC activity and for projecting future changes.

Atmospheric instability is another key factor for the TC development. An unstable atmosphere favors a rising air parcel to continue going upward, expanding, cooling and releasing latent heat by condensation. The result of this process is the formation of a cloud tower called cumulonimbus. It is a *principal cloud*, *exceptionally dense and vertically developed*, *occurring either as isolated clouds or as a line or wall of clouds with separated upper portions* (AMS glossary, `https://glossarytest.ametsoc.net/wiki/Cumulonimbus`). Cumulonimbus convection is due to vertical coupling of the flows between lower and upper troposphere, and it is associated with a decrease in the gradient of the equivalent potential temperature between surface and upper troposphere. Finally, environmental mid-level relative humidity is necessary during the dynamics of TC genesis. If the air around the cumulonimbus cloud is dry, the dry air mix with air in the cloud (the so-called entrainment). This favours evaporation in the cloud, which extracts energy lowering the temperature of the cloud air. If the air parcel in the clouds is now cooler than the surrounding area, the parcel will sink, inhibiting the upward motion and the TC genesis.

0.4.2 Dynamic potential

The low-level vorticity is important as deep convergence associated with tropical disturbances enhances the environmental vorticity by producing a cyclonic spin-up. The larger is this positive low-level vorticity, the greatest is the potential of TC genesis. Coriolis effect is a consequence of Earth rotation. This effect is weak near the equator then TCs do not form within 4-5°C of it. The spin provided by the Coriolis effect supports tropical disturbances to develop a closed wind circulation typical of TCs. Low-vertical wind shear is fundamental as strong shear will disrupt the cloud tower of the forming storm.

0.4.3 Genesis index

Gray (1979) combined both dynamic and thermal potentials together into a first genesis index, which provided very good estimates of the long-term frequency of occurrence of tropical cyclones. Later, empirical studies redefined different versions of the genesis index largely based upon the parameters outlined by Gray, (e.g. Royer et al. (1998), DeMaria et al. (2001), Emanuel and Nolan (2004), Yokoi et al. (2009), Tippett et al. (2011), McGauley and Nolan (2011)). Unfortunately, a definitive understanding of TC genesis remains problematic.

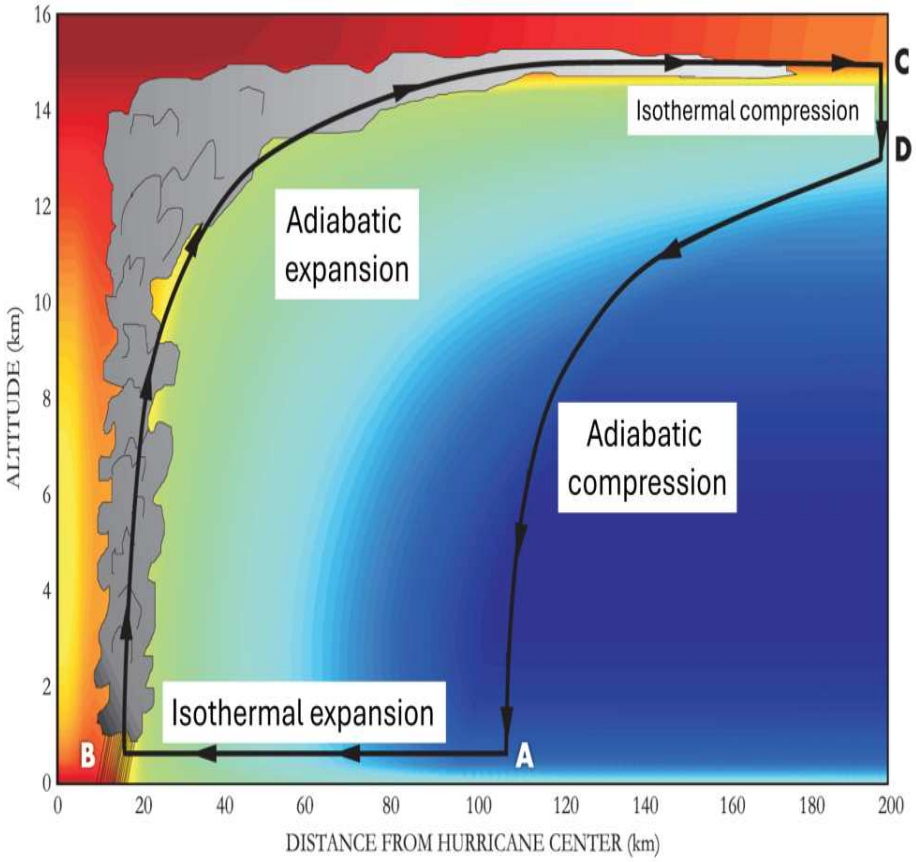

Figure 0.6: Cross section of an idealized tropical cyclone and its Carnot cycle. Arrows indicate the four branches of the Carnot cycle in a tropical cyclones (isothermal expansion, adiabatic expansion, isothermal compression and adiabatic compression) A-D the initial steps of each branch. Colors indicate the entropy gradients with cooler colors indicating lower entropy. Revised from Emanuel 2006.

0.4.4 Potential intensity theory

One of the most clear signal in the past decades is that climate change has already increased the intensity (Elsner et al., 2008) and number (Kossin et al., 2020) of major TCs. Potential intensity (PI) is a theoretical model for a limit to the maximum intensity that can be achieved by a TC. PI calculation is a way to evaluate the ability of the ocean-atmosphere thermodynamic state to promote TC growth. According to this theory, the intensification and maintenance of tropical cyclones depend on self-induced heat transfer from the ocean (e.g. Emanuel (1986) and Holland (1997)). A mature tropical cyclone transfers heat from the surface to the atmospheric boundary layer through release of latent heat, which is the fuel of a heat engine that can

be simplified into a Carnot cycle model (Emanuel, 1987). Figure 0.6 is an illustration of this heat engine, and colors represent entropy gradients. The evaporation of seawater transfers energy from sea to air making air spirals inward, towards the minimum central pressure (from A to B). During this process, it acquires entropy at a constant temperature by a nearly isothermal expansion. The maximum entropy and the tropical cyclone maximum potential intensity (Vmax) are near the radius of maximum winds. Here, the air spins faster as a result of conservation of angular momentum. Then, an adiabatic expansion is produced as air ascends within the storm's eyewall (from B to C). Considering an idealised model where no other weather systems are present, infrared radiation is exported into space by means of a nearly isothermal compression and releasing the entropy acquired previously (from C to D). In the final step, air is adiabatically compressed (from D to A), completing the Carnot cycle.

The maximum potential intensity of a tropical cyclone, Vmax, was derived by Bister and Emanuel (1998) and Emanuel (2003):

$$V_{\mathrm{MAX}}{}^2 = \frac{C_{\mathrm{K}}}{C_{\mathrm{D}}} \frac{T_{\mathrm{S}} - T_{\mathrm{O}}}{T_{\mathrm{O}}} (h_{\mathrm{O}}{}^* - h^*) \tag{1}$$

where C_{K} and C_{D} are the enthalpy and momentum surface exchange coefficients, respectively, $h_{\mathrm{O}}{}^*$ is the saturation moist static energy at the sea surface, and h^* is the saturation moist static energy of the air above the boundary layer. Terms ($h_{\mathrm{O}}{}^*$-h^*) and (T_{S}-T_{O})/T_{O} represent the TC thermodynamic disequilibrium and efficiency, respectively.

PI is often considered in prognostic and diagnostic indices of tropical cyclogenesis (e.g. the genesis potential index, GPI, Camargo et al. (2007); the tropical cyclone genesis index, TCGI, Tippett et al. (2011), and destructive potential (e.g., the power dissipation index, PDI, Emanuel (2005)) and intensification (e.g. the ventilation index, (Tang and Emanuel, 2012)).

What emerges from the TC physics is that TCs form from a different process than mid-latitude cyclones. Mid-latitude cyclones need to extract available potential energy from areas characterized by strong baroclinicity, an environment, which is completely different from that in Tropics, where horizontal temperature gradients are small. The primary source for TCs are the sea-air fluxes, which transport heat upward along the atmospheric column. This leads to the formation of the characteristic warm core, whereby the temperature in the center of the tropical cyclone is warmer than the surrounding environment. On the other hand, mid-latitude cyclones are characterized by a cold core and in general are associated with weather fronts.

0.4.5 TC structure

The TC structure is characterized by an eye in the center (Fig.0.7). The eye is a relatively calm, clear-sky area of sinking air of about 32-64 km of size, but some can also reach 100 km and above. Here, winds do not exceed 24 km/h. An eye usually develops when the maximum sustained wind speeds reach values above 119 km/h. The eyewall consists of a ring of tall thunderstorms all around the eye with the strongest winds and the heaviest rain. Rain bands are curved bands of clouds and thunderstorms, which develop in spiral from the eye to the outer part of a TC. Heavy bursts of rain and wind and tornadoes can form from these bands. Finally, the Central Dense Overcast (CDO) is the TC cirrus cloud shield coming from storms in the eyewall and rainbands. The CDO is typically uniform, with an eye appearing in the satellite images as the storm reach the highest TC levels.

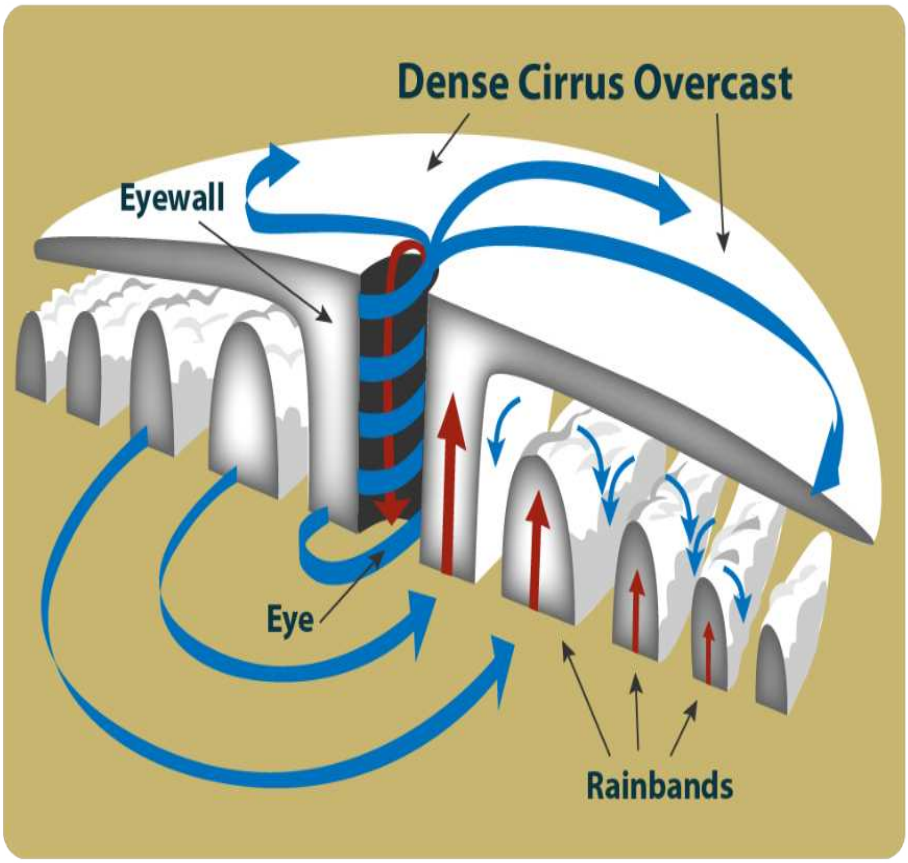

Figure 0.7: Cross section of a typical tropical cyclone. The figure shows the cross section of a tropical cyclone with its eye in the center characterized by descending air, the eyewall around the eye characterized by the strongest winds, the rain bands, which develop from the eye to the outer part of a TC and the Central Dense Overcast, a uniform cirrus cloud, which can have a hole in the middle (the TC eye) during stronger TCs. Credits NOAA.

0.4.6 Projected changes in TC activity

Future change in TC activity have been investigated in the recent decades, but a robust answer is missing for many TC metrics. An assessment of TC projections for the late 21st century was provided by Knutson et al. (2020), a report mandated by the World Meteorological Organization (WMO). The authors gave medium-to-high confidence in a global increase of TC precipitation rates, global increase in TC intensity, seen most prominently in higher-resolution models, and proportion of major hurricanes. On the other side, low confidence was assigned to a decrease of global TC frequency, a slowdown in TC translation speed and further

poleward expansion of the latitude of maximum TC intensity, especially in the North-West Pacific.

0.5 Monsoon dynamics and the role of SST pattern, surface albedo and bio-geo-physical feedback on multidecadal variability of Sahelian rainfall

Heating and moisture contrast between land and ocean is a key mechanism that triggers and sustains the summer monsoon circulations (Webster, 1987). Over recent decades, temperature and humidity trends have diverged between land and ocean, with land experiencing a greater increase in temperature, while the ocean has seen a more significant rise in specific humidity (Byrne and O'Gorman, 2018). These changes have resulted in similar alterations in the equivalent potential temperature and in the moist static energy (MSE, Yanai et al. (1973)) of the air over land and ocean, consistent with the convective quasi-equilibrium theory proposed by Byrne and O'Gorman (2013). The MSE quantifies the total energy that is approximately conserved during hydrostatic, moist adiabatic vertical motions (Ángel F. Adames Corraliza and Mayta, 2023). It comprises several energy components: the first is the dry–air enthalpy, the second accounts for latent heating contributions, and the third represents the specific gravitational potential energy. Given the atmosphere is nearly in hydrostatic equilibrium, MSE is analogous to equivalent potential temperature. The conversion of enthalpy and latent energy available in the lower troposphere into geopotential energy aloft serves as the primary indicator of convection, making MSE a direct measure of monsoonal convection and precipitation.

The heating contrast between land and ocean fails to explain the poleward extension of monsoon rainfall (Chou and Neelin, 2003). Additional mechanisms must be taken into account to explain the northward extent of the monsoon, pointing to land processes related to changes in soil moisture and surface albedo (Lofgren, 1995; Meehl, 1994; Xue and Shukla, 1993). In the African monsoon, the higher surface albedo compared to other monsoonal regions inhibits a greater northward extension of the convergence zone between the dry Harmattan winds and the humid monsoon flow (Chou and Neelin, 2003). High albedo reduces the net flux of energy into the atmosphere, which is a fundamental requirement for the poleward extension of summer monsoons.

The role of albedo has not been only considered for the latitudinal position of the convergence zone in the monsoon systems. The bio-geo-physical feedback described by Charney and colleagues in their famous 1975 paper (Charney et al., 1975) points on changes in surface albedo due to local human activities such as overgrazing to explain the Sahel droughts of '70s and '80s. During those two decades, the Sahel has been

hit by severe droughts after a period of relatively wet years (Fig.0.8).

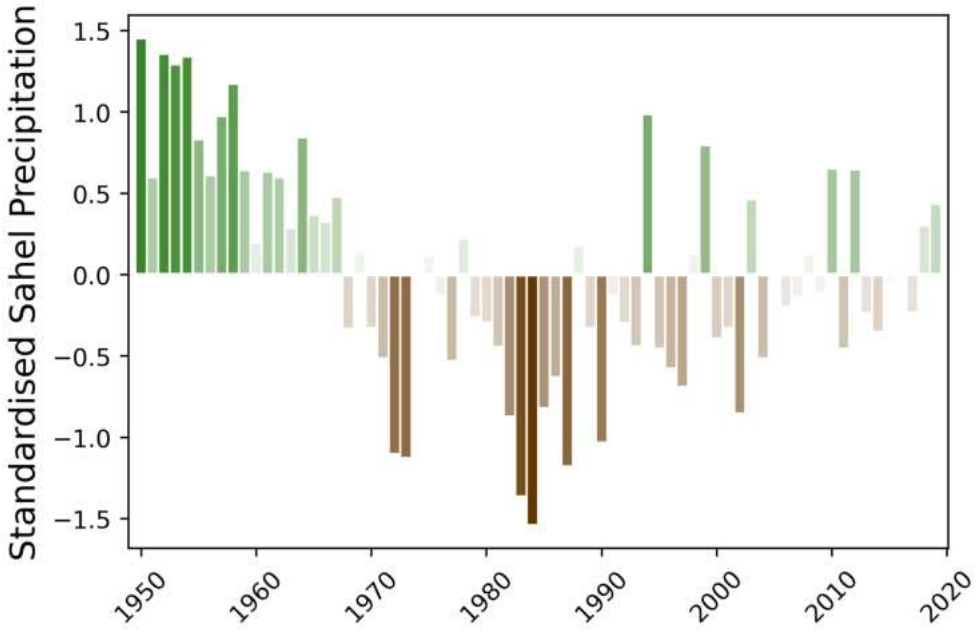

Figure 0.8: Standardized Sahelian precipitation. Standardized Sahelian precipitation from the Global Precipitation Climatology Centre dataset. Precipitation is calculated over the same area as Ali and Lebel (2009).

According to Charney's results, the decrease in plant cover and the resulting increase in surface albedo lead to a reduction in net incoming radiation and an increase in radiative cooling of the air. This cooling induces descending air motion to maintain thermal equilibrium through adiabatic compression, suppressing cloud formation and rainfall over the region. This, in turn, further reduces vegetation in a positive feedback loop, ultimately triggering droughts. The scientific hypothesis tested in this experiment was likely influenced by the prevailing beliefs of that time when the concept of desertification was still widely accepted in the scientific community due to limited knowledge of drylands and a lack of observational evidence from in situ and satellite data (see Sec.0.1 for further details). Additionally, new studies have shown that albedo changes across the region between dry and wet years reach a maximum value of 0.15 (Govaerts and Lattanzio, 2008), which is at the lower end of the range (0.15–0.35) considered by Charney et al. (1975) in their experiment. Furthermore, other studies found a modest contribution of land use change, with decreases of 4.6% and 8.7% (Taylor et al., 2002), which only partially explains the drought signal, accounting for approximately a 10–20% reduction in regional rainfall.

The role of bio-geophysical feedback as the primary driver of Sahelian rainfall has been challenged in the following decades by studies highlighting the influence of remote oceanic forcing. These studies focused on global-scale changes associated with SST pattern (Fig.0.9), which impact the tropical atmosphere over land and modulate the multidecadal variability - rather than the magnitude - of Sahelian rainfall (Hastenrath and Lamb, 1977; Folland et al., 1986; Palmer, 1986; Giannini et al., 2003; Zeng, 2003; Lu and Delworth, 2005). In particular, warming of the equatorial Indian Ocean and the South Atlantic has been directly linked to the multidecadal persistence of droughts, associated with changes in the North Atlantic Ocean.

In the Atlantic Ocean, the SST meridional gradient—the temperature difference between the northern and southern tropical Atlantic—plays a key role in influencing the position of the ITCZ. A cooler North Atlantic reduces the north-to-south meridional heat transport in the upper troposphere, leading to decreased moisture transport toward the Northern Hemisphere at the surface. As a result, the ITCZ shifts southward (Kang et al., 2008; Donohoe et al., 2013), weakening the monsoon flow and causing a decline in precipitation over the Sahel region. The role of natural variations in Atlantic temperature has also been emphasized by Shanahan et al. (2009) to explain the recurring decadal- to centennial-scale severe droughts in the Sahel prior to the20th century.

The role of the Indian Ocean in Sahelian rainfall variability is linked to the stabilization of the tropical atmospheric column due to warming in parts of the tropical oceans. Deep convection is favored by increased SST, which warm the upper troposphere and raise the convective threshold across the tropics. Specifically, for convection to occur, the atmospheric boundary layer must acquire sufficient moist static energy from additional moisture to become convectively unstable. However, in regions where moisture availability is limited - such as the Sahel or the edges of convective zones - the threshold may become too high to trigger convection and precipitation. This phenomenon, known as the «upped-ante» mechanism (Neelin et al., 2003), leads to negative precipitation anomalies along the margins of convective regions.

While SST patterns provide the broader context for Sahelian rainfall variability, they do not fully account for the magnitude of these changes. A secondary amplifying role is played by bio-geophysical feedbacks (Kucharski et al., 2013), wherein, for instance, reduced vegetation - resulting from decreased rainfall - leads to increased surface albedo and reduced evaporation, further intensifying the drying trend (Fig.0.9). This evidence underscores the potential climatic impact of significant LUCs at local and regional scales (see also Findell et al. (2009)). Initiatives such as the Great Green Wall warrant a thorough evaluation to assess their

regional climate implications.

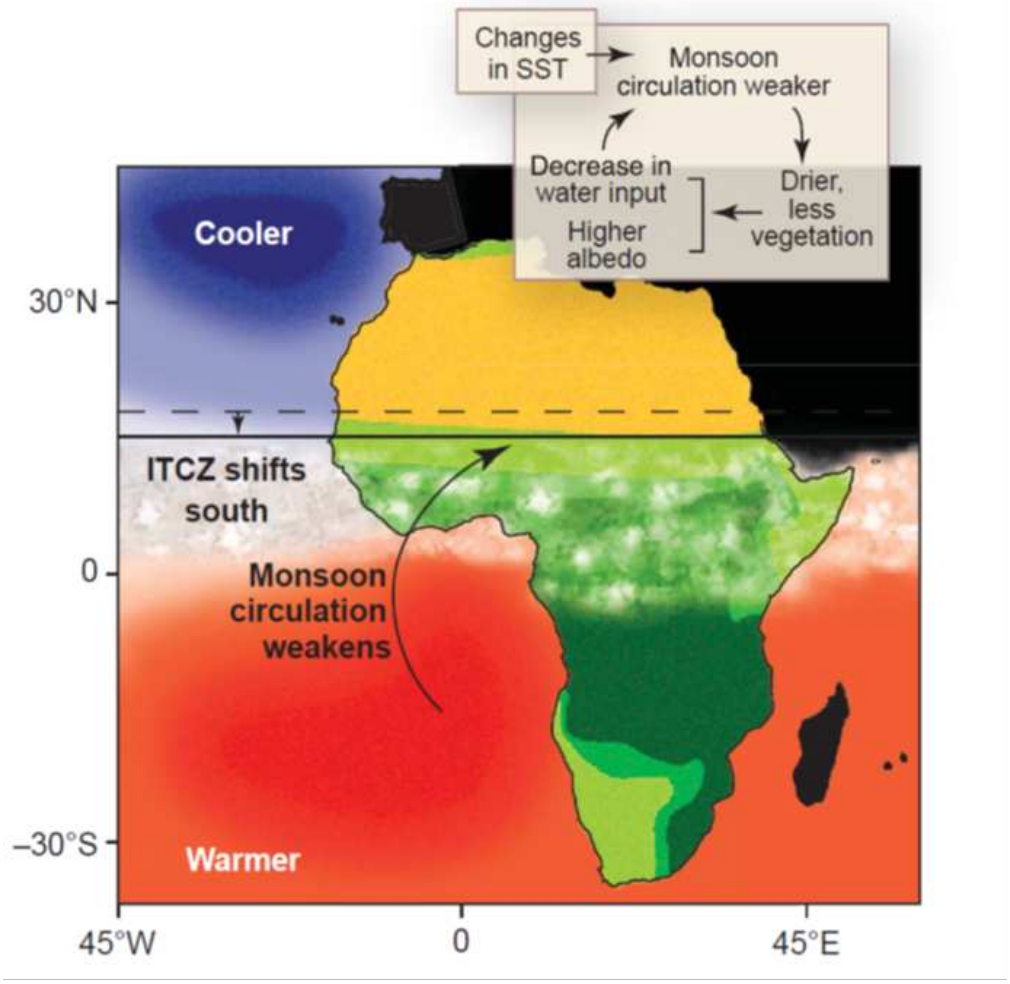

Figure 0.9: Schematic representation of main mechanism acting on Sahelian rainfall. Meridional gradient in Atlantic SST with a cooler north-Atlantic Ocean and warmer south Atlantic and Indian oceans determines a southward shift of the Hadley circulation and the ITCZ, weakening the African monsoon circulation. The decrease in precipitation is exacerbated by land-atmosphere feedbacks through natural vegetation and land cover change. From Zeng (2003).

0.6 The impact of the GGW over western Africa in climate model experiments

In recent years, only a handful of studies have investigated the potential impact of an afforested Sahara (Ornstein et al., 2009; Kemena et al., 2018) or a Sahelian green belt project (Bamba et al., 2019; Saley et al., 2019) over northern Africa using climate models. Ornstein et al. (2009) used the GISS GCM with 4°

latitude and 5° longitude resolutions, replacing Sahara with an evergreen, tropical rainforest. They found a significant increase in precipitation over the Sahara and the Sahel regions. Kemena et al. (2018) used the Community Earth System Model (CESM) 1.0 with 1.9°x2.5° horizontal resolutions in a 50 years simulation in order to study the atmospheric feedback from an irrigated and afforested (with a fully-grown tropical forest) Sahara. Their simulation showed a relevant cooling of the Sahara region and a significant increase in evaporated water, the majority of which, is advected out over the Sahel zone, the coast of Guinea and the tropical Atlantic. However, the conducted experiments were not representative of a realistic GGW, due to a wider afforested area over the whole Sahara compared to the GGW region.

The potential impact of reforestation in West Africa is evaluated by Abiodun et al. (2012) using the International Centre for Theoretical Physics Regional Climate Model (RCM), version 3 (RegCM3, Pal et al. (2007)) for the projected climate 2031–2050 under the SRES A1B greenhouse gas concentration scenario (Nakicenovic et al., 2000). They replaced the previous vegetation classes with tropical forest. The results showed that reforestation increases the friction to the monsoon flow and weakens the meridional temperature gradient over West Africa, reducing the speed of the monsoon through the reforested zone. The upwind zones of the reforested areas are characterized by a cooling, whereas downwind zones of the reforested area warm up.

Bamba et al. (2019) and Saley et al. (2019) investigated the potential impact of a green belt along the Sahel region on the West African summer climate system. Bamba et al. (2019) used the RCM RegCM4 driven by ERA-Interim reanalysis at 50 km horizontal resolution over West Africa for the period 2000–2011. In one of their experiments, they replaced the vegetation between 13°N and 17°N, a combination of grassland, semi-desert, desert and evergreen broadleaf trees, with forest (Fig.0.10, left panel). The results showed a significant temperature decrease over the Sudan-Sahel region. Furthermore, the precipitation increased between 1 to 3 mm/day in the summer rainfall band over the Sahel. Saley et al. (2019) used the same regional model at 0.5° horizontal resolution to study the impact of a GGW on extreme events in terms of temperature and precipitation. They replaced short grass with deciduous needle-leaf trees in a grid box between 14.08°N and 15.84°N (Fig.0.10, right panel). They found a significant increase in the number of rainy days (+9%) and in the intensity of heavy rain events over the Sahel and a decrease in extreme dry spells was detected (-4%). Moreover, the GGW area was characterized by a significant decrease in the maximum temperature during summer and an increase in other seasons while the diurnal temperature range increases significantly without an evident change in temperature trends.

All these experiments were carried out with relatively coarse horizontal resolutions and may likely not adequately reproduce the impact of greening actions on rainfall. Higher resolutions, indeed, may better capture small-scale processes (e.g. short-duration convective storms) and features (e.g. the local topography). They were also highly idealized and followed the original concept of a *"wall of trees"*, replacing the pre-existing vegetation with a uniform evergreen forest. In this work, we aim to address the limitations of previous studies by employing a regional climate model with a higher horizontal resolution than those used in past research. Additionally, we implement an experimental design that more accurately represents the current GGW project, focusing on localized ecological restoration efforts. This novel approach enables, for the first time, a comprehensive evaluation of the potential climate impacts induced by the GGW.

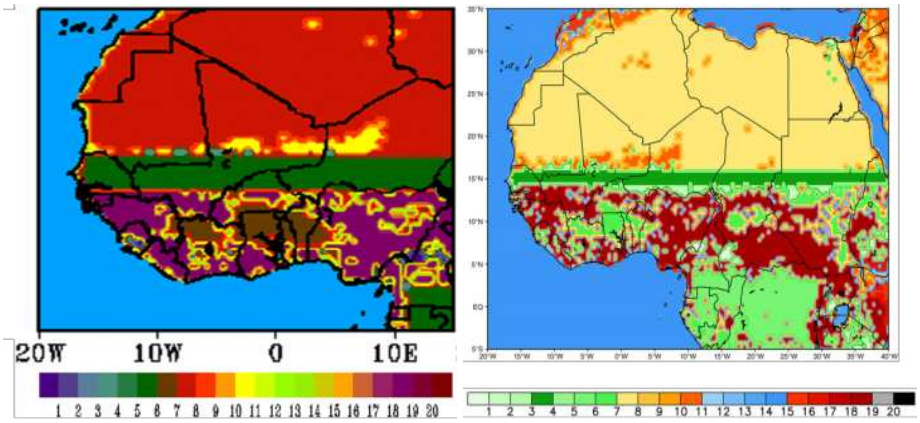

Figure 0.10: The Great Green Wall experimental designs in Bamba et al. 2019 (B19, left) and Saley et al. 2019 (S19, right). In B19, vegetation between 13°N and 17°N, a mix of grassland, semi-desert, desert and evergreen broad leaf trees was replaced with forest. In S19, short grass was replaced with deciduous needle-leaf trees in a grid box between 14.08°N and 15.84°N.

0.7 West African Monsoon and Atlantic Tropical Cyclones

One of the first studies, which showed a relevant relationship between Sahel rainfall and ATC activity was Gray (1990). He found that, in the last century, higher values of parameters such as the hurricane potential destruction or the number of tropical cyclone tracks occurred during wet years in the Sahel region, while the lowest values are associated with dry years. These dynamics are associated with contrasting SST anomaly patterns and different values of wind shear between the upper and the lower troposphere. Landsea and Gray (1992) proposed two physical mechanisms to explain the covariation between western Sahelian rainfall and Atlantic hurricane activity. The first mechanism is associated with stronger wind shear during dry years

and weaker wind shear during wet years over the main TC development region. The second mechanism looks at the AEWs. When their amplitude is bigger, during wet years, a more concentrated, persistent deep convection develops over the main formation region of TCs. On the contrary, during dry years, the amplitude of these atmospheric waves is smaller and the deep, organized, convection is inhibited. Also, Thorncroft and Hodges (2001) looked at the amplitude of the AEWs and found that ATC activity may be influenced by the number of low-level amplitudes AEWs leaving the West African coast, rather than the simple total number of AEWs.

Goldenberg and Shapiro (1996) pointed at the teleconnections among the Sahelian rainfall, the Atlantic major hurricane activity and the El Niño–Southern Oscillation (ENSO). ENSO is a periodical (2-7 years) natural phenomenon characterized by change in ocean temperatures (and consequently in the slope of the thermocline) in the equatorial Pacific, which is coupled with changes in the atmospheric circulation. ENSO influences climate patterns in various parts of the world by teleconnections, spatial patterns in the atmosphere that link weather and climate changes across the globe (Timmermann et al., 2018). Their results showed an association among positive eastern Pacific SST, negative Sahelian rainfall anomalies and a suppressed Atlantic basin tropical cyclone activity. The physical mechanism is based on a near-zonal circulation with upper-level westerlies and lower-level easterlies that increase the vertical wind shear in the main development region. Moreover, the inter-annual variability of major hurricane activity explained by Sahel rainfall is almost three times that explained by the eastern Pacific SSTs. A plausible explanation is that the SST-associated vertical shears are more equatorially confined, so that the vertical wind shear for the main development region have a stronger association with the rainfall over the Sahel.

Afterwards, a relationship between ATC multidecadal variability and its relationship with Sahel rainfall by means of the Atlantic Multidecadal Variability was proposed by Goldenberg et al. (2001). Atlantic SSTs seem to drive the interdecadal tropical storm activity over the Atlantic basin in the experiments ran by Vitart and Anderson (2001) by modulating the Convective Available Potential Energy (CAPE, a thermodynamic contribution) and wind shear (dynamic contribution). Multidecadal Sahel precipitation anomalies can force the atmospheric circulation, impacting on the wind shear multidecadal variability that in conjunction with change in SSTs influences the tropical cyclone activity (Aiyyer and Thorncroft, 2011). Finally, Russell et al. (2017) detected that 61% of TCs originated from AEWs and an additional 11% due to indirect effects of AEWs activity. They also found that the correlation between seasonal mean eddy kinetic energy (EKE), a quantity of AEW activity, and TC genesis, peaks in the lower troposphere below the southern AEW storm track,

whereas the mid-level AEW activity is a poor predictor of TC genesis. They concluded that 1000–800 hPa EKE below the southern side of AEW may be a useful precursor for seasonal TC activity.

The relationship between Sahelian rainfall, the WAM and ATCs has been also investigated by paleoclimatic studies. The Green Sahara Period (GSP, ∼11,000 – 5,000 years ago) was characterized by a strengthening of the WAM triggered by an increased boreal summer solar radiation between 15,000 and 6,000 years ago (Pausata et al., 2020). More intense summer rainfall led to an expansion of the vegetation, lakes and wetlands over northern Africa. Ocean and vegetation-dust–albedo–precipitation feedback played a role of amplification of the summer rainfall (Kutzbach et al., 1996; Timm et al., 2010; Pausata et al., 2016; Messori et al., 2019). GSP was characterized by more favorable environmental conditions for the ATC development due to the presence of vegetation over the region, leading to an increased ATC activity (Pausata et al., 2017a; Dandoy et al., 2021). Pausata et al. (2017a) found that the greening of the Sahara and resulting reduced airborne dust concentrations led to a more favorable TC environment compared to the simulation using sole orbital forcing, with the wind shear and the potential intensity representing the most important environmental parameters driving the changes in TC activity. Vegetation changes show a worldwide effect, related to westward migration of Walker circulation induced by WAM changes, whereas the impact of dust is limited to the Atlantic region. While the role of AEWs on TC activity change is clear at the synoptic scale, there is a vigorous debate in the scientific community about their influence on climate scales. The importance of atmospheric disturbances (the so-called TC seeds) such as the AEWs on TC genesis is still debated (Hsieh et al., 2020; Sobel et al., 2021; Emanuel, 2022). Some studies reproduced the interannual variability of Atlantic TC activity without including AEWs (Emanuel et al., 2008; Emanuel and Jagger, 2010; Saunders et al., 2017; Patricola et al., 2018; Danso et al., 2022). Some results pointed to large scale environmental conditions as important predictors of tropical cyclogenesis (Emanuel et al., 2008; Caron and Jones, 2012; Hoogewind et al., 2020; Emanuel, 2022). Different genesis indices have been designed to reproduce spatial and seasonal probability of TC occurrence based on this finding (DeMaria et al., 2001; Emanuel and Nolan, 2004; Tippett et al., 2011). On the other hand, other studies highlighted the role of TC seeds in TC frequency (Thorncroft and Hodges, 2001; Hsieh et al., 2020; Yang et al., 2021; Yamada et al., 2021; Hsieh et al., 2022).

The evidence presented in these studies raises the question of whether the GGW can influence tropical cyclone activity by altering WAM dynamics and Sahelian rainfall, and consequently affecting both large-scale atmospheric conditions and the disturbances that underpin TC genesis and motion—as well as, more broadly, the overall circulation over the Atlantic Ocean.

0.8 TC trackers and synthetic TC models: two different approaches for TC simulation

Climate projections are associated with a large range of uncertainty, especially with TCs. Short length of tropical storm records and their relative rarity, low resolution of GCMs – which inhibits simulations of realistic TCs (Camargo and Wing, 2016; Roberts et al., 2020) - and the global variability in population do not allow to obtain robust results. Uncertainties on the future evolution of TCs limits the scientific research as well as global risk analyses, influencing the evaluation of their financial impacts.

In the past decades, scientists have developed two different approaches to reduce uncertainties and produce more robust results. One approach is based on the use of TC trackers to detect and track TCs using large scale environmental factors from high resolution climate models. TC trackers used with high resolution regional climate models forced by GCMs (Landman et al., 2005; Knutson et al., 2008) represented an important improvement in TCc studies (Manganello et al., 2012; Murakami et al., 2015; Roberts et al., 2020). TC trackers can be divided in two main categories: “physics-based” and “dynamics-based”. Physics-based TC trackers are based on thermodynamical variables with detection of a local minimum sea-level pressure (SLP) and the TC warm core (Camargo and Zebiak, 2002; Murakami, 2014; Horn et al., 2014; Chauvin et al., 2006; Zarzycki and Ullrich, 2017). Different levels of criteria are also applied based on surface wind speed and/or vorticity. Dynamics-based trackers are more related to dynamical variables derivatives of the velocity such as vorticity (Strachan et al., 2013; Tory et al., 2013).

Limitations of TC tracking hinder accurate hazard and risk assessments. Specifically, TC tracking often fails to capture enough tropical cyclones, particularly major storms in specific regions. In particular, TC trackers struggle to generate a properly large number of consistent storms, making it challenging to accurately estimate robust return periods for extreme cyclones making landfall in different locations. These limitations make TC trackers not well-suited for modelling the financial risks associated with tropical cyclones. Furthermore, model resolutions can influence the ability of the models to simulate intense TCs (Reed and Jablonowski, 2011; Zhao et al., 2012; He and Posselt, 2015; Kim et al., 2018; Camargo et al., 2020) with low-resolution models (100-200 km horizontal resolution), which cannot simulate most intense TCs (Cat. 4-5) at all. Davis (2018) also challanged the ability of 25-km-grid models to accurately simulate category 4–5 TCs without errors in spatial attributes of the wind field. Dynamical and physics cores of the models can also affect simulated TC properties (Vidale et al., 2021). Higher-resolution models generally capture TC properties more realistically (IPCC, 2023). Furthermore, TC frequency is also highly dependent on criteria of tracking algorithms (Camargo, 2013; Wehner et al., 2015; Zarzycki and Ullrich, 2017; Roberts et al., 2020). Moreover,

detection rates in TC tracking are generally around 80% of the observed tracks, causing an underestimation of TCs (Bourdin et al., 2022) even when high resolutions are considered. Furthermore, this approach does not solve the problem of data scarcity and short temporal ranges.

To address these limitations, hybrid approaches—combining physical and stochastic methods—were introduced in the late 2010s in the field of catastrophe modeling and the reinsurance industry. These approaches are based on the idea to synthetically produce a huge amount of TC tracks. Purely statistical or statistical-dynamical techniques have been developed with a combination of statistical methods and simplified dynamical models forced by large-scale environmental conditions taken from reanalyses or GCMs. These models are characterized by three main components to produce genesis, track and intensity of a storm. We provide a more detailed description of the current status of synthetic TC models in Chapter 4.

A recent intercomparison among some of these global TC models (Meiler et al., 2022) showed a good agreement over basins rich in TCs whereas the largest variability and highest uncertainty are present over basins with few TCs and for infrequent and highly disruptive landfalls over all basins. Other sources of uncertainties come from the small size of the TC distributions and the type of information such as the number of variables, direct and indirect calculations.

0.9 Objectives of this thesis

The potential climate impacts of the most recent GGW plan have not yet been adequately evaluated in the scientific literature, depriving stakeholders of a reference to formulate effective policies for the realization of the project. Without a deeper understanding of the climate changes associated with the project, land restoration goals may not be achieved. GGW may, indeed, affect climate of northern Africa as well as far-afield regions as suggested by recent modelling studies (see Sec.0.7).

In the first part of the PhD project, we investigate the impacts of the GGW on the WAM and the northern African climate using a high-resolution atmospheric RCM under two future greenhouse gas concentration pathways. In the second part, we look at the potential change induced by the GGW on ATC activity using two different approaches. The former is based on TC trackers, which use large-scale fields of GCMs and RCMs to detect and track the storms over the TC basins. The second approach is based on synthetic TC modelling, a method, which produces thousands of synthetic TC tracks to overcome TCs data scarcity and short-length TC records (See Sec.0.8 and Sec.4). In this PhD work, we provide a more physics-based version

of a recent hybrid global TC model developed at the Université du Québec à Montréal, the UQAM-Tropical Cyclone Wind model (UQAM-TCW, Carozza et al. (2024)). This upgraded version allows to better investigate future changes in TC activity and risk under climate change compared to the previous version of the model. Moreover, in future works, it could be also possible to connect both approaches to evaluate potential GGW-induced impacts on TCs activity. In summary, the objectives of this thesis are:

1. The evaluation of the potential impacts of the Great Green Wall on the West African Monsoon (WAM) and northern Africa climate.;
2. The evaluation of the potential impacts of the Great Green Wall on the Atlantic tropical cyclone activity.;
3. The evaluation of future change in TC activity and risk in the North Atlantic. Preliminary results are also provided for the North-West Pacific in Section D.

0.10 Structure of the thesis

This thesis is structured into an introduction, a methodology part, three main chapters (each one with the corresponding Supplementary Materials), each focusing on one of the main objectives above mentioned, and conclusions.

In the first chapter, we evaluate the potential regional climatic impact of the GGW by looking at changes in mean and extreme temperature and precipitation as well as aridity and heat indices. We also provide potential mechanisms behind the regional climatic changes. The study has been published in One Earth in February 2024 (Ingrosso and Pausata, 2024) under the title: *Contrasting consequences of the Great Green Wall: Easing aridity while increasing heat extremes*.

The second chapter is focused on the impact of the GGW on Atlantic TCs activity. We focused on ATC genesis and some TC metrics changes investigating the role of AEWs and large scale factors on the effect of the GGW on ATCs. The manuscript is under review in Global and Planetary Change under the title: *Exploring the impact of the Great Green Wall on Atlantic Tropical Cyclone activity*.

Finally, the third chapter points to an extension of the UQAM-TCW model. UQAM-TCW is a statistical-dynamical TC model, which produces a large sample of synthetic TC tracks in order to properly assess cli-

mate risk associated with change in TCs activity. In this chapter we present the preliminary results of the implementation (UQAM-TCW2) of the cyclogenesis and the displacement modules and their connection with the intensity simulator already developed in Carozza et al. (2024). The idea behind this chapter is to provide a more physics-based model compared to the previous version by replacing ENSO phases and index predictors with large scale environmental factors involved in the TC formation and motion. The revised version of the model could be forced in future works not present in this chapter by environmental factors from GEM simulations described in the previous chapters to create a large set of TC tracks and assess the financial risk of the GGW project. The assessment of the financial impacts of climatic hazards, such as tropical cyclones, presents a fundamental challenge, as both the private sector (e.g., energy plants, coastal tourism, harbors) and coastal communities can suffer from physical damage to infrastructure, disruptions to business operations, and property losses. This type of analysis requires a robust sample to accurately estimate the likelihood of TC landfalls at specific locations with a given wind strength, enabling the proper calculation of return periods and probability distributions for each site. Traditional TC tracker approaches generate a limited sample of tracks, making them insufficient for this purpose. On the other hand, statistical and hybrid TC models provide a much larger dataset, allowing for a more comprehensive assessment of TC landfall probabilities.

The concluding section presents a summary of the results of the three different studies, discuss aspects of novelty and improving for the scientific community and risk modelling sectors and their limitations. Finally, potential ideas for future research are discussed.

CHAPTER 1

METHODOLOGY

1.1 Methods

1.1.1 Climate model simulations

To investigate the potential climate impacts of the GGW, we employed a higher-resolution ($\sim$13 km) atmospheric model (Canadian Regional Climate Model 4.8, CRCM/GEM4.8, Girard et al. (2014), McTaggart-Cowan et al. (2019)) with 57 vertical levels topping at 10 hPa. The regional climate model is driven by global simulations carried out with the Global Environmental Multiscale (GEM, Côté et al. (1998)) model at 0.55° horizontal resolution and 73 vertical levels topping at 2 hPa. We ran sensitivity experiments under two distinct greenhouse gas concentration pathways: the Representative Concentration Pathway (Moss et al., 2010) 2.6 (RCP2.6) and 8.5 (RCP8.5). Four distinct GGW scenarios characterized by varying vegetation densities (low, medium, high, and extreme) are considered. The scenarios are based on official documents of the GGW initiative (PAGGW, 2018) and the pronouncement of the "Commission de l'Union africaine and APA" in 2012.

1.1.2 Model evaluation

The evaluation of CRCM/GEM4.8 was based on a comparison with its parental global model GEM4.8, observations and one Reanalysis. Observations come from the Tropical Rainfall Measuring Mission (TRMM, Gebremichael and Hossain (2010)) and from the high-resolution gridded multivariate climate dataset from the Climate Research Unit (Harris et al., 2020) while reanalysis data from the European Centre for Medium-Range Weather Forecasting (ECMWF)'s fifth generation climate reanalysis dataset - ERA5 Reanalysis output (Hersbach et al., 2020). We consider mean precipitation distribution, the diurnal cycle and the rainfall intermittency in terms of Consecutive Dry Days (CDD) for the period 2000–2019.

1.1.3 Experimental design

The experiments were performed for two distinct 30-year periods One experiment was run under the present climate (Present Day, 1990–2019) and two under RCP2.6 and RCP8.5 future scenarios (2071–2100). They represent the reference experiments. Other four experiments were run under the four different levels

of vegetation density (GGW_{LOW}, GGW_{MED}, GGW_{HIGH} and GGW_{EXT}) per each emission pathway. Then a total of 11 experiments have been carried out (TableB.2). The model domain covers an area between 3°S-48° N and 99°W-52°E (Fig.A.1). This region allows to investigate potential changes over northern Africa as well as over the north Atlantic basin.

The referenced present-day (PD) simulation presents a percentage of desert and bare soil of 72% over the GGW region. The four GGW scenarios are characterized by a lower percentage of desert compared to the Present Day (See Experimental Procedure in Sec.2). The change in type of vegetation in the GGW scenarios follows the model vegetation scheme and the plantation plans present in the main documents produced by the PAGGW (2018). No change in percentage was considered for land cover categories such as urban, swamp or crops being difficult to quantify the potential future evolution of these categories. Potential limitations of this modelling study are represented by fixed SST and the lack of dynamic vegetation. Indeed, several studies show the importance of the feedback of SST or vegetation at the interannual and interdecadal variability (Zeng et al., 1999; Giannini et al., 2013; Rodríguez-Fonseca et al., 2015). Moreover, convection is parameterized in the model. This could be a limit to properly reproduce rainfall over a region where 70–90% of the annual precipitation is produced by Mesoscale Convective Systems (Nicholson et al., 2013). Jungandreas et al. (2023) showed similar results between parameterized convection simulations and convection-permitting models when increase vegetation over the Sahara/Sahel region is considered. On the contrary, other studies highlighted that parameterized convection models show an opposite change related to the soil-vegetation feedback compared with convection-permitting models in terms of land surface forcing response (Hohenegger et al., 2009; Taylor et al., 2013).

1.1.4 The TC tracker

The classic detection and assessment of TC activity and variability is generally based on tracking algorithms (TC trackers) used over climate models and reanalysis output. Trackers identify cyclonic environments associated with a warm core, creating the whole storm trajectory by linking them to its path. The TC tracker used in this study (Caron et al., 2011) applies a three-step procedure (storm identification, storm tracking and storm lifetime) to detect tropical cyclones, following Walsh et al. (2007)'s recommendations. The tracker provides a double filtering approach like the one applied in Caron and Jones (2012) to properly reproduces the genesis and dissipation phases of TCs, avoiding counting twice in the case of a temporary decrease of intensity followed by a restrengthening. Firstly, weaker detection criteria were considered to detect all storm

centers; secondly, enforced criteria are used to finally detect the storm. Finally, TC centers are classified as “strong” centers if they satisfy the enforced criteria. More information about the criteria used in the TC tracker here can be found in Dandoy et al. (2021). A potential limitation of approaches using TC trackers is in their TC underestimation compared to observations, with 80% of the observed tracks, which indicates low detection rates (Bourdin et al., 2022).

1.1.5 Climate indices

In this study, different temperature and precipitation climate extreme indices were here considered as defined by the Expert Team on Climate Change Detection and Indices (ETCCDI, Frich et al. (2002), Zhang et al. (2011). For the temperature, we calculated the annual extreme of daily maximum and minimum temperature (TXx and TNn, respectively), and the number of nights with daily minimum temperature above 20°C (tropical nights [TR20]). As a measure of drought, we considered the CDDs, the maximum number of consecutive days with precipitation lower than 1 mm. Finally, for change in heavy precipitation, we selected the annual maximum of the precipitation amount fell in 5 consecutive days (RX5), the annual total precipitation from days with an amount of precipitation above the 95th percentile (very wet days, R95p), and the number of days per year in which the daily precipitation exceeds 1 mm (rainy days, RR1mm). We also consider the De Martonne Aridity Index (AIDM, Martonne (1926)) to evaluate changes in aridity and water availability over the region. The AIDM is a simplified index, defined as a function of the annual mean temperature and precipitation, which provides similar results to other aridity indices present in the scientific literature. The heat index is based on Rothfusz’s regression equation (`https://www.weather.gov/media/ffc/ta_htindx.PDF`).

1.1.6 The UQAM-TCW2 model

UQAM-TCW (Carozza et al., 2024) is a statistical-dynamical model, which produces large samples of synthetic tracks and can be forced by reanalyses or climate models. In particular, the first version of their model is forced by the output of the 40-member ensemble of fully coupled NCAR CESM1- Large Ensemble (LE) simulations run under the RCP8.5 pathway. The model is based on different components such as cyclogenesis, displacement and intensity modules, which produce a storm with associated wind speed. The model also provides a wind profile along each track which is based on empirical approach to represent TC size and radial profiles. The method recalibrates that one in Willoughby et al. (2006) for each basin using IBTrACS’ wind radii data available since approximately 2000.

The El Niño–Southern Oscillation (ENSO) phase and index calculated by the monthly climate model output are used as predictors for the cyclogenesis and the displacements modules, respectively. The modules are based on an inhomogeneous spatial Poisson point process and 2-D Brownian motion, respectively. The intensity component is based on the FAST intensity simulator (Emanuel, 2017) fed by the monthly CESM1 variables. FAST is characterized by a set of 2 coupled nonlinear ordinary differential equations where the surface circular wind speed and inner core moisture are the prognostic variables.

In this study, we provide a more physics-based version of the model (UQAM-TCW2) to properly evaluate the future impact of climate change on TC activity and hazards. Cyclogenesis and displacement modules are based on a logistic and a multiple linear regression, respectively. In the former, physical variables, which represent important factors for TC genesis are considered as predictors of the model such as SST, potential intensity, relative or absolute vorticity at 850 hPa, wind shear between 250 and 850 hPa, and relative humidity at 700 hPa. In the displacement module, the meridional and zonal displacements of the storm represent the response variable while the Coriolis parameter, the steering flow calculated between 300 and 850 hPa for a radius of 200 km from the TC center and the previous meridional and zonal displacements are considered as good predictors for the storm motion (more details are provided in Chapter 4).

For the model training, we use the ERA5 Reanalysis output as predictors and the tracks from the International Best Track Archive for Climate Stewardship (IBTrACS, `https://www.ncei.noaa.gov/products/international-best-track-archive,dataaccess:03/10/2022`) as response for the period 1980-2019. This temporal range covers the modern era of satellite observations (Schreck et al., 2014). In the IBTrACS dataset, we select data from the U.S. agencies, with wind speeds as 1-minute average sustained winds. The first 20 (of 40) CESM1-LE member output are considered to force the model and determine past and future changes in TC hazard and risk over a period of 40 years for a total of 800 model years (MY) for each simulation. The North-Altantic basin - according to the basin definition on IBTrACS - is considered in this study (Chapter 4), but preliminary results for the North-West Pacific are also shown in the Supplementary Materials of Chapter 4 (Sec.D) . A potential limitation of this method is in the choice of the predictors, which can provide completely different results in future simulations (see for instance the “humidity” problem reported in (Lee et al., 2020)). Another limitation in our method is in the use of a single climate model ensemble (CESM1-LE), which limits the robustness of our results.

1.1.7 TC metrics

To analyse change in TC activity, we select the main TC indices and metrics associated with these storms, which are described below. The Genesis Potential Index was developed by Emanuel and Nolan (2004) (ENGPI). This index is a measure of potential genesis of TCs based on four environmental parameters: the low-level vorticity, the vertical wind shear, the midlevel relative humidity, and the potential intensity. It is one of the most widely used indices and it replaces sea surface temperatures considered in previous indices (Gray (1979), Ryan et al. (1992)) with potential intensity. It is defined as:

$$GPI = |10^5\eta|^{3/2}(H/50)^3(V_{pot}/70)^3(1+0.1V_{shear})^{-2} \tag{1.1}$$

where V_{shear} is the magnitude of the vertical wind shear (in ms^{-1}) between the upper (200 hPa) and lower (850 hPa) troposphere, η is the 850hPa absolute vorticity (in s^{-1}), H is the relative humidity at 700 hPa and $Vpot$ is the potential intensity (PI, in ms^{-1}).

Accumulated Cyclone Energy (ACE, Bell et al. (2000)) conflates frequency, lifetime, and intensity of tropical cyclones occurring in a basin over a given period. It is defined as the sum of the squares of the estimated 6-hourly maximum sustained surface wind speed (in knots) for all tropical cyclones, for snapshots in which the storms reach 35kt or higher divided by 10000. ACE is strongly influenced by the number of storms making a real comparison between observations and tracked TCs from climate model simulations or thousands of synthetic TCs impossible. To overcome this problem, we normalised ACE by dividing for the total number of storms.

The Lifetime Maximum Intensity (LMI) is the peak of wind speed reached by each TC during its lifetime (Elsner et al., 2008) and it represents an integrated statistic of TC intensification. Finally, the translation speed - i.e. the speed at which a storm is moving - is an important parameter as it is associated with total rainfall accumulation and TC damages (Mei et al., 2012).

1.1.8 Statistical analyses

For the statistical evaluation of the differences in the maps, the non-parametric Wilcoxon signed-rank test (Wilcoxon, 1945) is used. The level of significance considered is 5%. The Mann-Whitney and the Kolmogorov-

Smirnov tests are used to compare the distributions of different simulations in the boxplots. The Mann–Whitney (MW) test (Corder and Foreman, 2011) is used to check whether the difference in central tendency (such as the mean, the median and the mode) of two populations differs from zero. The Kolmogorov-Smirnov is generally used to check whether two variables have the same probability distribution (Conover, 1999).

CHAPTER 2

CONTRASTING CONSEQUENCES OF THE GREAT GREEN WALL: EASING ARIDITY WHILE INCREASING HEAT EXTREMES

Roberto Ingrosso[1,2,3], Francesco S.R. Pausata[1,2,3]

1 – Department of Earth and Atmospheric Sciences, Université du Québec à Montréal, Montréal, QC H2X3Y7, Canada

2 – Centres ESCER (Étude et la Simulation du Climat à l'Échelle Régionale)

3 – GEOTOP (Research Center on the dynamics of the Earth System)

ABSTRACT

The Great Green Wall (GGW) is a multibillion-dollar African initiative to combat desertification in the Sahel. However, the potential climate impacts of the most recent GGW plan on northern Africa have not yet been adequately evaluated, raising concerns about unforeseen climate ramifications that could affect stability in northern Africa and undermine the goals of the initiative. Using a high-resolution ($\sim$13 km) regional climate model, we evaluate the climate impacts of four GGW scenarios with varying vegetation densities under two extreme concentration pathways (low and high). Higher vegetation density GGW scenarios under both concentration pathways show enhanced rainfall, reduced drought lengths and decreased summer temperatures beyond the GGW region relative to the cases with no GGW. However, all GGW scenarios show more extreme hot days and higher heat indices in the pre-monsoonal season. These findings highlight the GGW contrasting climatic effects, emphasizing the need for comprehensive assessments in shaping future policies.

2.1 Introduction

The Sahel is a semi-arid transition region between the Sahara desert and the savannah and it has been considered one of the most important regional climate change hotspots throughout this century by means of a specific index defined as the Standard Euclidean Distance (Diffenbaugh and Giorgi, 2012; Turco et al., 2015). In the Sahara and Sahel regions, rainfall is closely linked with the intensity of the West African Monsoon (WAM), which is crucial for the socio-economic stability of millions of people living there (Agwe et al., 2005). Severe droughts, most likely triggered by sea surface temperature (SST) anomalies (Folland et al., 1986; Janicot et al., 1996; Giannini et al., 2003; Biasutti et al., 2008) in synergy with natural vegetation processes, land-use changes and anthropogenic emissions (Charney et al., 1975; Giannini and Kaplan, 2019), have ravaged the region in the last three decades of the 20th century (Zeng, 2003). In order to fight potential future droughts and land degradation, the Great Green Wall (GGW) has been conceived, based on the afforestation of about to 7,000-kilometre-long stretch of degraded land from Senegal in West Africa to Djibouti in the East, with the objective of enhancing the hydrological cycle, increasing local rainfall in the region. In 2007, the GGW was officially adopted by the 11 founding Sahelian countries. The initial project of a *wall of trees* has been replaced by a more feasible initiative, an integrated ecosystem management approach, which consists of a mosaic of different actions over an area within the 100 and 400 mm climatological annual isohyets (PAGGW, 2018; Turner et al., 2021). Such a project has been designed to improve both environmental and socio-economic conditions of the Sahelian countries (Goffner et al., 2019). The initiative has been selected among the first ten World Restoration Flagships of the UN Decade on Ecosystem Restoration (`https://www.decadeonrestoration.org/great-green-wall`).

Recent research on the potential effect of the Sahelian green belt project or of more generic reforestation in northern Africa is limited (Ornstein et al., 2009; Abiodun et al., 2012; Diba et al., 2016; Kemena et al., 2018; Bamba et al., 2019; Saley et al., 2019). Only a handful of studies using regional climate models (RCM) have been performed to investigate the local impact of the reforestation of part or the entire Sahel (Abiodun et al., 2012; Diba et al., 2016; Bamba et al., 2019; Saley et al., 2019). The RCMs used by such studies are relatively coarse (i.e. 40-50 km) and may likely misrepresent the impact of reforestation on rainfall. The previous experiments were highly idealized and followed the original concept of a "wall of trees", replacing the pre-existent vegetation with a uniform evergreen forest. However, the modelled area of the Wall was much broader than the 15-km width of the original initiative. Additionally, the modelling of Mesoscale Convective Systems (MCS) that are responsible for 70 to 90% of the annual precipitation in the region (Mathon et al., 2002; Lebel et al., 2003; Nicholson et al., 2013) may have been misrepresented by the relatively low resolution of these experiments. Finally, the length of their experiments ranges from 7 (Diba et al., 2016) to 14 (Saley et al., 2019) years and, therefore, not sufficiently long to capture the full extent of the climatic changes associated with the GGW.

Here, we delve into the crucial aspect of understanding the potential climate impacts of the GGW, a fundamental need to guide stakeholders in formulating effective policies for the realization of the project. To achieve this, we employed a higher resolution (13 km) climate model (Canadian Regional Climate Model, CRCM (Girard et al., 2014; McTaggart-Cowan et al., 2019)) to portray a more accurate representation of the GGW initiative. We conducted sensitivity experiments under two distinct greenhouse gas (GHG) scenario pathways - the Representative Concentration Pathway (RCP) 2.6 and RCP8.5 Moss et al. (2010)- encompassing four distinct GGW scenarios of varying vegetation densities (low, medium, high, and extreme) based on official documents of the GGW initiative (PAGGW, 2018) and the pronunciation of the Commission de l'Union africaine and APA in 2012 (see Section B for details).

Our findings revealed contrasting effects of the GGW: higher vegetation density increased rainfall, reduced drought durations, and cooled summer temperatures outside immediate borders. However, all scenarios exhibited amplified pre-monsoon heat extremes. These findings underscore the pivotal importance for policymakers to consider these multifaceted effects for effective environmental policy planning and comprehensive assessment of potential regional ramifications.

2.2 Results

2.2.1 GGW enhances mean and extreme rainfall

Our model simulates no significant changes in rainfall over the Sahel during the 30-yr averaged summer season (June to September - JJAS) for both greenhouse gas concentration scenarios (RCP2.6-only and RCP8.5-only), except for a dry anomaly over Senegal and southern Mauritania in the RCP8.5-only (Fig.B.2) relative to the PD experiment. This dry anomaly under the RCP8.5-only scenario is not found in the Regional Downscaling Experiment-Coordinated Output for Regional Evaluations (CORDEX-CORE) ensemble, which shows a moderately significant rainfall increase over the western Sahel (Fig. B.25a). CRCM/GEM4.8 seems to generally exhibit an underestimation of the mean precipitation compared to the CORDEX ensemble. However, this model bias should not affect the conclusions of this study as we focus on relative changes rather than absolute changes. Nevertheless, CRCM/GEM4.8 shows a good agreement with CORDEX in the extremes of the mean precipitation statistics (Fig.B.27), although CRCM presents a higher frequency of low rain rates compared to the CORDEX experiments. The CORDEX ensemble under RCP2.6-only does not show any particular change compared to the referece period (PD) (Fig.B.25c) although shows a lower frequency of low rain rates compared to our model. For more details on the model evaluations and comparisons see Section B.

When considering the GGW scenarios, a significant enhancement of the JJAS precipitation over a large area of the Sahel is simulated in three of the GGW experiments in both RCP2.6 and RCP8.5. While no significant change, with the exception of a few small pockets, is found in the GGW_{LOW}, the GGW_{MED} and GGW_{HIGH} experiments under both concentration scenarios show a significant intensification in summer rainfall. Such intensification is more pronounced over the western Sahel, especially in GGW_{HIGH} where an increase of 100 and 200 mm is present, corresponding to an increase of 50-150% (Fig.2.1C-F). Moreover, the GGW_{HIGH} scenario shows a further increase over central and southern parts of northern Africa, affecting the regions relatively far from the wall such as southern Nigeria, Cameroon and Central African Republic. An increase between 25 and 100 mm is also present over the northern and the eastern Sahel. In the extreme experiments (GGW_{EXT}), the signal is much stronger compared to the other scenarios, with a remarkable increase in precipitation over the entire northern Africa including the Sahara Desert. The widespread rainfall increase ranges between 100 and 200 mm over the Sahelian region, representing an increase between 50% in the southern Sahel and 200% over the northern sections relative to the RCP-only experiments (Fig.2.1G-H). In addition, an increase between 250 and 500 mm is simulated in south-western Sahel. The aforementioned

dry signal over the western Sahel in the RCP8.5-only simulation is partially or totally compensated in all experiments.

The zonal means of daily precipitation over western Africa for the GGW_{HIGH} and GGW_{EXT} indicate that the effect of the GGW is not confined to the summer season, but also extends into spring and fall (Fig.B.3). Furthermore, a strengthening of the WAM south of the GGW region is simulated, bringing more precipitation outside the project area as well. A significant increase of about 1 mm/day in these GGW scenarios is present over the western Sahel from April to November compared to RCP-only projections, with peaks above 3 mm/day in August for the GGW_{EXT} simulation under the RCP2.6 pathway (Fig. B.3d). However, the strengthening of the WAM - more pronounced in the second half of the summer in both GGW_{HIGH} and GGW_{EXT} experiments - is not associated with a notable lengthening of the monsoon season. While in the RCP8.5-only (but not in RCP2.6-only) experiment the monsoon season is significantly longer (11 days, Fig.B.3f) than in the PD, no significant differences are detected between the RCPs-only and the more extreme GGW scenarios.

The positive rainfall anomalies associated with the presence of the GGWs are also reflected in a change in extreme events, decreasing the drought length and increasing the number of rainy days and the intensity of rainy events. In particular, the RCP-only experiments do not show any notable differences relative to PD in terms of Consecutive Dry Days (CDD, Fig.2.2B-C). Similar results with no clear changes in CDD are shown by several studies with the exception of a modest signal over western Sahel (Klutse et al., 2018; Diedhiou et al., 2018; Dosio et al., 2022). Opposite CDD changes considering different climate models such as the CMIP5/6 and CORDEX ones are found by Dosio et al. (2021). Finally, the Coupled Model Intercomparison Projects 6 (CMIP6) models presented in the WGI-AR6 report (Seneviratne et al., 2021) show a high model agreement in CDD decrease over central and western Sahel between 5 and 15 days in the 4°C global warming scenario. Although not significant, due to the high variability of the index in our experiments, we found a CDD decrease up to 20 days. A potential limitation in detecting CDD change in the future could also be associated with the convection parametrization as highlighted by Kendon et al. (2019), which shows better performance of a convection-permitting model at 4.5 km horizontal resolution compared to a convection-parameterized model at 25 km resolution. The GGW scenarios exhibit a significant CDD decrease over the central Sahel, with differences depending on the level of vegetation density. The GGW_{LOW} scenario shows significant CDD changes of up to -40 days under both concentration pathways between Mali and Niger (Fig.2.2D-E). A similar, but broader pattern is shown in the GGW_{MED} scenarios (Fig. 2.2), where the CDD decrease reaches parts

of Mauritania and Chad. In the GGW_{HIGH} and GGW_{EXT} experiments, the change involves a wider area up to -52 days in the central Sahel (Fig.2.2H-K). Given that the region experiences lengths of about 150 CDD in the southern Sahel and 300 CDD in the northern Sahel a year in the PD simulation (Fig.2.2A), such changes are remarkable. They indeed correspond to a shortening of droughts between 5% and 20% in the GGW_{LOW}, GGW_{MED} scenarios and up to 40% in the GGW_{HIGH} and GGW_{EXT} experiments.

The increased vegetation also leads to a significant increase in rainy days (days with daily precipitation higher than 1 mm, R1mm), between 50% and 150% over the whole area of the project in all GGW experiments, with the exception of eastern Sahel in the GGW_{LOW} scenario (Fig.B.4). Changes of more than 14 days in the GGW_{LOW} and more than 18 days for the other GGW scenarios compared to the RCP-only experiment are simulated over the project domain, cancelling out the R1mm decrease over the western Sahel under the RCP8.5 scenario. No significant change in very wet days (R95p, Fig.B.5) and 5-consecutive-day rainfall maximum (RX5, Fig.B.6) is associated with the GGW_{LOW} and GGW_{MED} experiments except for few limited areas in the latter. Changes in R95p and RX5 over central and western Sahel in the GGW_{HIGH} and GGW_{EXT} experiments are significant with an increase in both indexes of up to a 100 mm compared to RCP-only projections. Once again, this increase in precipitation is more intense and widespread in the GGW_{EXT} experiments, with an anomaly in the R95p and RX5 indexes above 125 mm over the south-western Sahel relative to RCP-only simulations.

2.2.2 Potential mechanisms behind the precipitation changes

The RCP8.5-only experiment does show a significant increase of the shallow convection just before the surface convergence zone with no evident latitudinal displacement of the convergence system (Fig.B.7c). The RCP2.6-only experiment shows no significant change in the regional circulation compared to the PD simulation (Fig. B.7 b and Fig.B.8b), which is consistent with no increase in precipitation in this experiment (Fig. B.2a). However, no significant change of the Tropical Easterly Jet (TEJ) and only a light strengthening of the African Easterly Jet (AEJ, Fig.B.8c) is simulated. Such conditions are not favourable to increased precipitation (Newell and Kidson, 1984). On the contrary, a northward expansion of the monsoon flux is detected in all GGW experiments with a stronger and more pronounced penetration of the WAM in the more extreme GGW scenarios compared to the PD and RCP-only experiments (Fig.B.7h-k). In such GGW experiments, much deeper convection relative to RCP-only experiments develops, reaching the mid-troposphere (500-600 hPa) at 15-18°N, explaining the northward expansion of the rainfall (Fig.2.1). In the GGW_{EXT} simulation,

the enhanced deep convection also occurs further south (10°N), coherently with the increase in precipitation over the whole northern Africa. Following the monsoon expansion, the northward component of the monsoon and the southward component of Harmattan winds weaken as the density of vegetation increases (and consequently the precipitation), suggesting a waning of the shallow meridional circulation (SMC), which plays a role in the amount of rainfall in the Sahel (Shekhar and Boos, 2017). This weakening may partially be due to the increase in surface roughness related to replacing desert and bare soil with trees and shrubs (Tab.B.5). The monsoon northward expansion is associated with a proportional increase of the easterly jet at higher altitudes and a decrease of the AEJ, going from almost no changes in the GGW_{LOW} simulations (Fig.B.8d-e) to large and significant changes in the GGW_{EXT} experiments (Fig.B.8f-k). At the synoptic scale, a remarkable increase in the African Easterly Waves (AEWs), which are responsible for most of the precipitation over the Sahel, is simulated in the presence of the GGWs under both concentration pathways with a clear increase over the whole southern part of western Africa, peaking over the Atlantic Ocean at around 10°N (Fig.B.9). Such an increase in AEWs, combined with the change in the easterly jets, leads to more precipitation over the area due to increased potential vorticity (Nicholson et al., 2007). The increase in AEWs may be triggered by the increase in heat release associated with the increase in convection (Thorncroft et al., 2008) and enhanced by positive feedback with the convection itself (Nicholson et al., 2013).

The large increase in the moisture flux and total moisture flux convergence (TMFC) in the RCP-only experiments compared to the PD experiment (Fig.B.12c and Tab.B.4) over the region is not associated with increased precipitation in these experiments. This change does not indeed trigger any significant modification in deep convection (Fig.B.7b,c). In the GGW experiments, a slight increase in the TMFC compared to the RCP-only experiments is found. The changes in vegetation density in the GGW only modestly perturb the TMFC. In relative terms, the main difference compared to the RCP-only experiments is an increase in evapotranspiration due to the GGW (Fig.B.11 and TabB.4). This is proportional to the vegetation density and allows deeper and more effective convection (Fig.B.7), leading to an overall increase in precipitation in the region. This suggests a fundamental role of evapotranspiration in the GGW-induced changes in rainfall, with the increase in the TMFC giving a limited contribution. Consequently, land-atmosphere interactions through vegetation and albedo feedbacks (Kutzbach et al., 1996; Messori et al., 2019) seem to play a crucial role in triggering the change in the WAM dynamics rather than large-scale circulation change associated, for example, with anomalous SST as in the RCP8.5-only experiment.

2.2.3 GGW impacts on temperature

Surface temperature in the Sahel is characterized by a bimodal pattern of the annual cycle with two maxima before and after the rainy summer season. The hottest season corresponds to the boreal spring, just before the onset of the WAM, which then causes a temperature decrease. The RCP2.6-only and RCP8.5-only simulations show highly significant warming over the whole of northern Africa during the monsoon season (JJAS, Fig.2.3 A-B). In particular, in the Sahel, the warming ranges between 0.5°C and 1°C in the RCP2.6-only experiment and over 4°C warming region, with a peak of more than 5°C over the eastern side, in the RCP8.5-only scenario, in overall good agreement with the CORDEX-CORE ensemble (Fig.B.26, for more details, see Note B.1).

When the impact of the GGW is considered, no significant JJAS change in the mean temperature is shown in the GGW_{LOW} scenario compared to the RCP-only simulations (Fig.2.3 C-D) whereas a cooling over the central-western Sahel with a peak of up to 1.5°C is simulated in the GGW_{MED} experiment (Fig.2.3E-F). The GGW_{HIGH} scenario shows a significant decrease in temperature over a much wider area than the GGW domain itself, a clear consequence of the strengthening of the WAM (Fig.2.3G-H). This cooling ranges between 0.5°C and 1°C for both concentration scenarios, with a peak larger than -1°C in central Mali and southern Niger. These anomalies are doubled and extend well into the Saharan desert when considering the GGW_{EXT} experiment (Fig.2.3I-J). In the GGW_{HIGH} experiment under the RCP2.6 pathway, the GGW cooling largely offsets the warm season (JJAS) warming signal over the area (Fig.B.16b) caused by the increased GHG concentrations. This cooling is a consequence of increased cloudiness (Fig.B.13b, bottom), which reduces the amount of sunlight reaching the surface, and rainfall, which enhances evaporation. Moreover, the increase in evapotranspiration associated with the higher vegetation density (Fig.B.11) may also play a role in the simulated temperature decrease in summer. Hence, the potential warming associated with the reduced albedo is overshadowed by the cooling from evapotranspiration and increased cloud cover. On the contrary, warming is present during the pre-monsoon season (March to May, MAM, Fig.B.17). While the summer cooling extends well beyond the boundaries of the GGW, the warming is confined to the area in which the vegetation change has been applied and ranges between 0.25 and 1°C with a peak over 1°C in the central Mali and southern Niger(Fig.B.17a-f). The warming signal in the GGW_{EXT} is wider – consistent with a larger area of the wall – and stronger compared to the other GGW experiments- and is generally between 0.5° and 1.5°C with several peaks shy of 2°C in different parts of central Sahel (Fig.B.17g-h). Such warming is a clear consequence of the decrease in albedo associated with the vegetation cover (Fig.B.15). Furthermore, a lack

of enhanced evaporative cooling as this is in the dry season and the soil is probably dry so the trees don't evaporate as much as later in the season.

A cooling during the monsoonal season and a warming during the pre-monsoonal season show that the GGW produces contrasting seasonal impacts over the region. This effect can be clearly seen by looking at the annual cycle of maximum and minimum daily temperature over the Sahel, where the warming is also present during the fall and the winter (Fig.B.18a). The temperature range between the climatological hottest day of the year in spring and the summer coldest day increases by about 0.4°C in GGW_{MED}, and 1°C in GGW_{HIGH} and GGW_{EXT} scenarios relative to the RCP-only experiments. The summer minimum temperature in the GGW_{EXT} experiment under the RCP2.6 pathway presents values comparable to the PD (Fig.B.18b), increasing the seasonal temperature range between spring maximum and summer minimum temperature. Furthermore, in spring the minimum temperature also increases due to the higher heat capacity of grass, shrubs and trees compared to bare soil and desert, especially in the more extreme GGW experiments relative to RCPs-only.

In terms of temperature extremes, the annual hottest day (TXx) and coldest day (TNn) show an increase of about 4°C over the Sahel with peaks above 5°C in the western Sahel for TNn in the RCP8.5-only experiment relative to the PD (Fig.B.19). The GGW experiments show significant changes in temperature extremes compared to the RCP-only scenarios over the area of the project (Fig.2.4 and Fig.B.20) with an impact that is wider as we move from low to extreme cases. The increase in temperature of the coldest day of the year (TNn) reaches up to more than 1.5°C over the central Sahel in the medium to extreme vegetation density experiments (Fig.2.4A-D). The temperature increase of the hottest day (TXx) is instead smaller ranging between 0.3°C and 0.9°C with peaks of 1.2°C in central Sudan (Fig.2.4 E-H). The number of tropical nights (TR20) rises from 10 (GGW_{LOW}) to up to more than 25 (GGW_{MED}, GGW_{HIGH} and GGW_{EXT}) over the GGW area under both concentration scenarios (Fig. 2.4 I-L and B.20 i-l). For the GGW_{EXT} experiment, the results show a wider area interested with a change in TXx (Fig.2.4H and Fig.B.20h) compared to the other GGW scenarios, consistent with the larger vegetated area. Generally, the increase in the temperature extremes is primarily due to the decrease in albedo and increase in relative humidity related to the presence of the GGW: more solar radiation is absorbed during the day (lower albedo), whereas less heat is released at night (higher humidity). During the monsoonal season, the increase in cloudiness and precipitation favours a decrease in mean temperature as mentioned before. During the spring, a much smaller increase in clouds (Fig.B.14) and rainfall compared to the summer does not compensate for the increased solar radiation absorbed by

the changes in surface albedo. The minimum temperatures also increase due to an overall humidification associated with the vegetation changes, which reduces night time cooling. In the GGW_{LOW} scenarios no significant cooling in the mean and extreme daily temperature during the summer is simulated, whereas a clear increase in both mean and daily extreme temperature is simulated during the pre-monsoonal season.

2.2.4 A less arid Sahel

To detect a potential change in water availability over northern Africa associated with the GGW, we adopted the De Martonne Aridity Index (AI_{DM}, Martonne (1926). The AI_{DM} is a simple and efficient index that is defined as a function of the annual mean precipitation and temperature (for details see the Experimental Procedures), with lower (higher) values indicating higher (lower) levels of aridity. We also highlight the AI_{DM} change of the seven of the most important Sahelian cities (Fig.2.5). In the PD experiment, AI_{DM} clearly shows the abrupt transition from desert to slightly-arid conditions, with a prevalence of semi-arid/arid climate over the entire Sahel. No significant changes in the region are found in the reference future projections, except for an expected slight decrease in the AI_{DM} over the western Sahel (Fig.2.5 B-C), concurrent with the simulated precipitation deficits (Fig.B.2b).

When the GGW is considered, a significant AI_{DM} increase over central and western Sahel is present for the GGW_{MED}, GGW_{HIGH} and GGW_{EXT} scenarios, even doubling over northern Sahel in the last two cases (Fig.2.5F-K). In the GGW_{LOW} experiment, a weak significant change in AI_{DM} is simulated, especially in the southern part of Mauritania, Mali and Niger (Fig.2.5 D-E). Changes in the aridity conditions among the areas of the most important cities in the region have been assessed. Parakou in Benin is the city that shows the largest benefits moving from slightly arid to moderate humid conditions in the GGW_{LOW} and GGW_{MED} scenarios under the RCP2.6 pathway. It becomes humid in the GGW_{MED} scenario under the RCP8.5 pathway and in both RCP pathways for GGW_{HIGH} and GGW_{EXT} experiments. Bamako in Mali sees a shift from a semi-arid to moderately-arid climate in the GGW_{HIGH} and GGW_{EXT} experiments and even to slightly-arid in the GGW_{EXT} scenario under the RCP2.6 pathway. Geneina, in West Durfur (Sudan), moves from desertic to arid conditions in all GGW experiments, except the GGW_{LOW} under the RCP2.6 pathway. This wet signal reaches the southern parts of northern Africa, with Abuja, the capital of Nigeria, moving from moderate humid to humid conditions in all experiments, except in the GGW_{EXT} scenario where it jumps to very-humid conditions. Even part of the Central African Republic is touched by this decrease in the aridity conditions with the city of Bambari moving from a moderately humid to a humid AI_{DM} values in the RCP8.5-only path-

way and almost all GGW scenarios, except GGW_{LOW} under the RCP8.5 pathway. Timbuktu in Mali, currently classified as desert, shifts to an arid climate in all GGW_{EXT} experiments and in the GGW_{HIGH} scenario under the RCP2.6 pathway. Dakar in Senegal does not show any change in AI_{DM} in the GGW experiments, however, the presence of the GGWs cancels out the dry anomaly associated with the increase in greenhouse gases, avoiding the possibility of approaching desert-like conditions, as the AI_{DM} value is just shy of aridity level in the RCP8.5-only experiment. Although a widespread increase of AI_{DM} is displayed over the Sahel and sub-Sahel region, it is not sufficient to cause a transition to a wetter AI_{DM} category in the other cities.

2.2.5 Increase in Heat Stress for the local population

While our previous analysis shows a decrease in the aridity conditions over most of the Sahel and sub-Sahelian regions associated with the GGW, higher temperature during the pre-monsoonal season together with higher humidity driven by increased evapotranspiration may cause more intense heat stress on the local population. In order to investigate such potential changes in human discomfort, we calculate the Heat Index (HI) or apparent temperature, which is a metric based on temperature and relative humidity, allowing us to assess the level of heat stress on the population. The HI is a measure of the temperature that the human body feels like. A HI above 37.8°–39.4°C (100°–103°F) is considered dangerous for the local population, whereas a HI above 49.4°–51.1°C (121°–124°F) is assessed as extremely dangerous (`https://www.weather.gov/ama/heatindex`).

In the RCP8.5-only scenario, the heat index significantly increases over the whole of northern Africa relative to the PD simulation with a surge in the number of days above the 75^{th} percentile (between 200 and 250), half of which is above the 95^{th} percentile (between 100 and 175 days) over the Sahel (Fig. 2.6 A-B). The only exception is represented by an area between central Ethiopia and southern Eritrea, which does not show any significant change. In the GGWs experiments, we also considered the number of days above the PD 75^{th} and the 95^{th} percentiles and calculated their change relative to the RCP-only experiments. The HI change reflects the same pattern seen before for the temperature anomalies with an increase of HI extremes compared to RCP8.5-only experiment that is proportional to the vegetation density (Fig.2.6 C-J). In the GGW_{LOW} experiment under the RCP8.5 scenario a peak increase of 20 days above the 75^{th} and 95^{th} RCP8.5-only percentiles is simulated between southern Niger and southern Mali (Fig.2.6C-D). The GGW_{MED} scenario shows an increase between 20 and 40 days compared to the RCP8.5-only experiment over a wider area that reaches southern Mauritania and Chad (Fig. 2.6E-F). As expected, As expected, the largest increases

are simulated in the GGW_{HIGH} and GGW_{EXT} scenarios. The GGW_{HIGH} shows intensification in HI extremes between 30 and 40 days in the south regions of Mauritania, Niger and Mali relative to the RCP8.5-only experiment (Fig.2.6G-H)), while between 20 and 30 days in central and eastern Sahel. Compared to RCP-only experiments, in the GGW_{EXT}, the number of HI extreme days increases by more than 50 days over Mauritania and Mali, with central and eastern Sahel experiencing up to 40 days in several areas (Fig.2.6I-J). Especially in these highest vegetation density experiments, northern Africa generally shows a significant increase in extreme HI days with some exceptions, especially over Morocco, the Horn of Africa and the coastline along the Gulf of Guinea that experience a decrease in extreme HI days compared to the standard RCP8.5 scenario. The impact of global warming in the high emission scenario on the Sahelian HI can be clearly seen in the shift of the HI value distribution under RCP8.5 (Fig.B.21, red curve): both mean and variance increase, leading to a significant shift of the right tail of the HI distribution (values above 95^{th} percentile). The presence of the more extreme GGWs further increases the variance and the skewness of the curves, causing even more extreme HI values compared to the RCP8.5-only/RCP2.6-only experiment (Fig.B.22, light and dark green curves) across the entire Sahel except for the easternmost part (see Sahel and Sahelian cities distributions in Fig.B.23). Such an increase in HI due to the GGW is mostly a reflection of albedo and humidity changes associated with the vegetation. However, contrary to the increase of extreme temperature (Fig.2.4, Fig.B.20), the changes in HI extend well outside the GGW, due to an increase in humidity, evaporation (Fig.B.10) and evapotranspiration (Fig.B.11) over a much wider area compared to the project. In the RCP2.6 scenario, the effect of the GGW on the HI seems to strengthen as the number of days exceeding the PD 75^{th} and 95^{th} percentiles increases by more than 50 compared to the RCP2.6-only experiment. In the GGW_{EXT}, these peaks cover almost the whole Sahel (Fig.B.21c-j). HI distribution under RCP2.6 also shows a shift in the right tails for the whole Sahel (Fig.B.22) and for the Sahelian cities (Fig.B.24) with the exception of Addis Ababa (Ethiopia) and Asmara (Eritrea), in the eastern Sahel. However, as expected the change in mean and variance are much more limited than in the RCP8.5 scenario.

2.3 Discussion and conclusions

Greening projects of the Sahel aim to improve the socio-economic conditions of one of the poorest regions in the world. However, they are constrained by anthropogenic-induced changes and natural climate variability, water scarcity and limited habitable conditions. While the original and generalized idea of GGW relied on the image of a literal green wall along the Sahel, the current project has evolved into a broader integrated ecosystem management approach based on dryland regulation, regeneration of vegetation, water

retention and ecosystem conservation (Turner et al., 2023).

This study investigates potential changes in rainfall and temperature and their extremes over northern Africa associated with the development of GGW initiative under two future concentration scenarios (RCP2.6 and RCP8.5). We use a higher resolution atmospheric RCM ($\sim$13 km) and a more realistic experimental design compared to previous studies (Diba et al., 2016; Bamba et al., 2019; Saley et al., 2019), offering a set of different vegetation density scenarios for the GGW. Our analysis shows no significant increase in mean precipitation in the GGW_{LOW} experiment compared to the standard RCP scenarios without vegetation changes. On the other hand, the GGW_{MED} and GGW_{HIGH} experiments reveal an increase in mean summer rainfall ranging between 25 and 200 mm over the western Sahel, and between 25 and 100 mm over the eastern Sahel, respectively. An increase of 100-200 mm over the whole Sahel is simulated in the GGW_{EXT} scenario, with peaks between 250 and 500 mm over the south-western Sahel (Fig.2.1). The negative anomaly over Senegal and southern Mauritania in the RCP8.5-only projections relative to PD is cancelled out in these experiments. Furthermore, the positive rainfall anomalies extend well beyond the domain of the GGW, in particularly south of the GGW in the GGW_{HIGH} scenario and the whole of northern Africa in the GGW_{EXT} experiments. In terms of extreme events, the GGW experiments exhibit a clear decrease in the length of dry spells (CDD) between 5% and 15% in the GGW_{LOW}, GGW_{MED} and GGW_{HIGH} scenarios, and up to 25% in the GGW_{EXT} case (Fig.2.2). The areas affected by this change broaden proportionally to the increase in vegetation density. A significant increase in rainy days between 50% and 150% characterises the whole area of the project in all experiments (Fig.S4). However, the areas affected by such changes depend on the vegetation density and the intensification of heavy rainfall events (RX5D and R95p) is only simulated in the GGW_{HIGH} and GGW_{EXT} scenarios (Fig.B.5, Fig.B.6). These results suggest that the vegetation density is crucial in determining the effects of the GGW on rainfall, with small or negligible impacts for the low vegetation case and clear, significant impacts for the high and extreme GGW scenarios.

Previous works (Diba et al., 2016; Bamba et al., 2019) showed a larger increase in rainfall (up to 4 mm/day). However, in these studies the vegetation was replaced by forest over a wider area than our modelled GGW. On the other hand, changes in climate extremes are generally more pronounced in our study compared to previous studies (Diba et al., 2016; Saley et al., 2019), likely due to the length of their experiments (7 to 14 years), which does not fully capture the amplitude of climate variability.

In terms of temperature changes associated with the GGW, we find a different response over the Sahel de-

pending on the period of the year. In summer, a temperature decrease ranging between 0.25° and 0.5°C and between 0.5° and over 2°C is simulated for the GGW experiments relative to both RCP-only scenarios with no vegetation changes with the only exception of the GGW_{LOW} in which no significant change is simulated (Fig.2.3). In the GGW_{HIGH} and GGW_{EXT}, this cooling extends over a wider area compared to the project domain as a consequence of the increased cloud cover and evaporation associated with the strengthening of the WAM. On the other hand, an albedo-induced increase in temperature confined to the GGW domain characterises the other seasons, especially during the pre-monsoonal period, when the highest temperatures are reached in the region. Such increase in temperature ranges between 0.25 and 1°C and peaks over 1°C in central Mali and southern Niger in the more vegetated GGW scenarios. The warming signal during the pre-monsoonal season is also reflected in the changes in temperature extremes, with an increase for the hottest and coldest day of the year between 0.3°C and 0.9°C, and more than 1.5°C, respectively, for the GGW experiments (except GGW_{LOW}) compared to the RCP-only projections. The number of tropical nights increases from 10 in the GGW_{LOW} experiment to up to more than 25 in the other GGW scenarios (Fig.2.4). While the GGW_{LOW} experiment does not reveal any significant cooling in the mean and extreme daily temperature during the summer, it exhibits a clear increase in both mean and daily extreme temperature in the pre-monsoonal season, leading to an increase in the hot extremes.

These results differ from Bamba et al. (2019), which show a cooling between February and October, peaking during the monsoon season. Diba et al. (2016) and Bamba et al. (2019) showed a bigger decrease in JJAS temperature ($\sim$3°C) over the area of the project than our experiments. This is probably due to both a different interplay between albedo and evapotranspiration effects in their model and the presence of the extensive forest rather than the diversified and less dense vegetation of our experimental design. On the other hand, Saley et al. (2019) – albeit using only 14-year-long simulations – found very similar results for the hottest day of the year, suggesting this variation as a robust response.

Previous studies have, however, not considered the impact of rising temperature associated with global warming that could even offset the benefits associated with the GGW increase in rainfall over the Sahel due to increased evapotranspiration. Furthermore, the GGW vegetation would also cause an increase in humidity that may exacerbate the heat stress on the local population. In our study, we show that albeit with higher future temperatures, the GGW enhanced rainfall and drove Sahel toward less arid conditions with slightly larger changes in the RCP2.6 than in the RCP8.5 scenario (Fig.2.5). In particular, Parakou in Benin moves from slightly arid to moderate humid or humid conditions in almost all experiments, while Bamako

in Mali sees a shift from a semi-arid to moderately-arid climate in the GGW_{HIGH} and GGW_{EXT} experiments. Southern parts of northern Africa are also affected by this increase in humid conditions, with Abuja in Nigeria moving from moderate humid to humid conditions in all experiments and Bambari moving from moderately humid to a humid AI_{DM} values in the GGW_{MED} under RCP2.6 scenarios, and in all GGW_{HIGH} and GGW_{EXT} experiments. With respect to human comfort, our analysis highlights the remarkable effect of the GGW on heat stress. The number of days in which the heat index is above the PD 75^{th} and 95^{th} percentile is further increased compared to the RCP-only scenarios between 10 and 50-60 days for all the GGW experiments. The area affected by those changes varies as a function of the vegetation density, covering a small area between southern Mali and southern Chad in the GGW_{LOW} scenario and almost the whole GGW domain in the GGW_{HIGH} and GGW_{EXT} experiments (Fig.2.6 and B.21). The HI distributions in the Sahelian cities generally show a future increase in the mean and the variance for the more extreme GGWs under both concentration scenarios (Fig.B.23 and Fig.B.24). The only exceptions are found for the capitals of Eritrea and Ethiopia, in the eastern Sahel. While the Aridity Index suggests an improvement in the water availability for the region due to the presence of the GGW, the increase in the HI could lead to a worsening of the habitable conditions due to the increase in heat stress on local populations as measured by the heat index.

Our results highlight the importance of the vegetation feedback and change in albedo for the northern Africa climate as suggested by previous studies (Kutzbach et al., 1996; Messori et al., 2019), by strengthening the WAM and triggering an increase in precipitation, depending on the density of the planted vegetation, and in temperature extremes. The discussion on the crucial aspects regarding the feasibility of the GGW project, such as the potential dynamics of the Saharan boundary and vegetation productivity limits over the Sahelian region, is still open (Elagib et al., 2021).

An important caveat of our experiment is the lack of the potential SST and dynamic vegetation feedback as both are prescribed. Indeed, several studies show the importance of both feedbacks at the interannual and interdecadal variability (Charney et al., 1975; Folland et al., 1986; Janicot et al., 1996; Zeng et al., 1999; Biasutti et al., 2008; Giannini et al., 2013; Rodríguez-Fonseca et al., 2015). Although how vegetation is treated in the model may dominate the signal, the higher sensitivity of the other CORDEX models to anthropogenic forcing could lead them to a stronger response to GGW vegetation changes (see the Experimental Procedures section for a comparison between CORDEX and CRCM/GEM4.8). Therefore, a coordinated multi-model intercomparison of different GGW scenarios will be beneficial to constrain the local and far-afield climatic impacts of this initiative. Another potential caveat can be associated with limitations in

soil nutrients and other mitigating factors that are not properly represented in the model. Finally, while our simulations are performed at high horizontal resolution (∼13 km), the convection is still parameterized. Some studies argue that parameterized convection models show an opposite change related to the soil-vegetation feedback compared to convection-permitting models in terms of land surface forcing response (Hohenegger et al., 2009; Taylor et al., 2013). However, Jungandreas et al. (2023) showed that the response of the monsoon circulation in a convection-permitting model to an increased vegetation cover over the Sahara/Sahel region is qualitatively similar – albeit stronger – to that in parameterized convection simulations. New studies with both convection-permitting and parameterized convection models are necessary to better constrain this response also in light of the potential underestimation in our model of the GGW impacts due to the aforementioned lower sensitivity to climate change compared to CORDEX models

As climate variability, water security and land fertility play a notable role in achieving food security, this study provides a GGW multi-scenario experiment where different levels of vegetation density give rise to different climate impacts on the region. The findings of our study help illuminate the complex, nuanced impact of the Great Green Wall (GGW) in northern Africa, revealing a mixed outcome: decreased aridity and summer temperatures alongside intensified occurrences of extreme hot days and heat indices in the pre-monsoonal season along the GGW domain. By delineating these contrasting trends, our research offers a crucial step toward understanding the multifaceted climatic consequences of the different GGW actions such as climate-smart agriculture, climatic-resilient infrastructure, and sustainable pastoralism.

Furthermore, the GGW may also affect climate far-afield (e.g., on the equatorial Atlantic and Pacific) as suggested by recent modelling studies performed under Green Sahara conditions (∼6,000 years ago), showing impacts on tropical cyclones (Pausata et al., 2017a) and on the El Niño Southern Oscillation (Pausata et al., 2017b) activities. Additional studies are therefore needed to address the Wall's potential far-afield climate impacts.

In conclusion, while further studies using different climate models are necessary to better constrain the impacts of the GGW on climate, our results underscore the importance of conducting comprehensive evaluations in environmental policy planning. Acknowledging the GGW impacts becomes pivotal in steering future strategies, ensuring that the GGW ambitions align with sustainable climate goals while mitigating potential adverse effects on regional stability and ecosystem integrity in northern Africa and beyond.

2.4 Experimental Procedures

2.4.1 Resource Availability

2.4.1.1 *Lead Contact:*

Further information about data and code should be directed to and will be fulfilled by the lead contact, Roberto Ingrosso (ingrosso.roberto@uqam.ca).

2.4.1.2 *Materials Availability:*

This study generated no new unique materials.

2.4.1.3 *Data and code Availability:*

All codes and data to generate the figures of this study are available in the online repository: `10.5281/zenodo.10323281`

2.4.2 Model description

We used the operational version of the Canadian Regional Climate Model/Global Environmental Multiscale (CRCM5/GEM4.8, Girard et al. (2014); McTaggart-Cowan et al. (2019)) at a horizontal grid spacing of 0.12° ($\sim$13 km) and 57 vertical levels topping at 10 hPa. To have atmospheric driving data that are conformed with the ocean, we first ran global simulations on a Yin-Yang grid with the Global Environmental Multiscale model (GEM, Côté et al. (1998)) at 0.55° horizontal resolution and 73 vertical levels topping at 2 hPa. GEM4.8 (the GEM version used in this study) is a fully non-hydrostatic model that uses a semi-implicit, semi-Lagrangian time discretization scheme on a horizontal Arakawa staggered C grid (see Hernández-Díaz et al. (2013) for further details).

These experiments were driven by the bias-corrected SST (Hernández-Díaz et al., 2019) and original sea ice fraction provided by the Earth System Model of the Max-Planck-Institut für Meteorologie (MPI-ESM-MR, `https://mpimet.mpg.de/en/science.html`) at the lower boundary and then used the output of those simulations to drive the regional simulations at the lateral boundary, using the same SST and sea ice fractions as for the global simulations at the lower boundary. The CRCM5/GEM4.8 lower boundary is coupled with the Canadian Land Surface Scheme (CLASS; Verseghy (2000)) and an interactive lake module, FLake lake

model (Mironov et al., 2010). For vegetation and land-water mask, CCI-LC vegetation and land-water mask the ESA CCI Land Cover (ESA, 2015) is used, while the Global Multi-resolution Terrain Elevation Data 2010 (`https://www.usgs.gov/coastal-changes-and-impacts/gmted2010`) has been used for the model topography.

2.4.3 Model evaluation

A previous experiment (Hernández-Díaz et al., 2013) over the African COordinated Regional Climate Downscaling EXperiment (CORDEX; Giorgi et al. (2009)) domain shows that CRCM5 drived by ERA-Interim (Dee et al., 2011) correctly detects the timing of the West African monsoon onset over the Sahel, but a dry bias is present over the region due to the southward position of the Saharan Heat Low compared to reanalyses. Consequently, the core of the African Easterly Jet is displayed slightly southward, giving rise to the above-mentioned dry bias in the region. The global experiment that drives the regional simulations exhibits a similar pattern in the RCP8.5-only experiment compared to PD . Both Coupled Model Intercomparison Project5 (CMIP5) and CMIP6 model generations generally depict a dipole pattern in precipitation change over Sahel under high emissions scenarios, with increases over the central-eastern Sahel and decrease in the western part of the region (Biasutti, 2013; Audu et al., 2024). However, uncertainty in these projections across the Sahel remains, as some global models do not reproduce this pattern. The GEM version used in this study aligns with these latter models, showing only a significant decrease in precipitation over the very western part of Sahel.

In this study, we further evaluate CRCM/GEM4.8, by comparing it with its parental model GEM4.8 (Côté et al., 1998) at 0.55° horizontal resolution, observations from the Tropical Rainfall Measuring Mission (TRMM, `10.5067/TRMM/TMPA/3H/7`) and the Climate Research Unit (CRU, Harris et al. (2020)), and one reanalysis product (ERA5,Hersbach et al. (2020)) in terms of mean precipitation distribution for the period 2000-2019 (Fig. B.29). The evaluation shows a better agreement of the high-resolution model with the observations in the West African Monsoon area (West Sahel) compared to GEM4.8, although the dry bias in terms of median and lower percentiles is still present, whereas no significant change is present when considering the whole Sahelian region. In order to evaluate the model skills in terms of reproducing the diurnal cycle and the rainfall intermittency, we compared CRCM5/GEM4.8 3-hourly data with TRMM. In terms of the diurnal cycle (Fig. B.30), the model clearly underestimates rainfall compared to the satellite observations. A maximum peak over the whole Sahel of 5 mm/day is found for TRMM at midnight, whereas a peak of 2.68

mm/day (3.8 mm/day over the western Sahel) is shown for CRCM5/GEM4.8 at 9 p.m. A minimum rainfall is detected at noon over the whole Sahel of about 1.91 mm/day for TRMM and 1.5 mm /day for GEM/CRCM4.8, while the model minimum rainfall is closer to observations over the western Sahel with 2.11 mm/day at 3 p.m. and 2.36 mm/day at noon, respectively. However, the general diurnal cycle pattern is well reproduced, with maximum precipitation during the early night and minimum precipitation during the middle of the day. As expected, the model diurnal cycle over the western Sahel is closer to observations compared to that one for the whole Sahel region, as also seen in the mean precipitation boxplots (Fig. B.29).

In terms of Consecutive Dry Days (CDD), the model distributions of annual CDDs show a similar behaviour compared to TRMM, with peaks of 250 days in both datasets (Fig. B.31). Over West Sahel, the CDD model distribution slightly moves towards a bit longer CDD. Both datasets are characterized by a maximum CDD of about 3400 days

2.4.4 The experimental design

A total of eleven simulations had been performed for two distinct 30-year periods (Tab. B.2). Three simulations without the Great Green Wall had been carried out and considered as reference cases: one under the present climate (1990-2019) and two under RCP2.6 and RCP8.5 (Moss et al., 2010) future scenarios (2071-2100). RCP8.5 is the high concentration scenario that better reproduces the recent CO2 emissions (Schwalm et al., 2020), even though its future emission trajectory could become less likely in the future, given the current policies (Hausfather and Peters, 2020). Additionally, a total of eight sensitivity experiments under the two future scenarios were carried out considering four different levels of vegetation density. The four levels have been named GGW_{LOW}, GGW_{MED}, $GGW_{HIGH}$and GGW_{EXT} (Fig. 2.7). GGW_{LOW} and GGW_{MED} are characterized by a total percentage of desert in the GGW region (100 – 400 mm mean annual precipitation) of 40% and 33%, respectively, whereas PD, GGW_{HIGH} and GGW_{EXT} show a percentage of 72%, 16% and 8% respectively (Fig.B.1). The chosen type of vegetation (e.g. evergreen and broadleaf trees) agrees with the species considered in the main documents produced by the PAGGW (2018) such as Acacia Senegal, Acacia nilotica and Balanites aegyptiaca. Desert and bare soil have been replaced by different percentage combinations – depending on the precipitation band area- of deciduous and evergreen broadleaf shrubs and trees, coherently with the vegetation classes present across the Sahel in the model scheme. No change in previous land cover categories such as urban, swamp or crops had been made because of the difficulty of evaluating the future evolution of these categories. More in detail, in GGW_{LOW}, we shifted northward

the desert fraction as present in the model scheme: the desert fraction present across the 100-200 mm area of mean annual rainfall is replaced by the fraction across 200-300 mm, the 200-300 mm fraction is replaced by 300-400 mm fraction, and the 300-400 mm fraction by that from 400-500 mm. 30% of trees are present in the third band (300 – 400 mm). GGW_{MED} has the same GGW_{LOW} mix of vegetation for the first band with 65% of desert, while shares the same mix of vegetation in the other two bands with GGW_{HIGH} where the percentage of trees in the third band moves to 50%. GGW_{HIGH} sees a percentage of 25% of desert in the first band. In the extreme case, a percentage of 10% of desert is present in the first two bands (50 – 300 mm), moving to 5% in the third one. Finally, in GGW_{EXT} experiment, the percentage of trees in the third band is still 50%, but with a higher concentration of evergreen broadleaf trees compared to GGW_{MED} and GGW_{HIGH}. In the Introduction, we mentioned that in previous studies the pre-existent vegetation had been replaced with a uniform evergreen forest over different latitudinal bands over the region. Although these studies do not provide values for the modification in albedo, rainforests have an albedo of the order of 0.12-0.13 (Giambelluca et al., 1997) while in our case the albedo ranges between 0.15-0.3 (Fig.B.15). Such albedo difference can play a critical role in altering the WAM dynamics (Pausata et al., 2020).

2.4.5 Climate extreme indices

Climate indices play an important role in monitoring the potential risks and damages of climate change. The definition of these indicators looks at the tails of the parameter distribution, which reflect the change in the extreme events. Consequently, the use of different temperature and precipitation climate extreme indices was here considered as defined by the Expert Team on Climate Change Detection and Indices (ETCCDI, Frich et al. (2002); Zhang et al. (2011)). A set of indicators from the 27 ETCDDI had been considered (Tab. B.3), in order to have a good representation of extreme temperature, precipitation and dry spells over the area. For the temperature we calculated the annual extreme of daily maximum and minimum temperature (TXx and TNn, respectively), and the number of nights with daily minimum temperature above 20°C (Tropical nights, TR20). As a measure of the longest yearly dry spells, we considered the consecutive dry days (CDD), the maximum number of consecutive days with precipitation lower than 1 mm. Finally, the annual maximum of the precipitation amount fell in 5 consecutive days (RX5), the annual total precipitation from days with an amount of precipitation above the $95t^{th}$ percentile (very wet days, R95p), and the number of days per year in which the daily precipitation exceeds 1 mm (rainy days, RR1mm) were considered to show potential changes in heavy precipitation.

2.4.6 Statistical analysis

For the statistical evaluation of the differences, two statistical tests were used: A two-tailed Student t test (Yuen and Dixon, 1973) for temperature, assuming a normal distribution for this parameter and the non-parametric Wilcoxon signed-rank test (Wilcoxon, 1945) for parameters such as precipitation or wind, where the normal assumption is not possible. The considered level of significance is 5% for both tests.

2.4.7 The WAM length and the African Easterly Waves

The monsoon's length is defined as the time between the onset and the withdrawal of the monsoon. The computation of the onset is based on Sultan and Janicot (2003). An empirical orthogonal function (EOF) analysis was performed on the zonally averaged daily rainfall data from March to November over the area between 15°W-15°E and 0°N-30°N. The zonally averaged daily rainfall time series at the maximum of the first mode (EOF1) was then filtered to remove variability below 10 days with a 10-day running mean. The monsoon's onset was defined as the date preceding the largest increase in precipitation over a 20-day period. Finally, the withdrawal was defined as the date on which the zonally averaged precipitation at 10.5°N falls below 2 mm/day, for at least 20 consecutive days (Zhang and Cook, 2014).

The African Easterly Waves (AEWs) are westward-propagating disturbances with wavelengths of approximately 3000-4000 km, a propagation speed of about 8 m/s (Paradis et al., 1995; Diedhiou et al., 1999) and a period of around 3 to 5 days. AEWs play a role in the initiation and organization of the mesoscale convective systems, which are the main contributors to the Sahelian rainfall. In this study, we detected the AEWs activity by filtering the daily means of the meridional wind between June and September (JJAS) with a 2- to 6-d band-pass filter (Skinner and Diffenbaugh, 2014).

2.4.8 Aridity Index

In this study, the De Martonne Aridity Index (AI_{DM}, Martonne (1926)) was used in order to evaluate changes in aridity and water availability over the region. The AI_{DM} is a simplified index, defined as a function of the annual mean temperature and precipitation, which provides similar results to other aridity indices present in the scientific literature (see Paniagua et al. (2019) and Sohoulande et al. (2022) for further details). Here, we defined a new category, desert, for AI values lower than 5. This category properly distinguishes the desertic climate (Fig. 2.6), facilitating the purpose of our analysis regarding potential changes in local climate,

characterized by high arid conditions. Specifically, the De Martonne index is defined as:

$$AI_{\text{DM}} = \frac{P}{T + 10} \tag{2.1}$$

where P is the annual mean precipitation and T is the annual mean temperature in degree Celsius at the reference height (2m).

2.4.9 Heat Index

The Heat Index (HI) calculation is based on the Rothfusz's regression equation (`https://www.weather.gov/media/ffc/ta_htindx.PDF`):

$$\begin{aligned} HI = {} & 42.379 + 2.04901523 * T + 10.14333127 * RH \\ & - 0.22475541 * T * RH - 0.00683783 * T * T - 0.05481717 * RH * RH \\ & + 0.00122874 * T * T * RH + 0.00085282 * T * RH * RH \\ & - 0.00000199 * T * T * RH * RH \end{aligned} \tag{2.2}$$

where T is the surface temperature in degrees Fahrenheit and RH is the percentage of relative humidity. The HI is converted into degrees Celsius and has an error of ±1.3°F (±0.7°C). Some adjustments are applied to the index (when RH is less than 13% and the temperature is between 80 and 112 degrees, or RH is greater than 85% and the temperature is between 80 and 87 degrees), following the instructions of the National Oceanic and Atmospheric Administration/National Weather Service (see `https://www.wpc.ncep.noaa.gov/html/heatindex_equation.shtml`).

2.5 Figures

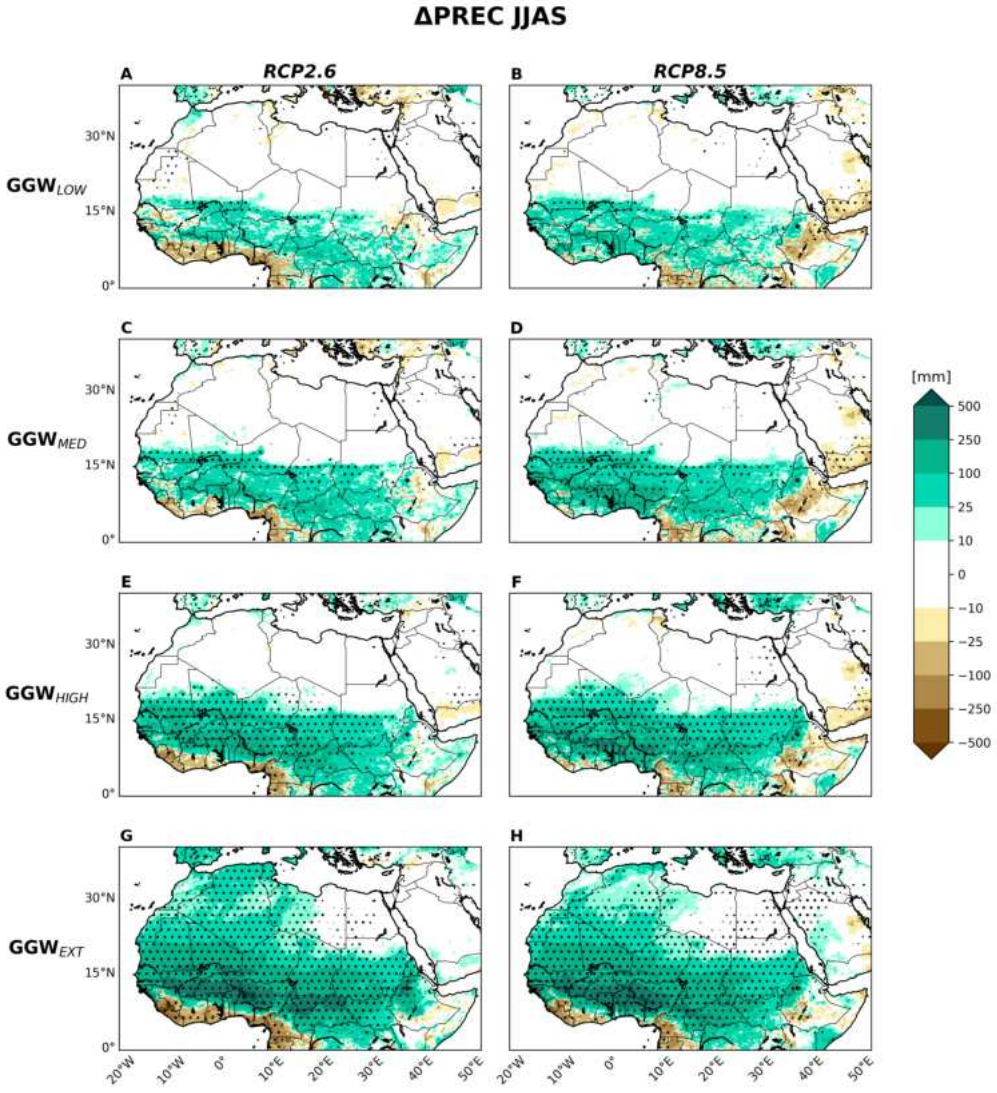

Figure 2.1: Summer rainfall changes in northern Africa. Changes in precipitation during summer (June to September – JJAS) for A-B) GGW_{LOW}, C-D) GGW_{MED} E-F) GGW_{HIGH}, G-H) GGW_{EXT} scenarios relative to the standard RCP2.6 (left) and RCP8.5 (right) pathways. Dots indicate values that are significantly different at the 5% significance level, using a local (grid-point) Wilcoxon signed-rank test.

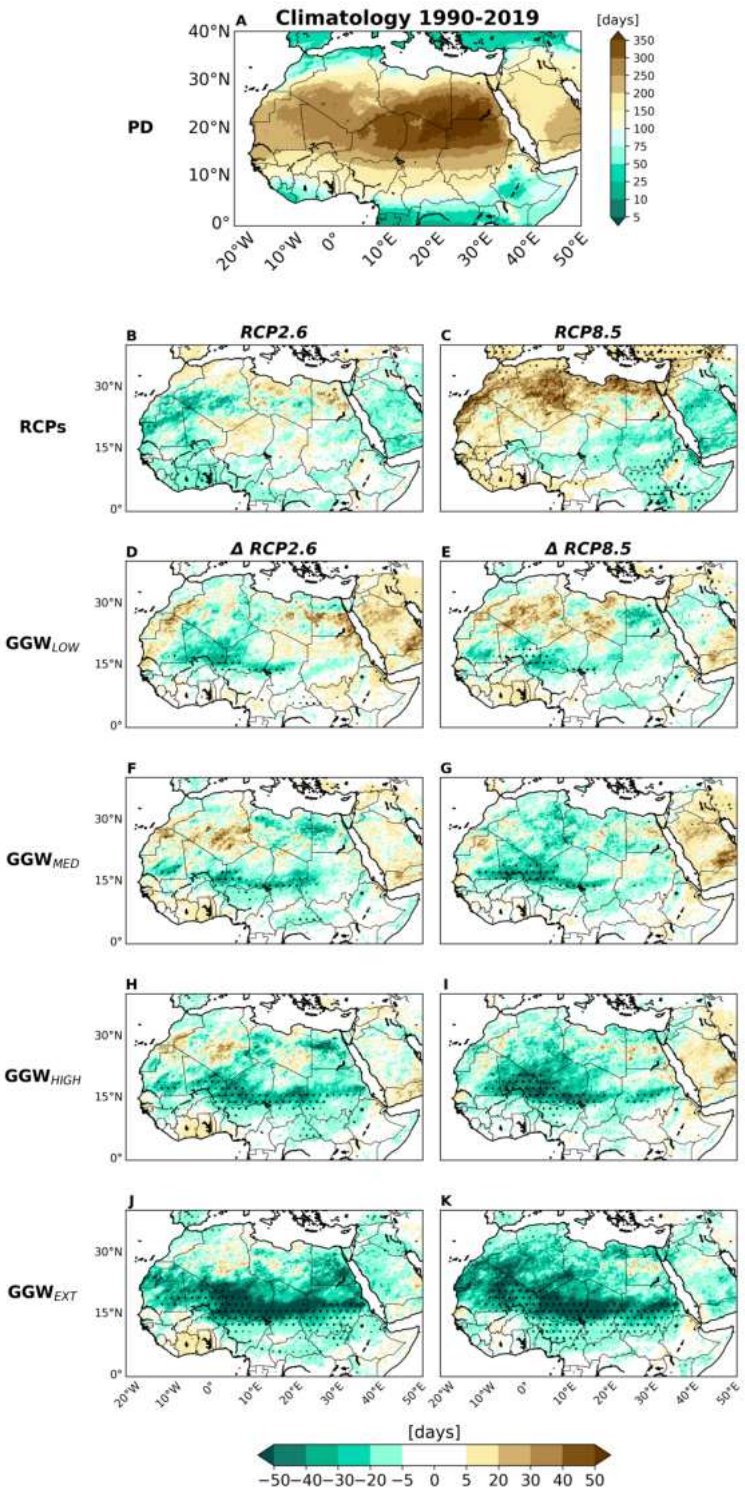

Figure 2.2: Annual Consecutive Dry Days. A) Climatological annual Consecutive Dry Days (CCDs) for the Present Day (PD) experiment and its changes during summer (June to September, JJAS) for B-C) RCP scenarios relatively to the PD experiment, and D-E) GGW_{LOW}, F-G) GGW_{MED}, H-I) GGW_{HIGH}, J-K) GGW_{EXT} scenarios relative to the standard RCP2.6 (left) and RCP8.5 (right) pathways. Dots indicate values that are significantly different at the 5% significance level, using a local (grid-point) Wilcoxon signed-rank test.

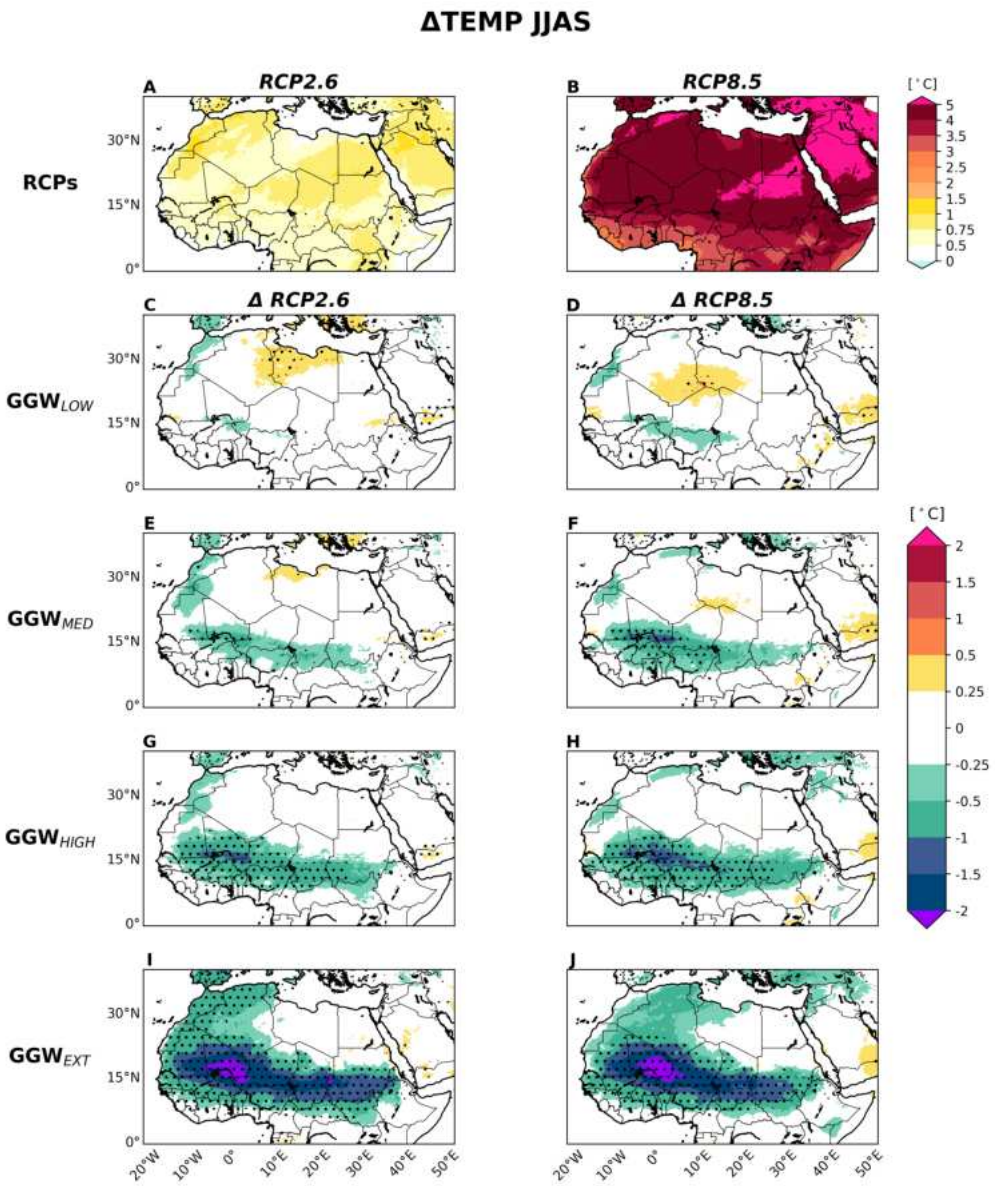

Figure 2.3: Mean temperature changes during JJAS. Changes in mean temperature during summer (June to September, JJAS for A-B) RCP scenarios relatively to the PD experiment and C-D) in the GGW_{LOW}, E-F) GGW_{MED}, G-H) GGW_{HIGH}, I-J) GGW_{EXT} scenarios relative to the standard RCP2.6 (left) and RCP8.5 (right) pathways. Dots indicate area with a statistical significance at the 5% significance level, using a local (grid-point) t test. In panels A) and B) all areas show significant differences (no dots shown).

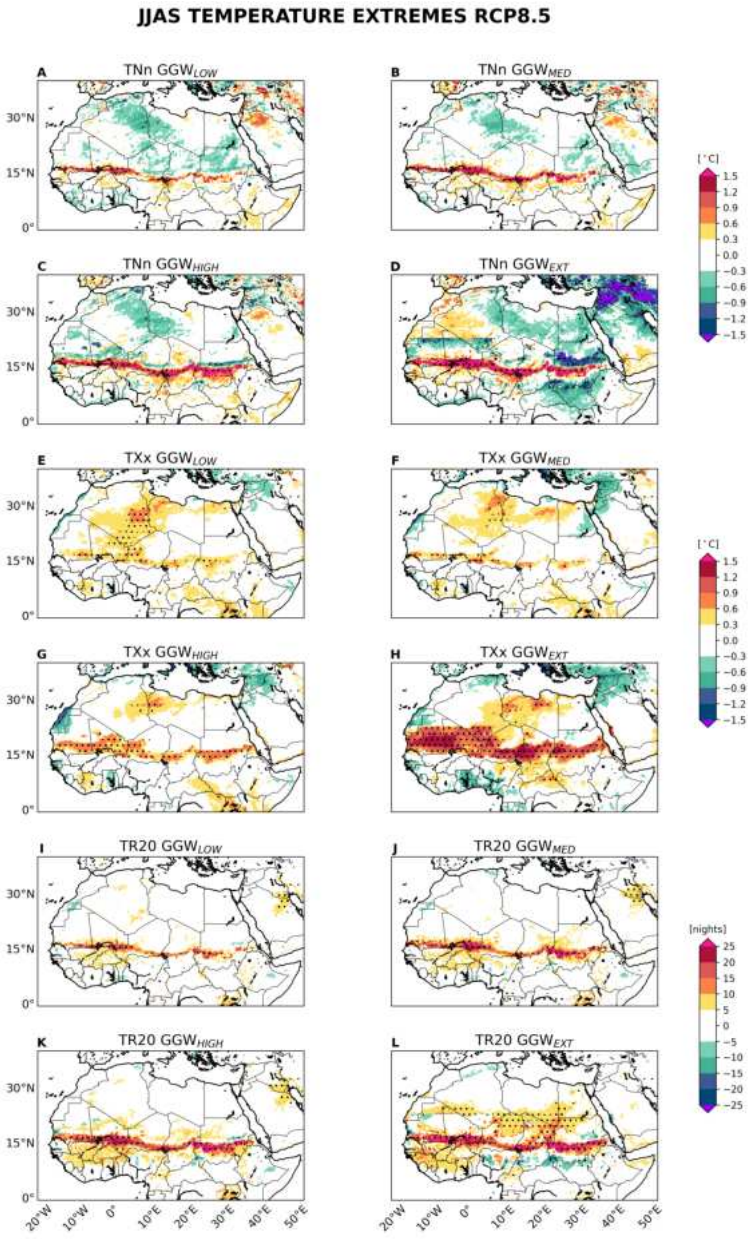

Figure 2.4: Change in the hottest and coldest day of the year and number of tropical nights. Change in the annual coldest day of the year (TNnx) for A) GGW_{LOW}, B) GGW_{MED} and C) GGW_{HIGH} and D) GGW_{EXT} scenarios relative to the standard RCP8.5 pathway. E-H) same as A-D) but for the hottest day of the year (TXx). I-L) same as A-D) but for tropical nights (number of nights with daily minimum temperature above 20°C, TR20). Dots indicate area with a statistical significance at the 5% significance level, using a local (grid-point) t-test.

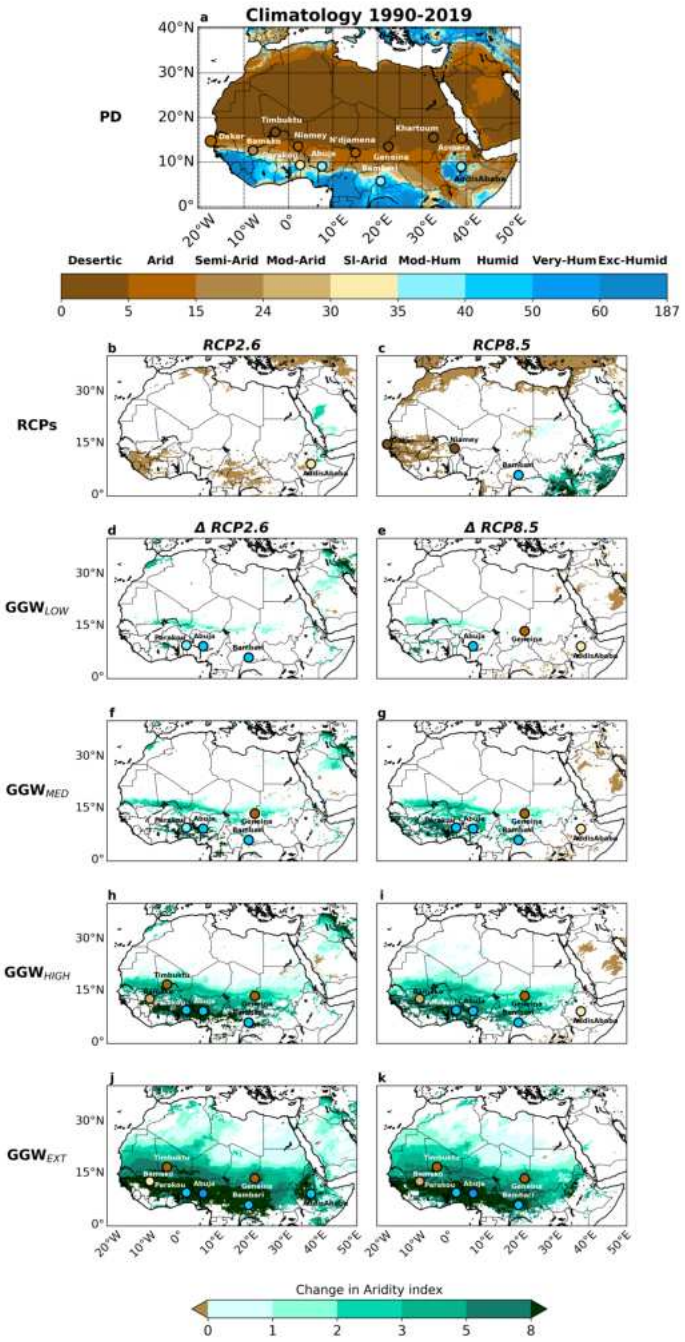

Figure 2.5: De Martonne Aridity Index (AI_{DM}). A) Climatology of the De Martone Aridity Index (AI_{DM}) for Present Day (PD). Change in AI_{DM} for B-C) the RCPs relatively to Present Day (PD) experiment, and for D-E) the GGW_{LOW} F-G) the GGW_{MED} H-I) GGW_{HIGH} and J-K) GGW_{EXT} scenarios relatively to the standard RCP2.6 (left) and RCP8.5 (right) pathways. Sl-arid, mod-Hum and Exc-Hum indicate slightly arid, moderately humid and excessively-humid conditions. E-G) Same as B-D) but for the RCP8.5 scenario. Dots indicate the associated AI_{DM} of that specific city. Only statistically significant change at the 5% significance level is shown, using a local (grid-point) Wilcoxon signed-rank test. In the maps of differences, only the cities characterized by change in the index are shown.

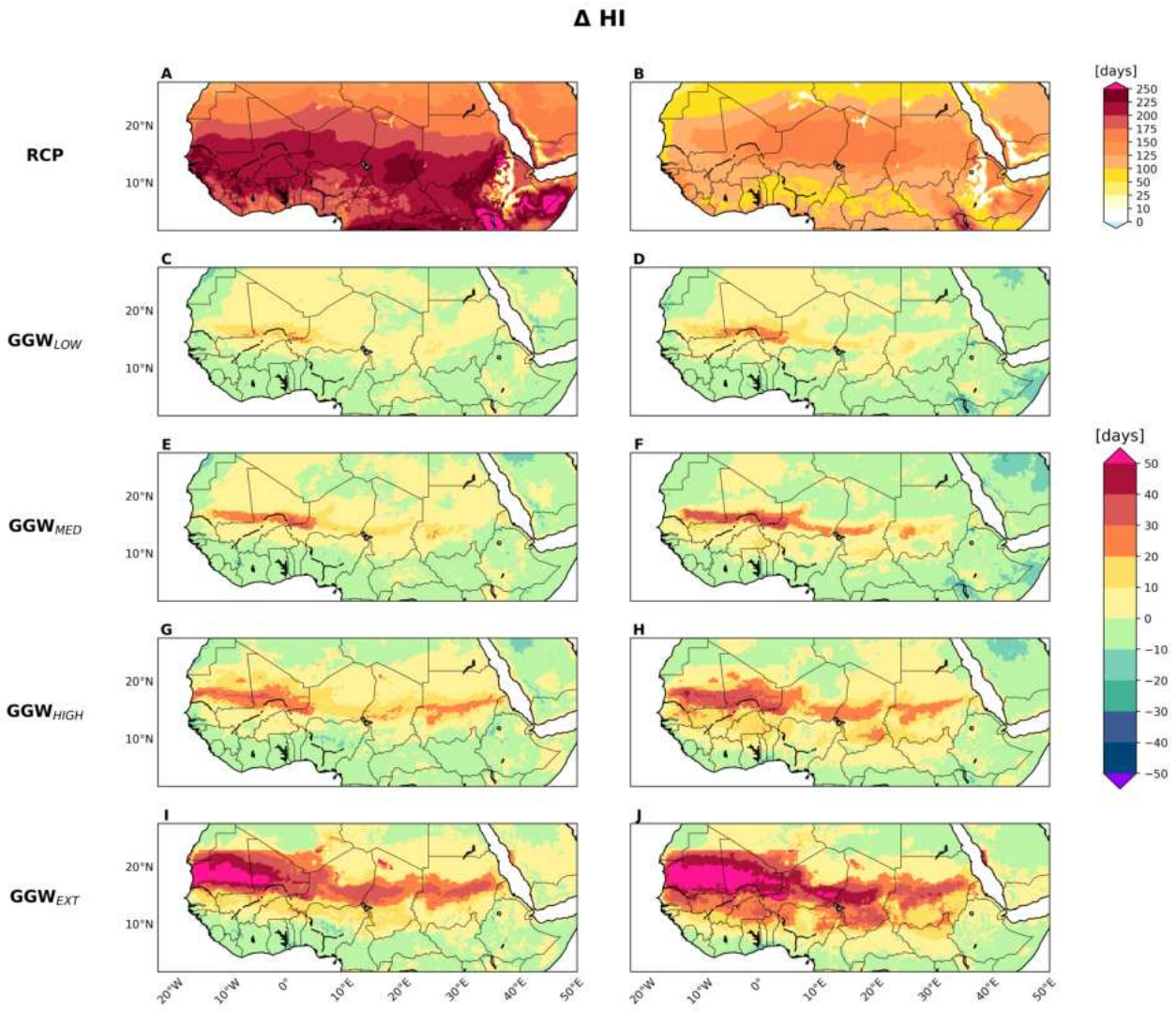

Figure 2.6: Heat Index (HI). A-B) Annual change in the number of days with HI higher than Present Day (PD) 75th (left) and 95th (right) percentile for RCP8.5-only. Difference in number of days with HI higher than PD 75th (left) and 95th (right) percentile for C-D) GGW$_{LOW}$, E-F) GGW$_{MED}$, G-H) GGW$_{HIGH}$ and I-J) GGW$_{EXT}$ relatively to RCP8.5-only experiment.

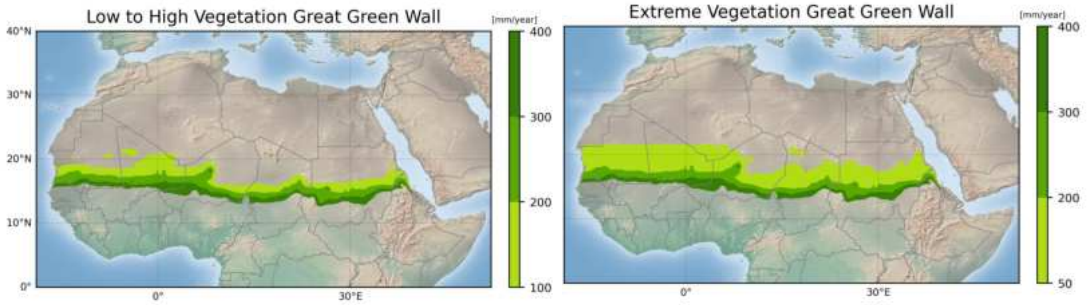

Low vegetation GGW	Medium vegetation GGW	High vegetation GGW	Extreme vegetation GGW
65% -> desert 20% -> short grass and forbs 5% -> evergreen broadleaf shrubs 10% -> deciduous shrubs	65% -> desert 20% -> short grass and forbs 5% -> evergreen broadleaf shrubs 10% -> deciduous shrubs	25% -> desert 25% -> short grass and forbs 25% -> evergreen broadleaf shrubs 25% -> deciduous shrubs	10% -> desert 25% -> short grass and forbs 30% -> evergreen broadleaf shrubs 35% -> deciduous shrubs
30% -> desert 30% -> short grass and forbs 5% -> evergreen broadleaf shrubs 15% -> deciduous shrubs 10% -> deciduous broadleaf trees 10% -> evergreen broadleaf trees	15% -> desert 20% -> short grass and forbs 10% -> evergreen broadleaf shrubs 20% -> deciduous shrubs 20% -> deciduous broadleaf trees 10% -> evergreen broadleaf trees	15% -> desert 20% -> short grass and forbs 10% -> evergreen broadleaf shrubs 20% -> deciduous shrubs 20% -> deciduous broadleaf trees 10% -> evergreen broadleaf trees	10% -> desert 15% -> short grass and forbs 15% -> evergreen broadleaf shrubs 30% -> deciduous shrubs 20% -> deciduous broadleaf trees 10% -> evergreen broadleaf trees
15% -> desert 25% -> short grass and forbs 15% -> evergreen broadleaf shrubs 15% -> deciduous shrubs 20% -> deciduous broadleaf trees 10% -> evergreen broadleaf trees	5% -> desert 15% -> short grass and forbs 15% -> evergreen broadleaf shrubs 15% -> deciduous shrubs 35% -> deciduous broadleaf trees 15% -> evergreen broadleaf trees	5% -> desert 15% -> short grass and forbs 15% -> evergreen broadleaf shrubs 15% -> deciduous shrubs 35% -> deciduous broadleaf trees 15% -> evergreen broadleaf trees	5% -> desert 15% -> short grass and forbs 15% -> evergreen broadleaf shrubs 15% -> deciduous shrubs 30% -> deciduous broadleaf trees 20% -> evergreen broadleaf trees

Figure 2.7: The GGW experimental design A) Schematic of the experimental design of the Great Green Wall (GGW), in which the prescribed vegetation type and abundance (in%) is provided for each of climatological rainfall interval (100–200 mm; 200–300 mm; and 300–400 mm). Each band corresponds to a different vegetation mix of woody and herbaceous species, according to the official GGW plans from the Pan African Agency of the Great Green Wall. B) Extreme case, with the first rainfall interval starts at 50 mm. The percentage of desert and bare soil over the GGW area in the Present Day (PD) simulation is 72% while it is around 40%, 33%, 16% and 8% in the GGWs experiments from low to extreme, respectively.

CHAPTER 3

EXPLORING THE IMPACT OF THE GREAT GREEN WALL ON ATLANTIC TROPICAL CYCLONE ACTIVITY

(UNDER REVIEW ON GLOBAL AND PLANETARY CHANGE)

Roberto Ingrosso[1,2,3], Francesco S.R. Pausata[1,2,3], Katja Winger[1,2,3], Suzana J. Camargo[4]

1 – Department of Earth and Atmospheric Sciences, Université du Québec à Montréal, Montréal, QC H2X3Y7, Canada

2 – Centres ESCER (Étude et la Simulation du Climat à l'Échelle Régionale)

3 – GEOTOP (Research Center on the dynamics of the Earth System)

4 – Lamont-Doherty Earth Observatory, Columbia University, Palisades, NY, USA

ABSTRACT

The Great Green Wall (GGW) initiative aims to restore 100 million hectares of degraded land over Sahel. However, its potential impacts on the far-afield climate have hitherto not been evaluated. Here, we use a high-resolution regional climate model to evaluate the potential impacts on Atlantic tropical cyclone (ATC) activity in four different GGW scenarios under two emission pathways. The results reveal a shift in Atlantic tropical cyclone (ATC) genesis from the subtropical Atlantic to the eastern Main Development Region under medium to extreme vegetation density scenarios, compared to cases without the Great Green Wall (GGW). An increase in genesis is also observed off the southeastern U.S. coasts under the high-concentration pathway. Our analysis highlights the primary role of African Easterly Waves in driving changes in TC genesis across the basin, with a secondary contribution from large-scale environmental factors. Hence, we find no significant impact of GGW on ATC activity, primarily due to counteracting changes a decrease in the central-western and an increase in the eastern basin. No changes induced by the GGW in the ATC intensity and translation speed and other TC metrics are found across the full basin.

3.1 Introduction

The Great Green Wall (GGW) is an African geo-engineering initiative to combat desertification and drought over the Sahel region. This multi-billion-dollar project involves a range of stakeholders including national governments, international organizations, economic sectors, and local communities. The GGW encompasses a mosaic of diverse actions implemented across areas within the 100 to 400 mm annual rainfall isohyets (PAGGW, 2018; Turner et al., 2021).

There is some evidence from modeling studies of the Green Sahara Period ($\sim$11,000 – 5,000 years ago) that Saharan vegetation may have led to more favourable Atlantic Tropical Cyclone (ATC) environmental conditions and increased ATC activity (Pausata et al., 2017a; Dandoy et al., 2021). However, no studies have looked at the potential impact of the GGW on the ATC activity yet. Ingrosso and Pausata (2024) investigated the potential effect of the latest version of the GGW project on the regional climate of northern Africa. They found significant changes in the characteristics of the West African Monsoon (WAM) associated to the GGW, including an increase in summer rainfall and the intensity of rainy events, a decrease in drought duration, more extreme hot days, and higher heat indices in the pre-monsoonal season. These impacts of the GGW are also related to changes in regional features of the WAM, in particular a weakening of the African Easterly Jet and a strengthening of the Tropical Easterly Jet and African Easterly Waves (AEWs). Such changes in WAM characteristics and AEW activity may potentially directly (changes in TC seeding) or indirectly (changes in environmental conditions) affect ATC activity. Landsea and Gray (1992) proposed two physical mechanisms to explain the covariation between western Sahelian rainfall and Atlantic hurricane activity. The first mechanism is associated with stronger wind shear during dry years and weaker wind

shear during wet years over the main TC development region. The second mechanism focuses on AEWs. Higher AEW amplitudes enhance the organization of deep convection in the MDR by providing pre-existing low-pressure disturbances and vorticity anomalies, which serve as 'seeds' for TC genesis.

Currently, there is a vigorous debate in the scientific literature about the role of TC seeds such as AEWs on TC genesis (Hsieh et al., 2020; Sobel et al., 2021; Emanuel, 2022). A clear connection between AEWs and ATCs has been identified on synoptic time scales (Landsea et al., 1998; Dieng et al., 2017; Russell et al., 2017). However, the relationship between AEWs and TC frequency is not as clear on climate scales. Studies based on regional dynamical models, statistical-dynamical TC models, as well as statistical models reproduced the interannual variability of Atlantic TC activity without including AEWs (Emanuel et al., 2008; Emanuel, 2010; Saunders et al., 2017; Patricola et al., 2018; Danso et al., 2022). Other studies argued that TC seeds, such as AEWs have an important influence in determining TC frequency (Thorncroft and Hodges, 2001; Hsieh et al., 2020; Yang et al., 2021; Yamada et al., 2021; Hsieh et al., 2022), and are important to determine the response of TC frequency to anthropogenic climate change (Sugi et al., 2020; Vidale et al., 2021). On the other hand, some results pointed to favorable regional environmental conditions as key factors to control tropical cyclogenesis (Emanuel et al., 2008; Caron and Jones, 2012; Hoogewind et al., 2020; Emanuel, 2017). This evidence is at the base of the success of different genesis indices designed to reproduce spatial and seasonal probability of TC occurrence (DeMaria et al., 2001; Emanuel and Nolan, 2004; Tippett et al., 2011). In this study, we employed a high-resolution ($\sim$13 km) climate model to carry out sensitivity experiments under two distinct greenhouse gas (GHG) concentration pathways and four distinct GGW scenarios with varying vegetation densities to examine the potential impact of the GGW on the ATC activity, as described below.

3.2 Data and Methods

3.2.1 The model setup

The developmental version of the Canadian Regional Climate Model/Global Environmental Multiscale (CRCM5-GEM4.8) at a horizontal grid spacing of 0.12°, $\sim$13 km) and 57 vertical levels topping at 10 hPa has been used to perform the GGW and GHG experiments (Girard et al., 2014; McTaggart-Cowan et al., 2019). The driving data for these regional model simulations are obtained from simulations of the Global Environmental Multiscale model (GEM, Côté et al. (1998)) at 0.55° horizontal resolution and 73 vertical levels topping at 2 hPa. GEM4.8 (the GEM version used in this study) is a fully non-hydrostatic model that uses a semi-implicit,

semi-Lagrangian time discretization scheme on a horizontal Arakawa staggered C grid (see Hernández-Díaz et al. (2013) for further details) These global model experiments were forced by bias-corrected sea surface temperature (SST; Hernández-Díaz et al. (2019)) and sea ice fraction provided by the Earth System Model of the Max-Planck-Institut für Meteorologie (MPI-ESM-MR, (https://mpimet.mpg.de/en/science.html) at the lower boundary. The CRCM5/GEM4.8 lower boundary is coupled with the Canadian Land Surface Scheme (CLASS; Verseghy (2000) and an interactive lake module, Flake lake model (Mironov et al., 2010).For vegetation and land-water mask, CCI-LC vegetation and land-water mask the ESA CCI Land Cover (ESA, 2015) are used, while the Global Multi-resolution Terrain Elevation Data 2010 (`https://www.usgs.gov/coastal-changes-and-impacts/gmted2010`) has been used for the model topography. The output of the GEM4.8 simulations are then used to drive the regional simulations at the lateral boundary, using the same SST and sea ice fractions. No spectral nudging has been performed in these experiments. The model domain covers the region between -3.35°S – 48.1°N and -99°W and 52°E (Fig.A.1).

3.2.2 The experimental design

A total of eleven simulations had been performed for two distinct 30-year periods (Tab. C.2). Three simulations without the GGW had been carried out and considered as reference cases: one under the present day (PD) climate (1990-2019) and two under RCP2.6 and RCP8.5 (Moss et al., 2010) future scenarios (2071-2100) for both atmospheric initial conditions and sea surface temperature driving data. The PD simulation presents a percentage of desert and bare soil of 72% over the GGW region between 100 and 400 mm. Additionally, a total of eight sensitivity experiments under the two future scenarios were carried out considering four different levels of vegetation density: low (GGW_{LOW}), medium (GGW_{MED}), high (GGW_{HIGH}) and extreme (GGW_{EXT}). Desert and bare soil have been replaced by different percentage combinations – depending on the precipitation band area- of deciduous and evergreen broadleaf shrubs and trees, coherently with the vegetation classes present across the Sahel in the model scheme. GGW_{LOW} and GGW_{MED} are characterized by a total percentage of desert in the GGW region (100–400 mm) of 40% and 33%, respectively, whereas GGW_{HIGH}, and GGW_{EXT} show a percentage of 16%, and 8%, respectively. No change in previous land cover categories such as urban, swamp or crops had been made because of the difficulty of evaluating the future evolution of these categories. For more details see Fig.2.7 and Ingrosso and Pausata (2024).

3.2.3 The genesis index

Many genesis indices have been developed, using different environmental variables, formulations and statistical methods (DeMaria et al., 2001; Emanuel and Nolan, 2004; Bye and Keay, 2008; Emanuel, 2010; Tippett et al., 2011; Waters et al., 2012; Bruyère et al., 2012; Murakami and Wang, 2022; Ascenso et al., 2023). However, there is not a general consistency between most of the genesis indices and high-resolution climate models. For example, most these genesis indices indicate an increase in TC frequency activity under warmer conditions whereas the climate models project a global decrease in TC (Camargo, 2013; Camargo and Wing, 2016; Lee et al., 2020).

In this study, we use the Genesis Potential Index developed in Emanuel and Nolan (2004) (ENGPI). This index is a measure of potential genesis of TCs based on four environmental parameters: the low-level vorticity, the vertical wind shear, the midlevel relative humidity, and the potential intensity. It is one of the most widely used indices and it replaces the sea surface temperatures threshold considered in previous indices (Gray, 1979; Ryan et al., 1992) with potential intensity (PI). A single SST threshold is not reliable for the global ocean as it has been highlighted by Emanuel and Nolan in their 2004 ENGPI paper. Instead, the GPI incorporates PI for the maximum intensity a tropical cyclone can achieve under given thermodynamic conditions (Emanuel, 1986). This makes the GPI a more robust and globally applicable metric for assessing TC genesis potential. ENGPI is defined as:

$$GPI = |10^5\eta|^{3/2}(H/50)^3(V_{pot}/70)^3(1+0.1V_{shear})^{-2} \tag{3.1}$$

where V_{shear} is the magnitude of the vertical wind shear (in ms^{-1}) between the upper (200 hPa) and lower (850 hPa) troposphere, η is the 850hPa absolute vorticity (in s^{-1}), H is the relative humidity at 700 hPa and Vpot is the potential intensity (PI, in ms^{-1}). For the PI calculation, the Tropical Cyclone Potential Intensity Calculations in Python (pyPI, v1.3, Gilford (2021)) package has been used.

3.2.4 African Easterly Waves

African Easterly Waves (AEWs) are synoptic-scale westward-propagating disturbances with wavelengths of approximately 3000-4000 km, a propagation speed of about 8 m/s (Paradis et al., 1995; Diedhiou et al., 1999) and a period of around 3 to 6 days. In this study, we detected the AEWs activity by filtering the daily

means of the meridional wind between June and November (JJASON) with a 2d- to 6-d band-pass filter (Ruti and Dell'Aquila, 2010; Skinner and Diffenbaugh, 2014). The intensity and the number of AEWs are calculated following the Skinner and Diffenbaugh (2014) methods, which are based on the magnitude of the 850-mb meridional wind and the number of instances in which the filtered daily mean meridional wind at the 850-mb location exceeds 1 ms^{-1}, respectively. In our case we used a section between 10°N and 15°N at 20°W as reference area at the north of the AEJ core over the ocean (Fig.3.7a).

3.2.5 Tropical Cyclone Tracker

The detection of TC activity and variability in models and reanalysis is based on tracking algorithms (TC trackers) applied to climate models and/or reanalyses output. Trackers identify cyclonic environments associated with a warm core, creating the whole storm trajectory by linking them to its path. The TC tracker used in this study (Caron et al., 2011) applies a three-step procedure (storm identification, storm tracking and storm lifetime) to detect tropical cyclones, following Walsh et al. (2007)'s recommendations. More information about the criteria used in the TC tracker can be found in Dandoy et al. (2021).

3.2.6 TC metrics

We also consider other TC metrics, specifically, the Accumulated Cyclone Energy (ACE), the Lifetime Maximum Intensity (LMI) and the translation speed. ACE (Bell et al. 2000) combines the frequency, lifetime, and intensity of tropical cyclones occurring in a basin over a given period. It is defined as the sum of the squares of the estimated 6-hourly maximum sustained surface wind speed (in knots) for all tropical cyclones, for snapshots in which reach the storms reach 35kt or higher divided by 10000. The LMI is the peak of wind speed reached by each TC during its lifetime (Elsner et al., 2008) and it represents an integrated statistic of TC intensification. Finally, the translation speed, i.e. the speed at which a storm is moving, an important parameter as it is associated with total rainfall accumulation and TC damages (Mei et al., 2012).

3.2.7 TC activity in the climate model

We compare TC metrics from the tracks produced by the TC tracker with observed tracks from the International Best Track Archive for Climate Stewardship (IBTrACS, Knapp et al. (2009); Knapp and Kruk (2010)), a dataset produced by the National Hurricane Center for the Atlantic basin.

TC genesis density is estimated using a Gaussian Kernel Density Estimation with a bandwidth of 2. The model broadly reproduces the observed pattern (Fig.3.1a,b) though a negative bias is evident across the Gulf of Mexico, while TC genesis is overestimated off the U.S. coasts and over the southern Caribbean Sea. In contrast, TC genesis across the MDR is well captured, particularly in its eastern region.

In terms of annual frequencies, the PD experiment shows an overestimation of TCs compared to the observations (Fig.C.1). A median of 20 TCs a year characterizes the model PD, five mores than the observations. The 5-th percentile of the model corresponds to the 25-th percentile of the observations while the 75-th percentile is slightly higher than the 95-th percentile of the observations. This result is in line with Caron et al. (2011) who found better performance (though with a slight overestimation) in simulating Atlantic TC activity for limited-area models driven by global GEM simulations compared to coarser-resolution models. However, this positive bias may be specific to the RCM used in both their study and ours, and caution should be exercised when generalizing these findings to other RCMs.

To differentiate in different TC categories, we consider the Saffir-Simpson scale Simpson (1974) defined by the minimum central pressure (Tab.C.1) instead of maximum wind speed Klotzbach2021. The PD experiment reveals an underestimation of Tropical Storms and stronger Hurricanes (Cat.4 and Cat.5) compared to the observations (Fig.C.2) although the seasonal cycle exhibits a good agreement with the IBTrACS data (Fig.C.3). A little underestimation in the percentage of the TCs is present in the model in September and October (26% and 15%, respectively) compared to the observations (32% and 18%, respectively). A small but significant overestimation is observed in July and November for the model TCs percentage (16% and 6.5%, respectively) compared to the observed TCs (12% and 4%, respectively). The PD distribution of the translation speed (Fig.C.4), the ACE (Fig.C.5) and the LMI (Fig.C.6) are overall consistent with the observation's distributions with a slightly higher median for the first two and a lower variability compared to the IBTraCS values. A moderate overestimation of the tropical cyclone LMI location compared to the observations is found in the model TCs (medians of 29.4°N and 25,6 °N, respectively, Fig.C.7). The PD tropical cyclogenesis density map (Fig.3.1b) shows similar pattern and densities compared to the observations (Fig.3.1a) although a little underestimation is present over the Main Development Region).

3.2.8 Statistical tests

For the statistical evaluation of the differences in the maps, the non-parametric Wilcoxon signed-rank test (Wilcoxon, 1945) is used. The level of significance considered is 5%. The Mann-Whitney and the Kolmogorov-

Smirnov tests are used to compare the distributions of different simulations in the boxplots. The Mann–Whitney test (Corder and Foreman, 2011) is used to check whether the difference in central tendency (such as the mean, the median and the mode) of two populations differs from zero. The Kolmogorov-Smirnov is generally used to check whether two variables have the same probability distribution (Corder and Foreman, 2011).

3.3 Results

3.3.1 Changes in ATC metrics induced by the GGW

3.3.1.1 RCP-only Scenarios

In the RCP8.5-only experiment, notable differences in TC genesis density emerge when compared to the PD experiment, with a shift from the MDR to the subtropics and western part of North Atlantic basin (a region spanning from 75°W and 35°W and 25°N and 35°N), alongside a decrease over the Caribbean Sea (Fig.3.1d). The mean seasonal TC count decreases significantly, from 18 in PD to 14 in RCP8.5-only, reflecting a basin-wide reduction in TC frequency (Fig.3.2). However, this decline is accompanied by an increase in the proportion of major hurricanes (categories 3 and 4), which rises from 18% to 23% and 2% to 6%, respectively (Fig.C.8). This shift toward more intense TCs is further supported by a modest but significant increase in LMI (Fig.3.3). Additionally, a minor poleward shift in LMI latitude is also observed (Fig.C.9). A smaller increase in TC genesis density across the northwestern tropical Atlantic is also observed in the RCP2.6-only experiment compared to the PD simulation, though some areas exhibit a negative change (Fig.3.1). Similar to the RCP8.5-only experiment, a decrease in TC activity is evident over the Caribbean Sea and off the coasts of Guinea and Sierra Leone. The RCP2.6-only experiment shows similar changes in TC density than RCP8.5-only but generally smaller in magnitude. No significant changes in TC frequency, intensity, or distribution are observed in the RCP2.6-only experiment compared to the PD simulation. This suggests that stabilizing GHG emissions at lower levels could mitigate future changes in TC activity. Translations speed (Fig.3.5) and normalized ACE (Fig.3.4) do not show any statistically significant change across all the RCP-only experiments.

3.3.1.2 GGW Scenarios

The introduction of the GGW is evaluated for its potential to modify TC activity under both RCP2.6 and RCP8.5 scenarios.

The most prominent impact of the GGW on the ATCs is the change in TC genesis density (Fig.3.1e-l). Under the RCP8.5 emission pathway, all the GGW scenarios show a shift from the subtropical Atlantic to the eastern MDR. Furthermore, a notable increase is found off the south-eastern U.S. coasts in all RCP8.5 experiments with GGW compared to RCP8.5 only. However, the GGW experiments exhibit a non-significant decrease in TC count compared to the RCP8.5-only baseline (Fig.3.2). The distributions for GGW_{HIGH} and GGW_{EXT} show a larger spread, suggesting increased variability in TC frequency. Despite this, the proportion of major hurricanes (Cat. 3 and 4) remains unchanged relative to RCP8.5-only, indicating that the GGW does not alter the intensification of TCs under high GHG emissions (Fig.C.8). A decline in category 1 TCs is observed in GGW_{MED} and GGW_{HIGH} experiments. The GGW's impact on TC intensity is further assessed using LMI (Fig.3.3). All GGW experiments under RCP8.5 exhibit LMI trends similar to RCP8.5-only, with no additional amplification or reduction. Similarly, the minor poleward shift in LMI latitude observed in RCP8.5-only is also present in GGW experiments, but the shift is not statistically significant (Fig.C.9). One exception is the ACE with a significant increase observed only in the GGW_{MED} experiment (Fig.3.4). GGW_{MED} exhibits a higher mean number of TC centers (storm length) than the other simulations, with approximately 1–1.5 more TC centers per storm, which explains the higher and significant increase in ACE. However, this change, being specific to a mid-level vegetation scenario, is more likely driven by stochastic variability rather than a physical mechanism.

The increase in TC genesis density is also observed across the eastern MDR in the GGW_{MED}, the GGW_{HIGH} and the GGW_{EXT} experiments under the RCP2.6 pathway. Additionally, a decrease in TC genesis density is found in experiments from medium to extreme vegetation over the central Atlantic at 30°N with a tongue extending toward the Caribbean Sea in the experiments under RCP2.6 emission scenario. However, this increase is less homogeneous compared to the RCP8.5 experiments. The increase in front of the south-eastern U.S is not found in these simulations. No significant changes in TC frequency, intensity, or distribution are observed, consistent with the negligible effects of RCP2.6-only. Similarly, LMI and ACE remain unchanged in all GGW experiments under RCP2.6.

Finally, translational speed shows no statistically significant changes across all GGW experiments under either RCP pathway. This suggests that the GGW does not influence TC movement, regardless of emission scenario (Fig.3.5).

3.3.2 Potential mechanism behind the change in tropical cyclogenesis density

A shift of TC genesis from the subtropical Atlantic to the eastern MDR for the experiments with medium-to-high vegetation density under the two RCP pathways is the most relevant impact of the GGW on the ATCs activity. To understand the causes behind such changes we analyze changes in both large-scale atmospheric conditions and TC seeds by looking at ENGPI and the AEWs, respectively.

For the large-scale atmospheric factors, in the RCP-only experiments, we found an increase in ENGPI over the eastern MDR for RCP8.5-only and in front of the coasts of eastern U.S. in all RCPs-only (Fig.3.6b-c) consistent with the increase in cyclogenesis density compared to the PD simulation. Similarly, a decrease in ENGPI off central-eastern America coasts matches with the decrease in TC density. However, in the RCP8.5-only experiment, the area characterised by increased ENGPI shows larger values than the area with the ENGPI decrease. Therefore, while ENGPI suggests an overall increase in the TC frequency across the basin, the TC counts in the model do not show a corresponding increase.

For the medium-to-high vegetation density experiments performed under RCP8.5 scenario, the change in TC genesis density is associated with a shift in the ENGPI over the eastern MDR (Fig.3.6f-k). The ENGPI has an increase in magnitude, as well as a pattern change as the vegetation density increases, whereas the increase in TC genesis (Fig.3.1g-l) is higher in the GGW_{HIGH} experiment compared to the GGW_{EXT}. In the case of the RCP2.6 experiments, the only significant change in ENGPI is shown in the extreme vegetation density simulation.

Regarding AEWs, there is a significant increase in the variance of the meridional wind component, which is a proxy of the AEWs activity encompassing both intensity and frequency of the waves, across West Africa for the RCP8.5-only experiment compared to the PD (Fig.3.7c). This finding aligns with previous results (Skinner and Diffenbaugh, 2014; Bercos-Hickey and Patricola, 2021), which find an intensification in the number and/or strength of AEWs along the Sahel/Sahara border in response to enhanced radiative forcing in the RCP8.5 pathway. Furthermore, an additional increase is observed when the GGW is considered, showing a direct correlation with the increase in vegetation density. This is particularly notable in the experiments conducted under the RCP8.5 pathway (Fig.3.7d-k). When separating the contributions of AEW intensity and frequency in the AEW activity (Tab.3.1), our results indicate that intensity, rather than frequency, drives the increase in AEW activity. This change is associated with an increase in TCs over the Eastern MDR (Fig.3.1). In our experiments, increased AEW activity triggers the increase in TC genesis changes across the eastern

MDR, aligning with Landsea and Gray (1992)'s second mechanism where amplified AEWs enhance convective organization. In the GGW experiments with medium-to-high vegetation density, there is a significant increase in precipitation over West Africa and along the coasts from Senegal to Sierra Leone. As discussed in Ingrosso and Pausata (2024), this precipitation increase is linked to changes in the WAM, characterized by enhanced deep convection due to a stronger Tropical Easterly Jet and a weaker African Easterly Jet. However, despite the strengthening in the Intertropical Convergence Zone (ITCZ) during the TC season, there is no associated latitudinal shift in TC genesis.

To better understand the ENGPI contribution to TC genesis change, we investigated the role of each ENGPI component and compared it to the influence of the AEWs. Changes in wind shear, potential intensity, relative humidity and absolute vorticity are shown in Fig.C.11, Fig.C.12, Fig.C.13 and Fig.C.14, respectively. AEW activity dominates TC genesis density changes in the eastern MDR, particularly off the coast of West Africa, where cyclogenesis peaks. Wind shear, relative humidity, and absolute vorticity play secondary roles in TC formation over this region, while PI's contribution is minimal and significant only in extreme vegetation experiments (an expected result due to prescribed SSTs). In the southern part of the basin, GPI decreases due to increased wind shear and decreased absolute vorticity, despite a rise in TC genesis. In the western portion of the eastern MDR, ENGPI, and particularly wind shear, contributes as much as AEWs to TC genesis density changes. Overall, wind shear drives most GPI variations. Additionally, increased TC density off the southeastern U.S. coast in all RCP8.5 GGW experiments is linked to a rise in ENGPI driven by favorable conditions in all components (except PI). Additionally, an increase in TC density off the southeastern U.S. coast is observed across all RCP8.5 GGW experiments, linked to a rise in ENGPI driven by favorable conditions in all components, except PI. These favorable conditions are not present in the RCP2.6 experiments - particularly regarding wind shear and relative vorticity - resulting in lower ENGPI values compared to RCP8.5 experiments, which are therefore unable to trigger the increase in TC genesis.

3.4 Discussion and conclusions

This study represents the first effort to explore the potential impacts of the African GGW project on the North Atlantic tropical cyclone activity under two future emission scenarios (RCP2.6 and RCP8.5) and vegetation density ranging from low to extreme levels using a high-resolution atmospheric regional climate model.

One of the key findings of this study is the significant increase in tropical cyclone genesis density over the

eastern part of the MDR in experiments with medium to extreme vegetation density compared to the case without vegetation (Fig.3.1g-l). A decrease in tropical cyclogenesis over the central-western Atlantic between 25°N and 35°N is also found. However, the counteracting changes between the two areas results in no significant change in ATC frequency across the basin.

The scientific community has been focusing on understanding the factors that control TC frequency. Attention has been directed toward both the large-scale atmospheric environment (e.g., relative humidity, potential intensity, vertical wind shear or their combined measures such as the ENGPI) and initial disturbances (often referred to as TC seeds) such as AEWs. Our findings indicate that variations in AEW activity (Fig.3.7) - particularly their intensity - are the primary drivers of changes in TC genesis over the eastern MDR, while other environmental factors (such as wind shear, relative humidity, and absolute vorticity, Fig.C.11, Fig.C.13 and Fig..C.14, respectively) play a secondary role. Specifically, an increase in AEW intensity is associated with a rise in TC genesis off the West African coast. In contrast, over the central-eastern MDR, both AEW activity and ENGPI components – especially wind shear - contribute comparably to TC genesis. Furthermore, the increase in ENGPI, driven by more favorable environmental conditions (i.e., decreased wind shear and increased relative humidity and absolute vorticity), supports a higher frequency of TC genesis off the southeastern U.S. coast. This result aligns with previous studies (Vecchi and Soden, 2007b; Camargo, 2013).

An increase in the AEW activity over the Eastern MDR is also present (Fig.3.7d-k) in all the GGW simulations, due to changes in WAM dynamics associated with the presence of the GGW (Ingrosso and Pausata, 2024). However, no change in AEW frequency is associated to the increase in AEW activity (Tab. 3.1). This finding corroborates previous conclusions by Patricola et al. (2018) and Danso et al. (2022), who excluded the role of the AEW frequency in driving changes in the mean number of Atlantic TCs. Here, the increase in AEWs activity is mainly due to the increase in AEWs intensity. This suggests a potential further role of stronger waves in controlling TC genesis frequency over the MDR, as suggested by Caron and Jones (2012).

Furthermore, the aforementioned dipole pattern in the tropical cyclogenesis density appears to be closely linked to stronger AEWs, which aligns well Caron et al. (2011)'s results. Stronger African waves in the GGW experiments create more favorable conditions for TC genesis across the eastern MDR, allowing more disturbances to develop into cyclones and resulting in fewer waves propagating westward. Caron et al. (2011) noted an inverse pattern where a shift in cyclogenesis location from MDR to subtropics was associated with

weaker waves.

A significant reduction in the number of TCs is projected in the high-emission scenario without GGW (Fig.3.2), despite the ENGPI indicating favorable conditions over the basin (Fig.3.6). This outcome is expected as the ENGPI and many other genesis indices, often show an increase in future TC frequency under a warming planet, even when the TC counts in those models decrease (Camargo, 2013; Camargo et al., 2014; Wehner et al., 2015).

The GGW does not impact the basin TC frequency or intensity. A significant decrease in TC frequency is found only for the RCP8.5-only experiment compared to the PD simulation (Fig.3.2) consistent with findings from previous studies (Bacmeister et al., 2018; Chauvin et al., 2020; Knutson et al., 2020; Murakami et al., 2020; Roberts et al., 2020). Achieving consistent future projections for TC frequency across Northern Hemisphere Ocean basins remains a challenge, even in high-resolution models (Sobel et al., 2021). A similar decrease compared to the PD is obtained in the GGW experiments, but it is not statistically significant. Additionally, an increase in the proportion of major hurricanes (Fig.C.8) and other TC metrics such as the LMI (Fig.3.3) and the normalized ACE (Fig.3.4) is also present, similar to other studies (Lee et al., 2020; Roberts et al., 2020; Knutson et al., 2020; Camargo et al., 2023) though only the LMI for the RCP8.5 scenario shows a statistically significant change. This increase is primarily attributed to the increase in greenhouse emissions rather than the GGW, consistent with previous literature (Knutson et al., 2020).

The use of a single atmospheric model with parameterized convection limits significance of the results of this study. One key caveat is the use of prescribed sea surface temperature and vegetation, which hinders the ability to consider atmosphere-ocean feedback associated with the presence of the GGW. In Knutson et al. (2020), the authors highlight how models with prescribed SST cannot reproduce important feedback such as TC-generated cool wakes, mixing, and salinity effects. Ogata et al. (2016) found differences between an atmosphere-only model and an atmosphere–ocean coupled model in detecting TC changes. Emanuel and Sobel (2013) show that the surface energy imbalance in models without ocean-atmosphere coupling can affect the reliability of TC potential intensity. Moreover, parameterized convection can be a limiting factor for land surface soil-vegetation feedback compared with convection-permitting models (Hohenegger et al., 2009; Taylor et al., 2013).

The GGW initiative is an ambitious endeavour focused on restoring and greening the Sahel to mitigate po-

tential climate change impacts on the region. The project could influence the pattern of tropical cyclone genesis, leading to an increase in the eastern Main Development Region and off the U.S. coasts, counterbalanced by a decrease in the subtropical Atlantic and other localized areas. Nevertheless, further studies, possibly employing convection permitting and atmosphere-vegetation coupled models are essential for a thorough evaluation of the GGW's broader climate effects. Such simulations could support policymakers in understanding and addressing any potential far-reaching repercussions of the GGW initiative.

3.5 Figures and Tables

Table 3.1: AEWs activity (units in m^2/s^2), AEWs intensity (units in m/s), number of African Easterly Waves, number of TCs and TC/AEW ratio for the season June-November (JJASON). AEWs activity, intensity and number are calculated at 15°N 20°W at 700hPa. TCs frequency is calculated over the eastern MDR.

Experiment	AEWs activiy	AEWs intensity	AEWs number	TCs
PD	4.9	3.2	39.4	4.4
RCP8.5-only	4.7	3	38.2	4.5
$GGW_{LOW8.5}$	5.1	3.2	39.3	4.9
$GGW_{MED8.5}$	5.2	3.3	38.7	5.8
$GGW_{HIGH8.5}$	5.3	3.4	37.5	6
$GGW_{EXT8.5}$	6	3.6	39.6	5.4
RCP2.6-only	4.8	3	40.3	4
$GGW_{LOW2.6}$	5.1	3.1	39.1	3.6
$GGW_{MED2.6}$	5	3.1	39.2	4.7
$GGW_{HIGH2.6}$	5.4	3.2	38.6	4.8
$GGW_{EXT2.6}$	5.6	3.4	37.5	4.8

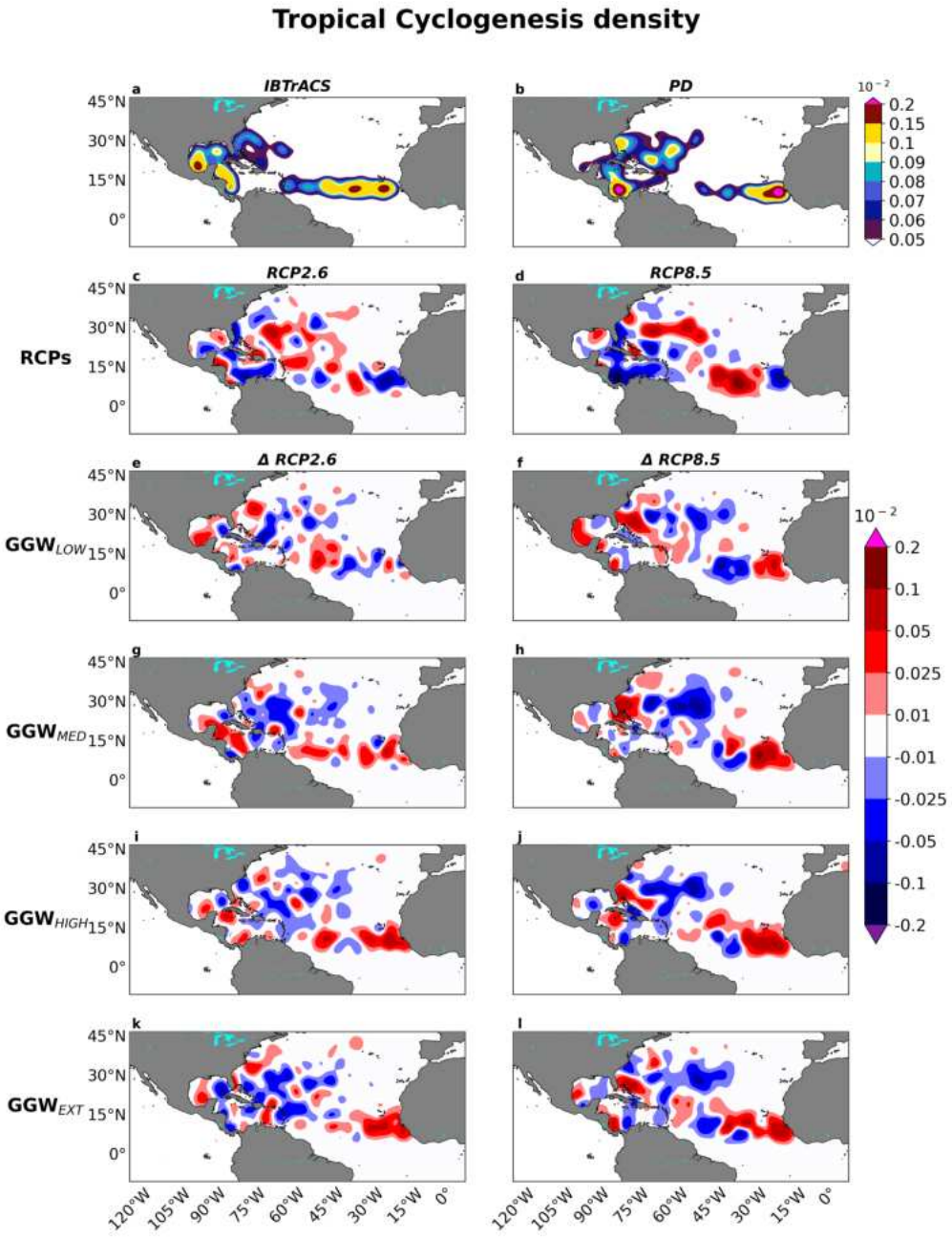

Figure 3.1: Tropical genesis density. a) TC genesis density for observations (IBTrACS) and b) for the PD experiment for the period 1990-2019. Change in TC genesis density for RCP2.6-only (c) and RCP8.5-only (d) relatively to PD. Change in TC genesis density for GGW_{LOW} (e-f), GGW_{MED} (g-h) GGW_{HIGH} (i,j) and GGW_{EXT} (k,l) relatively to RCP2.6-only and RCP8.5-only experiments. Hatches indicate values that are not significantly different at the 5% significance level using a local (grid-point) Wilcoxon signed-rank test.

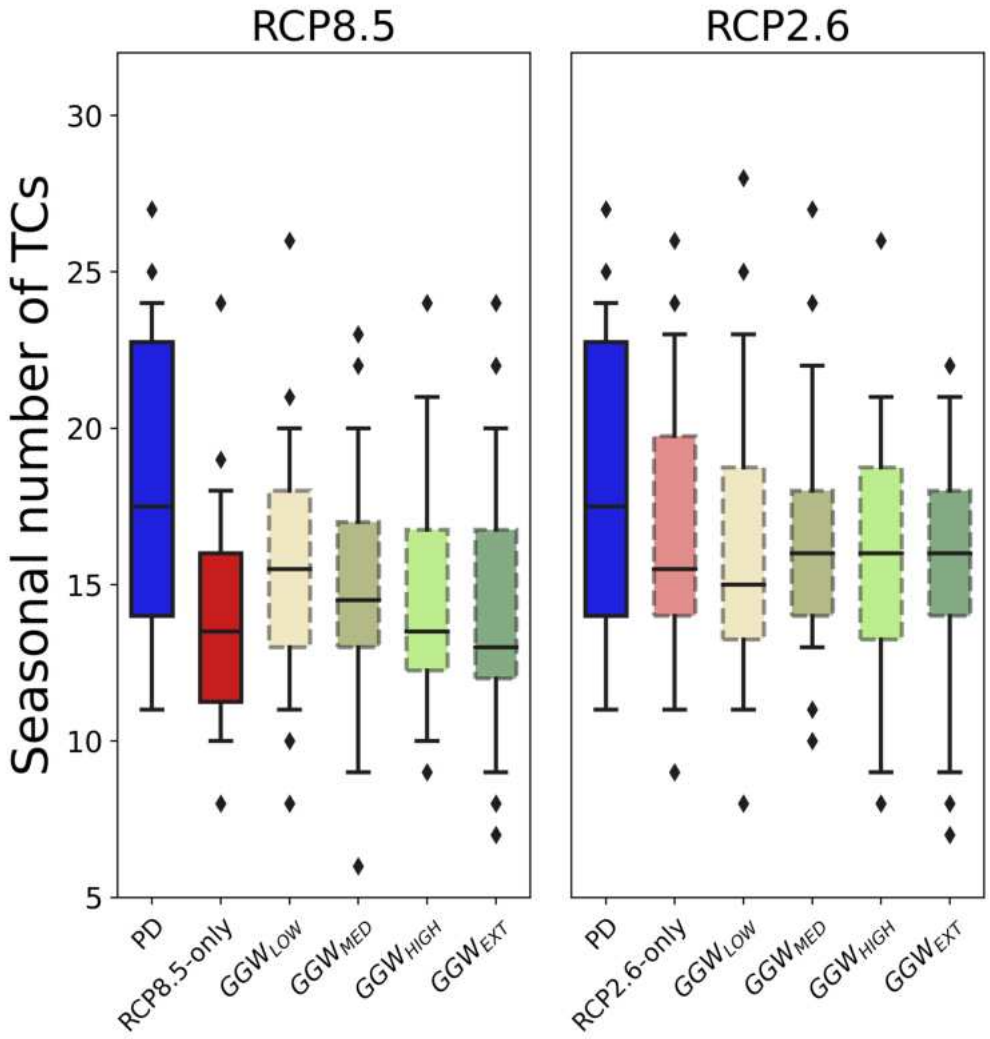

Figure 3.2: Seasonal number of TCs. Seasonal (June to November) number of TCs among the PD experiment (blue), the RCP-only (red), GGW_{LOW} (yellow), GGW_{MED} (olive green), GGW_{HIGH} (light green) and GGW_{EXT} (dark green) experiments between June and November for the period 1990-2019. RCP8.5 experiments are in the left panel, while RCP2.6 are in the right panel. Boxplots show the median (black line), the quartiles (the box), the 5-95-th percentiles (the wiskers) and outliers (dots). Dotted box indicates not significant differences from the Present Day experiment at the 5% significance level using a Kolmogorov-Smirnov and Mann-Whitney tests.

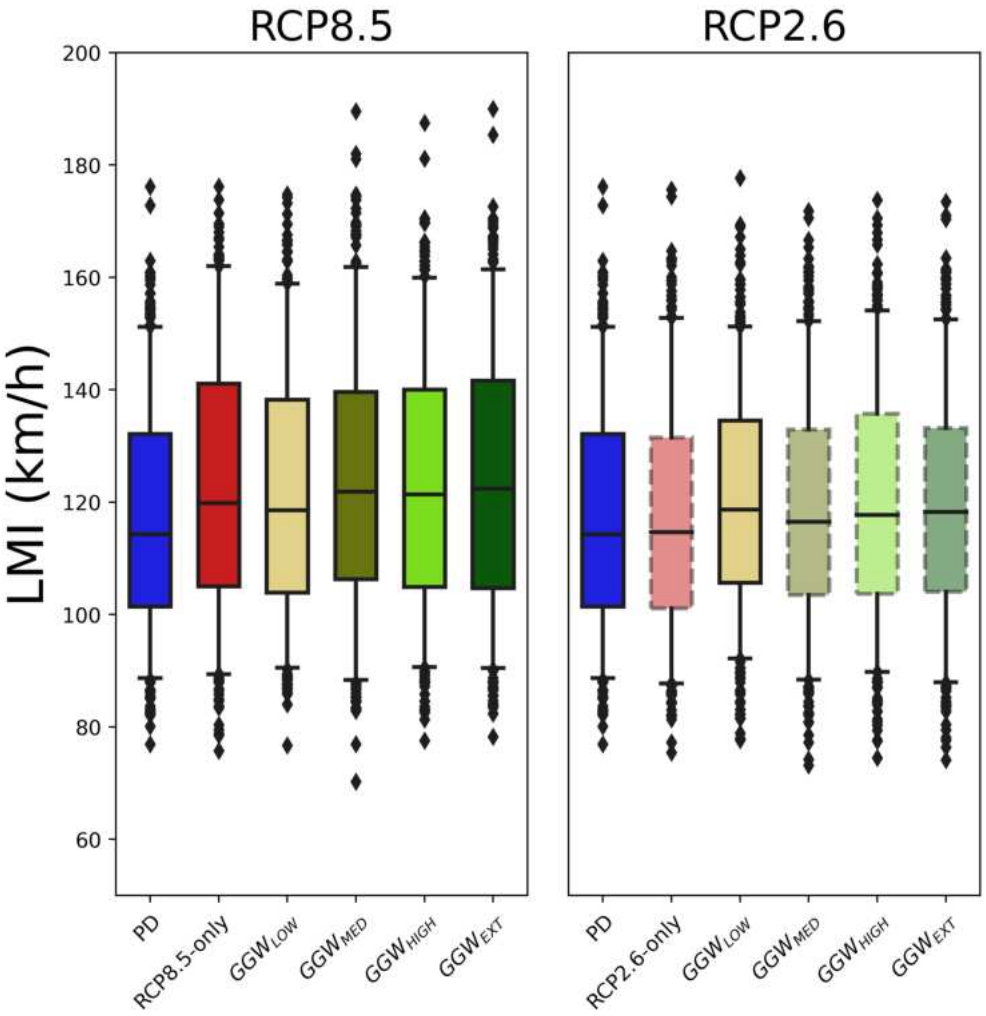

Figure 3.3: Lifetime maximum intensity (LMI). Left). LMI comparison among the Present-Day experiment (blue), the RCP-only (red), GGW_{LOW} (yellow), GGW_{MED} (olive green), GGW_{HIGH} (light green) and GGW_{EXT} (dark green) experiments between June and November for the period 1990-2019. RCP8.5 experiments are in the left panel, while RCP2.6 are in the right panel. Boxplots show the median (black line), the quartiles (the box), the 5-95-th percentiles (the wiskers) and outliers (dots). Dotted boxes show not significantly differencies at 5% significance level.

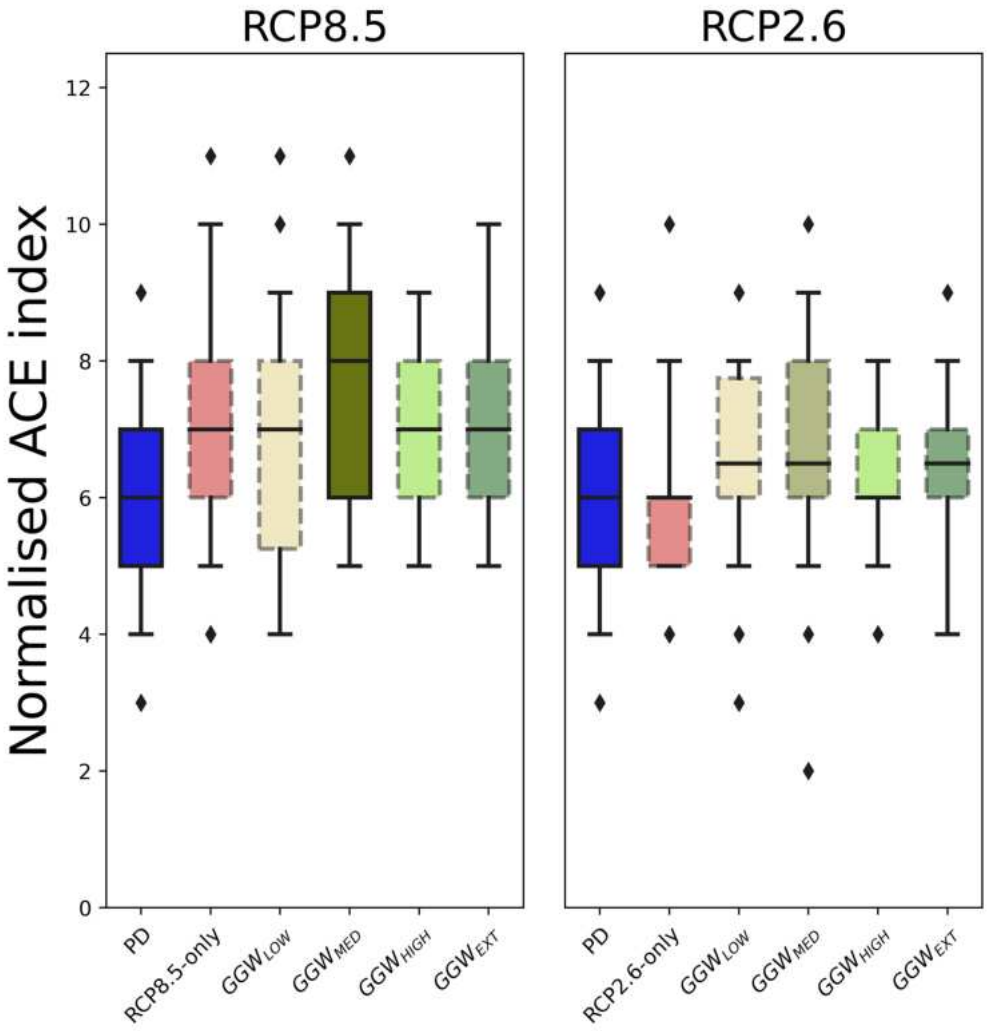

Figure 3.4: Normalised accumulated cyclone energy (ACE). Left). Seasonal normalised ACE comparison among the Present-Day experiment (blue), the RCP-only (red), GGW_{LOW} (yellow), GGW_{MED} (olive green), GGW_{HIGH} (light green) and GGW_{EXT} (dark green) experiments between June and November for the period 1990-2019. RCP8.5 experiments are in the left panel, while RCP2.6 are in the right panel. Boxplots show the median (black line), the quartiles (the box), the 5-95-th percentiles (the wiskers) and outliers (dots). Dotted boxes show not significantly differencies at 5% significance level.

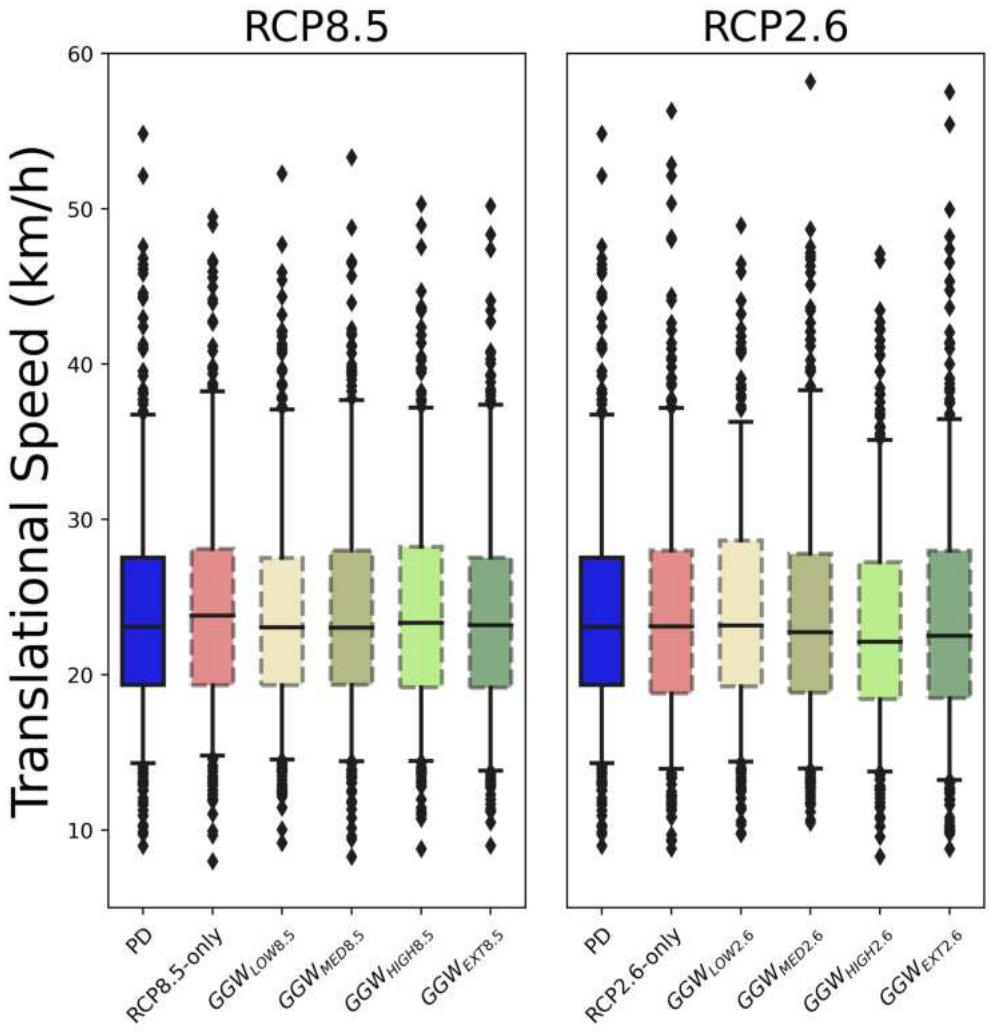

Figure 3.5: Translation speed location. Left). TC translation speed comparison among the Present-Day experiment (blue), the RCP8.5-only (red), GGW_{LOW} (yellow), GGW_{MED} (olive green), GGW_{HIGH} (light green) and GGW_{EXT} (dark green) between June and November for the period 1990-2019. Boxplots show the median (black line), the quartiles (the box), the 5-95-th percentiles (the wiskers) and outliers (dots). Dotted boxes show not significantly differencies at 5% significance level.

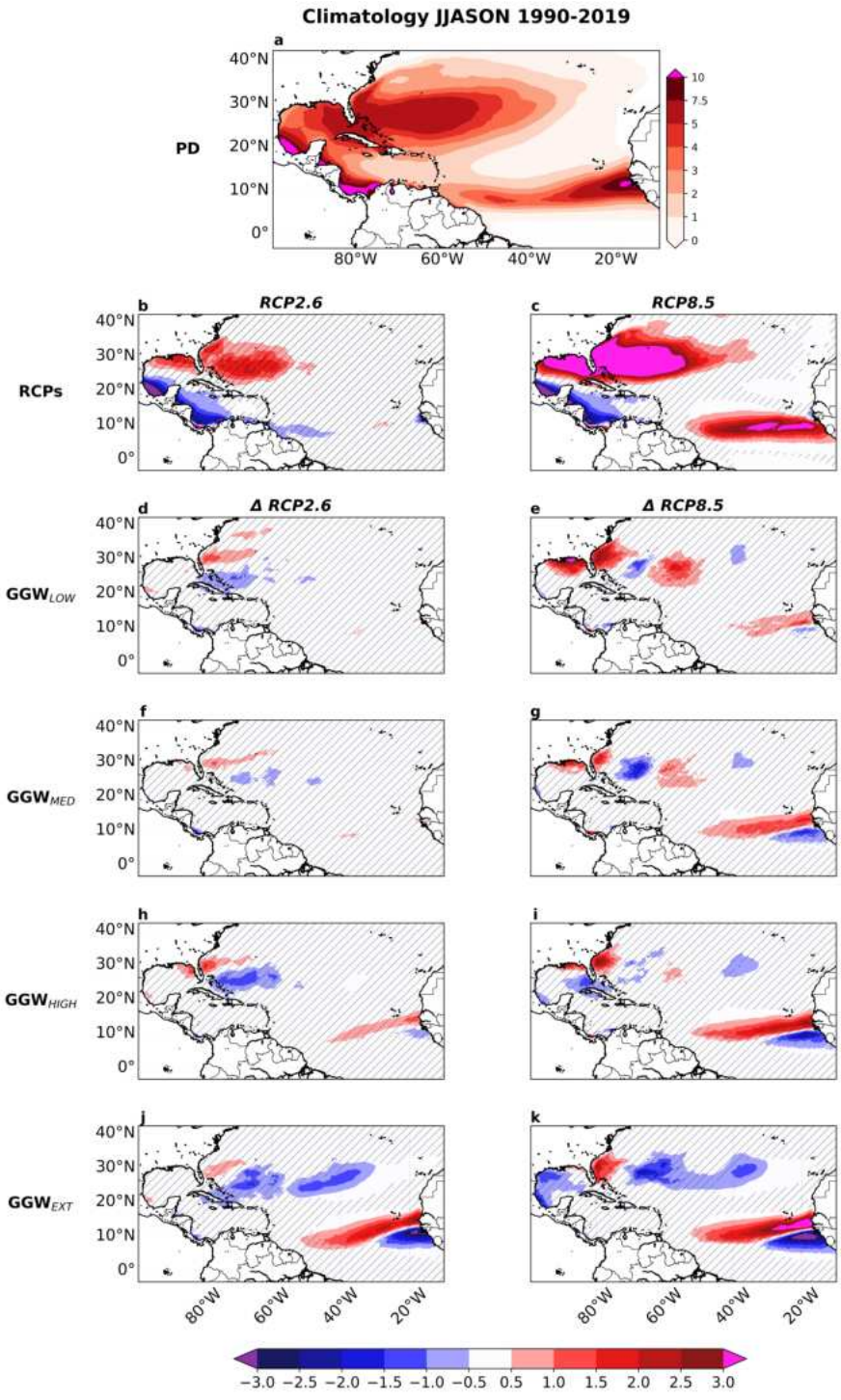

Figure 3.6: Genesis Potential Index. a) The Genesis Potential Index (GPI) climatology for the PD experiment between June and November for the period 1990-2019. Change in mean GPI for RCP2.6-only (b) and RCP8.5-only (c) relatively to PD. Change in mean GPI for GGW_{LOW} (d-e), GGW_{MED} (f-g) GGW_{HIGH} (h,i) and GGW_{EXT} (j,k) relatively to RCP2.6-only and RCP8.5-only experiments. Hatches indicate values that are not significantly different at the 5% significance level using a local (grid-point) Wilcoxon signed-rank test.

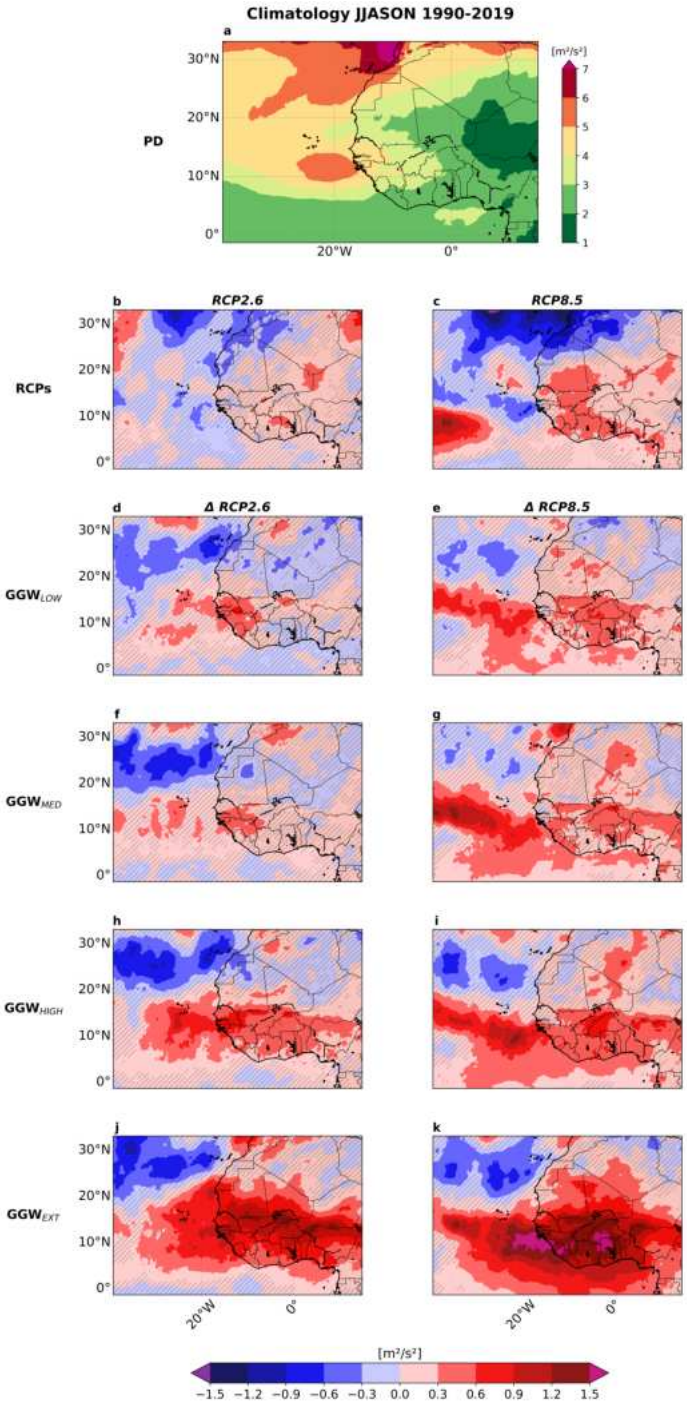

Figure 3.7: African Easterly Waves Activity. a) African Easterly Wave (AEW) activity climatology for the PD experiment between June and November for the period 1990-2019. Change in mean AEW activity for RCP2.6-only (b) and RCP8.5-only (c) relatively to PD. Change in mean AEW activity for GGW_{LOW} (d-e), GGW_{MED} (f-g) GGW_{HIGH} (h,i) and GGW_{EXT} (j,k) relatively to RCP2.6-only and RCP8.5-only experiments. Hatches indicate values that are not significantly different at the 5% significance level using a local (grid-point) Wilcoxon signed-rank test.

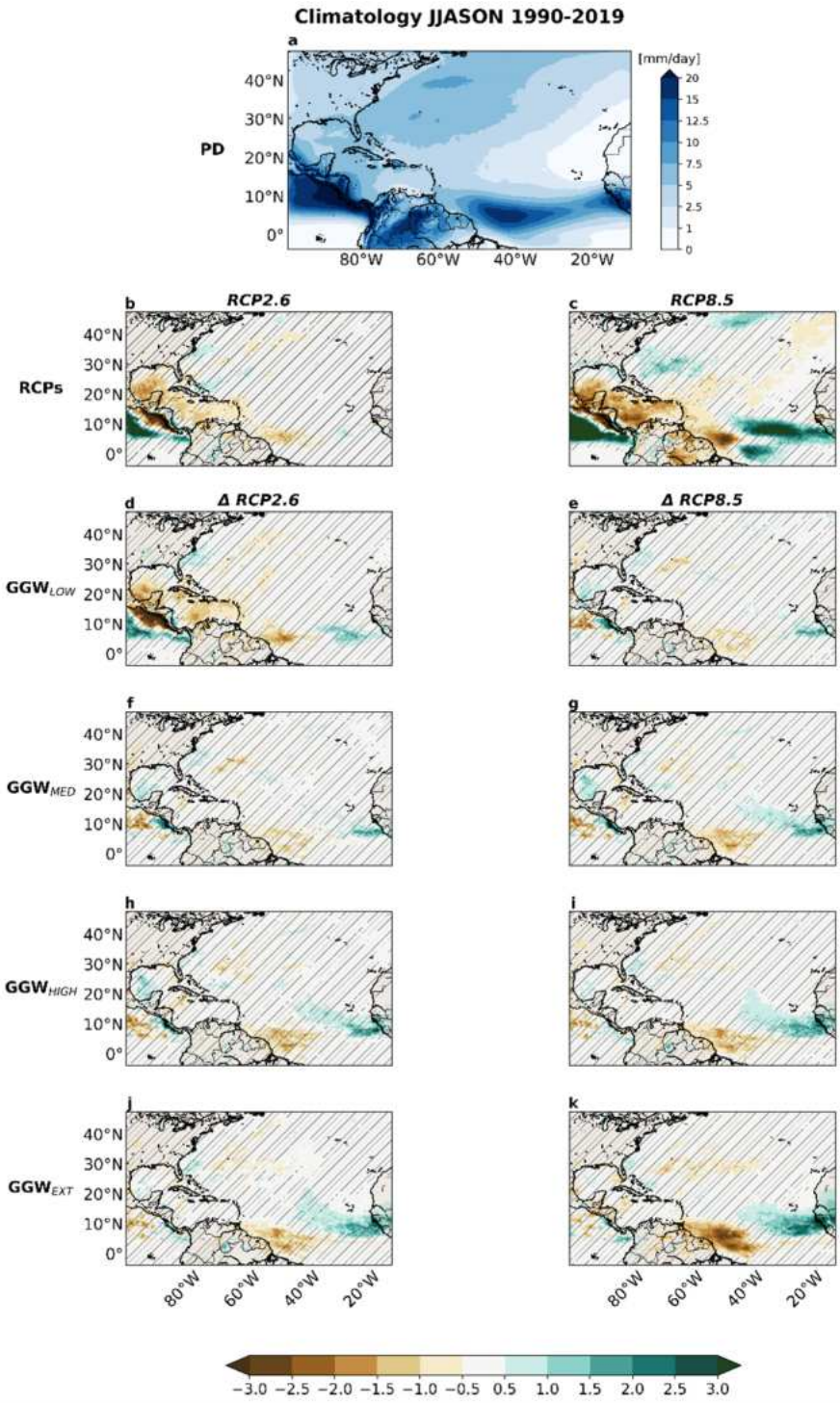

Figure 3.8: Mean Precipitation. a) JJASON Precipitation climatology for the Present Day (PD) experiment for the period 1990-2019. Change in mean precipitation for RCP2.6-only (b) and RCP8.5-only (c) relatively to PD. Change in mean precipitation for GGW_{LOW} (d-e), GGW_{MED} (f-g) GGW_{HIGH} (h,i) and GGW_{EXT} (j,k) relatively to RCP2.6-only and RCP8.5-only experiments. Hatches indicate values that are not significantly different at the 5% significance level using a local (grid-point) Wilcoxon signed-rank test.

CHAPTER 4

ASSESSING FUTURE TROPICAL CYCLONE RISK IN THE NORTH ATLANTIC USING UQAM-TCW2 MODEL

Roberto Ingrosso[1,2,3], Mathieu Boudreault[2,4], Francesco S.R. Pausata[1,2,3], David Carozza[4]

1 – Department of Earth and Atmospheric Sciences, Université du Québec à Montréal, Montréal, QC H2X3Y7, Canada

2 – Centres ESCER (Étude et la Simulation du Climat à l'Échelle Régionale)

3 – GEOTOP (Research Center on the dynamics of the Earth System)

4 – Department of Mathematics, Université du Québec à Montréal, Montréal, QC, Canada

This chapter forms the basis of two potential manuscripts, one on the methodology and another on climate change applications.

ABSTRACT

Assessing financial impacts caused by tropical cyclones (TCs), as well as understanding the natural variability and sources of uncertainties over present and future climates, is challenging. With questions arising about the insurability of coastal communities in the future, and the financial services industry requirements to stress-test their profitability to climate scenarios, it is therefore important to develop TC models that are computationally efficient to provide a full distribution of outcomes for the present and future.

To address these challenges, synthetic TC modeling has advanced significantly over the past two decades, enabling the creation of extensive synthetic TC datasets. One such model, the Université du Québec à Montréal Tropical Cyclone Wind model (UQAM-TCW), has been recently developed as a hybrid statistical-dynamical global TC model. In this study, we present a more physics-based implementation (UQAM-TCW2) of the model, which incorporates new statistical applications and multiple large-scale environmental variables influencing TC genesis and movement. The new model is defined by predictors from ERA-5 reanalysis and then driven by 20 (of the 40) members of the Community Earth System Model v.1 Large Ensemble (CESM1-LE). Three different versions of UQAM-TCW2 are considered, based on different combination of predictors.

We provide preliminary results for the North Atlantic basin under a high concentration scenario. Initial findings indicate an increase in TC frequency in the North Atlantic for two model versions and a slight decrease in the third one. Additionally, a rise in the proportion of major storms and an overall increase in TC intensity is found. The total future risk is projected to rise along the eastern coast of North America and in central and southern Mexico, driven by a combination of increased landfall rates and population changes (exposure). In contrast, parts of Mexico are expected to experience a decline in risk, primarily due to reduced landfall rates.

4.1 Introduction

Tropical cyclones (TCs) are among the strongest and deadliest natural disasters, affecting coastal communities, the environment, properties and businesses. With 38% of both disaster related deaths and economic damage for the period 1970-2019, tropical cyclones are, indeed, the most prevalent hazards with respect to human and economic losses (Douris et al., 2021). TCs cause USD 29 billion of direct damages and affect 22 million people on average every year (Guha-Sapir et al., 2017). Different estimates show that the costliest U.S. TCs such as Hurricanes Katrina (2005) and Harvey (2017) caused $200 and $158.8 billion 2024-USD (NOAA, 2024) in damage.

Despite their significant impacts on lives and properties, modelling the financial impacts of TCs remains a challenging task for financial risk management. Uncertainties related to the study of TCs limit global risk analyses and influence the evaluation of their financial impacts in terms of property losses. These uncertainties are primarily due to the short length of historical tropical storm records and their relative

rarity with medians of 80/85 TCs per year at global scale depending on the dataset (Schreck et al., 2014). Moreover, approximately only 12 of annual global TCs make landfall globally with wind speeds greater than 33 m/s (Weinkle et al., 2012). Global climate model (GCM) simulations used for TC tracking and analyses usually are based on a limited number of ensemble members and cover periods of maximum 100 years for both historical and future climate, which is not enough to produce an adequate sample of TCs. Moreover, the low resolution of GCMs does not allow simulating the most intense TCs (Roberts et al., 2020) and the global variability in human population further complicates risk analyses.

One way to overcome the limitations of the low resolution GCMs is to use high resolution GCMs (Roberts et al., 2020) or regional climate models forced by large-scale fields from GCMs (Landman et al., 2005; Knutson et al., 2008) to detect and track TCs with trackers. Unfortunately, even 25-km-grid models seem to struggle to simulate Category (Cat.) 4–5 TCs due to errors in spatial attributes of the wind field as suggested by Davis (2018). The inability for GCMs to reproduce intense storms can substantially affect risk analyses as Cat. 4–5 TCs accounted for almost half of normalized economic damage from TCs in the U.S. (PielkeJr. et al., 2008). Additionally, the detection rates of TC trackers are generally around 80% of the observed tracks, causing an underestimation of TCs (Bourdin et al., 2022).

Therefore, another approach has recently been developed focusing on the use of synthetic TC models to overcome data scarcity. These models use purely statistical (Vickery et al., 2000; Hardy et al., 2003; James and Mason, 2006; Bloemendaal et al., 2020; Arthur, 2021) or hybrid statistical-dynamical (Emanuel et al., 2006; Lee et al., 2018; Jing and Lin, 2020; Guenedal et al., 2022; Lin et al., 2023; Carozza et al., 2024; Xu et al., 2024) techniques to produce a large number of tracks, making the TC analysis more robust. Hybrid techniques combine statistical methods and simplified dynamical models forced by large-scale environmental conditions derived by reanalyses or GCMs output. Synthetic TC models are generally based on three main components for the creation of cyclogenesis, trajectories and storm intensity. Cyclogenesis modules generally seed the basin based on random seeding or probabilities coming from pure statistical or hybrid models. Trajectory components create tracks by means of statistical or hybrid models as well as models combining the *beta drift* effect (Li and Wang (1994),the drift of a tropical cyclone caused by the advection of the background potential vorticity field by the storm circulation) with mean advection, the so-called Beta Advection models (Marks, 1992). Finally, intensity components calculate wind speed over the whole track using dynamical as well statistical models.

In Carozza et al. (2024), the authors present a global hybrid model for tropical cyclone winds (hereafter UQAM-TCW) forced by the NCAR Community Earth System Model version 1 Large Ensemble (CESM1-LE, Kay et al. (2015)). The model is conditioned on El Niño–Southern Oscillation (ENSO) index and phases as predictors in the first two components (cyclogenesis and displacements), which allow to provide hazard maps with return periods for winds of different intensities during La Niña and El Niño events. More details about these models are provided in Section 4.2 and in Fig.4.1.

A subset of global synthetic TC models such as the MIT model (Emanuel et al., 2006), the Columbia HAZard model (Lee et al. (2018), CHAZ) and the Synthetic Tropical cyclOne geneRation Model (Bloemendaal et al. (2020), STORM) have been evaluated in a intercomparison analysis (Meiler et al., 2022). The model outputs were coupled with CLIMADA, an open-source software, which integrates hazard, exposure, and vulnerability to compute the necessary metrics to assess risk and to quantify socio-economic impact (Aznar-Siguan and Bresch, 2019). The study found that basins characterized by high TC activity like the North-West Pacific show better agreement among the models in several metrics whereas basins with few TCs like the Indian Ocean exhibit the largest variability and highest uncertainty. Infrequent and highly disruptive landfalls related to intense TCs are the costliest and rarest events. Consequently, they tend to show the highest variability among the models. This is an important limitation, given that these events are pivotal for risk assessment.

All these models have been designed based on the recent climate. This raises concerns about how these models could reproduce potential changes in TC activity and dynamics under climate change. The increase in global temperatures leads to larger extreme events, which affect not only the insurance sector, but coastal communities, governments, and the financial services sector. Future TC projections show medium-to-high confidence in a global increase in TC precipitation rates, global increase in TC intensity, and proportion of major hurricanes (Knutson et al., 2020). On the other side, low confidence is assigned to a decrease of global TC frequency, a slowdown in TC translation speed and further poleward expansion of the latitude of maximum TC intensity, especially in the western North-West Pacific. However, climate projections are associated with a large range of uncertainty, especially with TCs. Governments, coastal communities, insurance and financial companies, and nonprofit organizations rely on information about climate risks associated with hurricanes as well other extreme events such as tornadoes, wildfires and floods.

Future change in TC activity and risk under climate change have also been evaluated using some synthetic models. Emanuel et al. (2008) used the MIT model and produced sets of 2,000 events in each basin driven

by seven global climate simulations under the IPCC scenario A1b for the period 2181-2200 and compared them with a set of the same size for the period 1981-2000. Their results indicated changes in tropical cyclone activity depending on basins and the considered climate model. A decrease in TC frequency is found over the Southern Hemisphere while an increase in frequency is observed over the North-West Pacific. Furthermore, power dissipation and storm intensity tend to increase in the future. Lee et al. (2020) used CHAZ, downscaling six Coupled Climate Model Intercomparison Project's fifth generation (CMIP5) climate models under the Representative Concentration Pathway 8.5 (RCP8.5) covering the period 1981-2100. The tropical cyclone genesis index (TCGI) is considered as a predictor in the cyclogenesis component. They used two TCGI versions (Tippett et al., 2011; Camargo et al., 2014)) based on two different humidity parameters, which lead to different results. When the column-integral relative humidity is considered, a positive global trend in TC frequency is found in all CMIP5 models. On the contrary, when the humidity contribution comes from the saturation deficit parameter, the global trend is negative. However, the choice of the humidity parameter does not affect other TC metrics such as the lifetime maximum intensity (LMI), the fraction of major TCs and the fraction of storms undergoing rapid intensification (RI). Global LMI and RI exhibit a small positive trend, though significant variability is observed across different basins. These differences are reflected in the return periods, with the model incorporating column-integral relative humidity indicating an overall decrease due to an increase in tropical cyclone probabilities. In contrast, the opposite is seen when the saturation deficit is considered, especially for Cat.4+ TCs.

Bloemendaal et al. (2022) ran STORM to generate 10,000 years of synthetic TCs for the periods 1979–2014 and 2015–2050 under the Shared Socioeconomic Pathways Scenario 585 pathway (O'Neill et al., 2016). The STORM model and the dataset are publicly available to the community. They found a global increase in the frequency of major storms (except in the Bay of Bengal), in the magnitude of TC intensity, whereas a decrease is observed in the frequency of tropical storms. They also found an increase in wind speed at the 100 and 1000 return periods and higher probabilities to reach Cat.1 and Cat.3 TC wind speeds, except in the Bay of Bengal and the Gulf of Mexico.

Return period curves weighted by population indicate that chances of individuals experiencing major hurricanes in their life time increase under climate change in the Western and Eastern Pacific basins. Guenedal et al. (2022) produced first estimates in terms of damage projections under different Representative Concentration Pathways (RCPs, Moss et al. (2010)) at the global level and for individual countries. The authors highlight that their dataset may not be accurate enough to properly calibrate adaptation measures as it was

based on low-resolution data and limited number of simulations. The analysis suggested that assuming no adaptation under the RCP2.6 pathway, a growth of expected global annual financial losses from tropical cyclones would increase by a factor of 4.2 during the period 2070-2100. With no socioeconomic and population growth factors, they found that the expected financial loss grew by a factor of 1.6 due to increasing cyclone intensity. Considering adaptation, the expected damage grew by a factor of 2.6. For SSP2–RCP4.5 and SSP5–RCP8.5 with no adaptation, the average expected damage grew by a factor of 5.4 and 14.2, respectively.

In UQAM-TCW (Carozza et al., 2024), the connection between the TC model and climate model ensemble allows to assess impacts of climate change on TCs evolution. However, uncertainties still remain with respect to the impacts of climate change for various components of the model, such as cyclogenesis, trajectory, intensity and wind structure. As mentioned above, the model is based on ENSO index and phase as predictors. Biases in coupled GCMs could overestimate frequencies of El Niño events in the future as a consequence of the cold bias of their equatorial cold tongues (Seager et al., 2019). State of the art climate models predict reduction of the zonal sea surface temperature (SST) gradient across the equatorial Pacific with an increase in greenhouse gases, contrary to what observations show (Coats and Karnauskas, 2017). This could potentially impacts on the frequency and intensity of TCs in each basin. Given the importance of TC hybrid models for various stakeholders, a more physics-based version of the model is required to properly assess how global climate change could affect TC activity and risk.

Here, we present an extension of UQAM-TCW, hereafter UQAM-TCW2. The new model is built on the environmental large-scale predictors from the European Centre for Medium-Range Weather Forecasting (ECMWF)'s fifth generation climate reanalysis dataset - ERA5 Reanalysis output (Hersbach et al., 2020). Then, the model is forced by 20 (of 40) members of the NCAR CESM1-LE (Kay et al., 2015) under the historical period and an extreme concentration scenario, the RCP8.5, for the future in the North Atlantic. In particular, in Section 4.2, we present materials and methods: An implementation of the cyclogenesis and the displacement modules in UQAM-TCW2 is provided. Three different UQAM-TCW2 models are created with different combinations of four predictors (Fig.4.2). This approach is designed to assess the influence of each large-scale factor identified in the scientific literature that may affect TC genesis. The goal is to determine the most effective interplay between these factors and their impact on TC frequency and landfall locations. In Section4.3, we present a statistical evaluation of the cyclogenesis and displacement modules. In addition, a comparison between UQAM-TCW2 and observations is provided in terms of TC density, fre-

quency and other TC metrics such as the LMI and the Accumulated Cyclone Energy (ACE). A validation for TC hazards in terms of landfalls rates is also shown. In Section 4.4, we present an evaluation of future changes in TCs statistics, while in Section 4.5, we discuss the simulated estimate of TC landfall rates and risk change associated with climate change. Finally, in Section 4.6, we summarize key findings and present conclusions. Note that some preliminary results for the North-West Pacific are also shown in Section D.3.

4.2 Material and methods

4.2.1 The UQAM-TCW2 model

UQAM-TCW (Carozza et al., 2024) is a statistical-dynamical model, which can be used in conjunction with a climate model large ensemble to generate large samples of TC seasons. It is forced by the output of NCAR CESM1-LE, which includes a 40-member ensemble of fully-coupled CESM simulations run under the RCP8.5 pathway. The NCAR CESM1-LE has a nominal 1° horizontal resolution in the atmosphere, 30 vertical levels in the atmosphere, and 60 vertical levels in the ocean. The ENSO phase and index calculated by the monthly climate model output are used as predictors for the cyclogenesis and the displacements modules, respectively. The FAST intensity simulator (Emanuel, 2017) fed by the monthly CESM1 variables provides the wind speed in each TC center.

The use of ENSO as predictor can limit the ability of the model to properly predict future change in TC activity. Strong disparities are, indeed, present among climate models about the ENSO future evolution under climate change (Collins et al., 2010; Stevenson, 2012; Beobide-Arsuaga et al., 2021). Majority of climate models predict more El Niño-like state over the next several decades for the equatorial Pacific under greenhouse gas–induced warming (Sobel et al., 2023). This leads to a reduced zonal SST gradient and weakened Walker circulation. El Niño conditions generally suppress TC activity over the North Atlantic and favor it over the eastern and central North Pacific. The TCs genesis regions are shifted eastward and equatorward over the North-West Pacific with increased TC intensity. However, observations show the opposite trend, toward a more La Niña-like state in the last 50 years (Seager et al., 2022; Lee et al., 2022). Furthermore, ENSO is not the only factor, affecting TC activity. Other factors such as the Pacific Decadal Oscillation, Atlantic and Pacific modes and the Atlantic Multidecadal Oscillation could also play a role (see Camargo et al. (2010) for more details). In this study, we provide an update of the model (UQAM-TCW2), where the cyclogenesis and the displacement modules are based on a logistic regression and a multiple linear regression, respectively, and variable related to TC formation and motion are used as predictors (Fig.4.2). The tracks from the Inter-

national Best Track Archive for Climate Stewardship (IBTrACS, `https://www.ncei.noaa.gov/products/international-best-track-archive,dataaccess:03/10/2022`, Knapp and Kruk (2010)) are used as response to train the model. 1980-2019 is the 40 years period to train the model (Fig.4.2), a temporal range considered to aligns with the modern era of satellite observations (Schreck et al., 2014). The ERA5 Reanalysis variable are used as predictors to define the different model versions. In the IBTrACS dataset, we select data from the U.S. agencies, with a wind speeds as 1-minute average sustained winds. The first 20 (of 40) CESM1-LE member output are considered to force the model and determine past and future changes in TC hazard and risk over a period of 40 years for a total of 800 model years (MY) for each simulation. The years between 2006-2019 from the RCP8.5 CESM1-LE output are added to the historical data to cover the period 1980-2019.

The North Atlantic basin is considered in this study, according to the basin definition on IBTrACS. However, preliminary results for the North-West Pacific are also provided in the Supplementary Materials of this work. We consider all TCs with LMI of at least tropical storm intensity (18 ms^{-1}). TCs are divided in different categories according to the Saffir-Simpson TC intensity scale (Simpson, 1974). In this work, we divide the TCs in: *all storms*, which refers to TCs with maximum near-surface winds of at least 18 ms^{-1}, *Cat.1+*, which reach a maximum wind speed of at least 33 ms^{-1} and *Cat.3+* or *major storms*, which reach a maximum wind speed of at least 50 ms^{-1}. TC density, landfall rates and risk maps are provided at 1° horizontal resolution, consistent with the resolution of the CESM1-LE forcing.

4.2.2 The cyclogenesis module

UQAM-TCW is based on an inhomogeneous spatial Poisson point process to statistically reproduces TC genesis locations (see Fig.4.1). ENSO can modulate global tropical TC genesis by altering the large-scale atmospheric and oceanic environments (Bove et al., 1998; Camargo et al., 2010; Chand et al., 2013; Sobel et al., 2016; Lin et al., 2020). The ENSO phases are reproduced in the CESM1-LE and used as predictor.

Other global TC models use random seeding techniques (MIT and Lin et al. (2023), hereafter MIT/FAST) or Poisson regressions and distributions to produce synthetic cyclogenesis (STORM, CHAZ and the Cyclone generation Algorithm including a THERmodynamic module for Integrated National damage Assessment-CATHERINA, Guenedal et al. (2022); Fig.4.1). The Princeton environment-dependent probabilistic tropical cyclone-PepC (Jing and Lin, 2020) and the Risk Analysis Framework for Tropical Cyclones-RAFT (Xu et al., 2024) employ a Poisson regression and Gaussian kernel-based probability distribution, respectively, to sim-

ulate genesis, but their domain is constrained to North Atlantic.

In this study, the cyclogenesis module is developed by using more physics-related variables compared to the original model version as predictors of a logistic regression (Berkson, 1944) where observed TC genesis from the IBTrACS dataset for the period 1980-2019 is used as a response (Fig 4.2). 70% of the sample data is used to train the model and 30% is used for testing. The training data are then balanced (90:10) to avoid a disproportion among the two categories of events (cyclogenesis vs not cyclogenesis). Please, note that we took only cyclogenesis which reach tropical storm level from IBTrACS, assuming that all the other grid cells of the domain are not affected by (future tropical storm) cyclogenesis. At the end, predicted probabilities are adjusted following Saerens et al. (2002) to match observed probabilities.

Monthly averaged predictors such as the SST, the potential intensity (PI), the relative and absolute vorticity at 850 hPa, the wind shear between 250hPa and 850 hPa, and the relative humidity at 700 hPa are considered (Fig.4.2). For the absolute vorticity, we used «clipped» values based on an upper bound of 3.7 X 10^{-5} s^{-1}, following the suggestions from Tippett et al. (2011). These parameters represent the main environmental variables reasonably expected to be important predictors of tropical TC genesis and used in the classic definitions of the genesis potential indices (Emanuel and Nolan, 2004; Camargo et al., 2007). Both ERA5 and CESM1-LE output as well as observed TC genesis from IBTrACS are aggregated over a grid at 2°horizontal resolution in order to obtain a proper amount of occurrences in each grid cell.

Three different versions of UQAM-TCW2 are defined on the basis of different combinations of the above mentioned predictors: (1) the RV model based on the SST, the relative vorticity, the relative humidity and the wind shear; (2) the AV model based on the SST, the absolute vorticity, the relative humidity and the wind shear; (3) the PI model, which uses the PI, the absolute vorticity, the relative humidity and the wind shear. Hence, we define three model versions fitted with ERA5: RV-ERA5, AV-ERA5 and PI-ERA5; and three other versions forced by CESM1-LE: RV-CESM, AV-CESM and PI-CESM. Potential intensity is calculated by using the Tropical Cyclone Potential Intensity Calculations in Python (pyPI, v1.3) package developed by Gilford (2021).

4.2.3 The displacement module

In UQAM-TCW, the trajectory module is based on an inhomogeneous two-dimensional (2-D) Brownian motion, which is an extension of James and Mason (2006) using covariates. The module reproduces meridional and zonal displacements of TCs using correlated normal distributions whose means and standard deviations

are different per latitudinal bands and ENSO index.

MIT, CHAZ, MIT/FAST and RAFT create synthetic tracks using a beta-advection model (Marks, 1992) whereas STORM and CATHERINA apply regressions to create meridional and zonal displacements of each synthetic TC, following the method used by James and Mason (2006) in their statistical model (Fig.4.2). PepC trajectories are produced by an Analog-Wind Track Model based on a random forest regression. The ImpeRIal college Storm (IRIS) global model (Sparks and Toumi, 2024) employs a different approach, which only simulates the decay from the point of LMI. Here, "parent" tracks from IBTrACS are perturbed to create stochastic "child" tracks following the National Hurricane Centre (NHC) forecast cones. Finally, models based on pure statistical approaches generally use autoregressive schemes for analyses at sub-regional and regional scale (Vickery et al., 2000; Hardy et al., 2003; James and Mason, 2006; Arthur, 2021).

In UQAM-TCW2, storm trajectories are always defined in terms of their zonal and meridional motions every three hours. We decided to replace a module based on an indirect predictor as the ENSO index and the latitudinal bands approach, which could not properly capture future changes, with a more physics-driven module based on explicit variables and one single application for each basin (Fig.4.2).

There is a strong relationship between surrounding large-scale flow and tropical cyclone movement, which affects tracks direction (Chan and Gray, 1982). Hence, the module is now characterized by a multiple linear regression (Wilkinson and Rogers, 1973) with 300-850 hPa steering winds (the mean of the wind magnitude between 300 and 850 hPa over an area around the TC center with size of 2°), the Coriolis parameter and the previous zonal and meridional displacements. Consequently, the model is auto-regressive. This approach extends the method used by Mathon et al. (2002) by incorporating additional covariates beyond displacements as predictors. Again, training and testing data represent 70% and 30% of the initial data, respectively. A specific model trained only by the 300-850 steering flows and the Coriolis parameter is defined to produce the initial displacement.

As cyclogenesis and displacement modules are defined, synthetic trajectories can be produced. A binomial random variate generation (Kachitvichyanukul and Schmeiser, 1988) based on 100 simulations is used to produce synthetic TC genesis based on their probabilities coming from the first module (see Sec. 4.2.2). TC genesis is randomly created over a 2° grid cell, coherently with the horizontal resolution of the predictors used in the cyclogenesis component. Then the simulated cyclogenesis locations are passed to the

displacement component to determine the storms' further evolution. Note that in this part of the model, the trajectories are still not physically constrained by the intensity of the storm. Then, the only limitation is represented by the physical domain of the basin.

4.2.4 The intensity module

The intensity module is based on the FAST TC wind simulator (Emanuel, 2017), a fast and physically consistent algorithm for estimating TC intensity along given tracks. It is based on two coupled ordinary differential equations predicting the evolution of wind speed and inner core moisture. These equations represent a prognostic tool describing ocean interaction, ventilation, dissipative heating, and the pressure dependence of the surface saturation mixing ratio. Input required by FAST are tracks, the potential intensity, the outflow temperature along track, the 850-250 hPa vertical wind shear, the SST, the upper ocean mixed layer depth and the sub-mixed layer thermal stratification and the ocean bathymetry. More details regarding the use of FAST in the first version of the model are provided in (Carozza et al., 2024).

In the other TC models, intensity components encompass several approaches. CHAZ uses autoregressive models, MIT/FAST and UQAM-TCW apply the FAST intensity simulator (Emanuel, 2017), MIT employs a dynamical intensity model (Emanuel and Nolan (2004),CHIPS) while STORM implements an empirical wind-pressure relationship. In CATHERINA, a thermodynamic module is created to produce storm intensity. This module is based on calculations in five steps: the wind–pressure relationship, the local thermodynamic, the maximum pressure drop, the depression dynamics (by means of an auto-regressive stochastic equation) and a statistical decay relationship. Regional models such as PepC and RAFT use a Markov intensity model and a deep learning model (Xu et al., 2021), respectively.

Finally, monthly means of atmospheric reanalysis products are generally used as predictors in the different components to build/fit synthetic TC models. For instance, STORM, MIT/FAST, UQAM-TCW, CATHERINA, RAFT use the European Centre for Medium-Range Weather Forecasting (ECMWF)'s fifth generation climate reanalysis dataset - ERA5 Reanalysis output (Hersbach et al., 2020) Reanalysis. CHAZ and PepC employ ERA-interim (Dee et al., 2011), the previous version of ERA5. MIT points to/applies/uses/ the National Centers for Environmental Prediction-National Center for Atmospheric Research (NCEP-NCAR, Kalnay et al. (1996)) products.

4.2.5 Algorithm

A description of the different steps to generate event sets for each MY of the CESM1-LE is provided in this section.

For each basin and each of the 800 CESM1-LE member-years, we create a set of accepted TC tracks, which are consistent with the yearly environmental conditions. We refer to each of these as event sets that are connected by the following components:

1. Climate forcing: The large-scale environmental conditions in the selected MY and basin;
2. Cyclogenesis location: Based on Step 1, simulate the cyclogenesis probability per each grid cell by means of a logistic regression;
3. Trajectory: Based on Step 2, simulate the entire trajectory (meridional and zonal displacements every 6 hrs) with a model based on a multiple linear regression;
4. Intensity: Initialize trajectory intensity at the cyclogenesis location with a wind speed of 10 ms^{-1} (Emanuel, 2017), and calculate the intensity every 4 min using the FAST model over the entire trajectory with the climate model variables for the MY in question (Step 1). Add 60% of the translation velocity to the intensity to calculate the ground-relative intensity from the storm-relative intensity (Emanuel and Jagger, 2010);
5. Acceptance/Rejection: Retain trajectory if the LMI is 18 ms^{-1} or larger. End trajectory where the storm intensity falls below 2.5 ms^{-1}. If the storm is too weak and is therefore rejected, then repeat Steps 2–5;

Note that although trajectories in Steps 2–3 are still driven by the underlying large-scale environmental conditions (predictors), they remain conditionally random, and therefore not physically, nor dynamically consistent (Emanuel et al., 2006). The climate forcing from Steps 1, 4 and 5 fill this gap, providing realistic and dynamically consistent trajectories.

4.2.6 The pre and post-processing

A one-dimensional bias correction has been applied to the CESM variables, which are pre-processed by removing model bias through a comparison against ERA5 output. Despite the application of pre-processing, the low resolution of the NCAR CESM1-LE output may hinder the accurate replication of observed TC intensity.

Here, we adjusted the simulated LMI distributions using regressions on quantiles. The bias correction supposes a linear function between observed and modelled quantiles below a certain threshold and a log-linear relationship above that threshold. We suggest scaling simulated TC wind speeds such that the quantiles of the simulated LMI distribution match observed quantiles (from IBTrACS).

4.3 Model evaluation

4.3.1 The cyclogenesis component

4.3.1.1 Model performances

Simulating TC genesis can be viewed as a classification problem, where qualitative responses are categorized into one of K distinct classes or categories (Hastie et al., 2021). In this paper, TC genesis is modelled as a two-class or binary response (0-1) for each grid-cell-month, 1 when the cyclogenesis occurs and 0 when not. Linear regression methods do not provide meaningful estimates of probabilities for classification problems. Consequently, logistic regressions can be used as an approach to provide cyclogenesis probabilities based on physical variables as predictors.

In order to evaluate model performances, we consider the Receiver Operating Characteristic (ROC) curve, which simultaneously displays two types of errors (false postives or false negatives) for all possible thresholds. The Area Under the ROC Curve (AUC) represents the overall performance of a classifier, then the larger the AUC the better the classifier.

AUC values for each version are quite high, 0.82 and for the RV model (Fig.4.3a) and 0.81 for the AV and PI versions (Fig.4.3b-c). Values above 0.8 mean that the models have more than 80% chance of distinguish between positive and negative classes, and they are generally considered excellent (Hosmer et al., 2013).

Regarding spatial TC genesis probability for the period 1980-2019, the pattern shown by observations is

well captured by the model trained by ERA5 variables as predictors (Fig.4.4). In particular, the RV-ERA5 version adequately reproduces TC genesis probability over the Main Development Region (MDR) with a little underestimation over the northern part of the MDR and an overestimation in the southern part (Fig.4.4b). The TC genesis probability over the Gulf of Mexico is lower compared to IBTrACS while a large overestimation is present across the southern part of the Caribbean Sea. This large overestimation is due to high values of the relative vorticity present over the area in the ERA5 dataset, which affects the cyclogenesis module with this variable. The AV-ERA5 and PI-ERA5 versions exhibit similar results showing good agreement with observations over the Gulf of Mexico. However, they both underestimate TC genesis compared to RV-ERA5 in the northern side of the MDR (Fig.4.4d,f). When the versions forced by CESM1-LE are considered, RV-CESM shows a greater overestimation of TC genesis over the southern Caribbean Sea compared to the RV-ERA5 version and it presents a higher number of TC genesis across the MDR relative to IBTrACS (Fig.4.4c). AV-CESM and PI-CESM show a similar pattern compared to AV-ERA5 and PI-ERA5 with a larger underestimation relative to observations over the Gulf of Mexico.

The ERA5-driven versions accurately reproduce the inter-annual variability over the North Atlantic basin. High significant correlations are observed between RV-ERA5 (0.84), AV-ERA5 (0.7) and PI-ERA5 (0.71) and the observations (Fig.4.5,a). Moreover, the temporal trends show a significant increase of 1.35 TCs per decade for the RV-ERA5 and PI-ERA5 versions and 1.43 TCs per decade for AV-ERA5, lower than the observed trend (2.16 TCs per decade). The model do not adequately reproduce the record seasons of 2005 and 2020, which each had 28 TCs. However, these years are among the most prolific in all model versions, particularly in RV-ERA5 (18 TCs). The seasonal distribution of frequencies in the ERA5 forced versions is smaller than observations (Fig.4.5,b). The 5^{th} percentile in the ERA5-forced versions roughly corresponds to the 25^{th} percentile of the observations. The 95^{th} percentile of the AV-ERA5 and PI-ERA5 is slightly higher than the 75^{th} percentile of the observations and the RV-ERA5 version. This indicates that the model tends to struggle with reproducing seasons at the tails of the frequency distributions, particularly those with a low number of TCs. Medians of the distributions are about 13 TCs for RV-ERA5 and 12 TCs for the AV-CESM and PI-CESM versions, similar to the 12 TCs of the observed median of observations. When the model is forced with CESM1-LE, RV-CESM tends to overestimate the number of TCs (median of 16 TCs) compared to observations (median of 12 TCs, Fig.4.5,c) and shows lower variance. Its 25^{th} percentile, indeed, reaches the 75^{th} percentile of IBTrACS, while the 95^{th} percentile is almost close to observations. AV-CESM and PI-CESM medians are about 8 TCs, lower than observations. These versions do not present a clear inter-annual variability with the $5^{th}/95^{th}$ percentiles of 8/9.3 and 7.8/9.2 TCs, respectively.

4.3.2 The displacement component

4.3.2.1 Analysis of residuals

In this section, we aim to analyze the residuals (difference between observed and predicted values) of the displacement module, and whether there are systematic patterns. We run two exercises: first we determine whether residuals of dx and dy each correlate with either longitude and latitude, or whether they correlate together. Second, we plot residuals and relative residuals over the basin.

Dx and dy displacements residuals show a slightly significant correlation (at 5% significance level) of 0.016 (Fig.D.1). However, such a small value suggests there is no clear dependence between dx and dy residuals. Moreover, no correlations are found between the displacement residuals and their corresponding latitude and longitude values except for a small significant correlation of -0.04 for dx residuals with longitude. Most values are clustered around the zero line, indicating no significant slopes. However, there are some extreme positive outliers, with deviations close to 2°, observed in the residuals of meridional displacements at higher latitudes (above 40°N) and across longitudes. No systematic spatial pattern is found in the bias between the model and observed residuals of displacements (Fig.4.6). The bias is generally greater at higher latitudes where steering winds are stronger and storm speed is faster. Additionally, the physical distance covered by one degree is shorter compared to the Tropics. Relative errors are generally higher in residuals of the meridional displacement with many values above ±150%, although these differences are present over a region where the bias is small, lower than ±0.1° (and generally smaller than the bias of zonal displacements over the same region).

A similar analysis is conducted for the specific model of initial displacements (see Section SD for more details).

4.3.3 TC activity and landfalls

In this section, we combine all the components, cyclogenesis, displacements and intensity modules to evaluate the model output compared to observations. TC intensity distributions, TC metrics such as LMI and ACE as well as landfall rates are considered.

4.3.3.1 TC intensity distribution

A clear overestimation of tropical storms is observed among all versions compared to observations whereas major storms are generally underestimated with almost no Cat.5 storms produced by the model (Fig.4.7,a). When the post-processing is applied, the model keeps showing an overall overestimation of tropical storms and underestimation of Cat.1 TCs of about 10% and 5% for the RV-CESM and the AV-CESM/PI-CESM versions, respectively, compared to (Fig.4.7,b). A little underestimation is also present in Cat.1 TCs. However, the proportion of the major storms is now adequately reproduced.

4.3.3.2 TC spatial density

A TC kernel density estimation is provided to estimate the TC probability density function in a non-parametric way. A comparison of TC density between observations and the three model versions is presented for all storms, Cat.1+ storms and Cat.3+ (major) storms. The model adequately reproduces (Fig.4.8b,e,h, Fig.D.4b,e,h and Fig.D.5b,e,h) the observed pattern with peaks in TC density over the Main Development Region (MDR), the Caribbean Sea and Gulf Of Mexico, which characterizes the observed density (Fig.4.8a,d,g, Fig. D.4a,d,g and Fig. D.5a,d,g). UQAM-TCW2 tends to underestimate the number of all storms along the Eastern U.S. coasts and over the Yucatan peninsula (Fig.4.8c, Fig.D.4c and Fig.D.5c). As expected, RV-CESM highly overestimates TCs compared to observations in the southern Caribbean Sea (see Sec. 4.3.1 for the problem relative to the relative vorticity in RV versions). The AV-CESM and PI-CESM versions show lower density values compared to observations in the central part of the MDR. When only Cat.1+ storms are considered, the underestimation along the eastern U.S. coasts nearly disappears (Fig .4.8f, Fig. D.4f and Fig. D.5f). This indicates that the model does not properly reproduce tropical storms in that area. Conversely, the underestimation across the entire Caribbean Sea is more pronounced when considering only Cat.1+ storms compared to all storms (Fig.4.8, Fig.D.4 and Fig.D.5, middle). A dipole pattern is now observed over the central-western MDR, with fewer TCs across the central MDR and a higher number of TCs off the northern coasts of South America compared to observations. For major storms (Fig.4.8i, Fig. D.4i and Fig. D.5i), all versions exhibit a more significant underestimation over the Caribbean Sea compared to observations, which extends into the MDR, reaching the negative pole of the previously mentioned dipole pattern. This dipole pattern is more pronounced compared to the maps for Cat.1+ storms.

4.3.3.3 TC metrics

UQAM-TCW2 tends to slightly underestimate LMI, although they accurately reproduce the variance in the distribution (Fig.4.9, left). When the post-processing is applied, the model adequately reproduces the observed LMI medians (Fig.4.9, right). In particular, observed LMI exhibits a median of 33.4 ms^{-1} with 5th and 95th percentiles of 18 and 66.9 ms^{-1}, respectively. CESM-forced versions show similar distributions with medians of 33 ms^{-1} and 5th and 95th percentiles of about 20 and 68 ms^{-1}, respectively.

ACE is an integrated measure including TC frequency, duration, and intensity. Considering the big amount of synthetic TCs compared to observations, we normalize the seasonal ACE by dividing it by the number of storms. Observed seasonal normalized ACE shows greater variability and generally higher values compared to the model ACE. The observed median is 8.2 with 5^{th} and 95^{th} percentiles equal to 3.4 and 14.4, respectively (Fig.4.10). All versions present a median of 5 with the 5th and 95th percentiles equal to 4 and between 6 (RV-CESM)- 7 (AV-CESM and PI-CESM), respectively. The extreme values in the right tail of the model distributions are lower than the median of the observed data.

4.3.3.4 Landfall rates

Landfall is defined as any point on land reached by the center of the original storm. To ensure consistency between observed landfalls and those from our synthetic tracks, an adjustment is produced each month by dividing the number of synthetic landfalls by the total number of storms and then multiplying this ratio by the number of storms in that specific month.

Observations show landfall peaks for all storms and Cat.1+ storms over Florida and along the Eastern U.S. and the Gulf of Mexico coasts. Peaks in Cat.3+ storms are more pronounced over the North and South Carolina, southern Florida, and the Yucatan Peninsula (Fig.4.11a,d,h; Fig.D.6a,d,h and Fig.D.7a,d,h) The model tends to underestimate landfalls for all storms and Cat.1+ along the coasts of the eastern U.S. and Mexico and over the Caribbean islands (Fig.4.11c,f; Fig.D.6c,f and Fig.D.7c,f). Cat.3+ landfalls are generally underestimated along the coasts of North and South Carolina and over the Yucatan Peninsula (Fig.4.11i; Fig.D.6i and Fig.D.7i).

4.4 Projected Future Change in TC activity

In the next sections, we assess potential future change relatively to 2020 in TC frequency and density as well as LMI and ACE. The considered periods are then divided in 2021-2060 (future period) relative to 1980-2019 (past period).

4.4.1 Change in frequency and density

Looking at the period 1980-2020, RV-CESM shows a significant upward trend in the seasonal number of TCs of 1.34 TC per decade (Fig.4.12,a) while AV-CESM and PI-CESM exhibit a slightly positive significant trend of 0.2 and 0.13 TCs per decade. For the period 2021-2060, three different trends are observed (Fig.4.12,b). Increasing trend in RV-CESM is still present with a rate of 3.85 TC per decade, nearly three times higher than the trend in the past. The AV-CESM version also exhibits a positive trend (0.27 TCs per decade) consistent with the trend observed over the last 40 years. In contrast, PI-CESM presents a significant small negative trend of -0.24 tropical cyclones per decade, which is the opposite of the trend observed from 1980-2020.

Projected relative changes equals to 76%, 24% and 16% in Cat.4 and 87%, 34% and 31% in Cat.5 for RV-CESM, AV-CESM and PI-CESM, respectively. If we consider relative changes of Cat.4 and Cat.5 together, the increase is 80%, 27% and 21%, for RV-CESM, AV-CESM and PI-CESM, respectively. The relative change in the proportion of tropical storms (Fig.4.13) decreases by approximately 2.5% in RV-CESM (from 59.6% to 57%) and AV-CESM (from 55.9% to 53.3%) and by about 5% in PI-CESM (from 55.6% to 50.8%). Increases of approximately 1% for Cat.4 and 0.8% in Cat.5 are observed in RV-CESM and AV-CESM. In contrast, PI-CESM shows larger increases, with a 2% rise in Cat.4 and 1.6% rise in Cat.5. The other intensity categories of storms do not show notable changes.

When all storms are considered, the model does not show any change in TC density for the future projections compared to the past (Fig.4.14c, Fig. D.8c, Fig. D.9c). A small increase off the coast of the eastern U.S. occurs in Cat.1+ storms (Fig.4.14f, Fig.D.8f, Fig.D.9f). For major storms (Cat.3+), all versions indicate a notable increase off the coasts of the eastern U.S., suggesting a robust and coherent future change across all the models.

4.4.2 Change in TC metrics

Future changes in LMI and ACE are considered in this section. LMI exhibits a general increase in all model versions under climate change. Its medians move from 33 ms^{-1} for all versions to 34 ms^{-1} for RV-CESM and AV-CESM and 35 ms^{-1} for PI-CESM (Fig.4.15). The 5th percentile does not varies overall while the 95th percentile move from 68 ms^{-1} for all versions to 70 ms^{-1} for RV-CESM and AV-CESM and 71 ms^{-1} for PI-CESM.

The normalized ACE significantly increase in all versions (Fig.4.16). The medians shift from 5 to 5.3 in RV-CESM and from 5.3 to 5.6 and 6 in AV-CESM and PI-CESM, respectively. Extreme values in the ACE distributions also shift to the right, with the 5^{th} percentiles increasing from 4.4 to 6.2, 6.4 and 6.6 and the 95^{th} percentiles moving from 6.2, 6.4 and 6.6 to 6.3, 6.6 and 7.3 in RV-CESM, AV-CESM and PI-CESM, respectively. PI-CESM normalised ACE values are generally higher compared to the other two versions, due to higher storm intensity (maximum wind speed in each TC center). The increase in the future that is common in all versions is due to a contribution from both length (number of TC centers) and intensity of the future storms.

4.5 Past and future change in landfall rates and risk

In this section, we aim to investigate changes in landfall rates and overall risk, comparing the past and future to the present day. To achieve this, we analyze three distinct 20-year periods: the past (1981–2000), the reference-period (2011–2030), and the future (2041–2060). The total risk is determined by the combined effects of two factors: exposure (population changes) and hazard (landfall rate changes). Additionally, we quantify the contributions of these factors to better understand their respective roles in altering tropical cyclone (TC) risk.

4.5.1 Change in landfall rates

Change in landfall rates is here calculated as: Reference-period landfall rates / Past landfall rates – 1 (the same method is applied for future vs reference-period landfall rates).

When considering the reference-period change, RV-CESM shows an increase in landfall rates ranging from +20% to +80% across the eastern U.S., Mexico, Caribbean Islands and the northern side of South America for all types of storms (Fig.D.10a-b). The increase in major storms shows higher peaks compared to all storms

and Category 1+ cases, with increases exceeding 100% over the eastern U.S (Fig.D.10c). The relative change in hazard for the AV-CESM and PI-CESM versions is consistently positive and affects the same areas as RV-CESM, but it is generally smaller, with values between 0 and 40% (Fig.4.17a-b and Fig.D.11d-e). Some areas show a slight decrease between 0 and 20% in PI-CESM over the eastern U.S. region for all storms (Fig.4.17a). Peaks of relative change between +60% and +80% and between +80% and +100% are observed for major storms in AV-CESM and PI-CESM, respectively (Fig.4.17c and Fig.D.11c).

The future relative change indicates a smaller increase for RV-CESM compared to the reference-period change case for all storms and Cat.1+, with values ranging from 20% to up to 80% over the eastern U.S. (Fig.D.10d-e). Over Mexico, the observed change shows opposite signs with values between -20% (central and southern part) and +20% (northern part). The Caribbean islands are characterized by an increase in landfall rates of roughly 0-20%, while the northern part of southern America exhibits an increase between 20% and 40%. Cat.3+ storms exhibit a similar pattern, but with higher peaks, with some values exceeding 100% over the eastern U.S (Fig.D.10f). The increase over the eastern coasts of North America is only present from South Carolina to Canada in AV-CESM for all storms and Cat.1+, with values between 0 and 40% (Fig.D.11d-e). For major storms, the increase is larger compared to all storms and Cat.1+, peaking between 60% and 80% over Virginia and Pennsylvania (Fig.D.11f). PI-CESM shows an opposite pattern compared to RV-CESM (Fig.4.17d-e). The region between eastern Canada and the Atlantic coast of South America experiences a decrease in landfall rates ranging from 0 to 60% for all storms and Cat.1+, with the exception of the eastern Venezuela. However, a positive relative change between 0 and 40% in Cat.3+ storms is observed across Texas, Florida, North and South Carolina, Pennsylvania and New York State (Fig.4.17f).

4.5.2 Change in Risk

The original population data, with a resolution of 1 km (approximately 30 arc-seconds) is provided by the Socioeconomic Data and Applications Center (SEDAC, `https://doi.org/10.7927/q7z9-9r69`) and is then regridded to a 1° horizontal resolution. The change in exposure is calculated as: Reference-period exposure / Past exposure – 1 (the same method is applied for future vs reference-period exposure).

Then, the change in total risk is calculated as: (1 + % ch. landfall rates) x (1 + % ch. exposure) - 1. Changes in populations for North Atlantic can be found in the Supplementary Materials (Fig.D.12).

In this section, we evaluate the change in total risk for both reference-period and future scenarios, quan-

tifying the contribution of each factor (exposure and landfall rates). For the reference-period, the model indicates a general increase in total risk compared to the past, regardless of storm intensity. The RV-CESM version shows an increase between 0 and 150% in total risk along the eastern coasts of North America, Mexico, the Caribbean Islands and northern South America with some peaks between 200% and and above 250% (Fig.D.13a-c). These peaks are generally present over Florida, the U.S. coasts in front of the Gulf of Mexico, the Yucatan Peninsula and the south-eastern coasts of Canada. A similar pattern is shown by AV-CESM and PI-CESM although the increase in risk is here smaller compared to the past, generally ranging between 0% and 100% (Fig.4.18a-c and Fig.D.14a-c). For RV-CESM, the contribution from the increase in landfall rates spans between 20% and 80% whereas the exposure increase exhibits a larger variance, spanning between 10% and to up to 100% (Fig.D.10a-c and Fig.D.12, left). This suggests that the increase in landfalls generally accounts for at least one-third to half of the total risk increase (between 0% and 150%), with the remaining portion attributable to changes in exposure. A similar result is observed in the AV-CESM and PI-CESM versions, where the slightly smaller increase in risk (0-100%) compared to RV-CESM is associated with a roughly 0-40% increase in landfall. (Fig.4.17a-c and Fig.D.11a-c)

On the contrary, the future change in risk shows different results across the model versions. RV-CESM presents an increase in risk between 50% and 150% over the eastern coasts of North America (Fig.D.13d-f). Isolated peaks between +200% and +250% are also observed, especially in the southeastern coasts of Canada. A slightly negative decrease ranging between 0 and 50% is found over central and southern Mexico whereas a little increase between 0 and 50% is observed over the northern coasts of South America. In AV-CESM, the increase over the eastern coasts of North America is generally smaller compared to RV-CESM, between 0 and 50% in the southern part and between 50% and 100% in the northern part (Fig.D.14d-f). The change is slightly negative over Mexico (between 0% and 50%) for all types of cyclones, and similarly negative for eastern Texas when considering all storms. In PI-CESM, the slightly negative change for all storms extends from Mexico to Louisiana and part of Mississippi and Alabama (Fig.4.18d-f). An increase ranging from 0% to 50% is observed over the rest part of the eastern U.S. coasts.

The contribution from landfall rates (+20%-+60%) over the eastern U.S coasts for RV-CESM accounts for one-third to one-half of the increase in the total risk (50%-150%, Fig.D.10d-f). The observed decrease over central and southern Mexico is in part due to the decrease in landfall rates and part the result of the combined decrease in population (Fig.D.12, right) and landfalls. The increase in risk over the northern coasts of South America is generally related to the increase in landfall rates, with the increase in population playing

a similar role in some areas. In AV-CESM, the observed increase in risk over the eastern coasts of North America—ranging from 0% to 50% in the southern part and 50% to 100% in the northern part—is primarily due to increased exposure. This is because the landfall rates show a decrease in the southern part of the eastern U.S. coasts (Fig.D.11d-f). A little positive contribution from landfall rates (0-40%) is observed over the northern part of the Atlantic U.S. coasts and the southern part of the Canadian coasts, reaching almost one half of the contribution in some areas. The decrease in total risk over Mexico (between 0% and 50%) - particularly when considering all storms - is primarily due to an overall reduction in landfall rates. However, in some areas, a similar contribution from a decrease in population is also observed. In PI-CESM, the slightly negative change affecting Louisiana and parts of Mississippi and Alabama is driven by a decrease in landfall rates of up to 40% in Mexico and those regions (Fig.4.17d-f).

4.6 Discussion and conclusions

An extension of the UQAM-TCW model is provided here to assess potential future changes in tropical cyclone characteristics, as well as landfall rates and risk, over the North Atlantic under a high concentration scenario (RCP8.5). The model now incorporates logistic and multiple linear regressions in its two primary components: cyclogenesis and displacements. The previous limitations related to the use of ENSO indices and phases hampered the capacity of the model to accurately reproduce future changes in tropical cyclone landfall rates and risk. ENSO phases and indices have been replaced with new variables such as SST, potential intensity, wind shear, low-level vorticity, mid-level humidity, steering winds, and the Coriolis parameter. Three distinct model versions are defined based on various combinations of these predictors in the cyclogenesis component (see. Sec.4.2.2 for details). Consequently, UQAM-TCW2 is more physics-driven, enhancing its ability to robustly evaluate the future evolution of tropical cyclone activity and associated climate risk.

Here, we summarize preliminary results related to the validation of UQAM-TCW2, as well as future changes in tropical cyclone characteristics and risk. Where it is possible, we compare these observed changes with findings from previous studies.

4.6.1 Validation

This study provides a validation of the UQAM-TCW2 model. TC genesis spatial patterns and TC frequency are evaluated considering versions forced by ERA5. The model adequately reproduces the spatial pattern of the observed TC genesis probabilities (Fig.4.4 for the period 1980-2020). The observed inter-annual

variability (correlations higher than 0.7) and trends (slightly underestimation compared to observations) in TCs frequency are adequately reproduced by the model for the North Atlantic (Fig.4.5A).

At the time of writing this manuscript, no tracks have been produced using model versions forced by ERA5. Consequently, the validation of tracks is conducted solely with model versions forced by CESM1-LE. The proportions among different TC categories according to the Saffir-Simpson scale are adequately replicated in the model results (Fig.4.7b) after a post-processing adjustment on TC wind speeds. This is applied because of the original underestimation of major storms (Fig.4.7a). However, a slight worsening of replication of Cat.1 storms is found after this post-processing, which probably suggests further investigations to improve this technique.

Model TC density is generally in good agreement with observations. However, the model underestimates TCs over the Yucatan peninsula (Fig.4.8c, D.4c and D.5c) and, specifically, AV-CESM and PI-CESM also underestimate TCs in the central part of the MDR. Weaker storms are generally underestimated along the eastern U.S. coasts in all versions. In Cat.1+ storms, a dipolar pattern is present over the central-western MDR: lower storm density over the central MDR and higher storm density off the northern coasts of South America (Fig.4.8f, D.4f and D.5f) compared to observations. For Cat.3+ similar results but with larger differences compared to Cat.1+ are observed (Fig.4.8i, D.4i and D.5i).

TC hazard - here represented by landfall rates - is crucial for global risk analysis and management. Our results indicate that all model versions tend to underestimate landfall rates for all storms and Cat.1+ along the coasts of the eastern U.S. and Mexico and over the Caribbean islands (Fig.4.11, Fig.D.6 and Fig.D.7).

This is caused by an underestimation of TC frequency under the model versions forced by CESM. More investigation to follow with the model will be forced with ERA5.

4.6.2 Future Changes

In this section, we summarize the main findings on projected changes in tropical cyclone (TC) activity and associated risks, and we compare these results with insights from previous scientific literature.

The work by Knutson et al. (2020) assessed future projections of tropical cyclones under climate change scenarios, specifically focusing on the impacts of a 2°C global warming. CMIP5 models, including CESM1-LE

(see Holland et al. (2024)), project a global mean surface temperature warming of 2°C relative to 1986–2005 baseline by approximately the year 2055 under the RCP8.5 scenario, which aligns with the latter part of our future period. In Section 4.1, we also introduced the results of recent studies from synthetic models to assess future changes in TC metrics and risk. Bloemendaal et al. (2022) analyze periods from 1979–2014 and 2015–2050, which are quite similar to the original periods considered in our study. We also select alternative historical (1981-2005) and future (2006-2060) periods to roughly compare our results with those in Knutson et al. (2020) and Lee et al. (2020). Consequently, the comparisons between our results with those present in these studies may show slight differences from the results presented in Section 4.4.

Our model shows varying future relative changes in the TC number for the North Atlantic basin depending on the version. While the RV-CESM and AV-CESM versions suggest a future increase in TCs of approximately 59% and 13%, respectively, PI-CESM sees a decrease of about 3%. The percentage change in RV-CESM represents an outlier compared to the models considered in Knutson et al. (2020). AV-CESM is between 75^{th} and 95^{th} percentiles and PI-CESM is closer to their median. When relative humidity was considered instead of the saturation deficit, Lee et al. (2020) found upward trends of 1.2 TCs per decade. This corresponds to an increase of 12% in the North Atlantic by the end of the century. These results almost align with the AV-CESM future change although they refer to the end of the century. On the contrary, no significant trend in any scenario is found in Fosu et al. (2024), who downscaled 12 models of the CMIP6 employing CHAZ. In Bloemendaal et al. (2022), the signs of changes in the number of tropical cyclones vary among the four models used to drive STORM. However, in the North Atlantic, three of the four models suggest a decrease in TCs ranging between 9% and 31%. Increasing TC frequencies are also reported by Emanuel et al. (2008) for the North Atlantic in the majority of MIT runs forced with seven GCMs. However, since they consider changes between the periods 1981-2000 and 2181-2200, the comparison is only indicative.

This diverging trend in the future TC seasonal number in our model versions can be explained by looking at the models statistics and the trend maps of the model predictors (Fig.D.15). In RV-CESM cyclogenesis module, three of the four predictors - SST, wind shear and relative vorticity - show coefficients, which are statistically significant. The trend map shows a future increase in SST over the whole basin and in relative vorticity over the southern Carribean, an area where a positive bias of ERA5 driven RV version is found (see Sec. 4.3.1). The coefficient for the SST predictor is more than double the coefficient in the AV model, that means much more weight for SST in the RV version. These properties of the RV version seem to favour an increase in TCs over the North-Atlantic despite the upward trend in wind shear over the Carribean sea,

which should inhibits the TC formation.

In AV-CESM, the absolute vorticity is statistically significant in the model as well as the other three predictors. This predictor shows a negative trend across the northern Carribean. SST coefficient is smaller than in the RV-CESM, giving less importance to this predictor compared to the others. Furthermore this model version is not impacted by the positive bias over the southern Carribean due to the relative vorticity. This explains a smaller upward trend in TC frequency in this version of UQAM-TCW2. Finally, in PI-CESM, SST is replaced by PI, which is also significant in the cyclogenesis module. PI does not show any notable trend over the MDR, except for the northern part of the Gulf of Mexico. This difference in the PI trend compared to the SST trend helps to explain why PI-CESM exhibits a TC negative future trend.

Future relative changes in North Atlantic Cat.4-5 storms are higher than the median of the observed changes in Knutson et al. (2020). RV-CESM changes (+92%) are close to the 95^{th} percentile of the relative changes in Knutson et al. (2020), whereas AV-CESM and PI-CESM changes (+40% and +38%) are between the median of the Knutson et al. (2020)'s models and their 75^{th} percentile. Relative changes for Cat.4-5 storms frequency are also considered in Bloemendaal et al. (2022). AV-CESM and PI-CESM changes (+27% and +21%) are included in their range of changes, which is within 0% and +35% for the North Atlantic. RV-CESM change (+80%) is considerably higher than Bloemendaal et al. (2022)'s range of changes. The higher future relative changes in Cat.4-5 storms in RV-CESM compared to AV-CESM are due to the higher future trend in TCs. However, the increase in Cat.4-5 of 21% for PI-CESM is opposite to the decrease in all storms of 3%, suggesting a clear increase in the proportion of intense storms. The influence of future trends is mitigated when examining the proportion of Cat.4-5 tropical cyclones. The relative positive change in proportions of most intense storms is equal to approximately 1%. As expected, the only exception is in PI-CESM over North Atlantic, where the relative change corresponds to an increase of 2% and 1.6% in Cat.4 and Cat.5, respectively. These values are lower than projected changes in median (about +13%) in Knutson et al. (2020), but they fall within the range of the models' relative changes (between 0 and +30%). Then, the future increase in the proportions of most intense storms appears to be a robust result. Furthermore, a common result across all versions is the increase in TC density off the eastern coasts of the U.S. for major storms (Fig.4.14, Fig.D.8, Fig.D.9).

An increase in LMI is also present. The LMI relative change in the North Atlantic equals +4% in RV-CESM and AV-CESM and +6% in PI-CESM, which is consistent with Knutson et al. (2020) where the relative change

in median in North Atlantic is about +3% and the interquartile extremes are approximately +2% and +5%. PI-CESM value falls between the 75th and the 95th percentiles.

The projected increase in ACE over the North Atlantic aligns with Roberts et al. (2020)' findings for low-resolution models; however Roberts et al. (2020)'s study analyzed the changes between the reference period 1950-1980 and the future between 2020-2050. It is worth noting that in their study, the increase in ACE results from both an increase in tropical cyclone frequency and intensity. In contrast, our observed increase in ACE is primarily driven by the rise in intensity, as the index has been normalized by the number of storms.

The three model versions show contradictory results regarding future changes in landfall rates and risk, reflecting the trends observed in Fig.4.12 and Fig.D.28. An increase in landfall rates is present over the eastern U.S coasts, the Caribbean islands and the northern part of South America in RV-CESM for the period 2041-2060 relative to 2011-2030 (Fig.D.10). This increase is limited to the area between South Carolina and Canada and generally lower in AV-CESM, whereas a decrease is found along the other coasts of the Gulf of Mexico and the northern part of South America (Fig.D.11). In contrast to RV-CESM, PI-CESM shows a general reduction in landfall rates (Fig.4.17) although some areas between Texas and New York State exhibit some positive changes in landfall.

These changes in landfall rates partially contribute to the overall change in total risk. In the North Atlantic, an increase in risk is observed over the eastern coasts of North America (between 50% and 150%) and the northern coasts of South America (between 0 and 50%) and a decrease is found over central and southern Mexico ((between 0 and 50%) in RV-CESM (Fig.D.13). In the AV-CESM version, the increase is generally smaller compared to RV-CESM along the eastern U.S. and Canada (Fig.D.14). A decrease is present over Mexico (between 0% and 50%) and eastern Texas when all storms are considered. A negative change in risk is observed from Mexico to Louisiana and part of Mississippi and Alabama in PI-CESM (Fig.4.18), whereas positive changes are found over the eastern U.S. coasts (between 0% and 50%). The contribution from landfall rates for RV-CESM is between +33% and +50% of the increase in the total risk while the observed decrease over the central and southern Mexico is due to the combined effect of exposure and landfall rates. Exposure is generally the main driver for the increase in risk over the eastern coasts of North America in AV-CESM. A significant contribution from landfall rates is observed primarily over the northern part of the eastern U.S. coasts and the southern part of the Canadian coasts. In contrast, landfall rates are the dominant

factor driving the decrease in total risk over Mexico in AV-CESM, and over Mexico, Louisiana, and parts of Mississippi and Alabama in PI-CESM.

We will determine the best version of the model once the entire process is complete, including trajectory validation with ERA-5.

4.6.3 Future Work

In this final section, we outline key areas that need to be addressed before this draft can be submitted to a peer review scientific journal. We also present potential future work to further investigate changes in landfall rates and risk post-submission. Given the volume of results and the expanded coverage across additional basins, we plan to dedicate a first manuscript on methods and validation of the UQAM-TCW2 model, while a second manuscript will focus on findings on projected changes in TC activity and associated risks under climate change.

4.6.3.1 Before submission.

Here, we list some points to address before manuscript submission, as well as potential areas for future work:

1. Expansion to All Basins:

   Currently, the study focuses on the North Atlantic, while some preliminary results are also provided in the Supplementary Materials for the North-West Pacific basin. The final manuscript will include an analysis of all oceanic basins.

2. Validation with ERA5:

   The validation for trajectory and intensity components with model versions forced by ERA5 is currently missing. Including this validation will help identify potential model biases compared to observations and refine post-processing methods. This step is crucial for producing a complete dataset of tracks and enhancing model accuracy.

3. Additional TC Metrics:

Future analyses could incorporate additional TC metrics, such as translation speed, rapid intensification, and the location of LMI. These metrics can provide deeper insights into future changes in tropical cyclone activity and enhance the overall risk assessment.

4. Integration of radius of maximum wind and wind profiles:

   A connection will be provided between the first three modules of the UQAM-TCW2 model and its final part, which includes the simulation of the radius of maximum wind and wind profiles. Establishing this connection could significantly improve hazard and risk analysis by providing a more comprehensive understanding of storm characteristics.

5. Return Periods:

   Calculation of return periods for hazard and risk assessments will be valuable. This addition will facilitate comparisons with published results from other synthetic models and provide a more detailed understanding of extreme event frequencies for TC risk assessment.

By addressing these points, the manuscript will be better positioned for submission and provide a more robust analysis of future changes in tropical cyclone hazard and risk.

4.6.3.2 Future research.

In UQAM-TCW2, several key predictors for tropical cyclone formation and motion have been selected. For future work, exploring new combinations of predictors or incorporating additional variables could improve model performance and accuracy. For instance, SST could be replaced by relative SST (Vecchi et al., 2008). Studies based on observations, an upper limit to TC intensity, and high-resolution models identify relative SST in the tropical Atlantic as ATC main controller (Swanson, 2008; Vecchi and Soden, 2007a; Knutson et al., 2008). Relative SST is seen explaining tropical convection inter-annual variations better than SST anomalies in observations and climate models (Izumo et al., 2020) and regulates the spatial distribution of mid-tropospheric humidity (Lin et al., 2015). Ramsay and Sobel (2011) also showed that potential intensity is more sensitive to relative SST than absolute SST.

It would also be interesting to investigate whether the diverging future trends (Lee et al., 2020), using saturation deficit instead of relative humidity as a predictor in the cyclogenesis module, are confirmed in our model versions.

Another important limitation of this study is its reliance on a single GCM ensemble (CESM1-LE) and only one concentration pathway (RCP8.5). Future research should incorporate a broader range of climate models, including those at both low and high resolutions, and consider multiple emission scenarios.

These steps will enhance the robustness of the results, providing a more nuanced understanding of future tropical cyclone activity and its associated risks.

4.7 Figures and Tables

Model	Cyclogenesis	Trajectory	Intensity	Dataset (response)	Dataset (predictors)	Coverage
CHAZ (Lee et al. 2018)	Seeding Based on TCGI (Poisson regression)	Beta-Advection model	Autoregressive model -empirical multiple linear regression model (large scale env. cond.) -stochastic component	HURDAT2 JTWC	ERA-Interim (Monthly, except for daily steering winds)	Global
MIT/FAST (Lin et al. 2023)	Weighted random seeding (Emanuel 2006,2022)	Beta-Advection model	FAST	IBTrACS	ERA-5 (Monthly)	Global
MIT (Emanuel et al. 2006)	Random seeding technique	Markov chain (first version only) Beta-Advection model	Dynamical intensity model (CHIPS)	HURDAT	NCEP-NCAR	Global
STORM (Bloemendaal et al. 2020)	Poisson distribution Weighted	Regression formulas Weighted latitudinal bands	Randomly generation pressure change with an autoregressive model Empirical wind-pressure relationship	IBTrACS	ERA-5 (Monthly)	Global (no South Atlantic)
TCW-UQAM v1 (Carozza et al. 2024)	Inhomogeneous spatial Poisson point process	Inhomogeneous 2-D Brownian motion	FAST	IBTrACS	ERA-5 (Monthly)	Global (no South Atlantic)
TCW-UQAM v2	Logistic regression (Combinations of large scale env factors)	Multiple linear regression	FAST	IBTrACS	ERA-5 (Monthly)	North Atlantic and West Pacific
IRIS (Sparks and Toumi 2024)	No cyclo	Poisson count "Parent" tracks perturbed to create stochastic "child" tracks (zero-mean normal distribution with a standard deviation of 0.025 deg/hr) Post LMI	Physically informed algebraic decay Least squares method to estimate the decay coefcient	IBTrACS	ERA-5 (monthly)	Global
RAFT (Xu et al. 2024)	Gaussian kernel-based probability distribution	Beta-Advection model	Deep learning model (Xu et al. 2021)	IBTrACS	ERA-5 (Monthly)	North Atlantic
PepC (Jing and Lin 2020)	Poisson regression	Analog-Wind Track Model (random forest regression)	Markov intensity model (MeHim)	IBTrACS	ERA-Interim	North Atlantic
CATHERINA (Le Guenedal et al. 2022)	Poisson distribution Weighted	Regression formulas Weighted latitudinal bands	Thermodynamic module	IBTrACS	ERA-5 (Monthly)	Global

Figure 4.1: Synthetic TC models. Description of the recent synthetic models for their three main components (cyclogenesis, trajectory and intensity), dataset used for response and predictor variables and their spatial coverage.

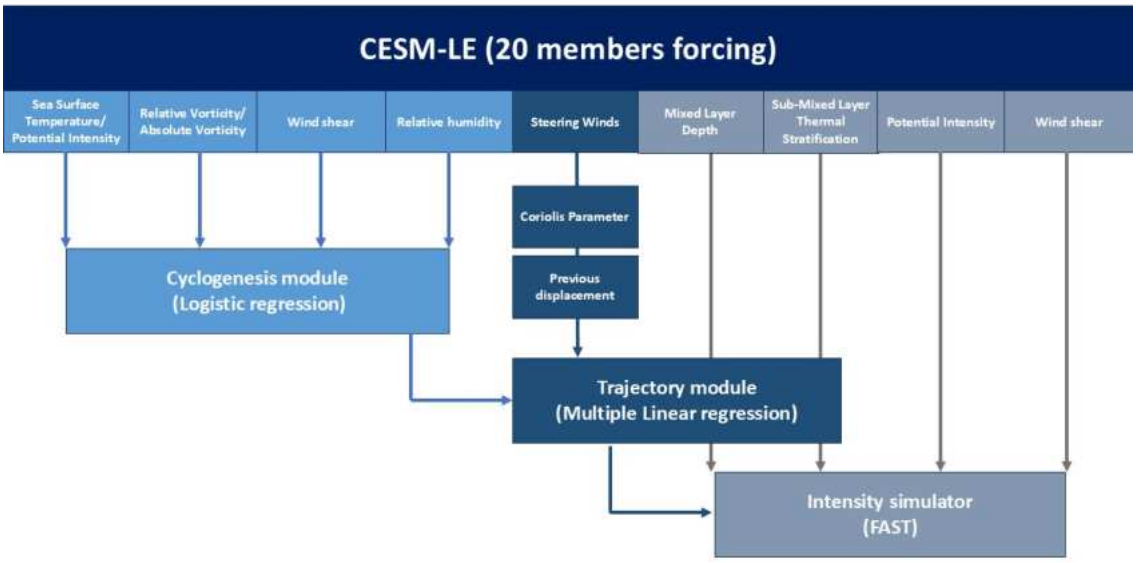

Figure 4.2: Model scheme. Schematic of the first three modules of the UQAM-TCW2 model: cyclogenesis, displacement and intensity.

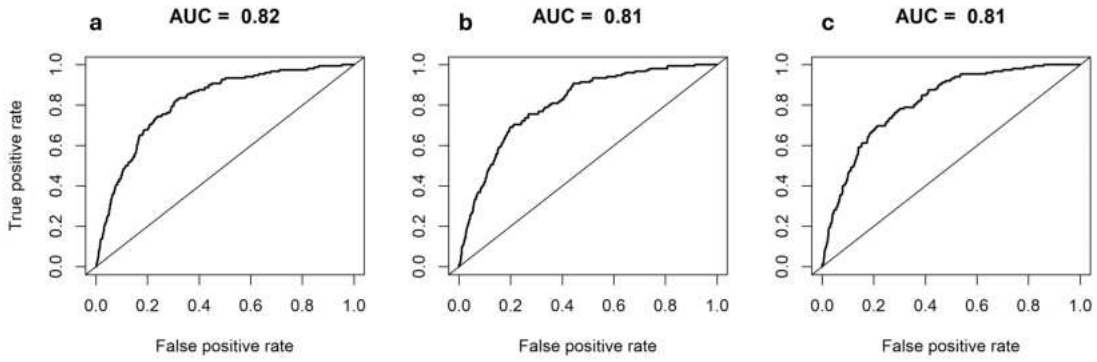

Figure 4.3: ROC curves and AUC values. ROC curves and AUC values for a) RV, b) AV, and c) PI versions for the North Atlantic basin.

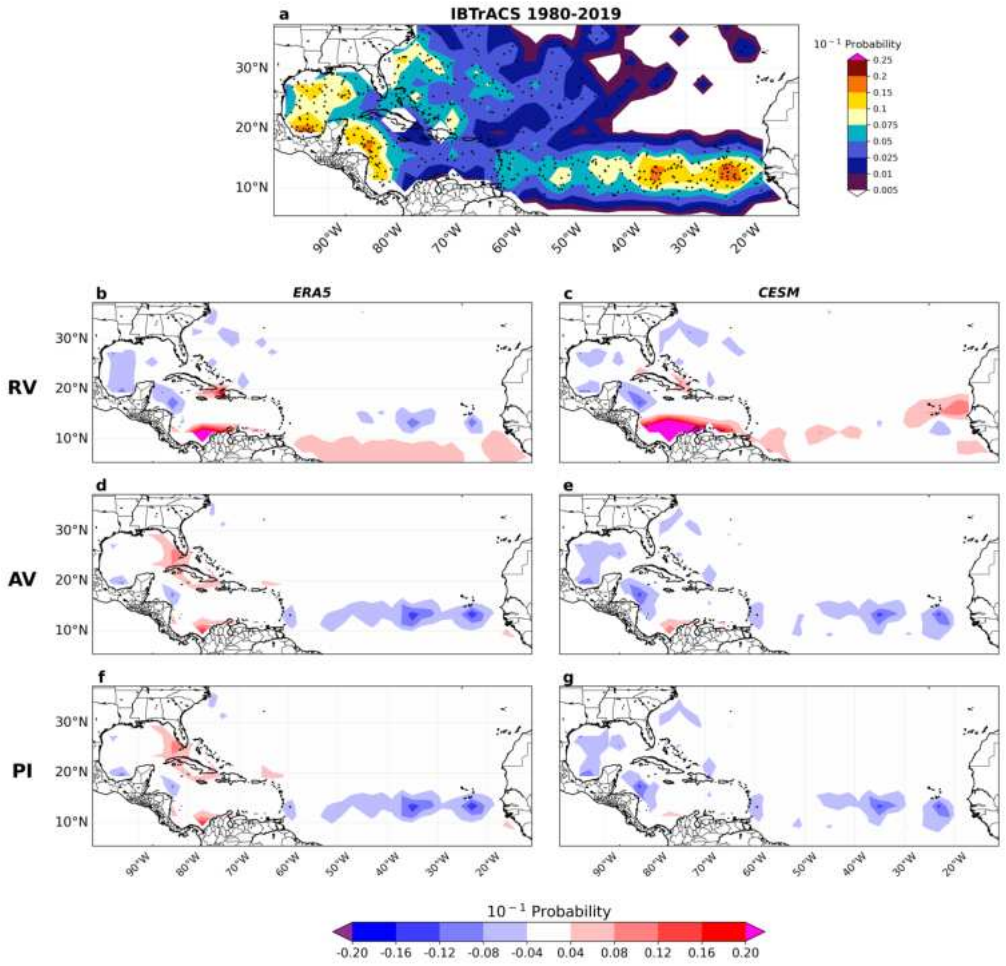

Figure 4.4: Difference in North Atlantic TC genesis probability between observations and model versions. JJASON TC genesis probability for the period 1980-2019 for a) IBTrACS (black dots represent historical cyclogenesis) and difference in TC genesis probability for b-c) the RV-ERA5 and RV-CESM versions, d-e) the AV-ERA5 and AV-CESM versions, f-g) the PI-ERA5 and PI-CESM versions relative to IBTrACS.

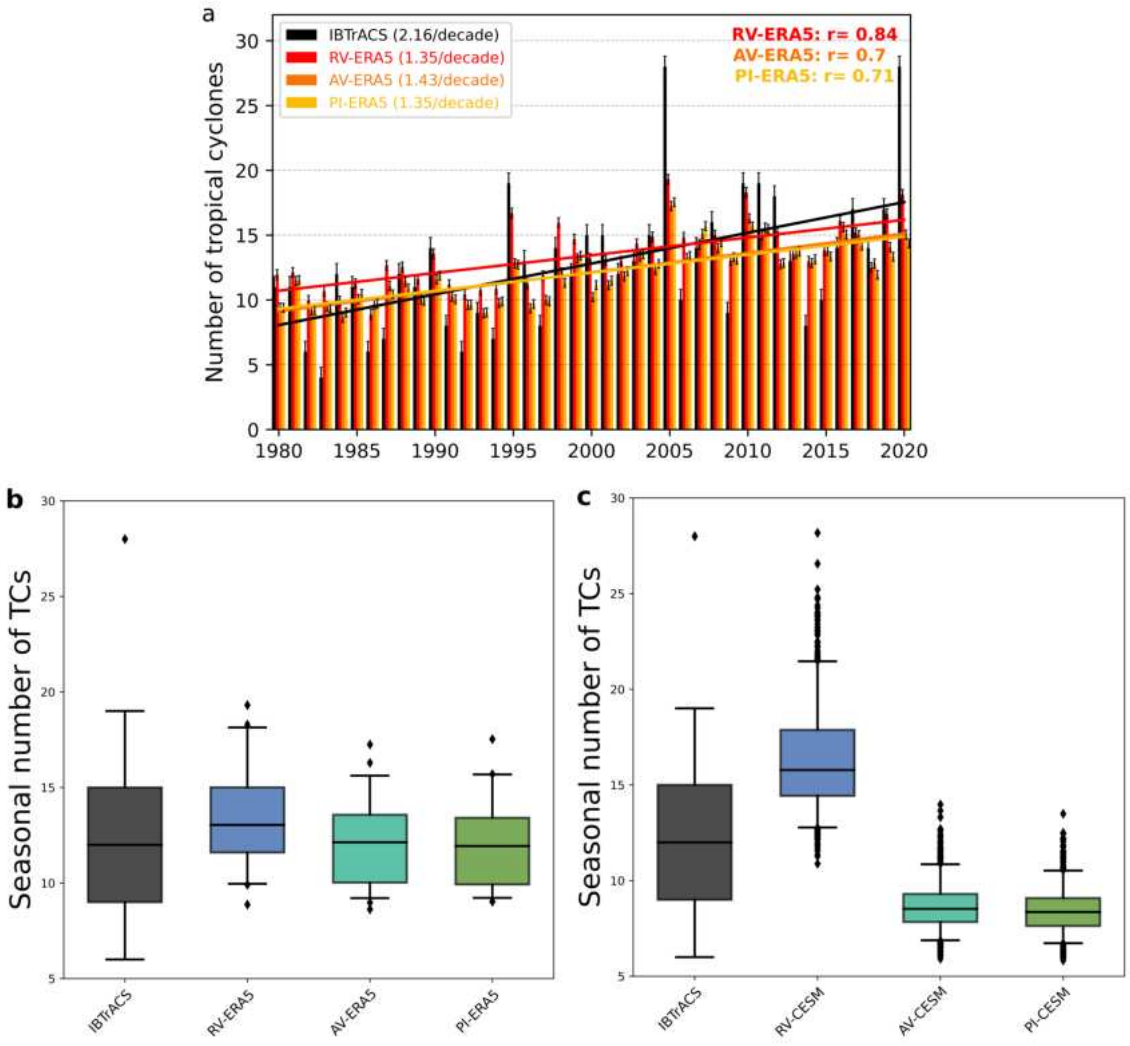

Figure 4.5: Seasonal number of TCs over North Atlantic and their distributions for the period 1990-2019. a) Seasonal (JJASON) number of tropical cyclones across North Atlantic during the period 1980-2019 for observations (black bars), RV-ERA5 version (red bars), AV-ERA5 version (orange bars), PI-ERA5 version (yellow bars). Continuous trend lines indicate significant values at 5% significance level. Trend values are shown in brackets at the top-left. Correlation values are shown at the top-right with values in bold indicating statistical significance. b) Seasonal number of TCs among IBTrACS (black) and the RV-ERA5 (blue), AV-ERA5 (green-blue) and PI-ERA5 (grassy green) versions. Boxplots show the median (black line), the quartiles (the box), the 5-95th percentiles (the whisker) and outliers (dots). c) Same as right but for versions forced by CESM1-LE.

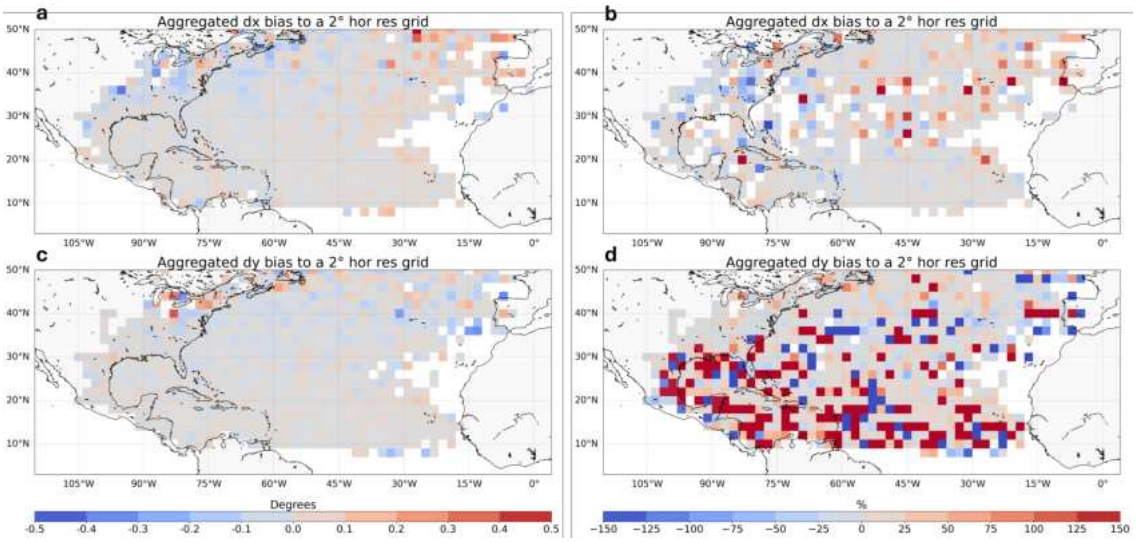

Figure 4.6: Maps of zonal and meridional displacement residuals over North Atlantic. Maps of North Atlantic of zonal (a,b) and meridional (c,d) displacements residuals in degrees (a,c) and percentage (b,d).

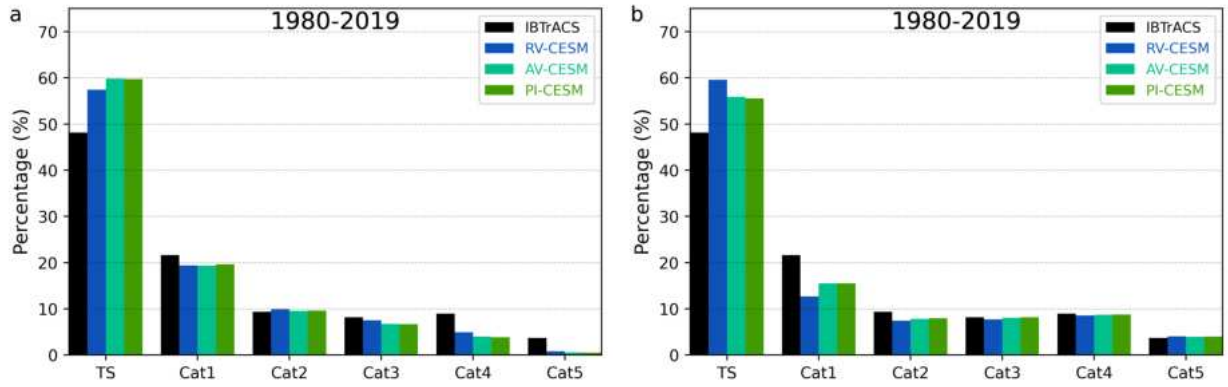

Figure 4.7: Percentage of Tropical Cyclones by category over North Atlantic Comparison for the North Atlantic seasonal (JJASON) percentage of tropical cyclones between observations (black bars), RV-CESM (blue bar), AV-CESM (green-blue bars) and PI-CESM (grassy green bars) versions during the period 1980-2019 a) before and b) after post-processing.

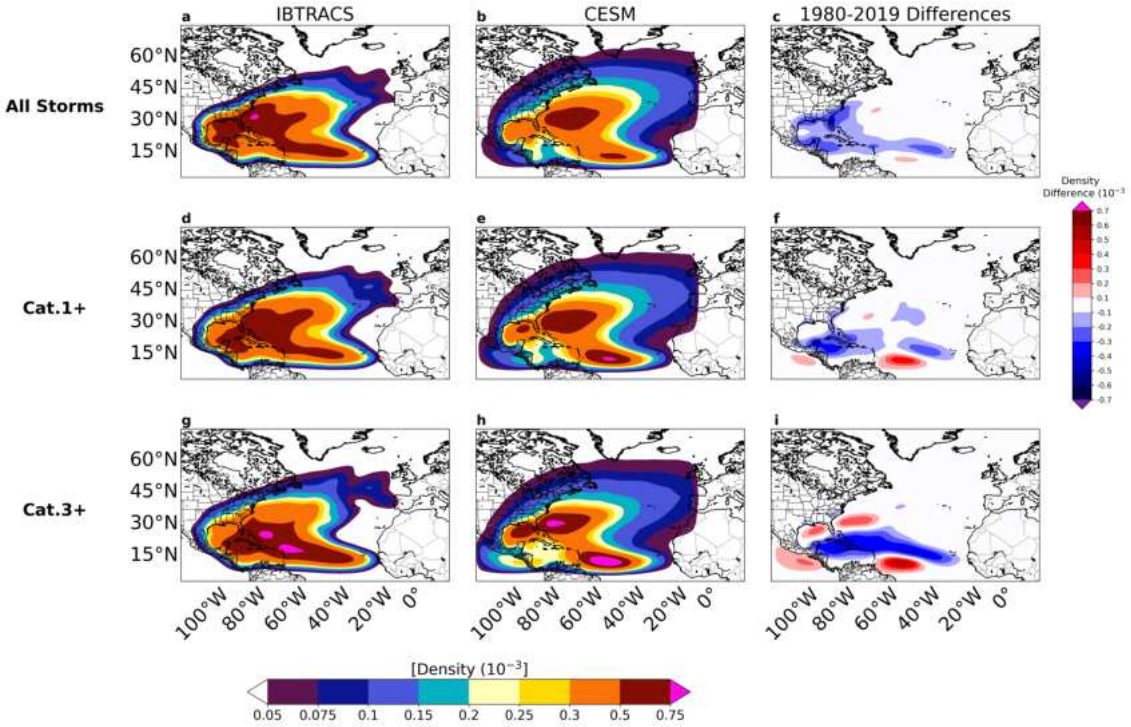

Figure 4.8: Difference in North Atlantic TC density netween observations and PI-CESM. JJASON TC density for the period 1980-2019 for a,d,g) IBTrACS and b,e,h) PI-CESM model and c,f,i) and difference in TC density for the PI-CESM versions relatively to observations. Top row) all storms, Middle row) Cat1+ and Bottom row) major storms.

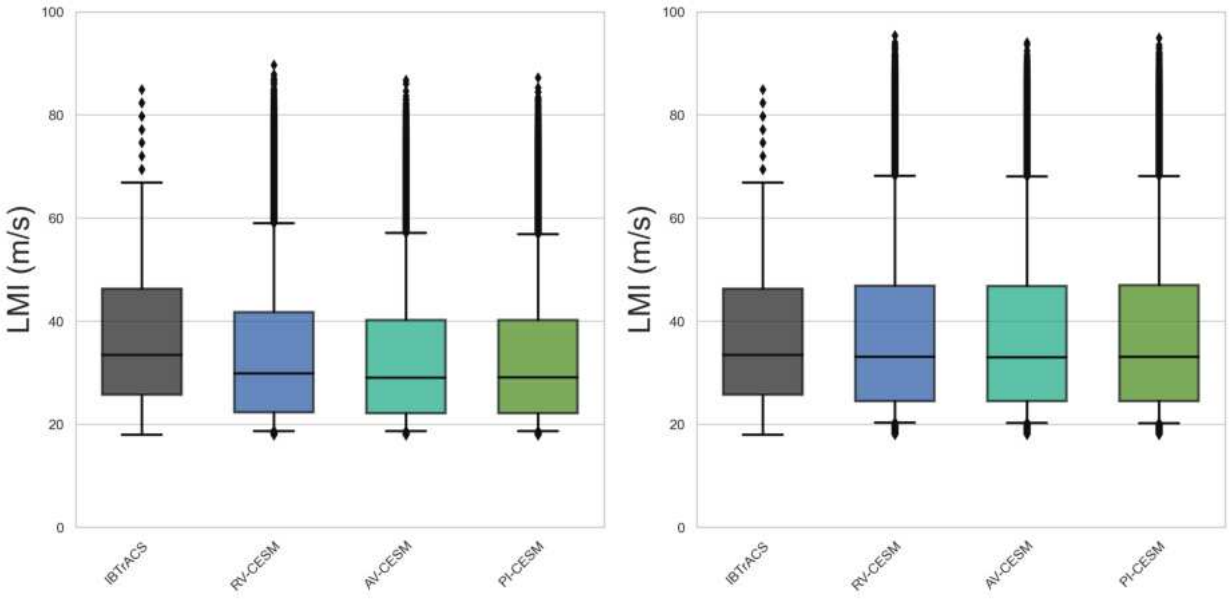

Figure 4.9: LMI boxplots over North Atlantic for the period 1990-2019. Boxplots of North Atlantic LMI for IBTrACS (black) and the RV-CESM (blue), AV-CESM (green-blue) and PI-CESM (grassy green) versions before (left) and after (right) post processing. Boxplots show the median (black line), the quartiles (the box), the 5th-95th percentiles (the whiskers) and outliers (dots).

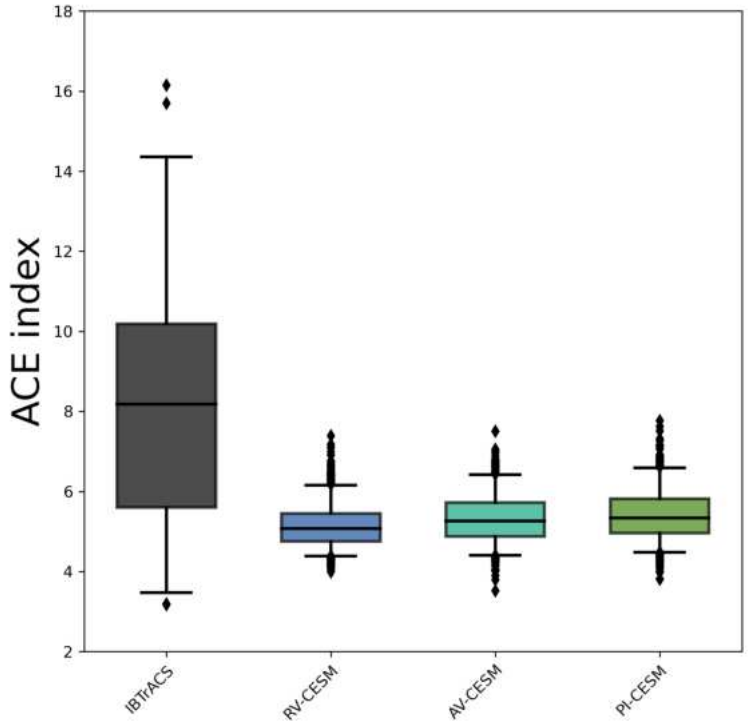

Figure 4.10: normalized ACE boxplots over North Atlantic for the period 1990-2019. Boxplots of normalized ACE for IBTrACS (black) and the RV-CESM (blue), AV-CESM (green-blue) and PI-CESM (grassy green) versions. Boxplots show the median (black line), the quartiles (the box), the 5th-95th percentiles (the whiskers) and outliers (dots).

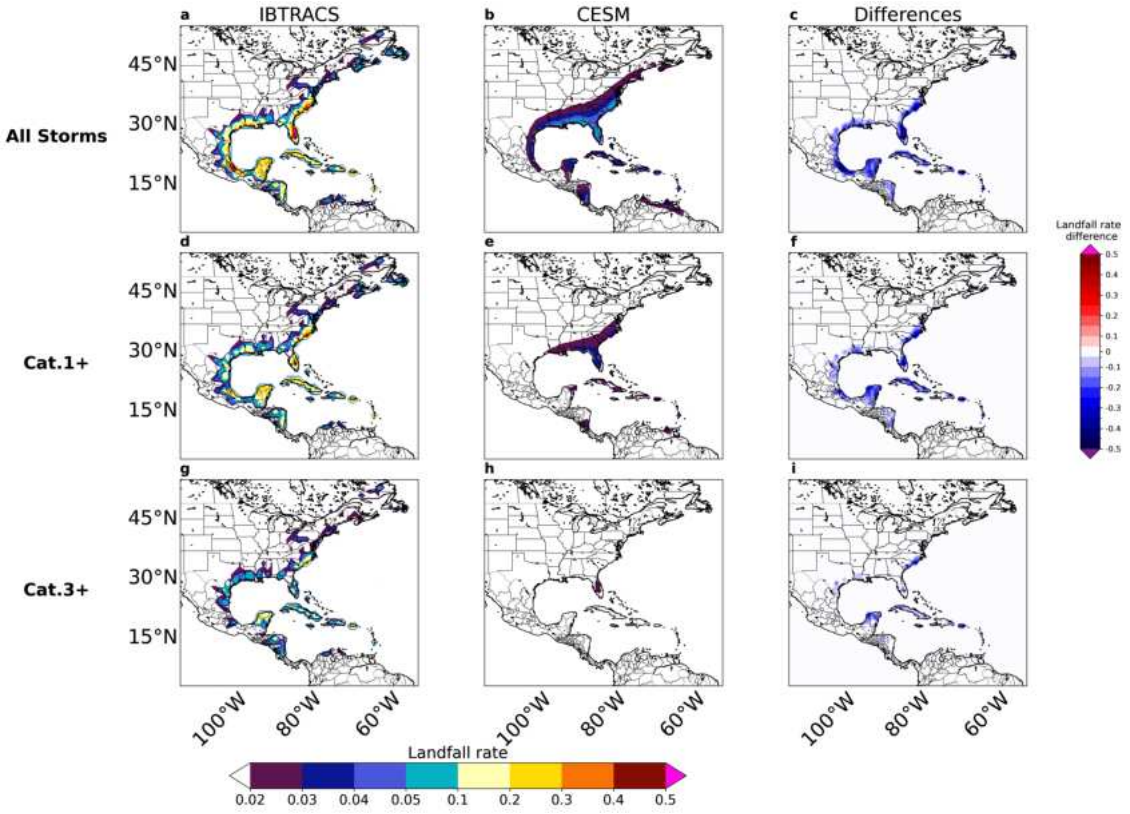

Figure 4.11: Difference in North Atlantic TC landfall rates between observations and PI-CESM. JJASON TC landfall rates for the period 1980-2019 for a,d,g) IBTrACS and b,e,h) PI-CESM and c,f,i) and difference in TC landfall rates for PI-CESM relatively to observations. Top row) all storms, Middle row) Cat.1+ and Bottom row) major storms.

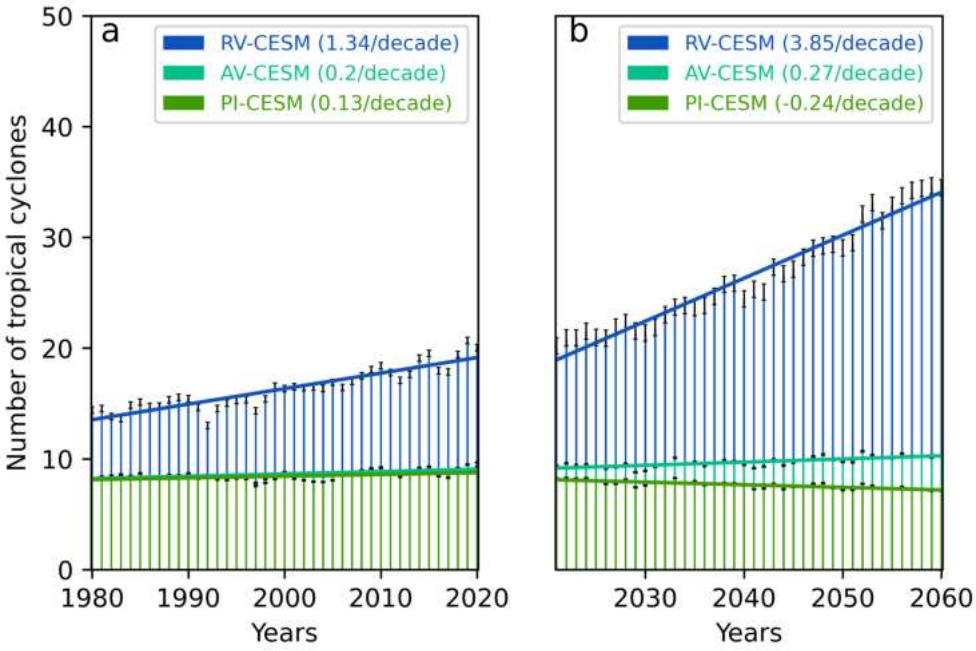

Figure 4.12: Past and future North Atlantic tropical cyclones frequency. Seasonal (JJASON) number of tropical cyclones across North Atlantic during the period a) 1980-2019 and b) 2021-2060 (right) for RV-CESM (blue bar), AV-CESM (green-blue bars) and PI-CESM (grassy green bars). Continuous trend lines indicate significant values at 5% significance level. Trend values are shown in brackets at the top-left.

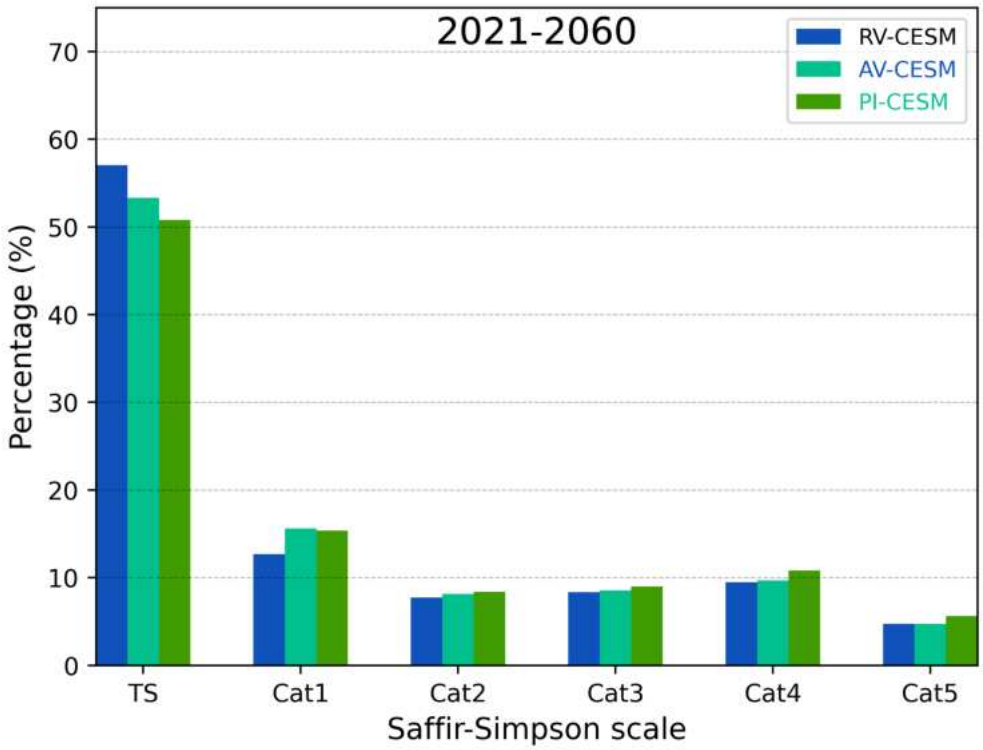

Figure 4.13: Percentage of future North Atlantic tropical cyclones for each category Comparison for the seasonal (JJASON) percentage of North Atlantic tropical cyclones between RV-CESM (blue bar), AV-CESM (green-blue bars) and PI-CESM (grassy green bars) during the period 2021-2060.

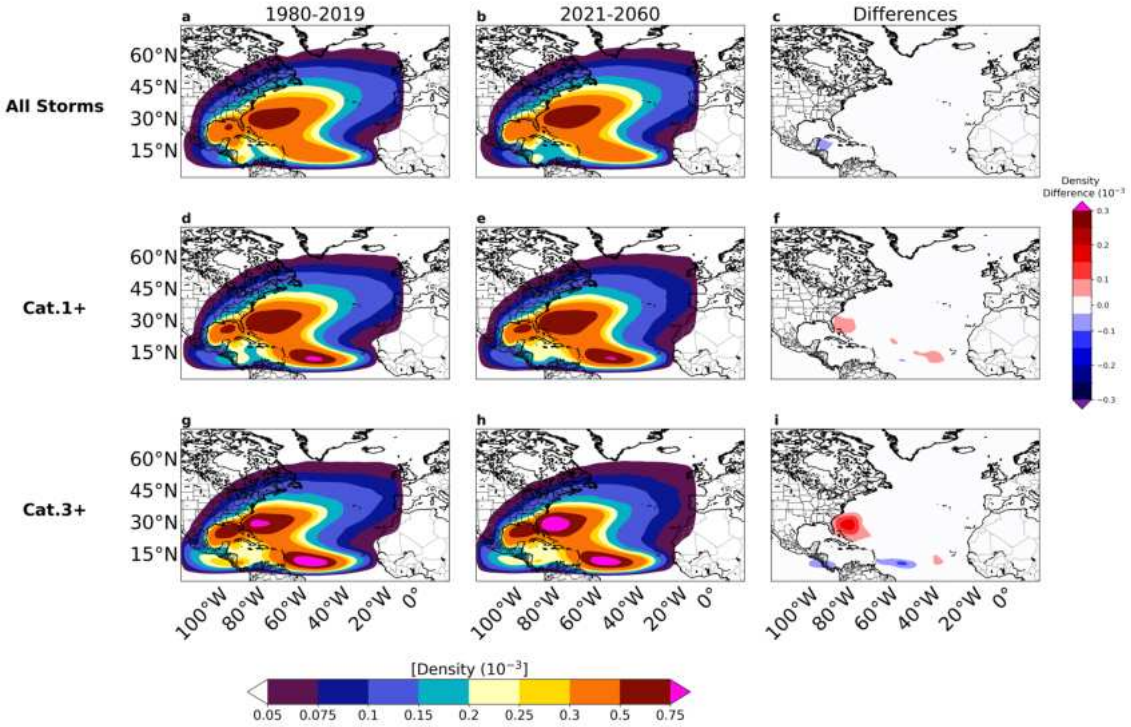

Figure 4.14: Future change in North Atlantic JJASON TC density. TC density for the period a,d,g) 1980-2019 and b,e,h) 2021-2060 and c,f,i) change in TC density for the PI-CESM version relative to observations. Top row) all storms, Middle row) Cat.1+ and Bottom row) major storms.

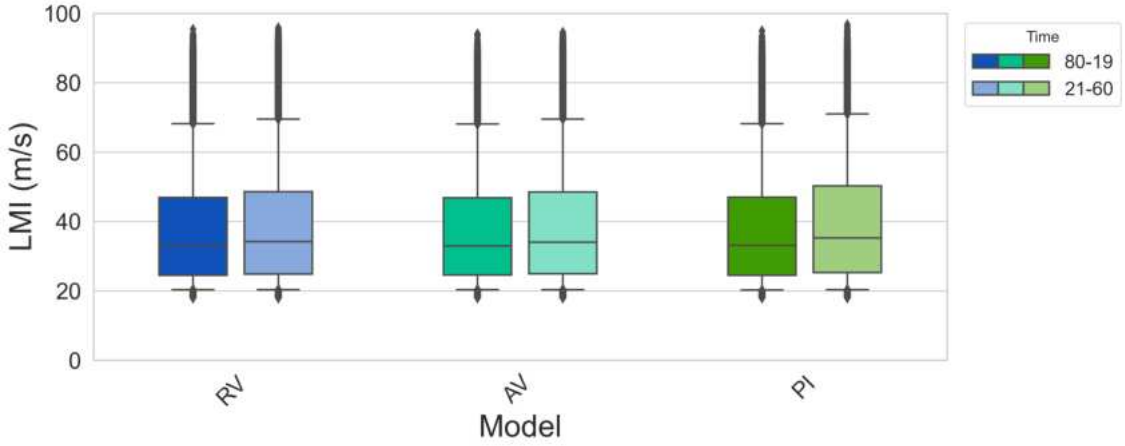

Figure 4.15: Comparison in North Atlantic LMI boxplots over North Atlantic for the periods 1980-2019 vs 2021-2060. Boxplots of LMI for IBTrACS (black) and RV-CESM (blue), AV-CESM (green-blue) and PI-CESM (grassy green) for the period 1980-2019 (left in each version) and 2021-2060 (right in each version). Boxplots show the median (black line), the quartiles (the box), the 5th-95th percentiles (the whiskers) and outliers (dots).

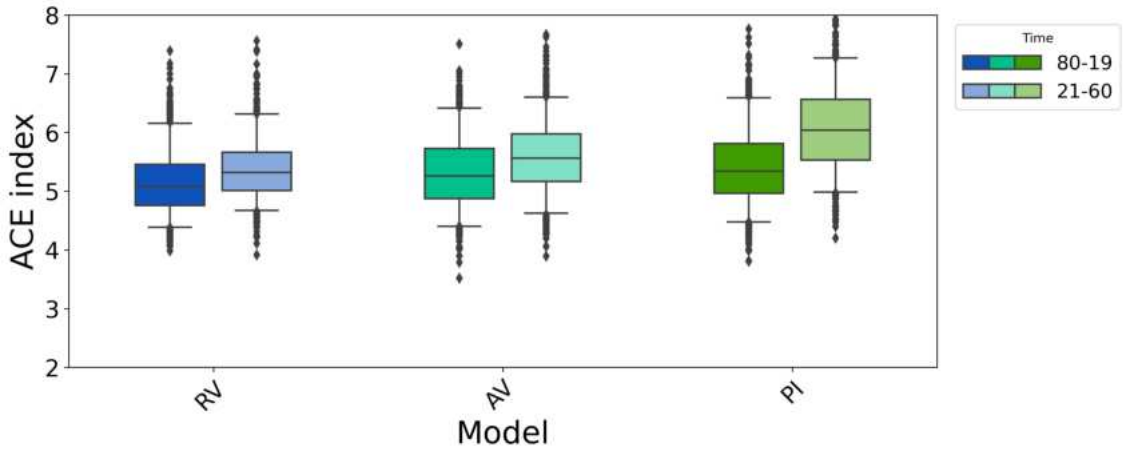

Figure 4.16: Comparison in normalized ACE boxplots over North Atlantic for the periods 1980-2019 vs 2021-2060. Boxplots of North Atlantic normalized ACE for IBTrACS (black) and RV-CESM (blue), AV-CESM (green-blue) and PI-CESM (grassy green) for the period 1980-2019 (left in each version) and 2021-2060 (right in each version). Boxplots show the median (black line), the quartiles (the box), the 5th-95th percentiles (the whiskers) and outliers (dots).

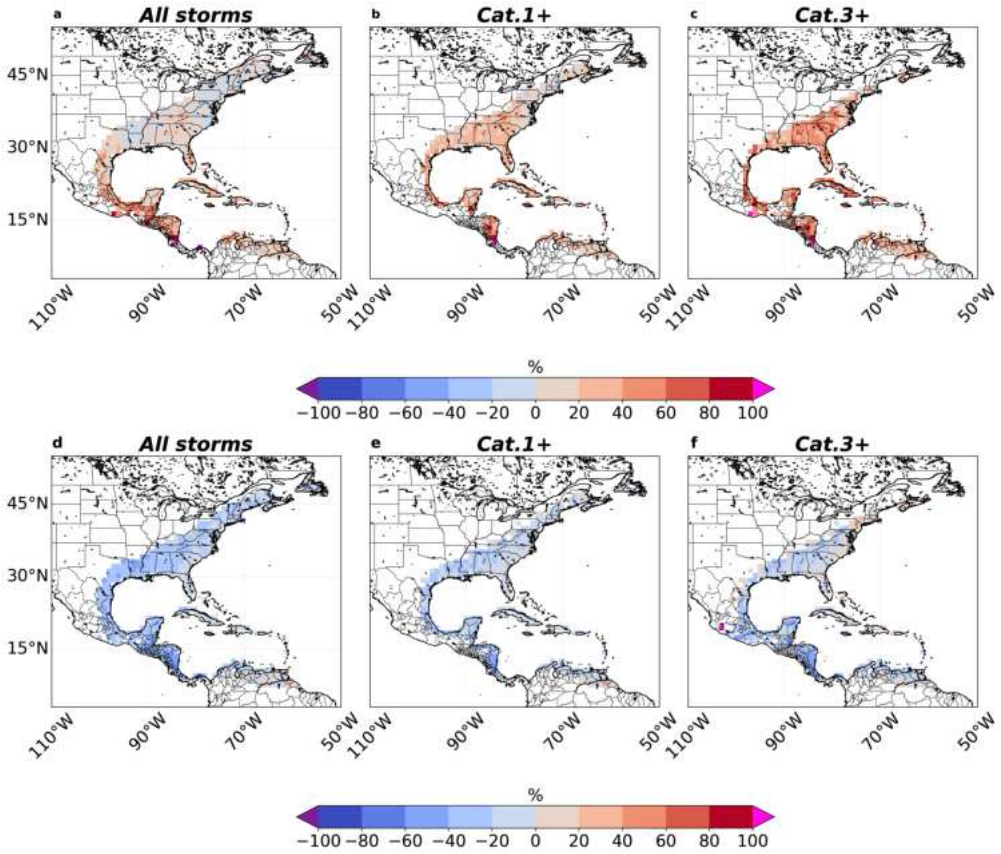

Figure 4.17: Change in North Atlantic landfall rates. a-c) Change (%) in landfall rates over in North Atlantic for the period 2010-2030 relatively to 1980-2000 for a) all storms, b) Cat.1+ and c) major storms in PI-CESM. d-f) Same as a-c but for 2041-2060 relatively to 2011-2030.

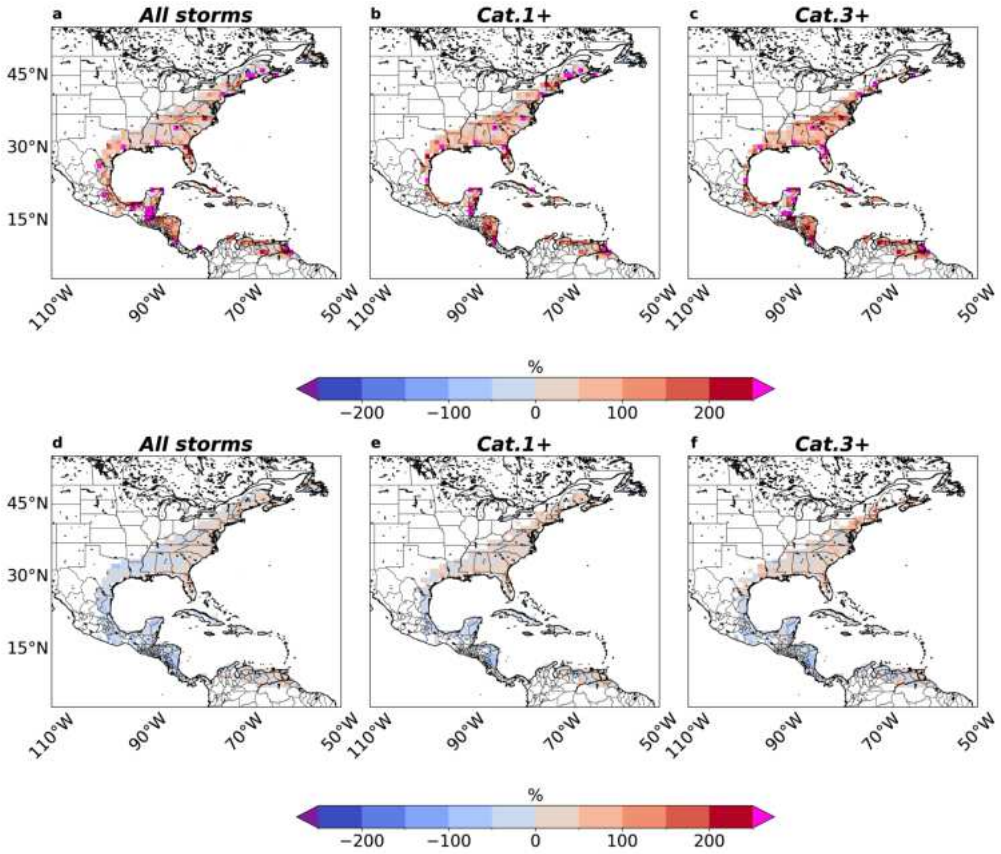

Figure 4.18: Change in North Atlantic total risk. a-c) Change (%) in total risk over North Atlantic for the period 2010-2030 relatively to 1980-2000 for a) all storms, b) Cat.1+ and c) major storms in PI-CESM. d-f) same as a-c but for 2041-2060 relatively to 2011-2030.

CHAPTER 5
CONCLUSIONS

5.1 Key outcomes of the thesis

This thesis investigates the potential climatic impacts of one of the most significant geo-engineering projects: the Great Green Wall. First, changes in both average and extreme climate patterns in northern Africa were assessed using a high-resolution ($\sim$13 km) regional climate model Chapter 2). A series of sensitivity experiments were conducted across four scenarios of increasing vegetation density for the GGW relative to reference simulations for both the Present Day (1990–2019) and Future (2071–2100) periods. All simulations were conducted under two extreme (low and high) greenhouse gas concentrations scenarios, resulting in a total of eleven experiments. In the second phase, a TC tracking system was employed to detect and track TCs in the North Atlantic basin, assessing potential changes in ATC activity based on the outputs of the afore-mentioned experiments (Chapter 3). Lastly, the study includes an implementation of the recent statistical-dynamical global UQAM-TCW model (Chapter 4), focusing on its first two components: the cyclogenesis and displacement modules to analyze the statistical distribution of TC risk in the future. The extension of UQAM-TCW presented in this chapter allows for a detailed investigation of the potential impact of the GGW on TC landfall probabilities along the coasts of Central and North America by generating a large dataset of synthetic TCs for each model version. Consequently, this approach provides a foundation for future financial assessments of GGW-induced TC impacts on coastal communities and private sectors in the region, which could not be possible with a study based on TC tracker algorithms, especially on decadal timescales. The impact of the GGW on the TC activity and risk are, indeed, not considered in this chapter. Given the weak impact of lower-level vegetation GGW, as shown in the results of Chapter 3, we will focus on large-scale environmental factors from higher vegetation density scenarios. Indeed, a significant effect of low vegetation GGW on these fields is unlikely.

5.1.1 Synthesis of the results

The main findings of this PhD work are listed below:

1. The GGW could have significant and contrasting impacts on the climate of northern Africa: while it increases rainfall and reduces drought duration, thereby improving aridity conditions in the region, it

also leads to more extreme heat events, potentially worsening or limiting habitability for local communities;

2. The increased strength of African Easterly Waves leads to a significant increase in ATC genesis over the eastern part of the Main Development Region (MDR) and a decrease over the central-western Atlantic under medium to extreme vegetation density scenarios, compared to cases without the GGW . An increase in ENGPI, driven by decrease in wind shear, favors an increase in TC genesis off the U.S. coasts. However, no significant changes were observed across the entire North Atlantic in various TC metrics, such as TC frequency, intensity, or speed. These findings suggest that the presence of the GGW is unlikely to induce major changes in overall ATC activity;

3. Simulations of three different versions of UQAM-TCW2 under RCP8.5 show contrasting future changes in TC frequency in the North Atlantic, with two models showing an increase and one exhibiting a decrease compared to the past. An increase in the proportion of major storms and in TC intensity is observed in all models. A combination of higher landfall rates and changes in exposure led to a future increase in risk along the eastern coast of North America and in central and southern Mexico.

5.1.2 Main results

5.1.2.1 Contrasting seasonal climatic impacts of the GGW

Our study showed that scenarios with low level vegetation resulted in minimal or negligible impacts, while higher vegetation density scenarios led to significant changes in Sahelian and northern African rainfall patterns, including an enhancement of the West African Monsoon. Specifically, we observed a significant increase in mean summer rainfall, ranging from 25 to 200 mm over the western Sahel and 25 to 100 mm over the eastern Sahel, in experiments with medium to extreme vegetation density. Notably, rainfall peaks of 250 to 500 mm were recorded over the southwestern Sahel in the GGW_{EXT} experiment. An important finding is that the increase in rainfall extends far beyond the GGW region, reaching the whole of northern Africa in the GGW_{EXT} experiment. A notable decrease in drought lengths is observed, with consecutive dry days decreasing by 5% to 25%, depending on the experiment, in line with the increase in vegetation density. Additionally, changes in both the number of rainy days and the occurrence of heavy precipitation were identified. Rainy days increased by 50% to 150% across the entire project area in all scenarios, while an intensification of heavy rainfall events (RX5D and R95p) was observed only in the GGW_{HIGH} and GGW_{EXT} scenarios. Change in rainfall can be explained by a northward expansion of the monsoon flux and much deeper

convection than in the reference experiments without GGW. A waning of the shallow meridional circulation is observed partially attributed to increased surface roughness caused by the presence of vegetation. An increase of the TEJ and a decrease of the AEJ are associated with an increase in the AEWs activity. This dynamic is typically responsible for increased precipitation over the Sahel. Moreover, land-atmosphere interactions, including vegetation and albedo feedback, such as increased evapotranspiration, appear to play a crucial role in triggering changes in WAM dynamics and driving the rise in rainfall across the region.

The change in rainfall extremes is generally larger compared with previous studies (Diba et al., 2016; Saley et al., 2019). A possible explanation for this discrepancy is that these studies may not have fully captured the amplitude of variability in regional rainfall due to their shorter temporal range (8–12 years), compared to our 30-year simulations.

Temperature changes induced by the GGW were also observed over the Sahel, showing opposite responses depending on the time of year. During the enhanced WAM, temperatures decreased by 0.25°C to 2°C in experiments with medium to extreme vegetation density, compared to RCP-only scenarios without vegetation. The highest vegetation density scenarios exhibited cooling across a broader area beyond the project's domain, driven by increased cloud cover and evaporation. In contrast, during other seasons, an albedo-induced temperature increase was noted along the project area. This temperature increase ranges from 0.25°C to 1°C, with peaks exceeding 1°C in central Mali and southern Niger under the most vegetated GGW scenarios during the pre-monsoon period, which is the hottest time of the year in the GGW region. This is reflected in the changes in temperature extremes, with increases observed for both the hottest and coldest days of the year — ranging from 0.3°C to 0.9°C for the hottest day, and over 1.5°C for the coldest day — in the GGW experiments with medium to extreme vegetation density. Additionally, the number of tropical nights increased by 10 to more than 25 nights.

These results strongly differ from those of Bamba et al. (2019), which show a cooling between February and October, peaking during the monsoon season. However, the increase in the hottest days, as also reported in previous studies (Saley et al., 2019), suggests that this change is a robust response associated with the GGW.

On one hand, the GGW enhanced rainfall and moving the Sahel toward less arid conditions. Some cities experienced significant improvements in aridity, with Parakou in Benin transitioning from slightly arid to

moderately humid or fully humid conditions in almost all experiments. Similarly, Bamako in Mali shifted from semi-arid to moderately arid in the GGW_{HIGH} and GGW_{EXT} experiments while Abuja in Nigeria moved from moderately humid to humid conditions in all scenarios. On the other hand, our study revealed a significant impact of the GGW on hot days and heat stress. The number of days with HI exceeding the 75^{th} and 95^{th} percentiles of PD is further increased by 10 to 50–60 days in all GGW experiments, compared to the RCP-only scenarios. The HI distributions in the Sahelian cities generally show a future increase in the mean and variance for the more extreme GGWs under both emission scenarios.

An important question that arises from our study is if the impact of rising temperature associated with global warming and further exacerbated with a worsening of the habitable conditions due to the increase in heat stress could offset the benefits associated with the GGW increase in rainfall and water availability.

5.1.2.2 No significant change induced by the GGW on ATC activity

Our study excludes a significant impact on TC activity over the whole Atlantic basin. Given the potential influence of vegetation changes on WAM and Sahelian rainfall (see Chapter 2), this is promising news for the project and its potential effects on distant regions.

However, our analysis reveals some changes in certain parts of the basin. A significant increase in tropical cyclone genesis density is observed over the eastern MDR, originating off the West African coast, in experiments with medium to extreme vegetation density compared to those without additional vegetation. This increase is accompanied by a decrease in tropical cyclogenesis over the central-western Atlantic, between 25°N and 35°N. This dipole pattern is consistent across all GGW experiments with higher vegetation densities (medium to extreme). An increase in TC genesis is also observed off the eastern U.S. coasts.

We investigated the potential mechanisms behind the dipole between the eastern MDR and the central-western Atlantic by examining large-scale environmental factors, represented by ENGPI developed by Emanuel and Nolan (2004), as well as tropical cyclone seeds, particularly AEWs. A vigorous debate exists within the scientific community regarding the factors that control TC frequency (see Chapter 3 for further details). Our findings suggest that AEW activity primarily drives the dipole formation across the North Atlantic through an increase in AEW intensity. This indicates that stronger waves play a key role in controlling TC genesis across the basin, consistent with the findings of (Caron et al., 2011). Additionally, large-scale factors such as wind shear contribute to the increase in TC genesis off the U.S. coasts.

Our experiments also indicated a significant decrease in the number of TCs projected under the high-emission scenario without GGW, despite an increase in the ENGPI, which would typically suggest more favourable conditions for TC genesis in the basin. ENGPI, like many other genesis indices, often shows an increase in future TC frequency under a warming climate, even as TC counts decrease in model projections (Camargo, 2013; Camargo et al., 2014; Wehner et al., 2015). Additionally, we observed an increase in the proportion of major hurricanes and other TC metrics, such as the LMI and normalized ACE, consistent with other studies (Lee et al., 2020; Roberts et al., 2020; Knutson et al., 2020; Camargo et al., 2023). However, only the LMI in the RCP8.5 scenario shows a statistically significant change. This increase is primarily attributed to rising greenhouse gas emissions rather than the GGW, aligning with previous findings (Knutson et al., 2020). In fact, the GGW has no significant impact on basin-wide TC frequency, intensity, or other metrics such as LMI location and storm translation speed.

5.1.2.3 Change in future hurricane risk over the North Atlantic

Our study presents three distinct versions of UQAM-TCW2, each based on different combinations of predictors used in the cyclogenesis component (see Chapter 4). When driven by CESM1-LE, we refer to these different model versions as RV-CESM, AV-CESM, and PI-CESM, named according to the specific predictor combinations defined in Chapter4).

The three UQAM-TCW2 versions yield contrasting results regarding projected changes in tropical cyclone frequency over the North Atlantic for the future period (2021-2060) compared to the past (1980-2019). Both RV-CESM and AV-CESM project an increase in TC frequency, with RV-CESM standing out as an outlier among the models assessed in Knutson et al. (2020), while AV-CESM appears in the right tail of their distribution. In contrast, PI-CESM projects a slight decrease in TC frequency, aligning closely with the median of the model distribution in Knutson et al. (2020)'s study. Similar findings in terms of relative change in TC number are observed in Lee et al. (2020), which uses a hybrid TC model, but focuses on the end of the century.

The projected future change in the proportion of the most intense storms (Category 4-5) is generally close to 1% across all models and basins, except for PI-CESM, which shows an increase of 2%. These values fall within the range of relative global changes (0% to 30%) reported in Knutson et al. (2020). The future increase in the proportion of the most intense storms is a well-established result in the scientific literature, and our models confirm this trend.

TC maximum wind speed (LMI) is projected to intensify across all models, with increases of 4% in the North Atlantic for RV-CESM and AV-CESM, and 6% in PI-CESM, aligning with the findings of Knutson et al. (2020). The observed positive changes in ACE over the North Atlantic are consistent with the findings of Roberts et al. (2020) for low-resolution models. However, while the increase in ACE in Roberts et al. (2020) is attributed to both higher tropical cyclone frequency and intensity, in our study, it is primarily driven by increased intensity.

RV-CESM and AV-CESM project an increased risk (as a combination of landfall rates and population exposed) along the eastern coasts of North America and the northern coasts of South America, while a decrease is observed over central and southern Mexico. PI-CESM, on the other hand, shows a reduced risk from Mexico to Louisiana and parts of Mississippi and Alabama, with positive changes along the eastern U.S. coasts. The rise in risk is generally driven by a combination of increased landfall rates and changes in population exposure. In contrast, the decline in risk over parts of Mexico is primarily attributed to reduced landfall rates.

Preliminary results for the North-West Pacific are also shown in Sec.D. UQAM-TCW2 predicts a notable increase in TC frequency, with RV-CESM and AV-CESM being outliers, and PI-CESM falling in the extreme right tail of the models' distribution presented by Knutson et al. (2020). Contrary to the North Atlantic, the projected increase in LMI for the North-West Pacific is more modest, around 1%, while a decrease in ACE is observed. This decrease in ACE differs from the results in Roberts et al. (2020), likely due to the projected decrease in TC frequency over the basin, as seen in future projections from low-resolution models. The model indicates a general increase in total risk along the coasts of the North-West Pacific. In AV-CESM, the rise in risk is particularly pronounced, consistent with its projection of a stronger positive trend in the annual number of tropical cyclones. In both RV-CESM and AV-CESM, the increase in landfall rates is the primary driver behind the heightened risk. In PI-CESM, changes in landfall rates are the main factor contributing to increased risk in the northern part of the basin, while, over South Asia, exposure plays a similar role to landfall rates.

5.1.3 Impact of the study, limitations and potential directions for future research

The GGW is an ambitious African initiative aimed at combating future droughts and restoring degraded land across the Sahel. Despite its scale, as one of the most significant geoengineering projects globally, its climatic impacts have not been thoroughly assessed by the scientific community. Understanding these

effects is crucial for policymakers to achieve the GGW's sustainable climate goals and mitigate potential regional and global repercussions. The results of this work will be of great interest to a wide range of scientists and stakeholders, representing a significant step forward in understanding the potential responses of WAM and ATC activity to such a major regreening initiative. Our findings could provide valuable insights into the key role of vegetation feedback in strengthening the monsoon. This feedback could be particularly relevant for the scientific community studying both future climate scenarios and past climates, including those involved in the Paleoclimate Modelling Intercomparison Project (PMIP) and researchers working on the African Humid Periods . Furthermore, the finding that the GGW may not significantly affect North Atlantic TC activity is crucial, as it could have implications for distant regions such as the Caribbean and central-north America, where TCs often make landfall. As a result, this study will provide an important reference for land management, vulnerability assessments, and land use policy as the project develops in the coming years.

Furthermore, the extension of the first version of UQAM-TCW (Carozza et al., 2024) guarantees a more physics-based version of the model, based on the main variables related to TC formation and movement. This provides a more reliable assessment of the statistical distribution of the impacts of climate change on tropical cyclones, with applications to the insurance and reinsurance industry, as well as the energy and engineering sectors, who require proper probability distributions and return periods on extreme events for specific areas. Moreover, the final version of the updated model could be forced by the environmental factors from our GGW simulations in future studies to further investigate the potential financial impacts induced by the GGW, focusing on changes in probabilities of TC landfalls over the central and north American continent.

Some limitations are, however, present in this study. The employment of a single atmospheric RCM implies the use of prescribed SSTs and fixed vegetation, making impossible to evaluate the feedback associated with these variables. A coordinated fully coupled multi-model intercomparison of different GGW scenarios could be beneficial to further investigate the climatic impacts of this initiative. Finally, while our simulations are performed at high horizontal resolution ($\sim$13 km), the convection is still parameterized. Some studies highlighted that models with that parameterized convection could not adequately reproduce the rainfall dynamics over northern Africa (Hohenegger et al., 2009; Taylor et al., 2013). A comparison between our results and those from convection-permitting models could significantly improve the findings about the GGW-induced climate impacts. Furthermore, the GGW may also affect climate far-afield (e.g., on the equa-

torial Pacific) as suggested by recent modeling studies performed under Green Sahara conditions. Then a new study could investigate the impact on ENSO variability due to the change in vegetation over Sahel.

The use of a hybrid model to study past and future changes in tropical cyclone activity and risk enables the creation of a large synthetic TC dataset, making the analysis more robust. However, there are some limitations in our study that need to be addressed before submitting the corresponding manuscript. One key improvement would be the validation of displacement and intensity components using ERA-5 data, which is essential for accurately evaluating the model's performance and investigating potential biases. Additionally, the model remains incomplete as it currently lacks simulations for the radius of maximum wind and wind profiles, which are critical for enhancing hazard and risk assessments, in addition to expanding to the remaining four cyclogenesis basins.

Finally, our model is driven by a large ensemble of a single GCM, which limits confidence in the simulation results. In future research, a multi-model ensemble approach could greatly enhance the robustness of the findings. Each model in the ensemble generates different projections by offering unique solutions to the governing equations, providing a more reliable estimate of climate change impacts than relying on a single model (IPCC, 2001). Furthermore, incorporating different GHG concentration pathways would offer a more comprehensive assessment of potential future changes in TC activity and risk.

APPENDIX A

SUPPLEMENTARY MATERIAL CHAPTER 1

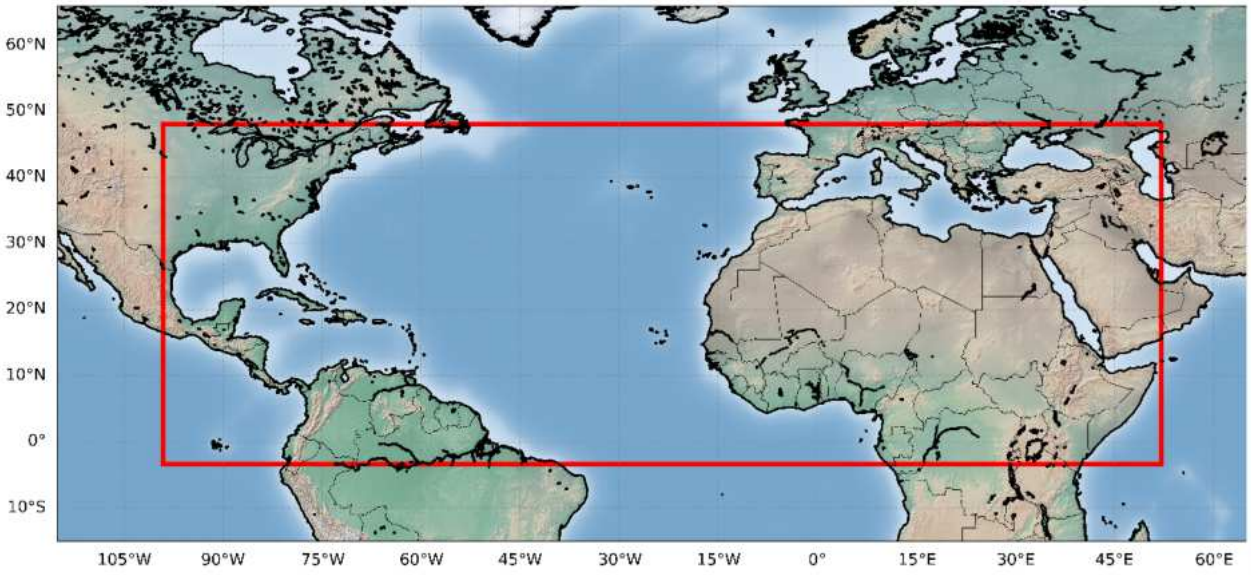

Figure A.1: Model domain. The red rectangle shows the model domain between -3.35°S – 48.1°N and -99°W and 52°E.

APPENDIX B

SUPPLEMENTARY MATERIAL CHAPTER 2

Table B.1: Driving models for CORDEX regional simulations run with the Rossby Centre regional climate model (RCA4) and their respective institutions.

Driving Model	Institution Name
CCCma-CanESM2	Canadian Centre for Climate Modelling and Analysis, Victoria, BC, Canada
IPSL-IPSL-CM5A-MR	Institut Pierre-Simon Laplace
NOAA-GFDL-GFDL-ESM2M	National Oceanic and Atmospheric Administration Geophysical Fluid Dynamics Laboratory
CNRM-CERFACS-CNRM-CM5	Centre National de Recherches Météorologiques, Météo-France
MIROC-MIROC5	The University of Tokyo Center for Climate System Research National Institute for Environmental Studies Japan Agency for Marine-Earth Science and Technology Frontier Research Center for Global Change
NCC-NorESM1-M	Norwegian Climate Center
ICHEC-EC-EARTH	Irish Centre for High-End Computing
CSIRO-QCCCE-CSIRO-Mk3-6-0	Commonwealth Scientific and Industrial Research Organisation
MPI-M-MPI-ESM-LR	Helmholtz-Zentrum Geesthacht, Climate Service Center, Max Planck Institute for Meteorology, Germany

Table B.2: Experimental set-up

ionsetupskip=0pt,justification=raggedright,singlelinecheck=off

Setup	CRCM5/GEM4.8
Simulations	Reference experiments:
	no GGW
	Sensitivity experiments:
	GGW_{LOW}, GGW_{MED}, GGW_{HIGH}, GG
Periods	Present day (1990-2019)
	Future climate (2071-2100)
Horizontal resolution	0.12°
Driving data	Global GEM at 0.55°
Emissions scenario	RCP2.6
	RCP8.5
Vertical levels	57

Table B.3: Climate indices

Label	Index definition	Unit
TXx	Annual maximum value of daily max temperature	°C
TNn	Annual minimum value of daily min temperature	°C
TR20	Annual count when daily min temperature $>$ 20°C	nights
CDD	Maximum number of consecutive days when precipitation $<$ 1 mm	days
RX5	Annual maximum consecutive 5-day precipitation	mm
R95p	Annual total precipitation from days $>$ 95th percentile	mm
R1mm	Annual count when precipitation $\geq$ 1 mm	days

Table B.4: Moisture contributions over the extreme GGW area. All the units are in mm/d. In bracket the 5-95th percentiles.

Scenario	Experiment	Evaporation	Evapotranspiration	Total Moist. Flux Conv.
	PD	**0.36** (0.08/0.77)	**0.45** (0.09/1.07)	**+6.63** (-5/17.40)
RCP2.6	RCP2.6	**0.39** (0.11/0.88)	**0.49** (0.12/1.10)	**+6.87** (-5.38/18.10)
	GGW$_{LOW}$	**0.37** (0.10/0.80	**0.58** (0.12/1.42)	**+7.50** (-5.02/+19.16)
	GGW$_{MED}$	**0.36** (0.10/0.68	**0.68** (0.11/1.73)	**+7.56** (-5.45/+19.92)
	GGW$_{HIGH}$	**0.43** (0.13/0.77)	**0.86** (0.15/1.42)	**+7.63** (-5.18/+20.08)
	GGW$_{EXT}$	**0.56** (0.28/0.92)	**1.29** (0.32/2.28)	**+7.84** (-6.18/+21.72)
RCP8.5	RCP8.5	**0.36** (0.11/0.71)	**0.45** (0.12/0.98)	**+8.95** (-6.57/+23.37)
	GGW$_{LOW}$	**0.36** (0.11/0.70)	**0.55** (0.12/1.30)	**+ 9.67** (-5.73/+24.27)
	GGW$_{MED}$	**0.38** (0.12/0.68)	**0.69** (0.14/1.69)	**+9.72** (-6.34/+25.11)
	GGW$_{HIGH}$	**0.43** (0.14/0.73)	**0.82** (0.16/1.79)	**+9.80** (-5.97/+25.17)
	GGW$_{EXT}$	**0.53** (0.16/0.83)	**1.16** (0.27/2.15)	**+10.05** (-6.90/+26.65)

Table B.5: Mean vegetation roughness length (meters) over the Great Green Wall area

Experiment	Roughness
NO GGW	0.078
GGW$_{LOW}$	0.35
GGW$_{MED}$	0.51
GGW$_{HIGH}$	0.53
GGW$_{EXT}$	0.55

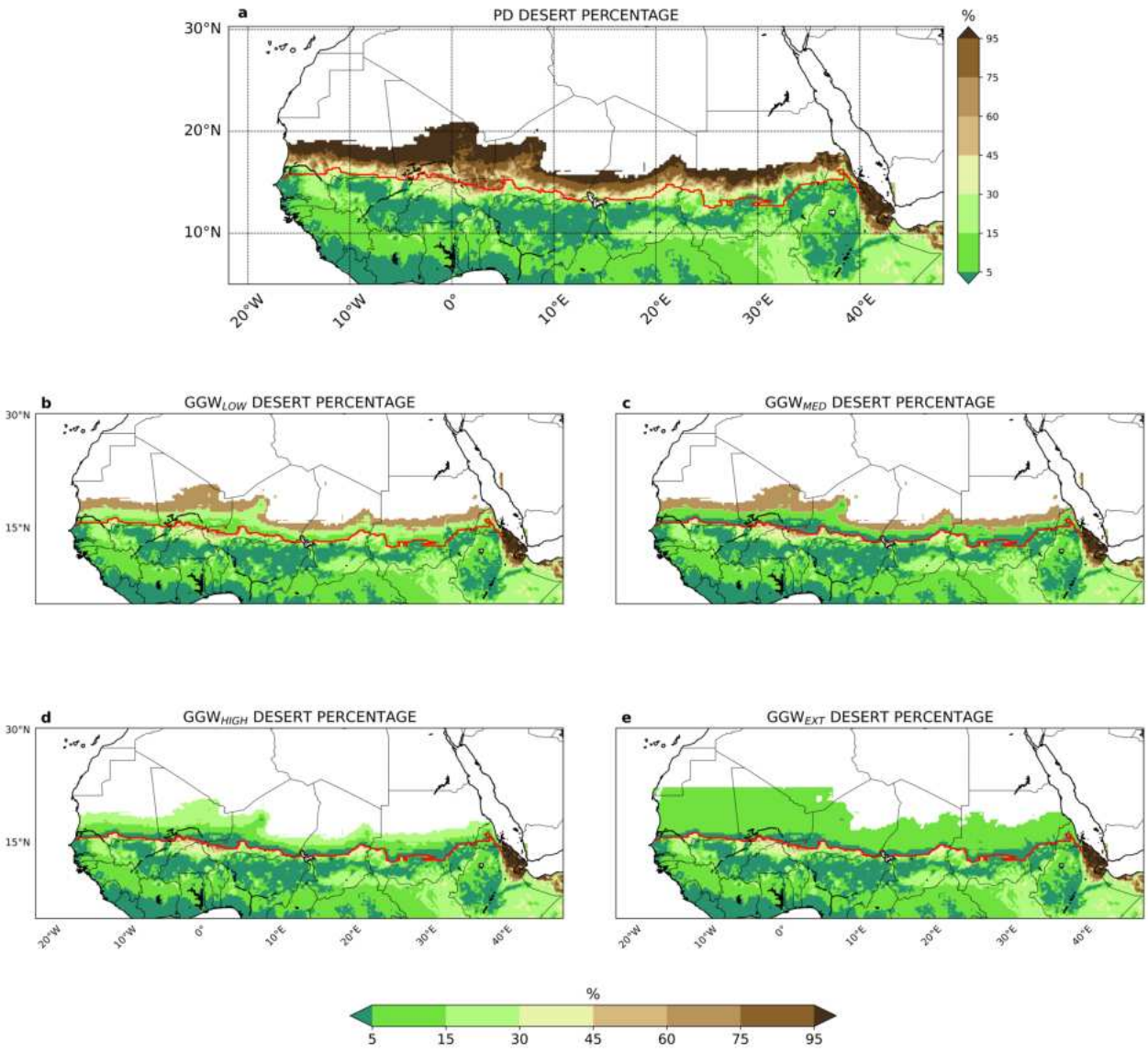

Figure B.1: Change in desert fraction. Original desert and nude soil percentage (a); change in desert and nude soil percentage for GGW_{LOW} (b), GGW_{MED} (c), GGW_{HIGH} (d) and GGW_{EXT} (e) experiments. The red line indicates the southern border of the GGW. The percentage of desert and nude soil over the GGW area in the Present Day (PD) simulation is 72% while it is around 40%, 33%, 16% and 8% in the GGW_{LOW}, GGW_{MED}, GGW_{HIGH} and GGW_{EXT} experiments, respectively. For clarity, all the percentage values above the northern GGW border are not shown.

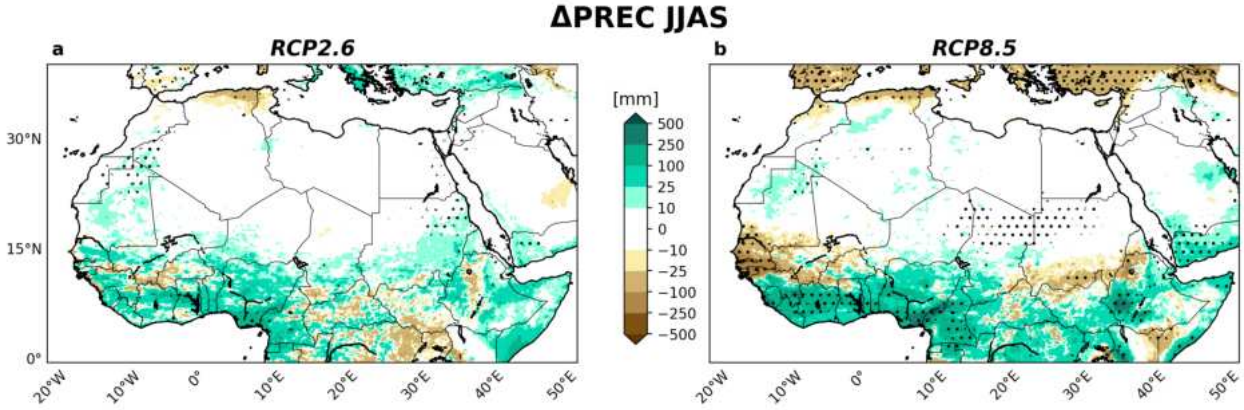

Figure B.2: Summer rainfall changes in northern Africa. Changes in precipitation during the period June-September (JJAS) for a) RCP2.6-only and b) RCP8.5-only experiments relative to the Present Day. Dots indicate values that are significantly different at the 5% significance level, using a local (grid-point) Wilcoxon signed-rank test.

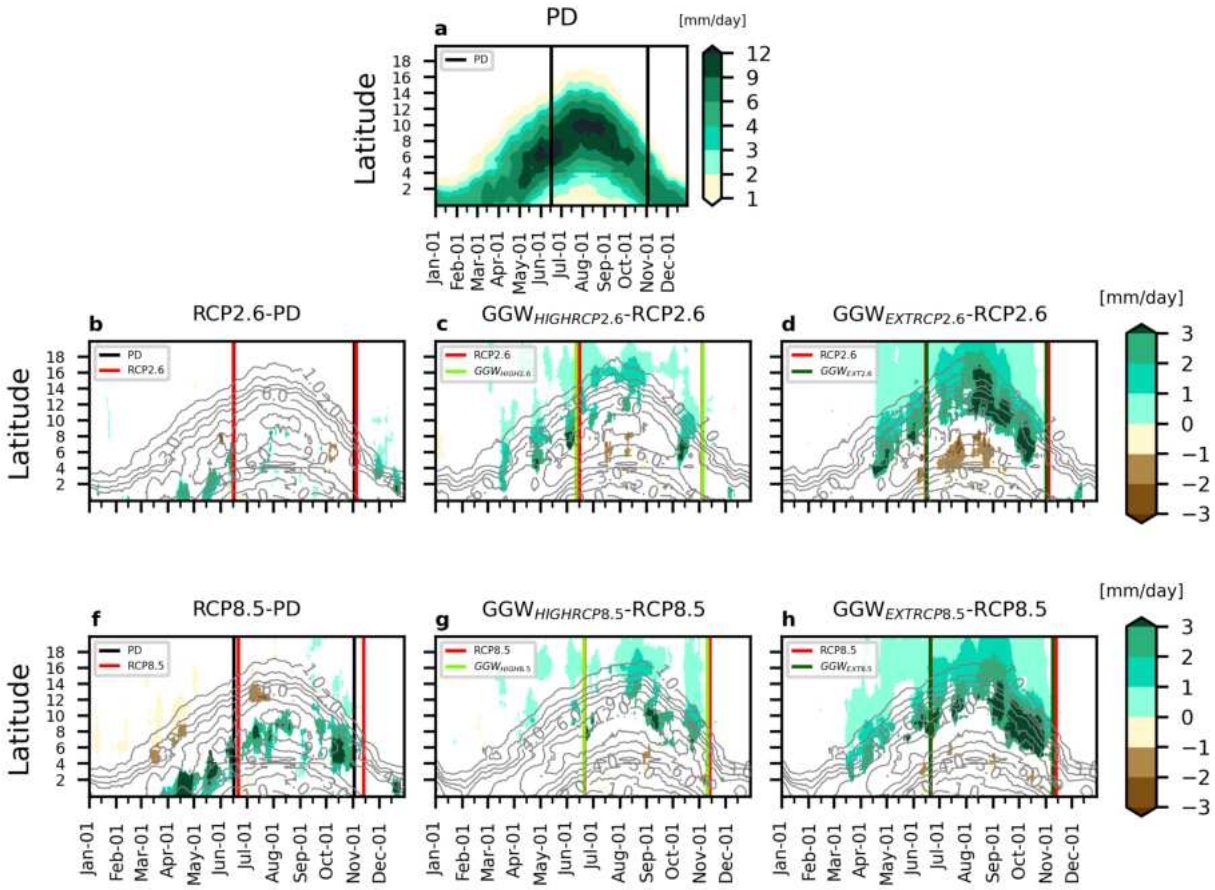

Figure B.3: Annual cycle of zonal mean rainfall. Annual cycle of zonal rainfall for Present Day (PD) between -15°W and 15°E (a) and their change for b) RCP2.6-only experiment relative to PD, c) $GGW_{HIGHRCP2.6}$ and d) $GGW_{EXTRCP2.6}$ experiments relative to RCP2.6-only. Grey contours represent the annual cycle of the reference experiments (PD for b,f and RCPs-only for c,d,g,h). Vertical lines indicate the mean day of the WAM onset and withdrawal e-h) Same as a-d) but under RCP8.5 scenario. Only statistically significant differences at the 5% significance level are shown, using a local (grid-point) Wilcoxon signed-rank test.

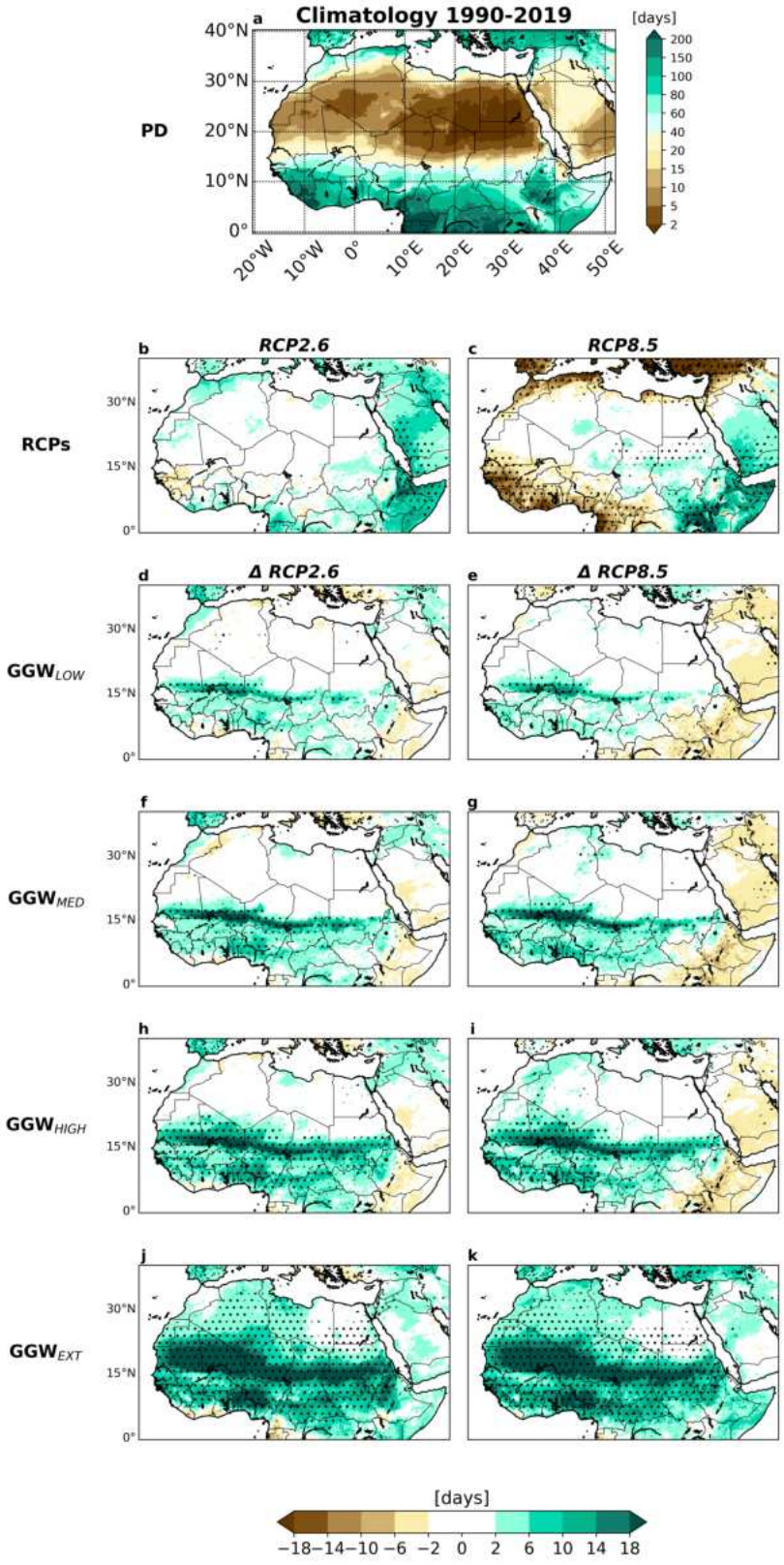

Figure B.4: Annual rainy days (R1mm) a) Climatological annual rainy days for the Present Day and its changes during JJAS for b-c) RCPs-only relatively to PD and d-e) GGW_{LOW}, f-g) GGW_{MED} h-i) GGW_{HIGH}, j-k) GGWEXT relative to RCPs-only under RCP2.6 (left) and RCP8.5 (right) scenarios. Dots indicate values that are significantly different at the 5% significance level, using a local (grid-point) Wilcoxon signed-rank test.

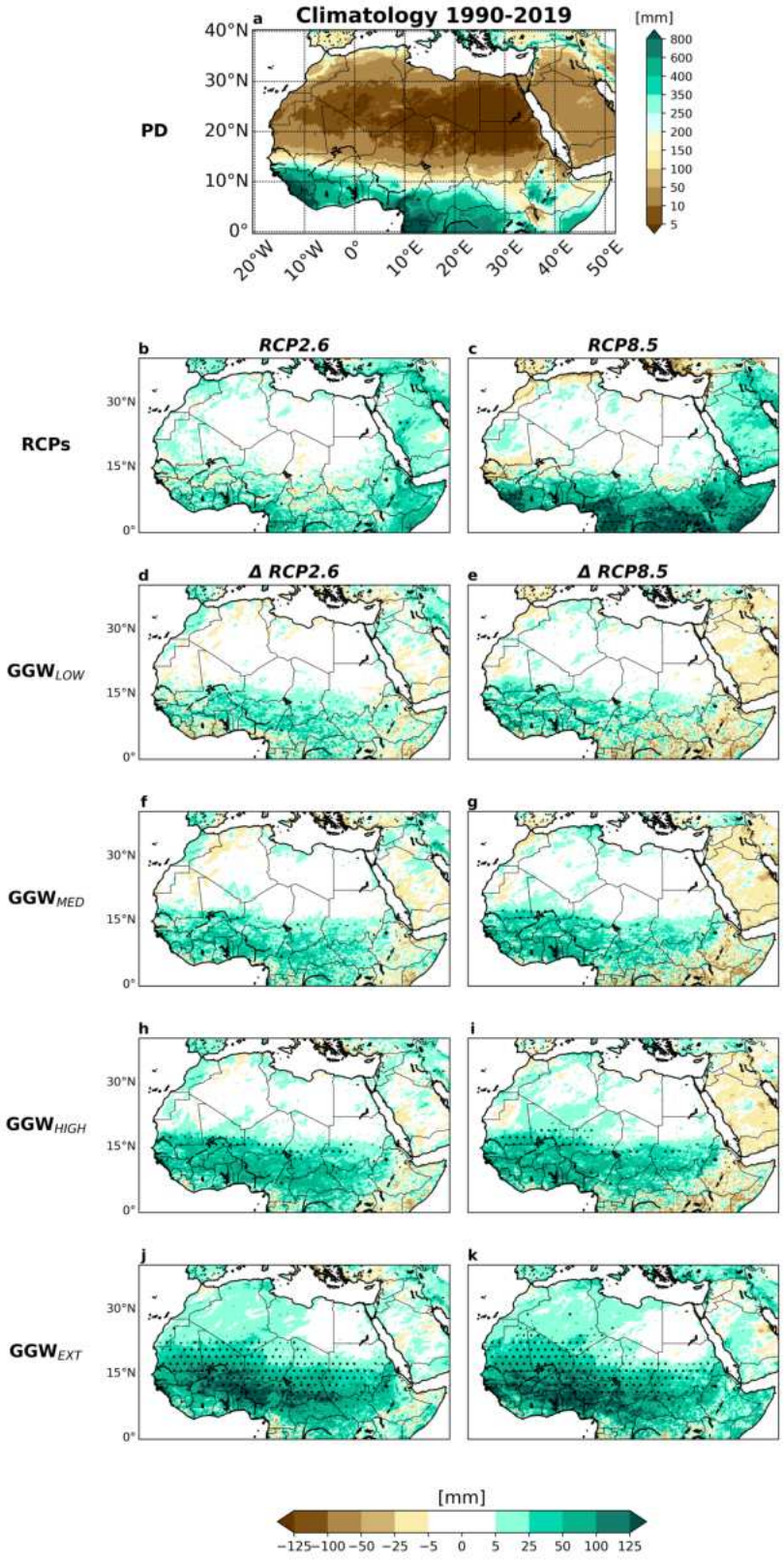

Figure B.5: Annual total precipitation from days > 95th percentile (R95p). a) Climatological annual R95p for the Present Day experiment (PD) and its changes and its changes during JJAS for b-c) RCPs-only relatively to PD and d-e) GGW_{LOW}, f-g) GGW_{MED} h-i) GGW_{HIGH}, j-k) GGWEXT relative to RCPs-only under RCP2.6 (left) and RCP8.5 (right) scenarios. Dots indicate values that are significantly different at the 5% significance level, using a local (grid-point) Wilcoxon signed-rank test.

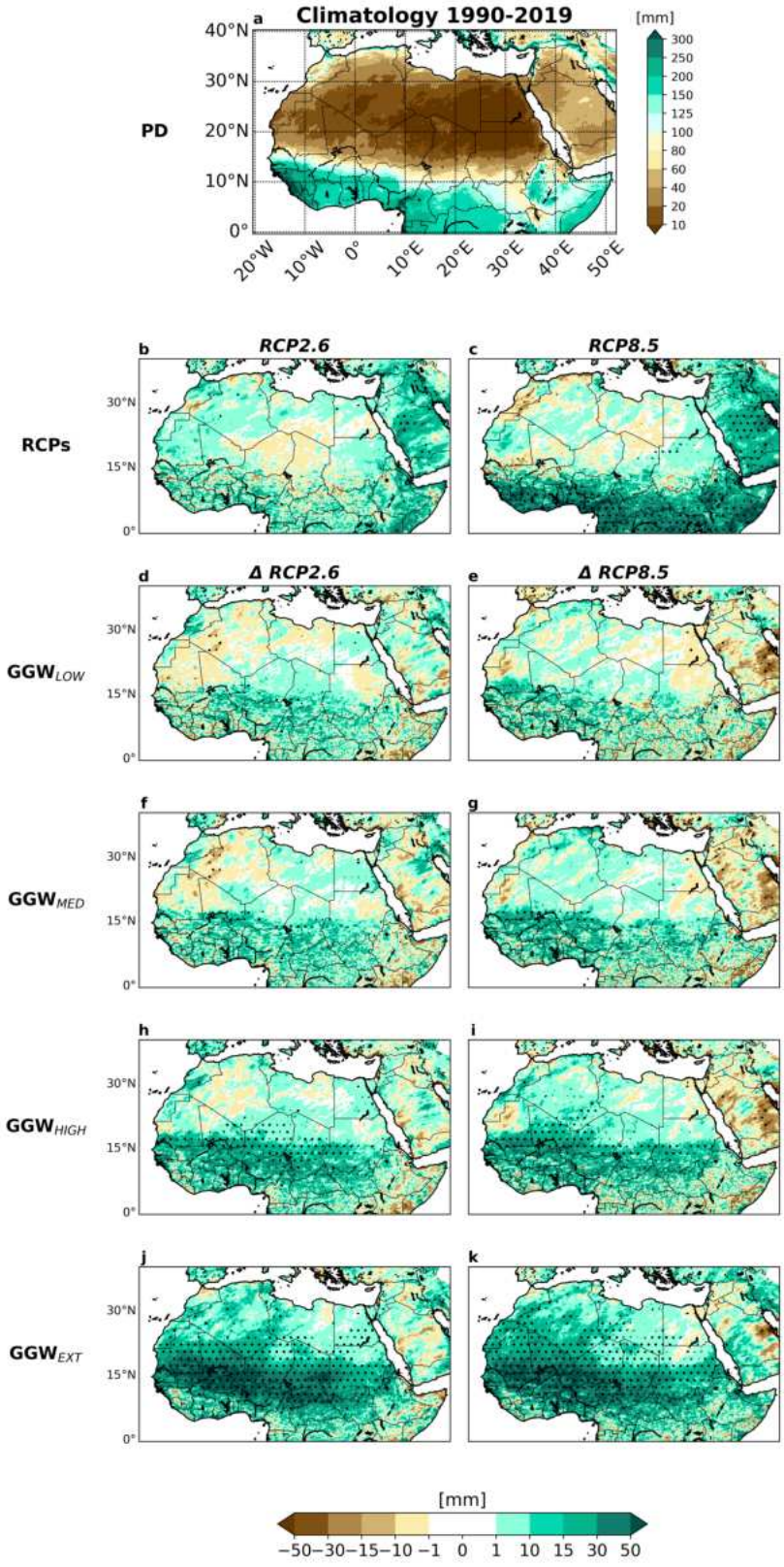

Figure B.6: Annual maximum consecutive 5-day precipitation (RX5D). a) Climatological annual RX5d for the Present Day experiment (PD) and and its changes during JJAS for b-c) RCPs-only relatively to PD and d-e) GGW_{LOW}, f-g) GGW_{MED} h-i) GGW_{HIGH}, j-k) GGWEXT relative to RCPs-only under RCP2.6 (left) and RCP8.5 (right) scenarios. Dots indicate values that are significantly different at the 5% significance level, using a local (grid-point) Wilcoxon signed-rank test.

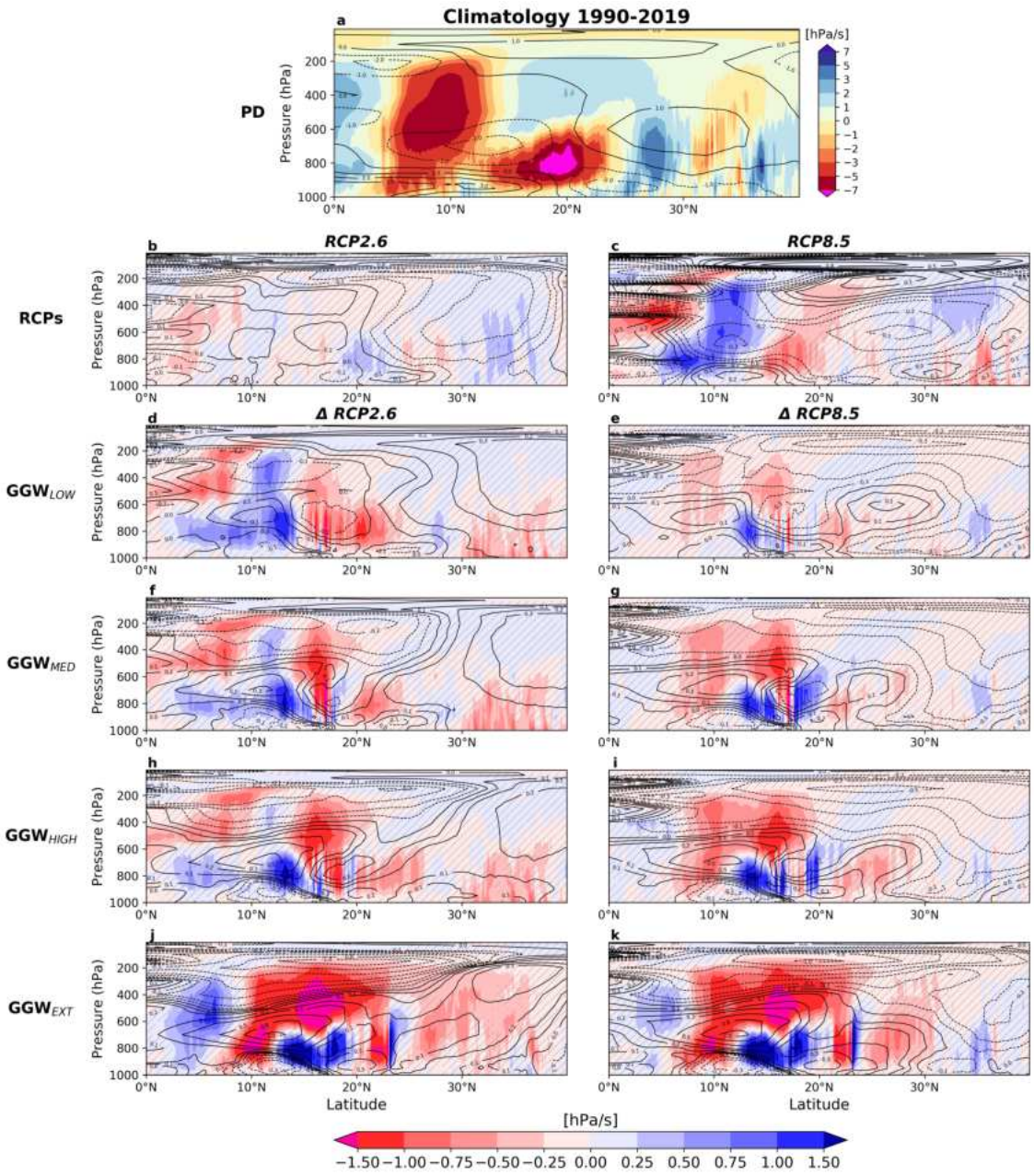

Figure B.7: Meridional and vertical circulation. a) Climatological meridional circulation (contours, m/s) and vertical motion (shaded, upward motion in negative values) averaged between 15°W and 15°E for the Present Day (PD) during the period June-September (JJAS) and their changes for b-c) RCPs-only relatively to PD and d-e) GGW_{LOW}, f-g) GGW_{MED} h-i) GGW_{HIGH}, j-k) GGWEXT relative to RCPs-only under RCP2.6 (left) and RCP8.5 (right) scenarios. Positive (blue) values of vertical motion indicate downward motion while positive values of meridional circulation indicate northward direction. Hatched areas covers the areas where the changes are not statistically significant at 5% of significance level.

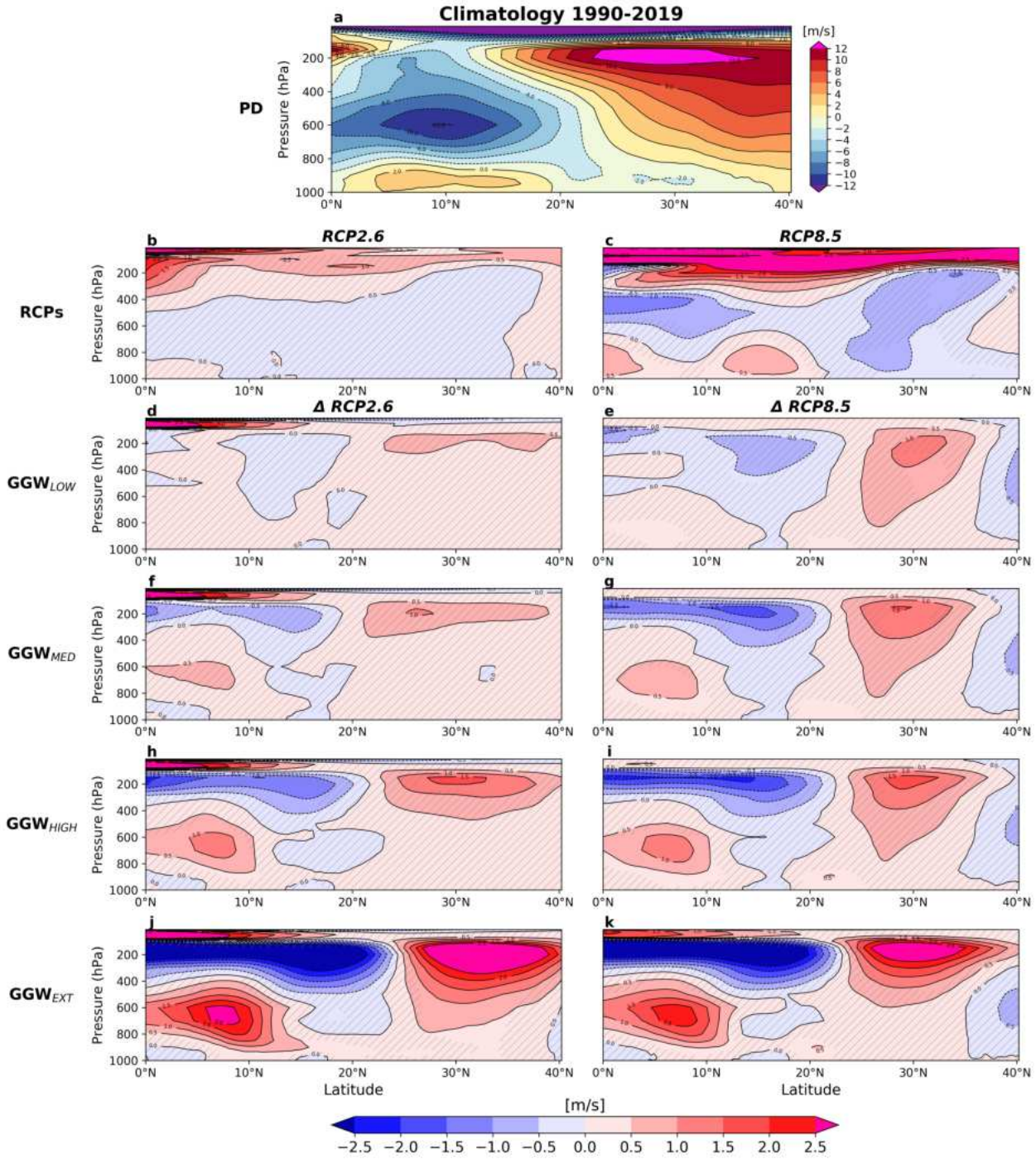

Figure B.8: Zonal circulation. a) Climatological zonal circulation averaged between 15°W and 15°E for the Presend Day (PD) during the period June-September (JJAS) and its changes for b-c) RCPs-only relatively to PD and d-e) GGW_{LOW}, f-g) GGW_{MED} h-i) GGW_{HIGH}, j-k) GGWEXT relative to RCPs-only under RCP2.6 (left) and RCP8.5 (right) scenarios. Positive values indicate westerly anomalies. Hatched areas covers the areas where the changes are not statistically significant at 5% of significance level.

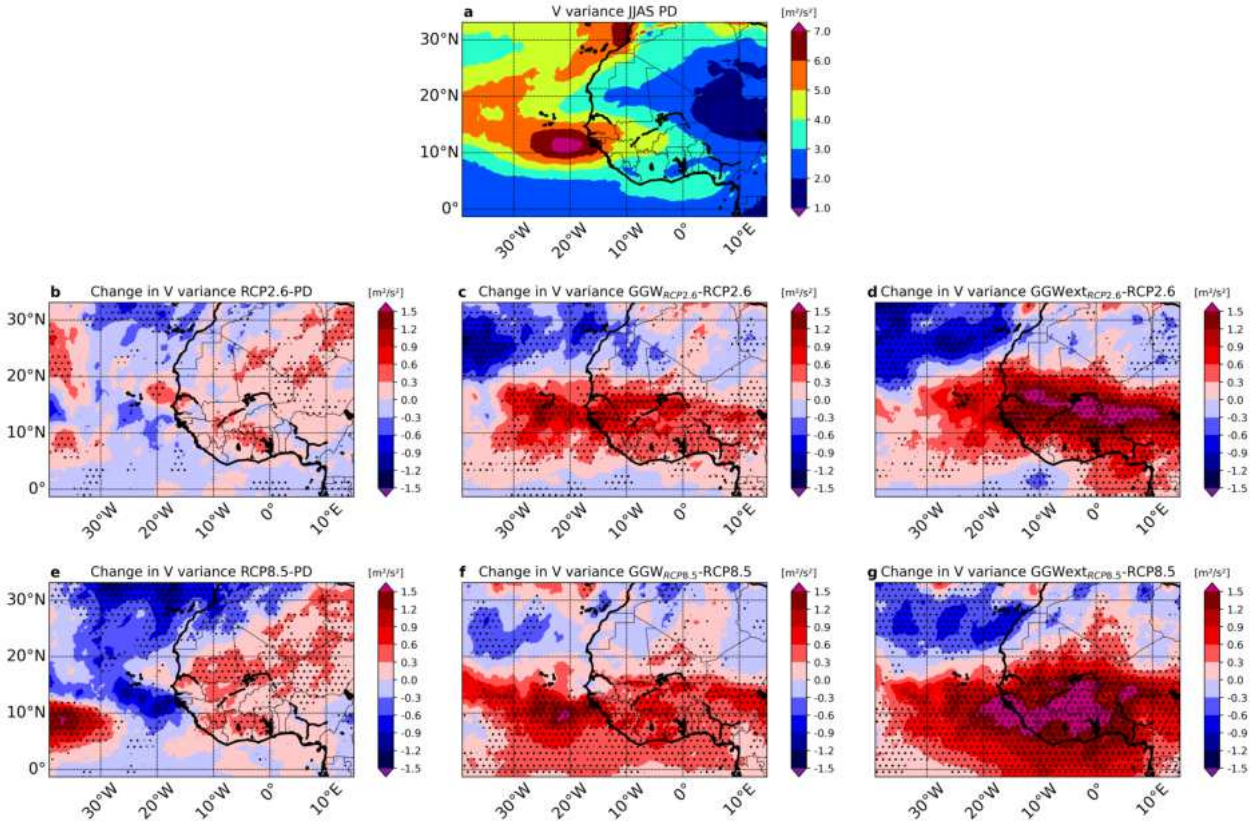

Figure B.9: African Easterly Waves . Summer (JJAS) change in the variance of the meridional wind at 700 hPa filtered in the 2–6-day band for the Present Day experiment (PD) and its changes and their changes for b) the RCP2.6-only experiment relatively to PD; c) $GGW_{HIGH\ RCP2.6}$ and d) $GGW_{EXT\ RCP2.6}$ experiments relative to the RCP2.6-only simulation. E-g) Same as b-d) but under RCP8.5 scenario. Dots indicate values that are significantly different at the 5% significance level, using a local (grid-point) Wilcoxon signed-rank test

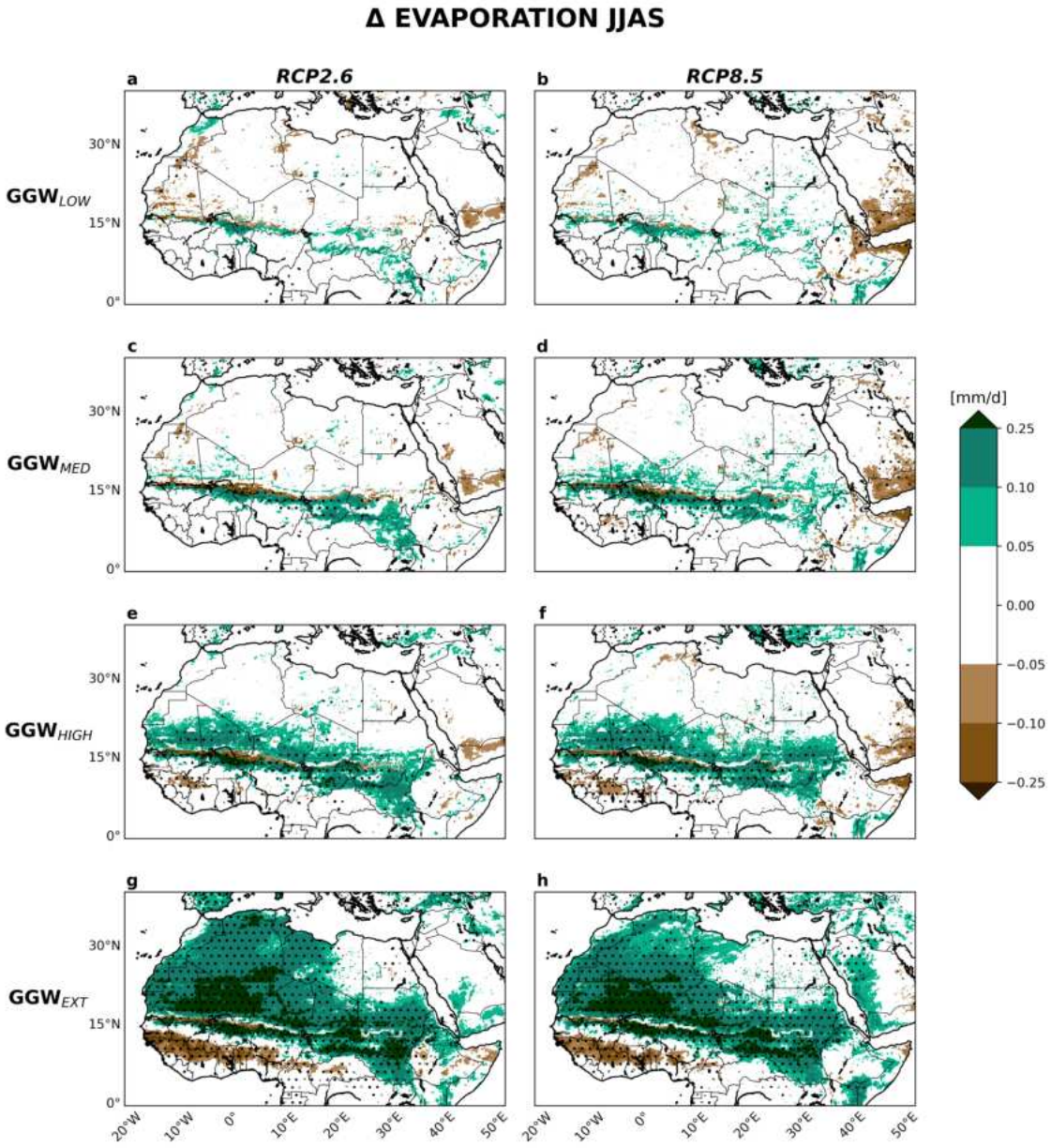

Figure B.10: Evaporation. Change in evaporation for the period June-September (JJAS) for a-b) GGW_{LOW}, c-d) GGW_{MED} e-f) GGW_{HIGH}, g-h) GGW_{EXT} relative to RCPs-only under RCP2.6 (left) and RCP8.5 (right) scenarios. Dots indicate values that are significantly different at the 5% significance level, using a local (grid-point) Wilcoxon signed-rank test.

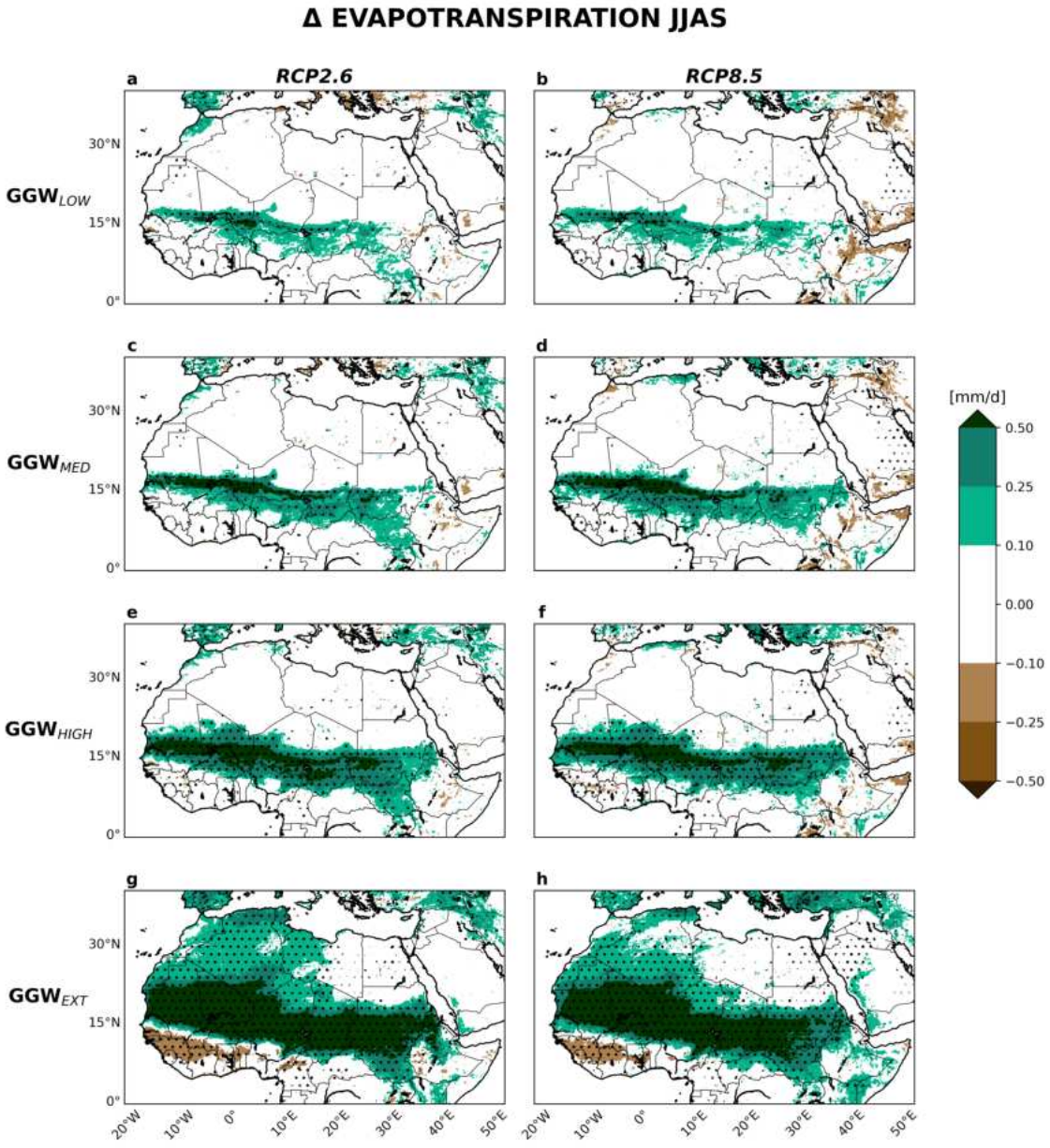

Figure B.11: Evapotranspiration. Change in evapotranspiration for the period June-September (JJAS) for a-b) GGW_{LOW}, c-d) GGW_{MED} e-f) GGW_{HIGH}, g-h) GGW_{EXT} relative to RCPs-only under RCP2.6 (left) and RCP8.5 (right) scenarios. Dots indicate values that are significantly different at the 5% significance level, using a local (grid-point) Wilcoxon signed-rank test.

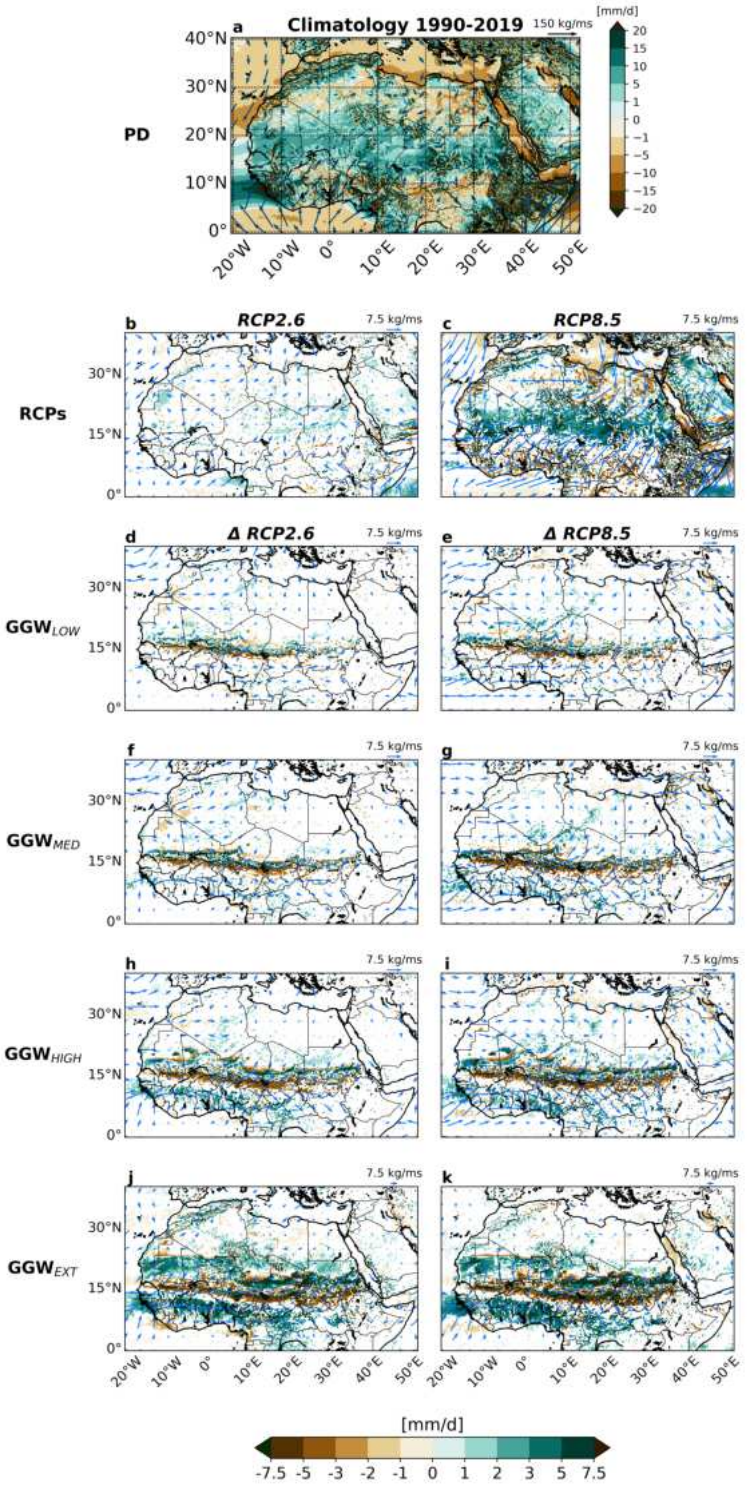

Figure B.12: Moisture flux and total moisture flux convergence. a) Climatological JJAS vertically integrated (between 1000-850 hPa) moisture flux (arrows) and moisture flux convergence (shaded) for the Present Day experiment (PD) and their changes for b-c) RCPs-only relatively to PD and d-e) GGW_{LOW}, f-g) GGW_{MED} h-i) GGW_{HIGH}, j-k) GGWEXT relative to RCPs-only under RCP2.6 (left) and RCP8.5 (right) scenarios. Dots indicate values that are significantly different at the 5% significancelevel, using a local (grid-point) Wilcoxon signed-rank test.

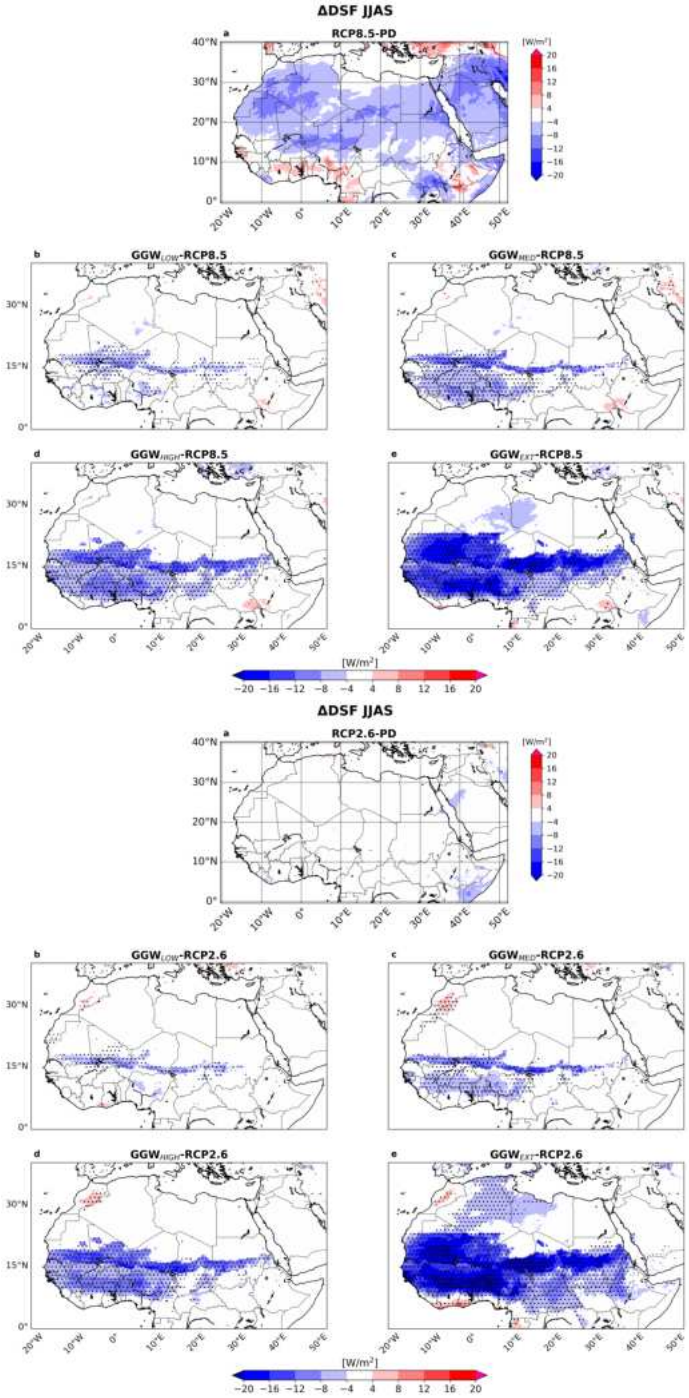

Figure B.13: Summer downward solar flux. Top) Downward solar flux change in June-September (JJAS) for a) RCP8.5 relative to PD experiments and for b) GGW_{LOW}, c) GGW_{MED}, d) GGW_{HIGH} and e) GGW_{EXT} experiments relative to RCP8.5 simulation, respectively. Dots show significant change with a significance level at 5% using a local (grid-point) Wilcoxon signed-rank test. Bottom) Same as left but for RCP2.6 scenarios.

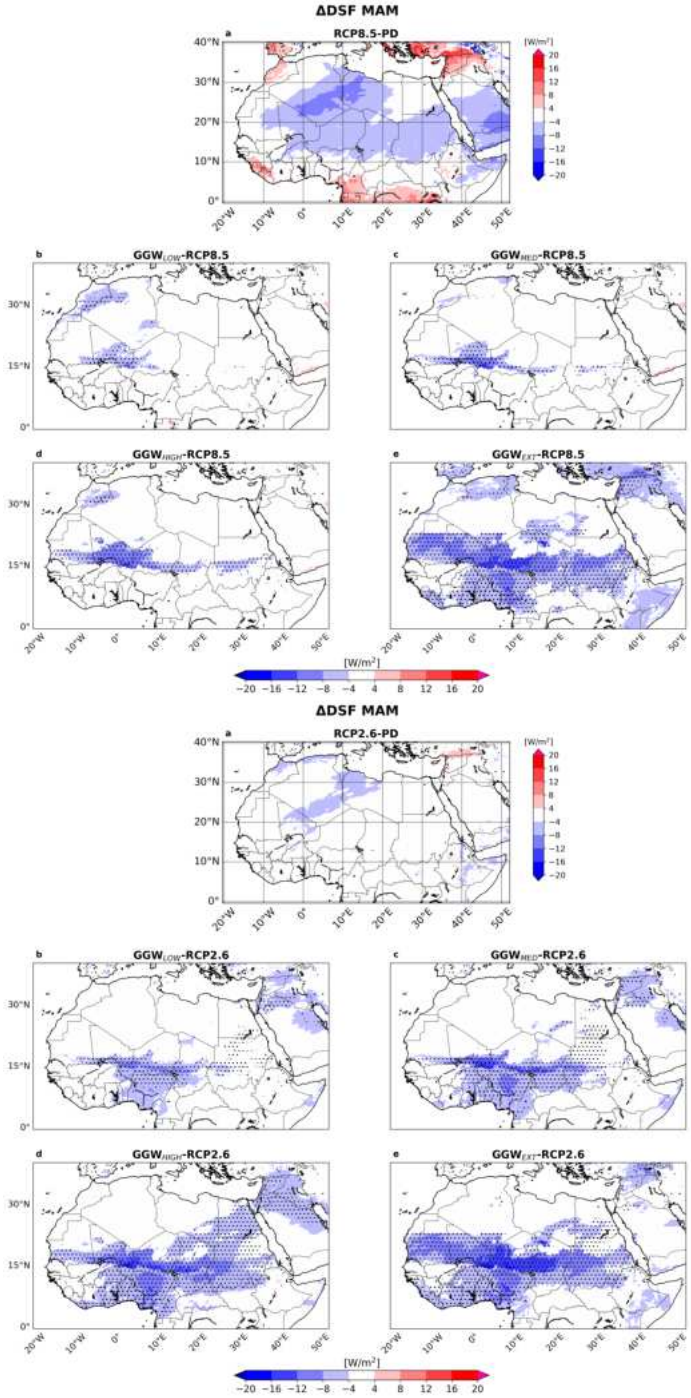

Figure B.14: Spring downward solar flux. Top) Downward solar flux change in March-May (MAM) for a) RCP8.5 relative to PD experiments and for b) GGW_{LOW}, c) GGW_{MED}, d) GGW_{HIGH} and e) GGW_{EXT} experiments relative to RCP8.5 simulation, respectively. Dots show significant change with a significance level at 5% using a local (grid-point) Wilcoxon signed-rank test. Bottom) Same as left but for RCP2.6 scenarios.

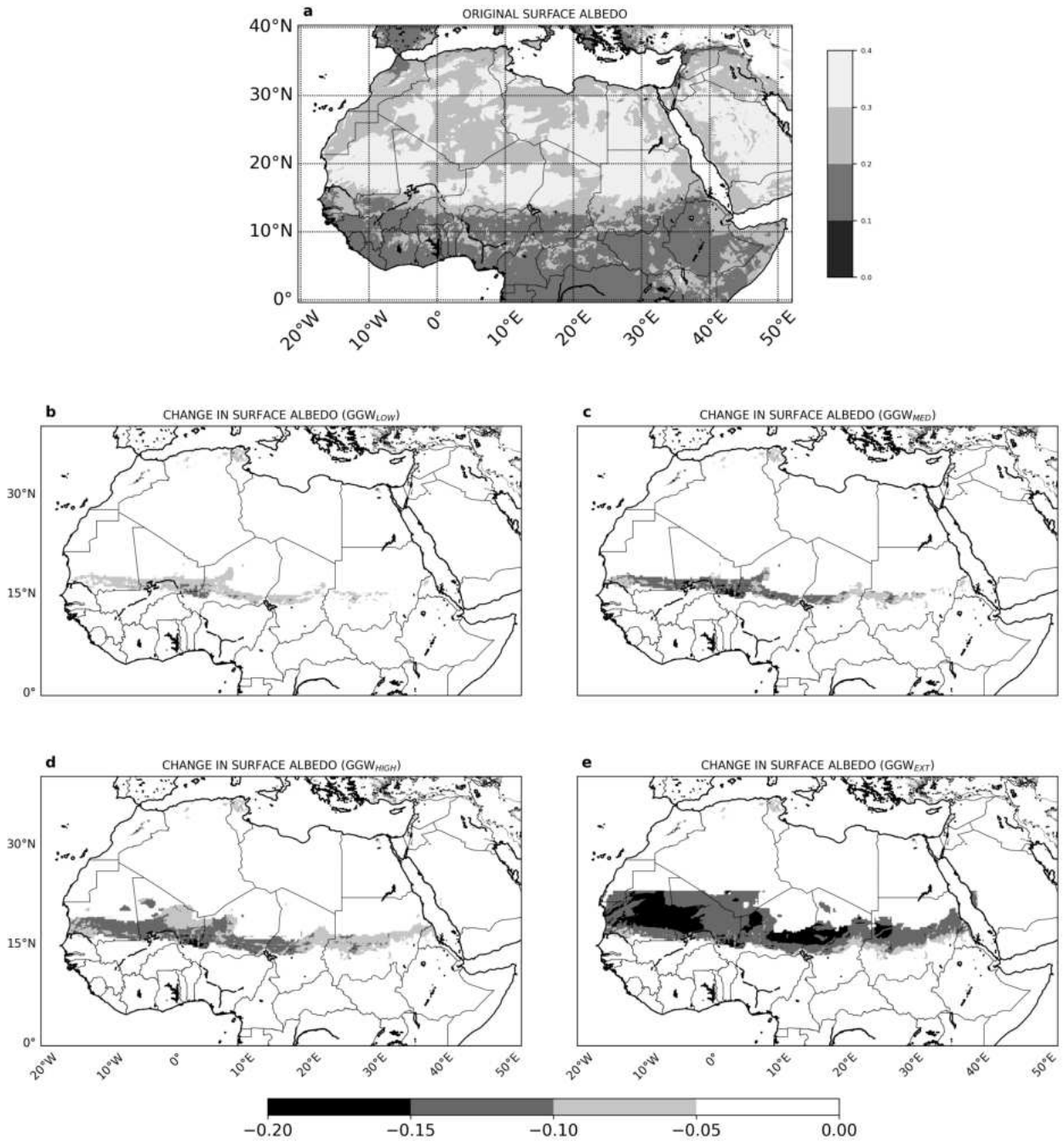

Figure B.15: Surface albedo. a) Surface albedo values for the Present Day experiment (PD) and its change for b) GGW_{LOW} and c) GGW_{MED} d) GGW_{HIGH} and e) GGW_{EXT} experiments relative to PD

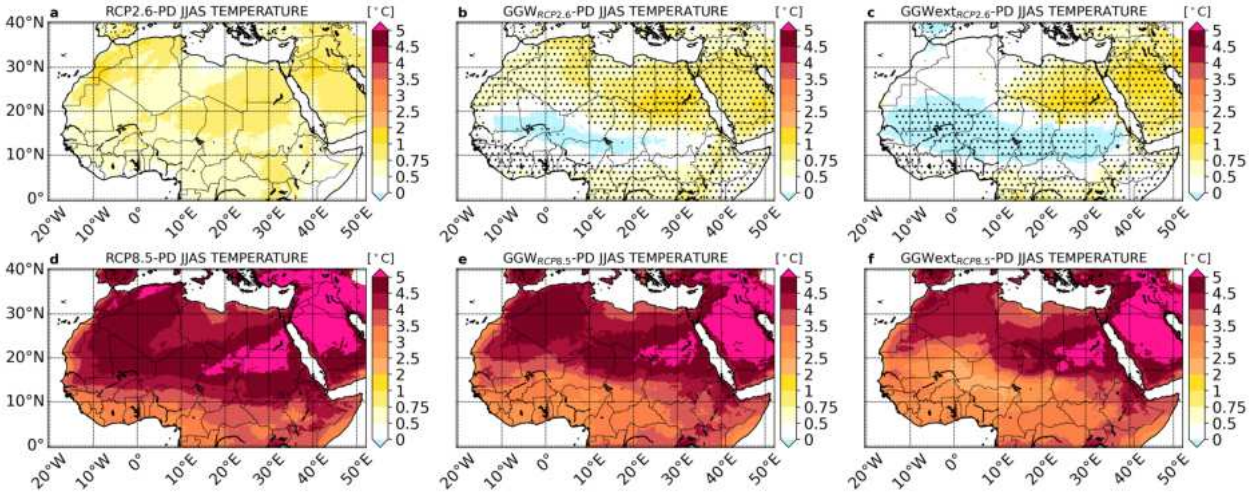

Figure B.16: JJAS mean temperature changes. Changes in mean temperature during the period June-September a) in the RCP2.6-only experiment b) in the $GGW_{HIGH\ RCP2.6}$ and c) in the $GGW_{EXT\ RCP2.6}$ experiments relative to Present Day (PD). d-f) Same as a-c) but under RCP8.5. Dots indicate area with a statistical significance at the 5% level, using a local (grid-point) t test. *In panels a) and d) all areas show significant differences (no dots shown)*.

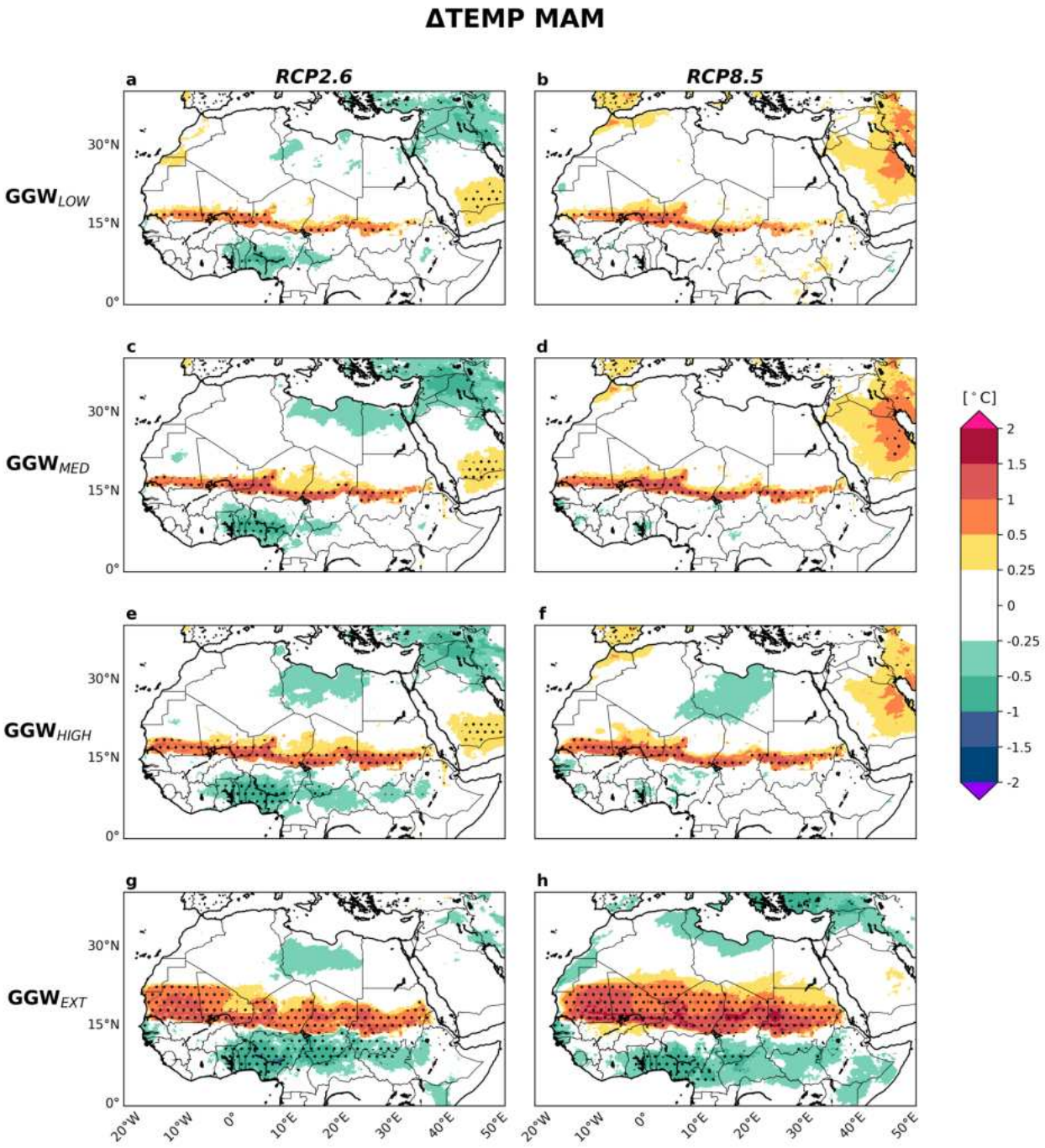

Figure B.17: MAM mean temperature changes. Changes in mean temperature during the pre-monsoonal season (March-May), MAM for a,b) GGW_{LOW}, c,d) GGW_{MED}, e-f) GGW_{HIGH}, g,h) GGW_{EXT} scenarios relative to the standard RCP2.6-only (left) and RCP8.5-only (right) pathways. Dots indicate areas with a statistical significance at the 5% significance level, using a local (grid-point) t-test.

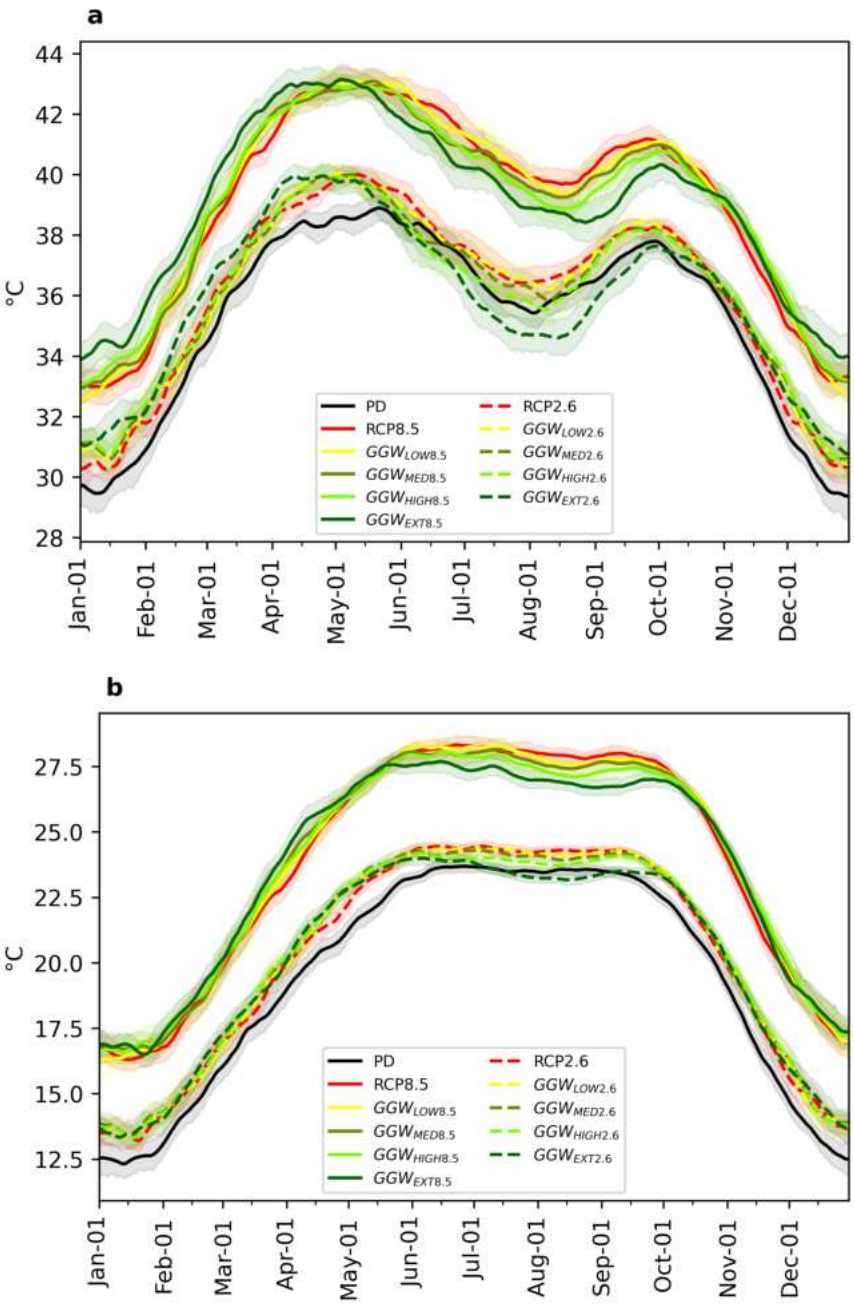

Figure B.18: Annual cycle of daily temperature extremes. Annual cycle of 10-day running means of daily maximum (a) and minimum (b) temperature averaged over the Sahel domain (20°W-40°E and 10°-20°N). Black line for the Present Day (PD) simulation, red solid (dashed) line for RCP8.5-only (RCP2.6-only) experiment, yellow solid (dashed) line for $GGW_{LOWRCP8.5}$ ($GGW_{LOWRCP2.6}$), olive green solid (dashed) line for $GGW_{MEDRCP8.5}$ ($GGW_{MEDRCP2.6}$), light green solid (dashed) line for $GGW_{HIGHRCP8.5}$ ($GGW_{HIGHRCP2.6}$) and dark green solid (dashed) line for $GGW_{EXTRCP8.5}$ ($GGW_{EXTRCP2.6}$). Shaded areas represent the 95% bootstrap (with 500 resamples) confidence interval.

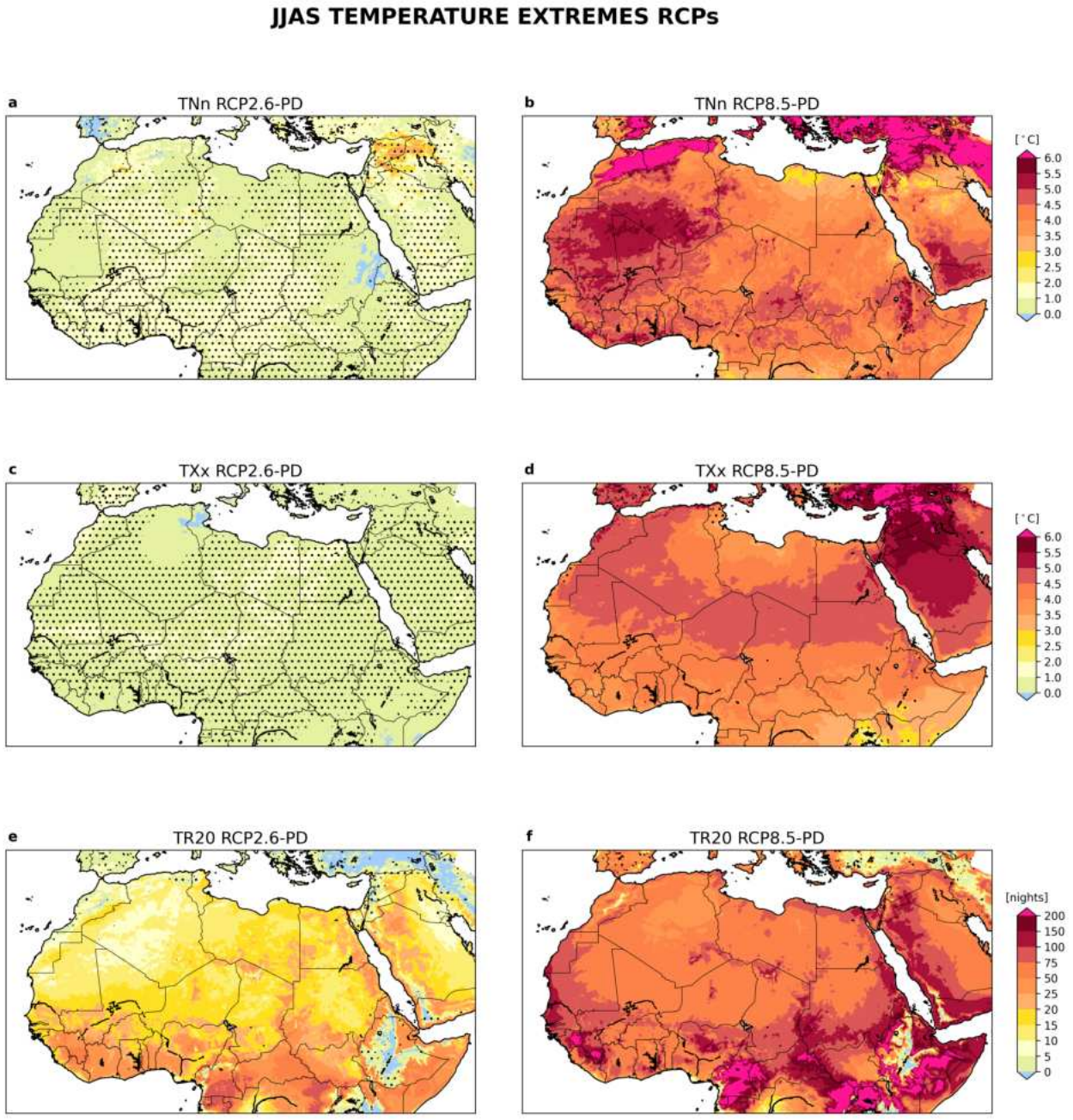

Figure B.19: Change in the hottest and coldest day of the year and number of tropical nights. a-b) Change in the annual coldest day of the year (TNnx) for RCP2.6-only (left) and RCP8.5-only (right) c-d) same as a-b) but for the hottest day of the year (TXx). e-f) same as a-b) but for tropical nights (number of nights with daily minimum temperature above 20°C, TR20). Dots indicate areas with a statistical significance at the 5% significance level, using a local (grid-point) t-test. In b,d,e,f no dots are shown as all differences are significant.

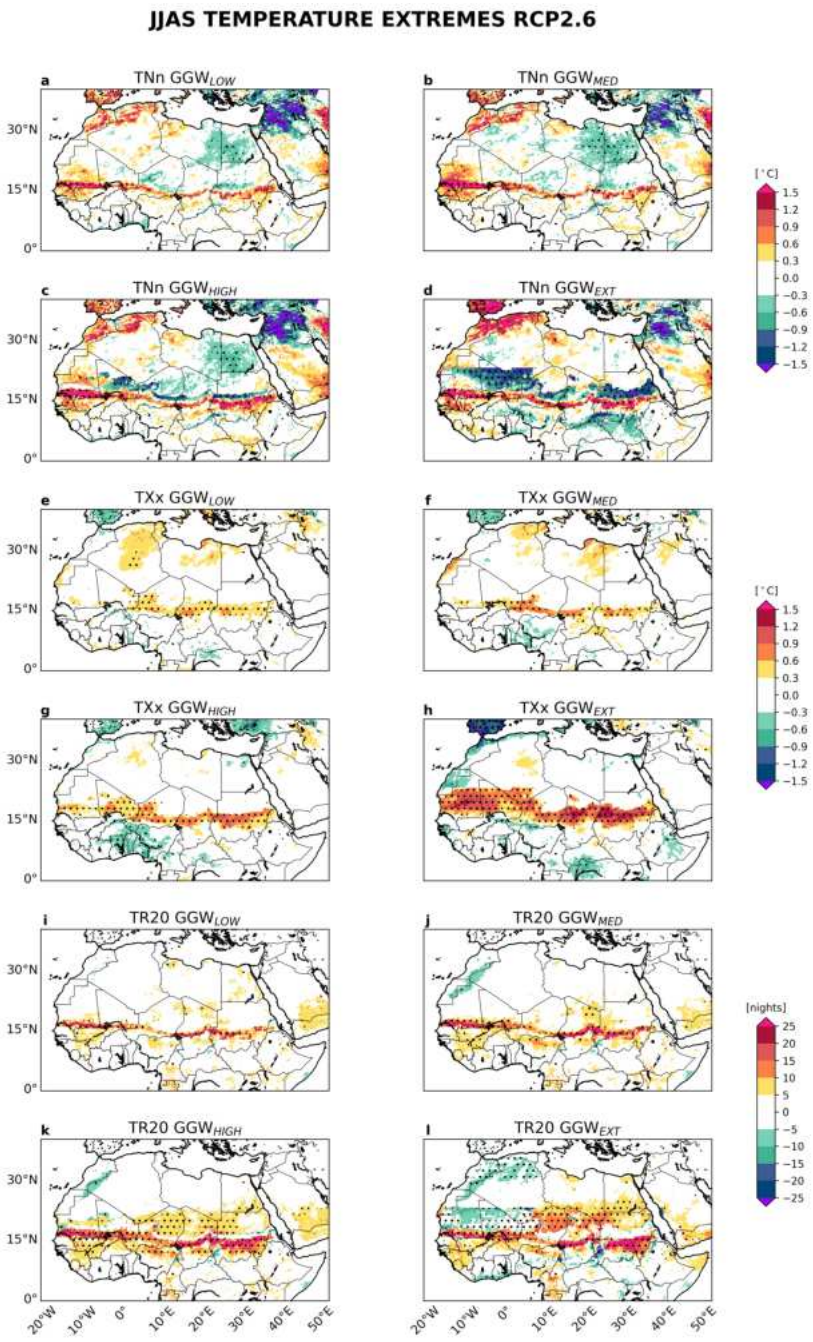

Figure B.20: Change in the annual hottest and coldest day of the year and number of tropical nights. Change in the annual coldest day of the year (TNnx) for a) GGW_{LOW}, b) GGW_{MED} and c) GGW_{HIGH} and d) GGW_{EXT} scenarios relative to the standard RCP2.6 pathway. e-h) same as a-d) but for the hottest day of the year (TXx). I-l) same as a-d) but for tropical nights (number of nights with daily minimum temperature above 20°C, TR20). Dots indicate area with a statistical significance at the 5% significance level, using a local (grid-point) t-test.

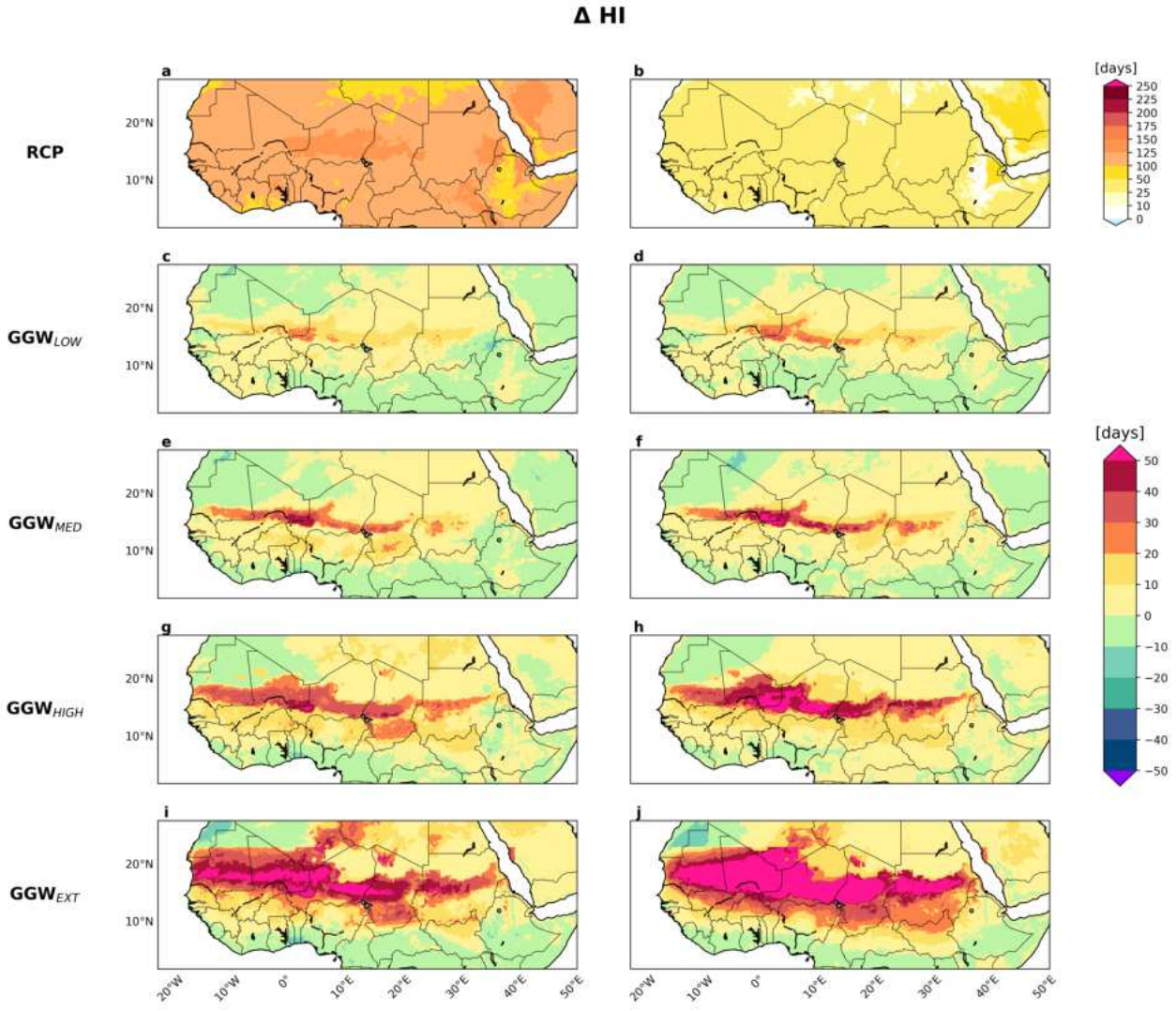

Figure B.21: Heat Index (HI). a-b) Annual change in number of days with HI higher than Present Day (PD) 75-th (left) and 95th (right) percentile for RCP2.6-only. Difference in number of days with HI higher than PD 75-th (left) and 95-th (right) percentiles for c-d) GGW_{LOW}, e-f) GGW_{MED}, g-h) GGW_{HIGH} and i-j) GGW_{EXT} relatively to RCP2.6-only experiment.

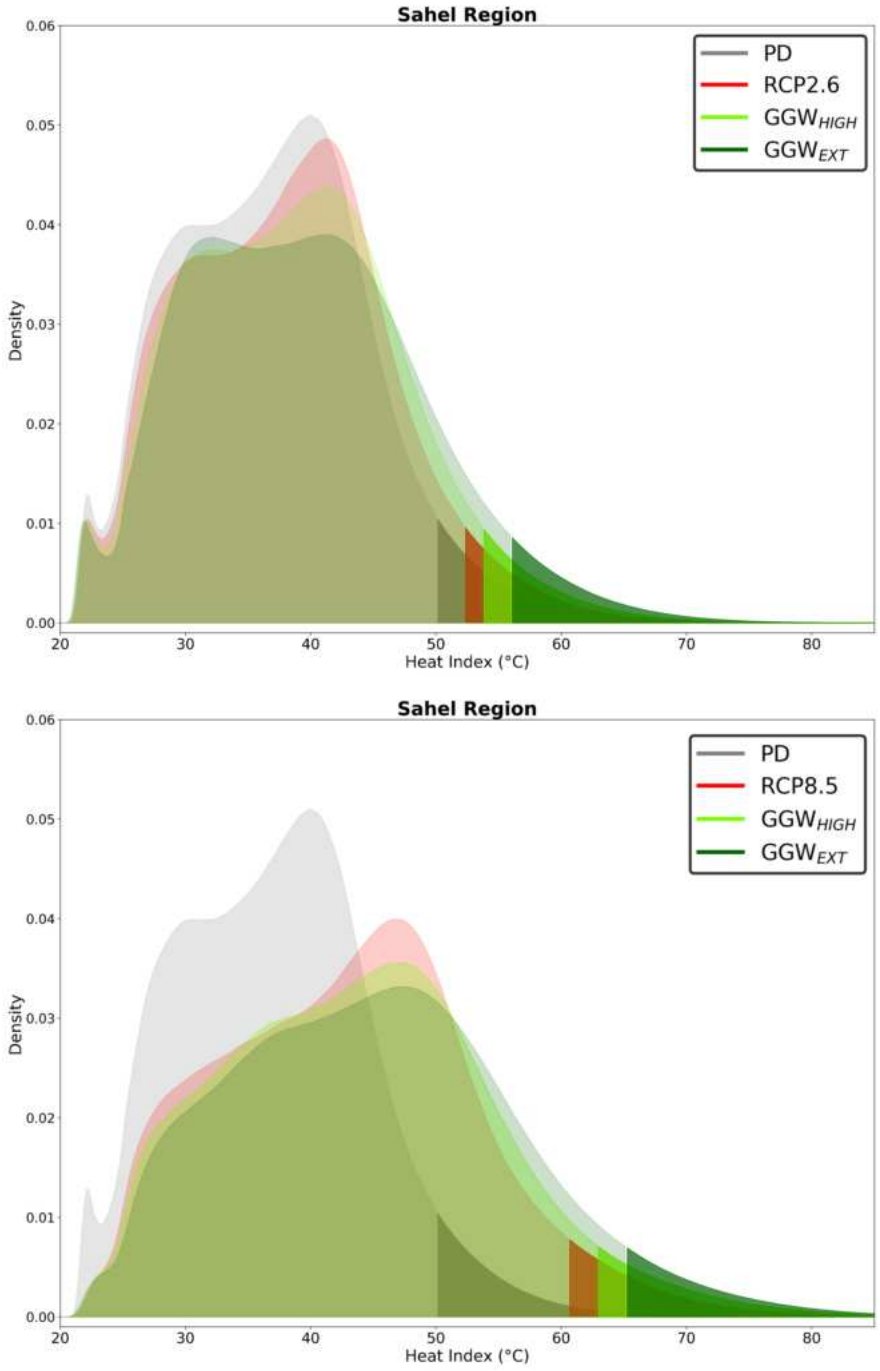

Figure B.22: Sahel HI distributions. Kernel density estimations of HI for the Sahel region under RCP2.6 (top) and RCP8.5 (bottom) pathways. Curves show Present Day (gray), RCP8.5-only (red), GGW_{HIGH} (light green) and GGW_{EXT} (dark green). Darker shaded tails highlight the 5th - 95th percentiles for each distribution.

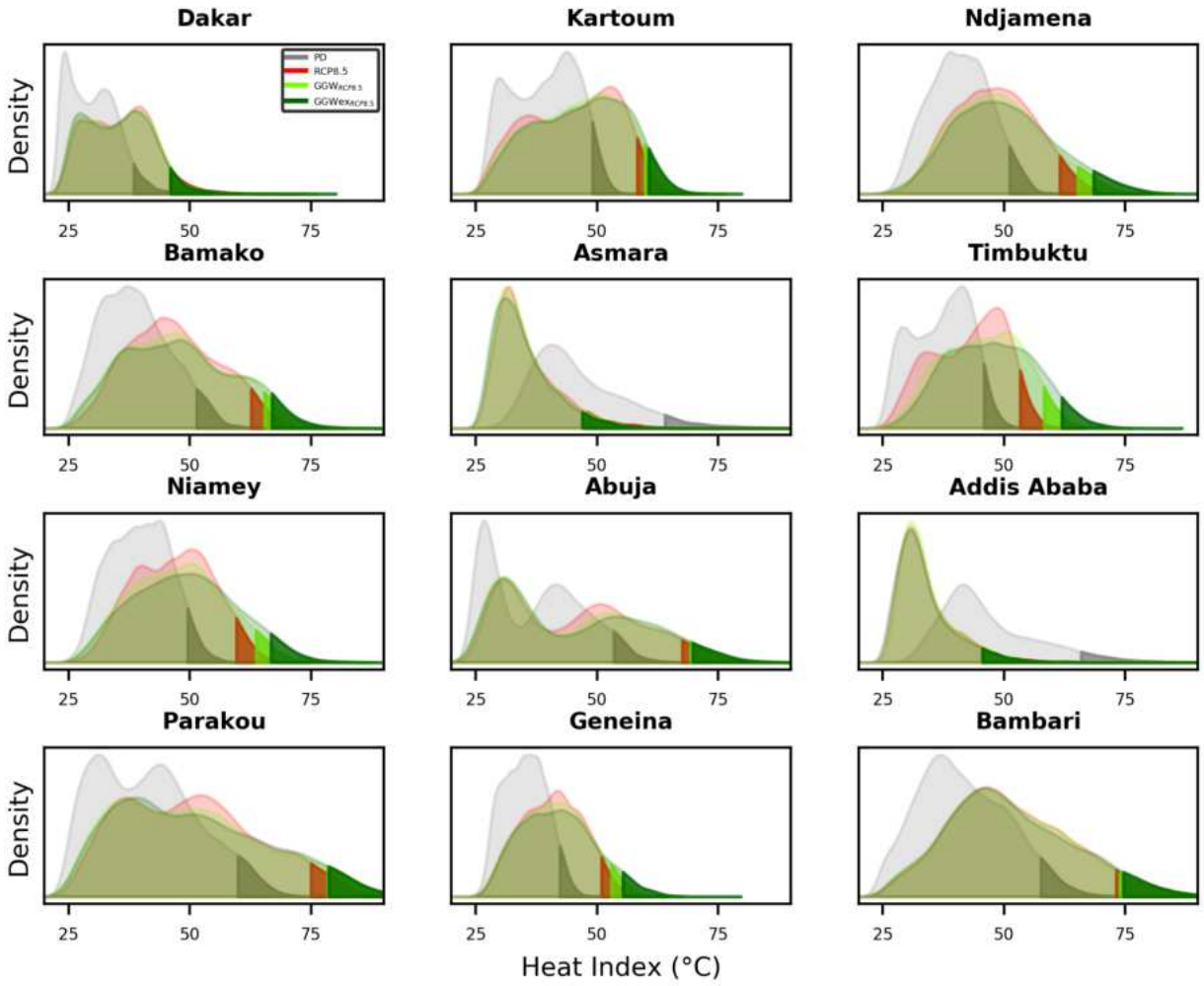

Figure B.23: Heat Index Kernel Density Estimation. HI KDE for 12 Sahelian cities. Shaded tails show the values above the 95th percentiles (comparison between Present Day and the future projections under the RCP8.5 scenario).

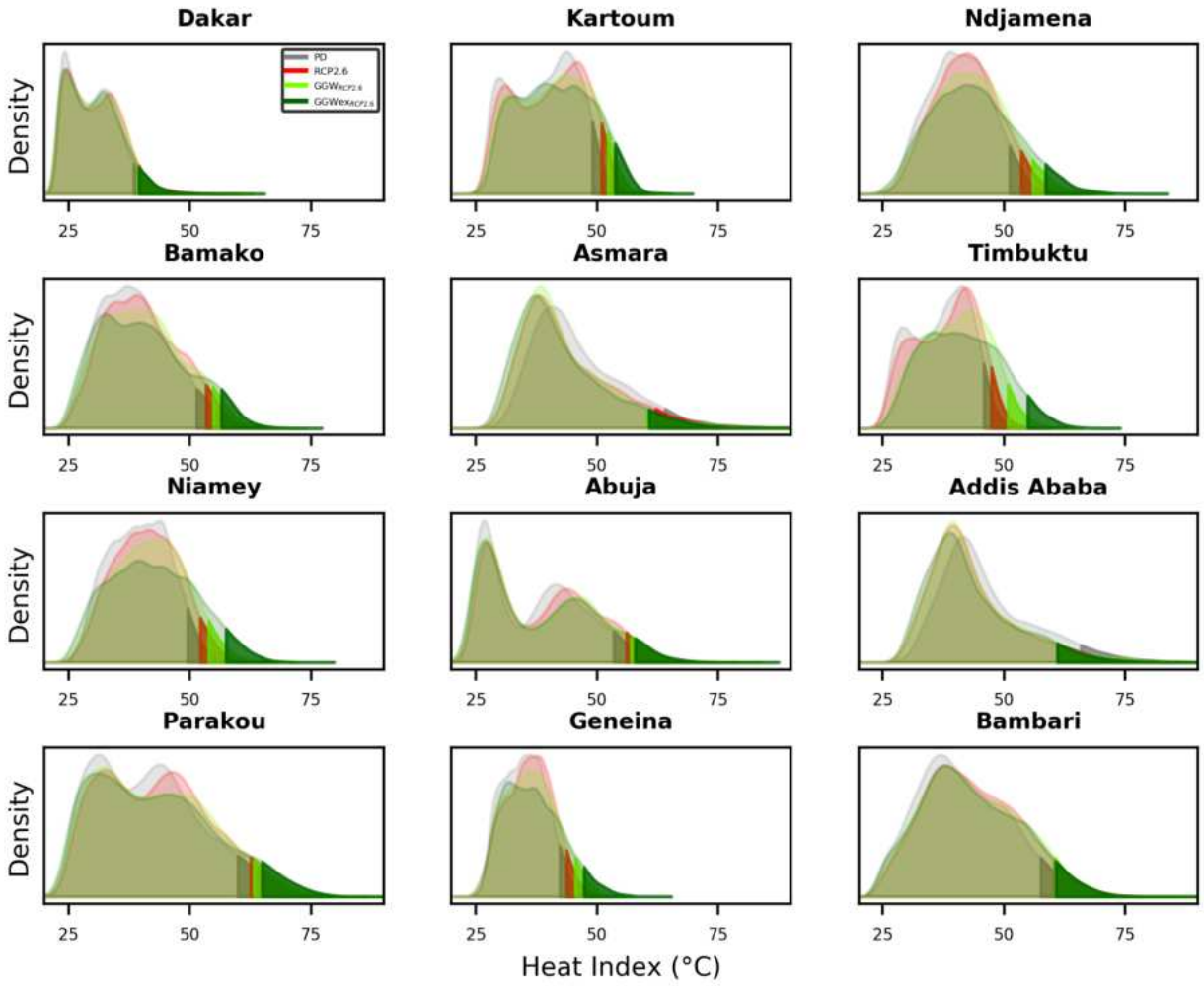

Figure B.24: Heat Index Kernel Density Estimation. HI KDE for 12 Sahelian cities. Shaded tails show the values above the 95th percentiles (comparison between Present Day and the future projections under the RCP2.6 scenario).

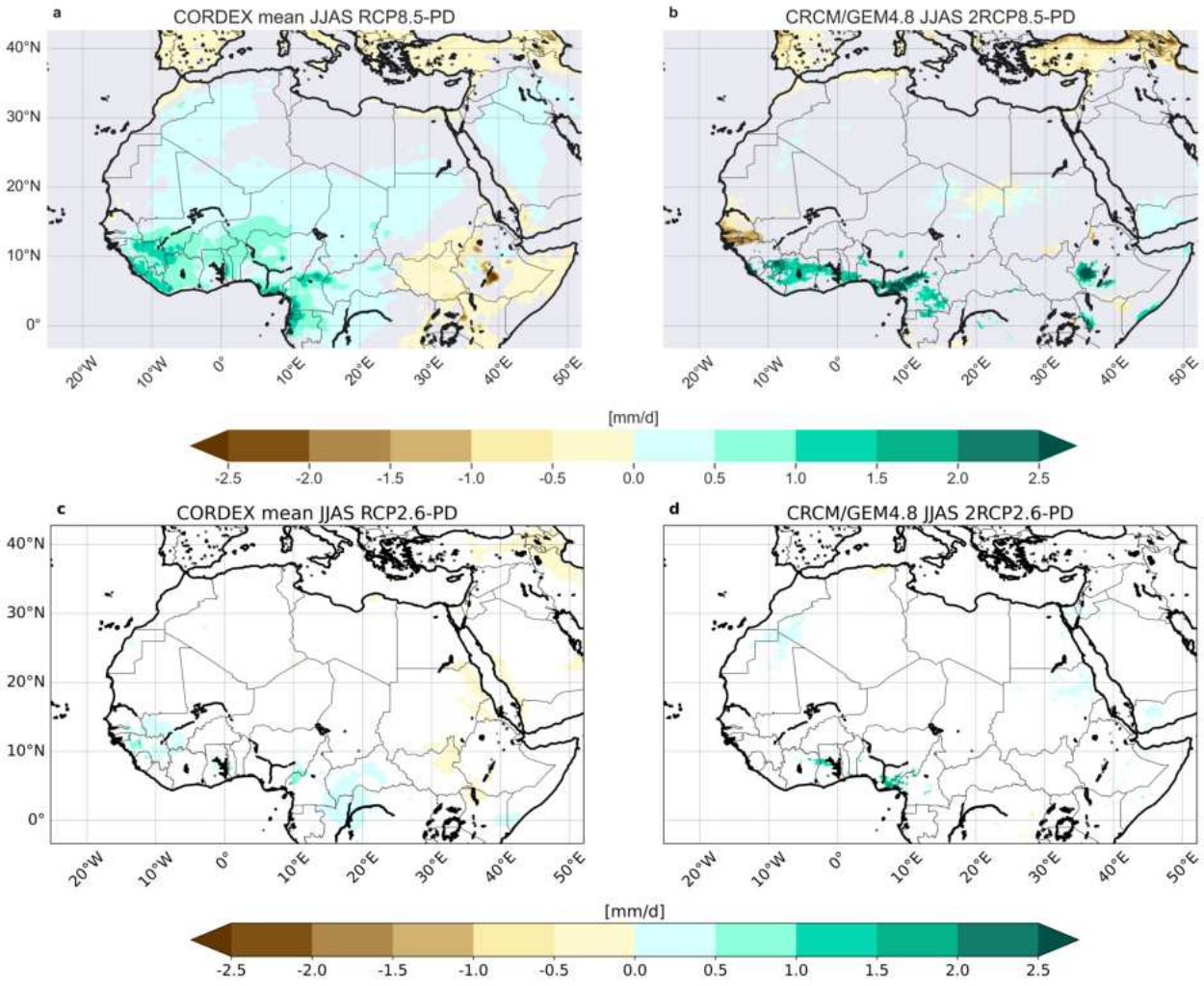

Figure B.25: CORDEX vs CRCM/GEM4.8 JJAS mean precipitation. Change in JJAS mean precipitation between RCP8.5-only and Present Day for a) CORDEX ensemble and b) CRCM/GEM4.8. c-d) same as a-b), respectively but for RCP2.6. Only statistically significant change at the 5% level is shown, using a local (grid-point) Wilcoxon signed-rank test.

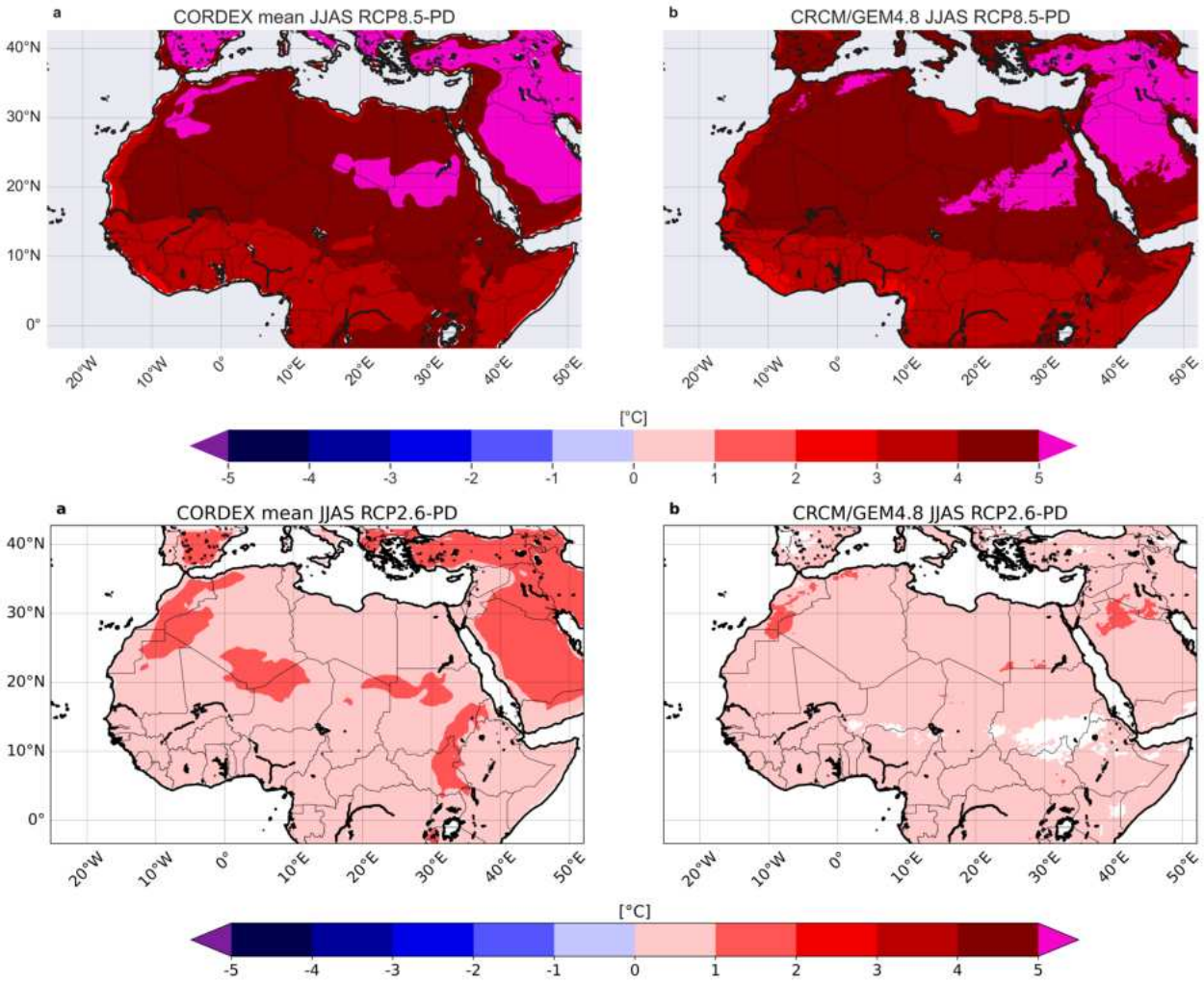

Figure B.26: CORDEX vs CRCM/GEM4.8 JJAS mean temperature. Change in JJAS mean temperature between RCP8.5-only and Present Day for a) CORDEX ensemble and b) CRCM/GEM4.8. c-d) same as a-b), respectively but for RCP2.6. Only statistically significant change at the 5% level is shown, using a local (grid-point) Student's t-test.

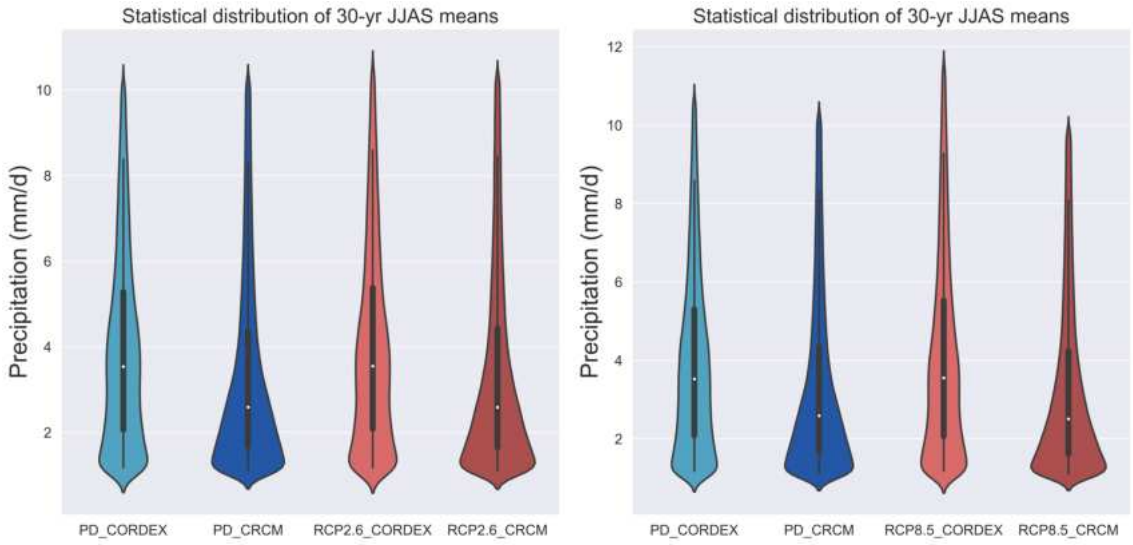

Figure B.27: CORDEX vs CRCM/GEM4.8 precipitation distributions. Left: Violin plots of JJAS precipitation from CORDEX and CRCM/GEM4.8 for both Present Day (PD) and RCP2.6-only for Sahel (20°W-40°E and 10°-20°N). The white dot is the mean, the edge of the boxplots shows the 25th and the 75th percentile, while the whiskers indicate the 5th and 95th percentile. Right: same as left but for RCP8.5

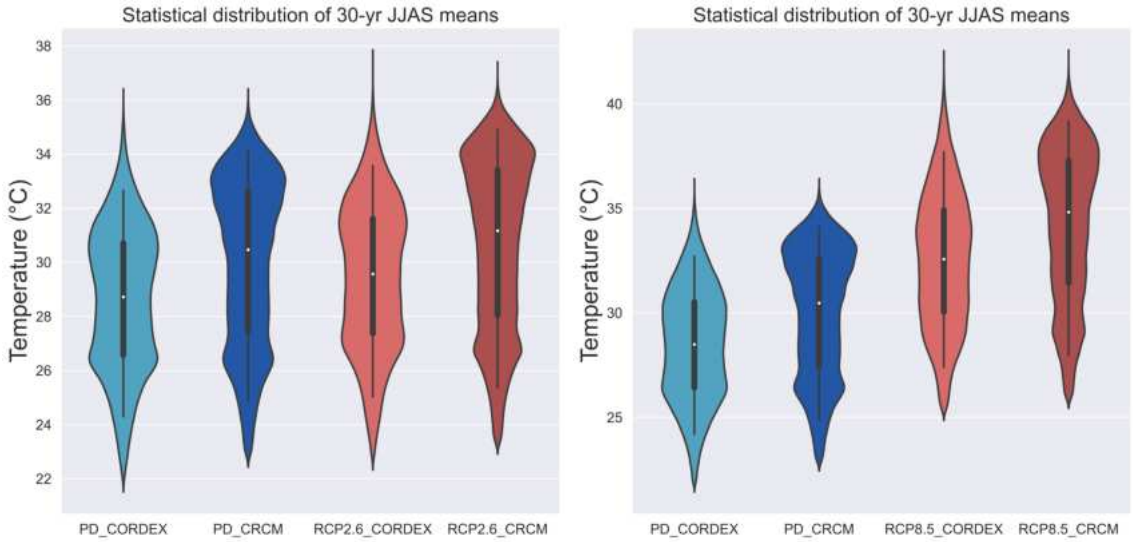

Figure B.28: CORDEX vs CRCM/GEM4.8 temperature distributions. Left: Violin plots of JJAS temperature from CORDEX and CRCM/GEM4.8 for both Present Day (PD) and RCP2.6-only for Sahel (20°W-40°E and 10°-20°N). White dot is the mean, the edge of the boxplots shows the 25th and the 75th percentile, while the whiskers indicate the 5th and 95th percentile. Right: same as Left but for RCP8.5.

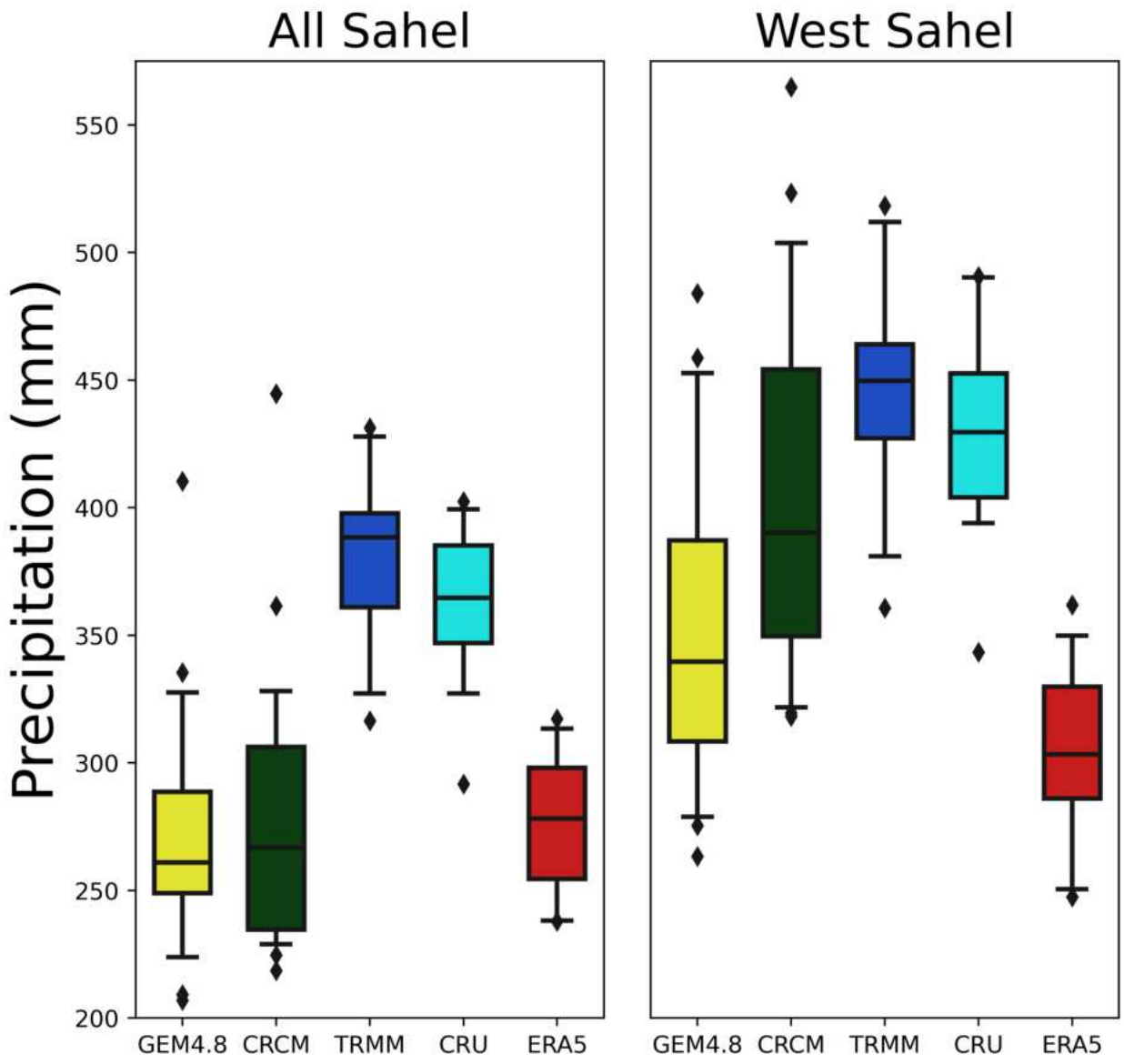

Figure B.29: Model evaluation.. Boxplots of Summer (JJAS) mean precipitation for GEM4.8 (at 0.55° horizontal resolution), CRCM/GEM4.8 (at 0.12° horizontal resolution), the Tropical Rainfall Measuring Mission (TRMM), Climate Research Unit (CRU) and ERA5 Reanalysis. The boxes show the 25-th, the 50-th and the 75-th percentile, while the whiskers indicate the 5th and 95th percentile. Black dots are outliers.

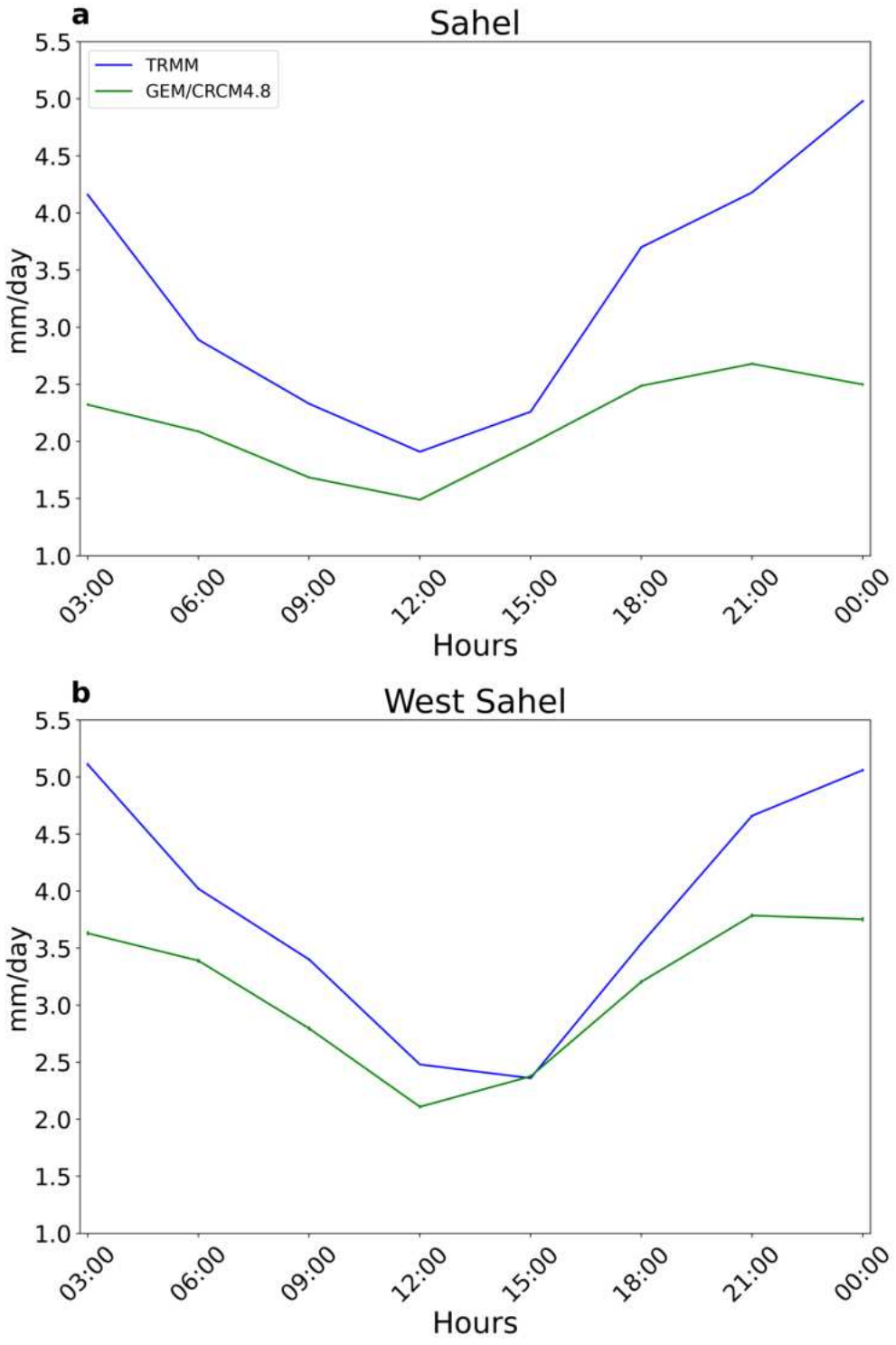

Figure B.30: Diurnal cycle. a) June-September (JJAS) diurnal cycle based on three hours of rainfall rates over the whole Sahelian region for the period 2000-2019. Blue line for TRMM data, green line for GEM/CRCM4.8 data. b) same as a) but for the western Sahel only.

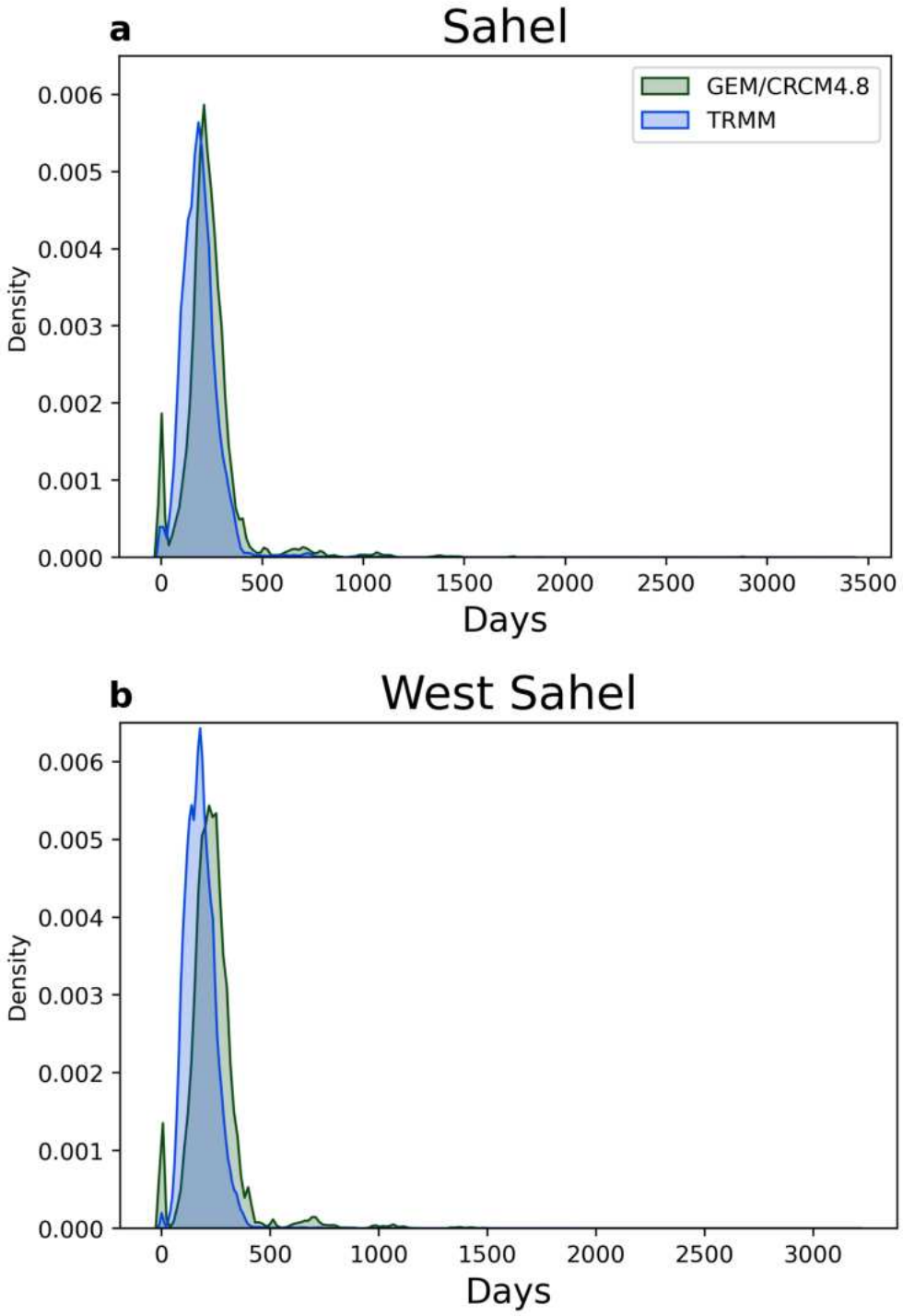

Figure B.31: Consecutive Dry Days distributions. a) Annual consecutive dry days (CDD) densities over the whole Sahelian region for the period 2000-2019. Blue line for TRMM data, green line for GEM/CRCM4.8 data. b) same as a) but for the western Sahel only.

Figure B.32: Map of Senegal. Credits: Google Map

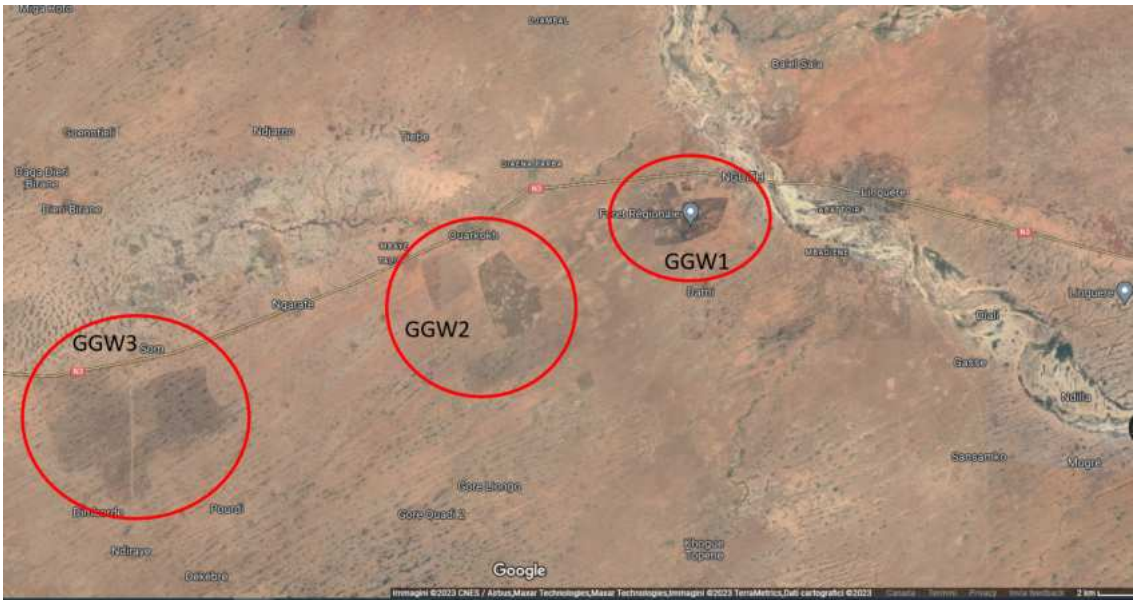

Figure B.33: The three reforested areas. Satellite image from Google Map of the three reforested areas.

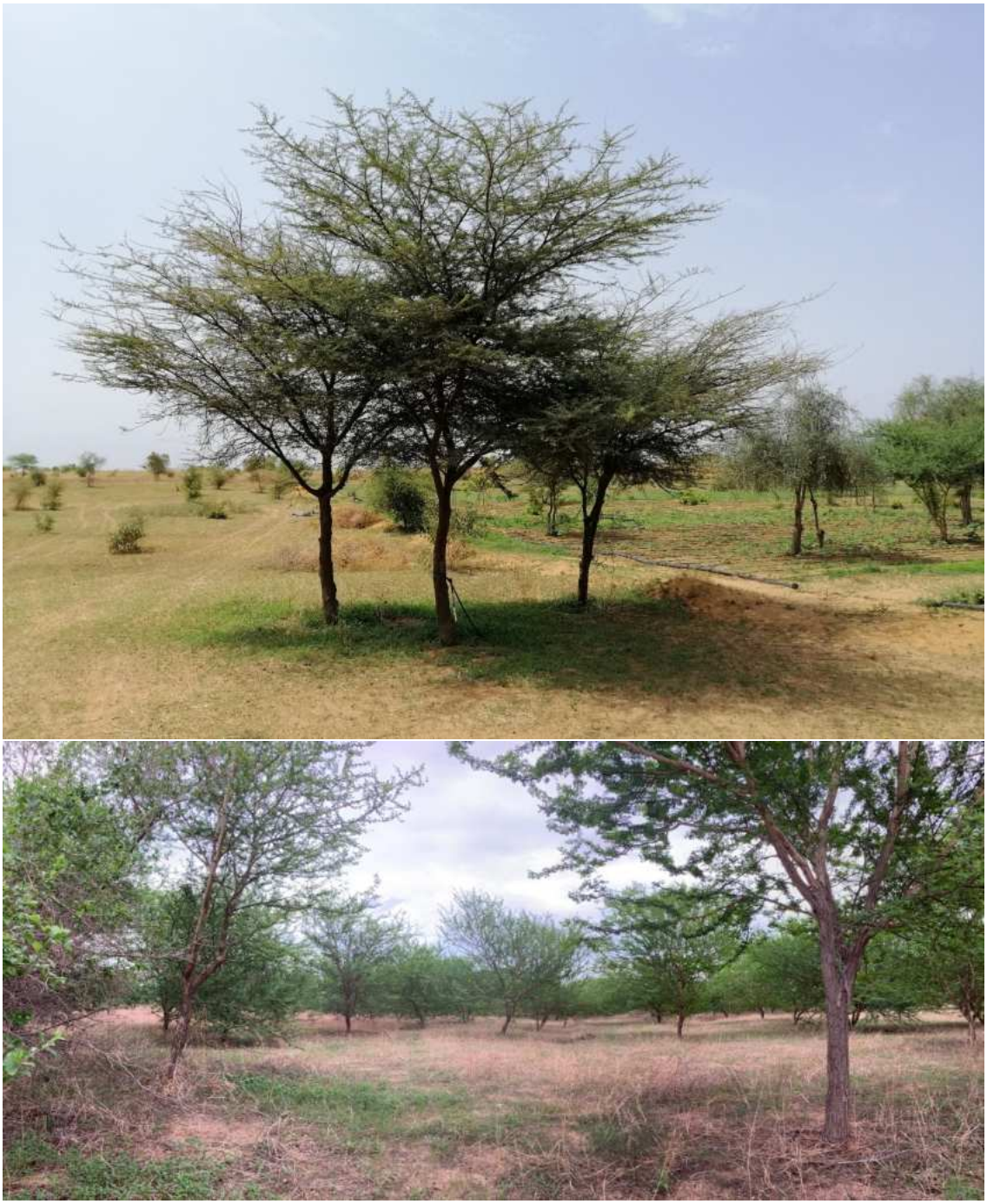

Figure B.34: Pictures from the GGW1 (top) and GGW2 (bottom) areas. Credits: Roberto Salustri

Figure B.35: Pictures from the GGW3 areas. In the figure on the bottom is possible to see an image of the area where areas with higher than 70% of the successful plantations are present in the right part of the area. Credits: Roberto Salustri

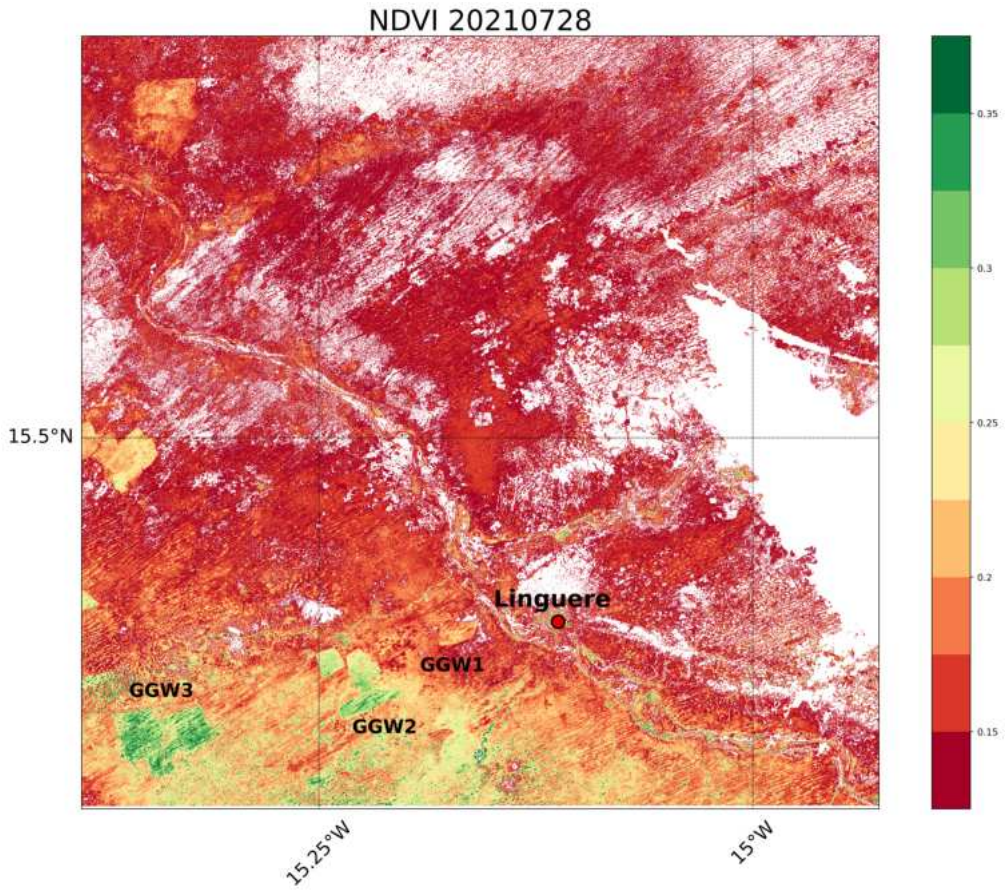

Figure B.36: NVDI index over the area around Linguère (Northern Senegal). It's possible to distinguish the three GGW areas: Dahra (left), Ouarkokh (GGW2) and Nguith (GGW1). Data from: `https://explorer.digitalearth.africa/products`

B.1 Note S1: Model comparison with CORDEX

The discrepancy between the temperature and precipitation means between the CORDEX ensemble and CRCM/GEM4.8 is also present if we look at the statistical distributions over the Sahel region. An underestimation of the Sahelian JJAS mean precipitation ($\sim$1.4 mm/day) from our model compared to CORDEX is clearly present in the PD (Fig. B.25), coherently with the results of Hernández-Díaz et al. (2013). This dry bias is exacerbated in the RCP8.5-only scenario with a difference of about 1.7 mm/day whereas in the RCP2.6-only is almost the same (1.3 mm/day). However, a similar range of values between the 5th and 95th percentiles in both PD and RCP8.5-only scenarios as well as the extreme values (values above the 5th and 95th percentile) is found, indicating an approximately general agreement between CRCM/GEM4.8 and the CORDEX ensemble looking at the whole distribution (Fig. B.27). In terms of temperature over the Sahel, CRCM/GEM4.8 exhibits a hotter anomaly of about 1°C-1.5°C compared to the CORDEX ensemble in both scenarios (Fig. B.26), with a larger concentration of higher temperature values in our model. Nevertheless, the distribution of the 90% of temperature mean values and the extreme values is almost comparable with the CORDEX ensemble (Fig. B.28) It should be noted that for RCP2.6 only three of the CORDEX models in Table S1 are provided: MIROC-MIROC5, MPI-M-MPI-ESM-LR, NCC-NorESM1-M.

B.2 Note S2: Project feasibility

In order to assess the feasibility of the project, we looked at ongoing actions over Sahel. In particular, we selected an area over northern Senegal where a clear example of a mosaic of different actions is present close to the small village of Linguère (Fig. B.32). Here, three different reforested areas have been built in the past years. Two as simple reforestation (GGW1 and GG2 in Fig. B.33) and one for economic purposes owned by the Asiyla Gum company (GGW3). GGW1, close to the village of Nguith, has an area of 350 hectares characterized by Acacia Senegalensis planted between 2011 and 2017 and is the youngest reforested area. No grazing is allowed in this area (Fig. B.34 top). GGW2 (Ouarkokh area) is characterised by three different zones of reforestation of 210, 362 and 368 hectares, respectively, planted between 2006 and 2010. Acacia Senegal is still the main species used for greening (Fig. B.34 bottom). Finally, GGW3 has an area of 1800 hectares close to Dahra (Fig. B.35). It was planted between 2006 and 2012 with Gum Arabica and it is owned by Asiyla Gum Company. The NVDI (Fig. B.36) shows a clear change in the vegetation greenness and density in the three GGW actions compared to the surrounding area with GGW1 showing lower values being the youngest forest. In particular, we can notice an NDVI of 0.1 – 0.25 in the areas surrounding the three areas, whereas values of up to 0.3-0.35 characterise the GGW2 and GGW3 areas. NVDI can be seen

as an indirect measure of albedo, being NDVI really anti-correlated to the surface albedo (Ma et al., 2011; Yuan, 2020; Zolfaghari et al., 2022).

APPENDIX C

SUPPLEMENTARY MATERIAL CHAPTER 3

Table C.1: Saffir-Simpson scale for tropical cyclone categories defined by the minimum central pressure.

Classification	Minimum central pressure (hPa)
Tropical Storm	1005-995
Category 1	995-980
Category 2	980-965
Category 3	965-945
Category 4	945-920
Category 5	< 920

Table C.2: ITCZ latitude index for the northern Hemisphere according the ITCZ centroid method developed by Adam et al. 2016 for the northern Hemisphere.

Experiment	ITCZ location (°N)
PD	4.13
RCP8.5-only	4.14
$GGW_{LOW8.5}$	4.14
$GGW_{MED8.5}$	4.15
$GGW_{HIGH8.5}$	4.14
$GGW_{EXT8.5}$	4.15
RCP2.6-only	4.13
$GGW_{LOW2.6}$	4.13
$GGW_{MED2.6}$	4.13
$GGW_{HIGH2.6}$	4.13
$GGW_{EXT2.6}$	4.14

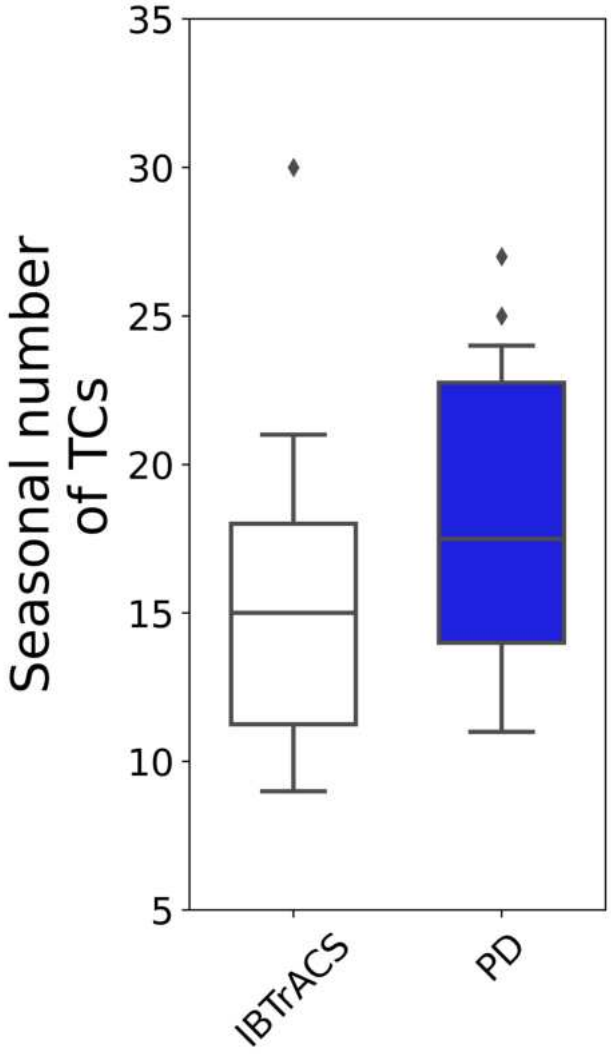

Figure C.1: Seasonal number of Tropical Cyclones over North-Atlantic. Comparison for the seasonal number of North-Atlantic tropical cyclones between observations (IBTrACS, white boxplot) and the model Present Day (blue boxplot) between June and November for the period 1990-2019. Boxplots show the median (black line), the quartiles (the box), the 5-95-th percentiles (the wiskers) and outliers (dots).

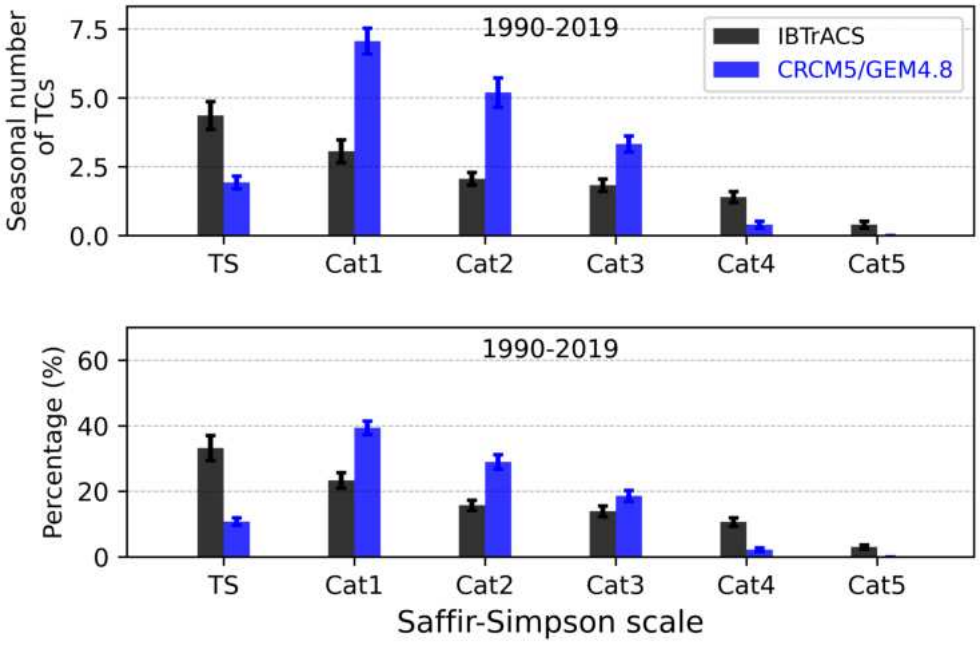

Figure C.2: Seasonal number of Tropical Cyclones for each category and relative percentages. Top) Comparison for the seasonal (JJASON) number of tropical cyclones between the observations (black bars) and the Present-Day experiment (blue bars) for different categories. Bottom) Same as above but in terms of percentages. The Saffir-Simpson scale is defined according to the low atmospheric pressure thresholds (see table C.1). Error bars indicate the standard error.

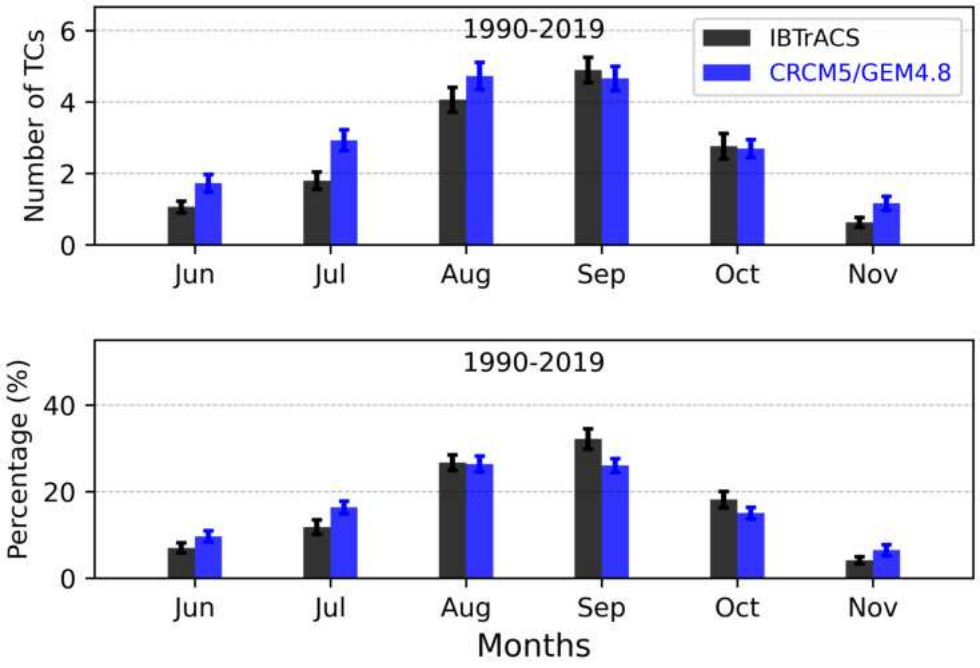

Figure C.3: Seasonal number of Tropical Cyclones for each month and relative percentages. Top) Comparison for the seasonal (JJASON) number of tropical cyclones between the observations (black bars) and the Present-Day experiment (blue bars) for different months. Bottom) Same as above but in terms of percentages. Error bars indicate the standard error.

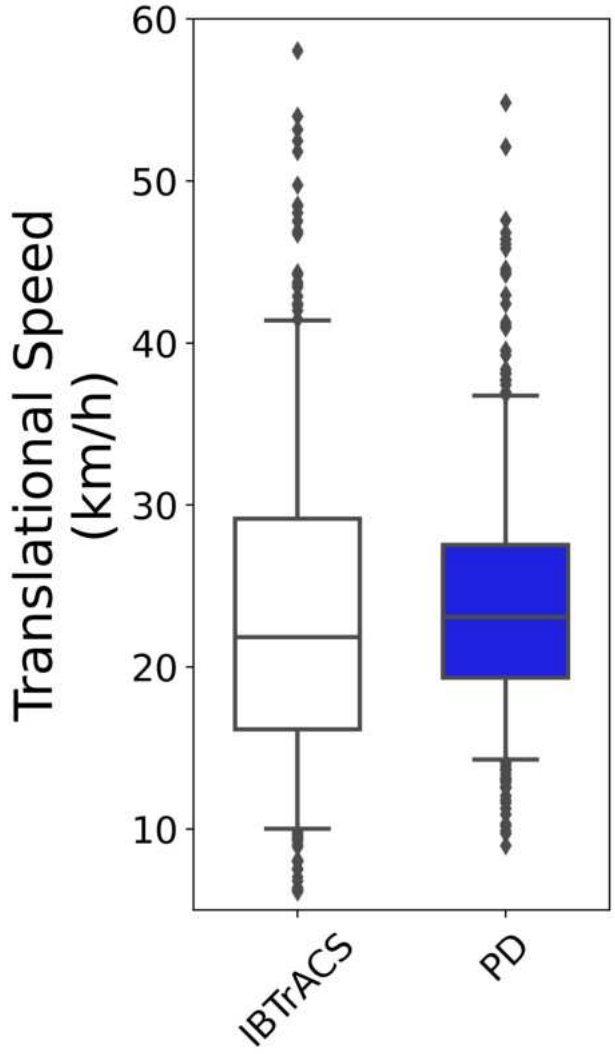

Figure C.4: Translation speed boxplots. Comparison for the translation speed between observations (IBTrACS, white boxplot) and the model Present Day (blue boxplot) between June and November for the period 1990-2019. Boxplots show the median (black line), the quartiles (the box), the 5-95-th percentiles (the wiskers) and outliers (dots).

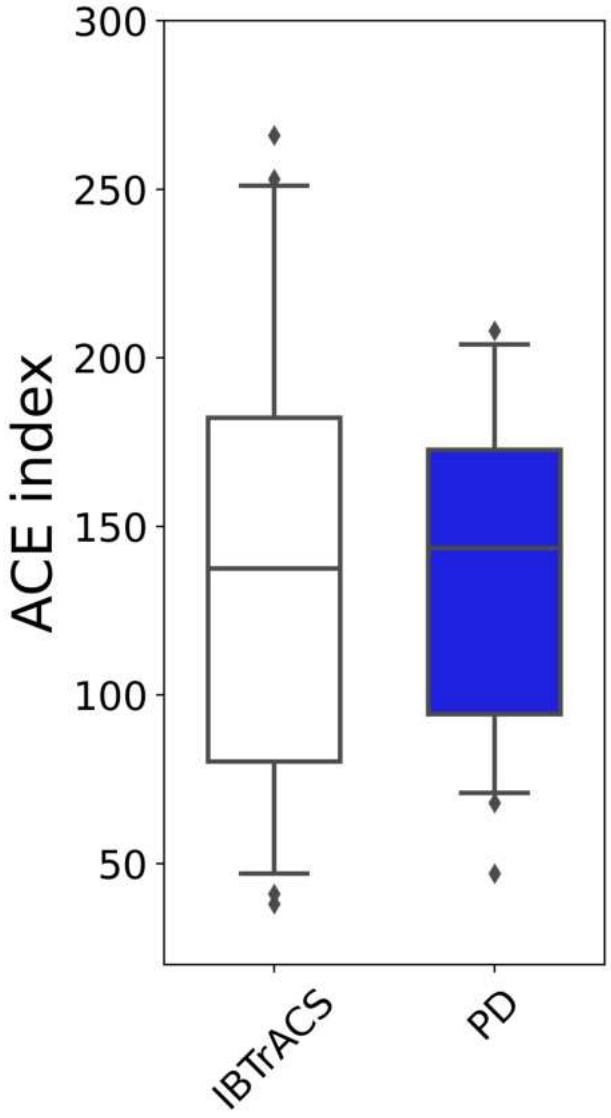

Figure C.5: Accumulated cyclone energy (ACE) boxplots. Comparison for the ACE between observations (IBTrACS, white boxplot) and the model Present Day (blue boxplot) between June and November for the period 1990-2019. Boxplots show the median (black line), the quartiles (the box), the 5-95-th percentiles (the wiskers) and outliers (dots).

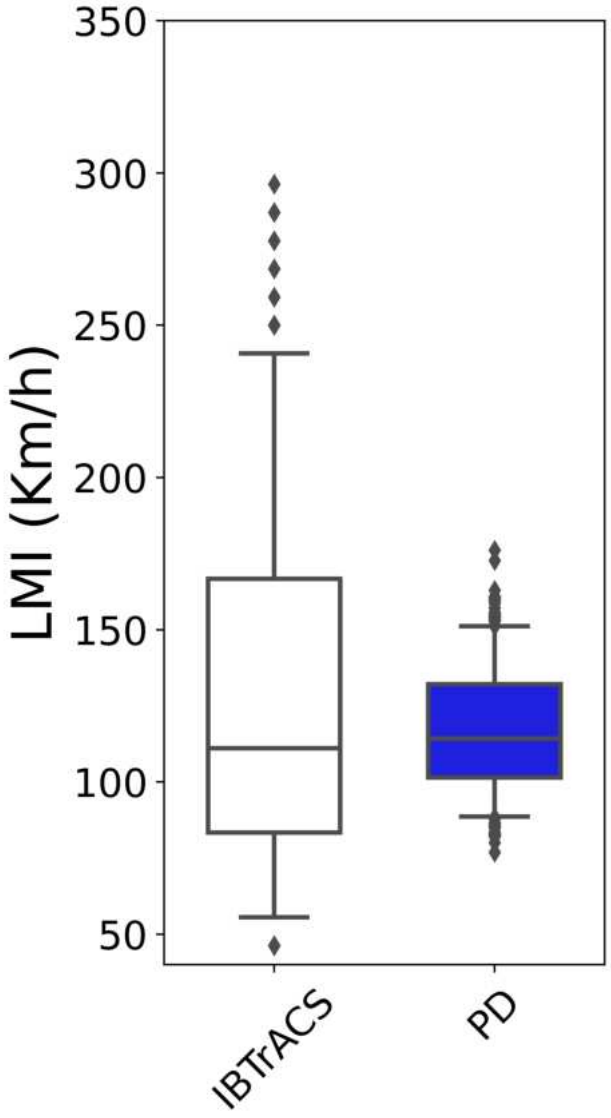

Figure C.6: Lifetime maximum intensity (LMI) boxplots. Comparison for the LMI between observations (IBTrACS, white boxplot) and the model Present Day (blue boxplot) between June and November for the period 1990-2019. Boxplots show the median (black line), the quartiles (the box), the 5-95-th percentiles (the wiskers) and outliers (dots).

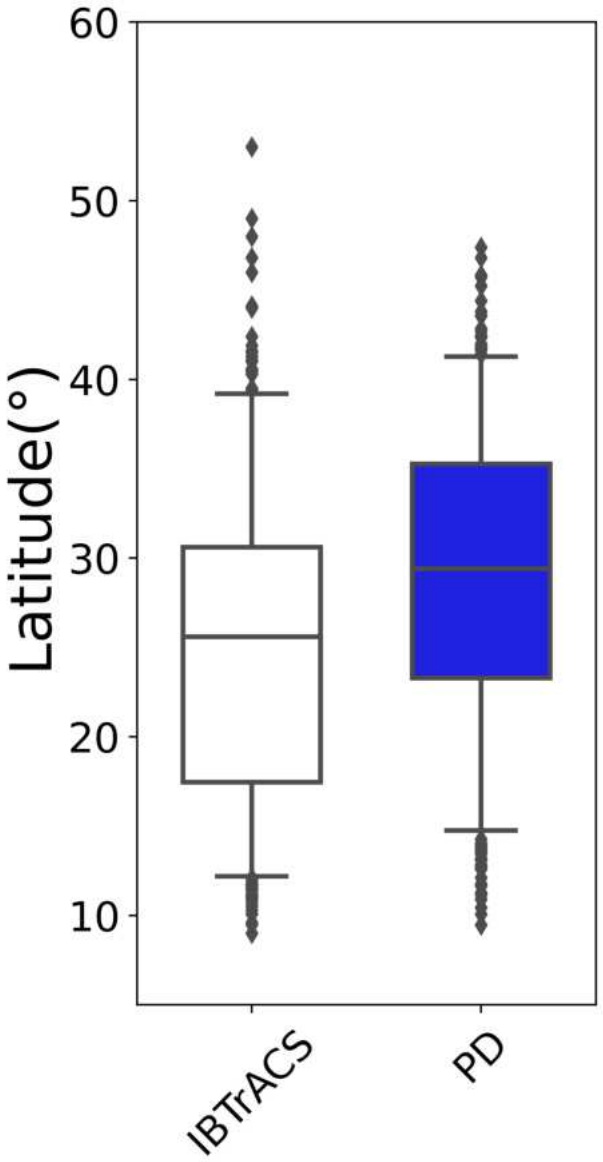

Figure C.7: Lifetime maximum intensity (LMI) location boxplots. Comparison for the LMI location between observations (IBTrACS, white boxplot) and the model Present Day (blue boxplot) between June and November for the period 1990-2019. Boxplots show the median (black line), the quartiles (the box), the 5-95-th percentiles (the wiskers) and outliers (dots).

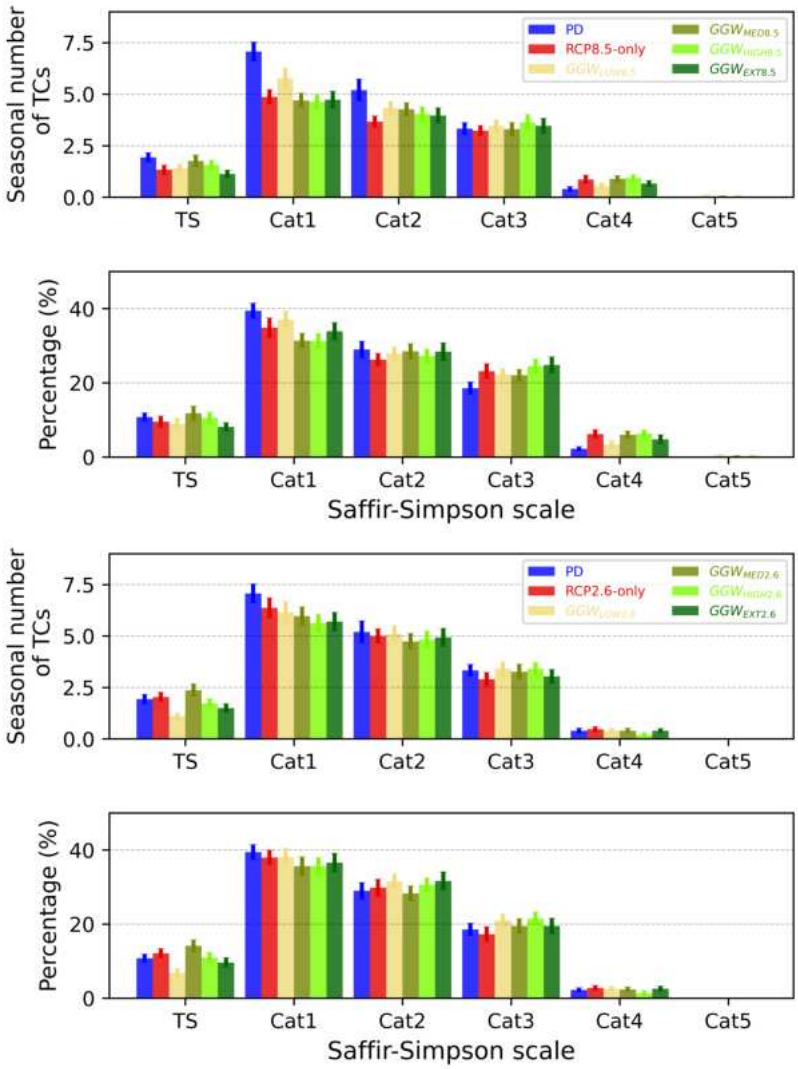

Figure C.8: Seasonal number of Tropical Cyclones for each category and relatively percentages. Left-top) Comparison for the seasonal (JJASON) number of tropical cyclones among the Present-Day experiment (blue), the RCP8.5-only (red), GGW_{LOW} (yellow), GGW_{MED} (olive green), GGW_{HIGH} (light green) and GGW_{EXT} (dark green) experiments for different categories. Left bottom) Same as left-above but in terms of percentages. The Saffir-Simpson scale is defined according to the low atmospheric pressure thresholds (see table S1). Error bars indicate the standard error. Right) Same as in the left column but with RCP2.6 scenario.

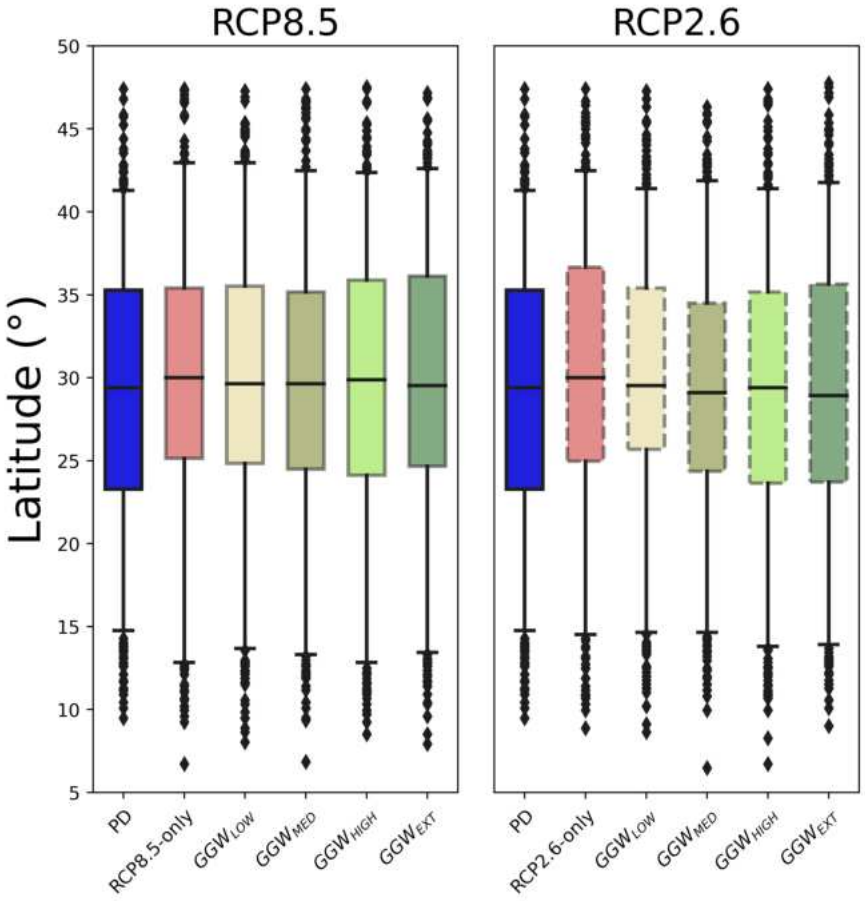

Figure C.9: Lifetime maximum intensity (LMI) location boxplots for all experiments. Left) LMI comparison among the Present-Day experiment (blue), the RCP-only (red), GGW_{LOW} (yellow), GGW_{MED} (olive green), GGW_{HIGH} (light green) and GGW_{EXT} (dark green) experiments between June and November for the period 1990-2019. RCP8.5 experiments are in the left panel, while RCP2.6 are in the right panel. Boxplots show the median (black line), the quartiles (the box), the 5-95-th percentiles (the wiskers) and outliers (dots).

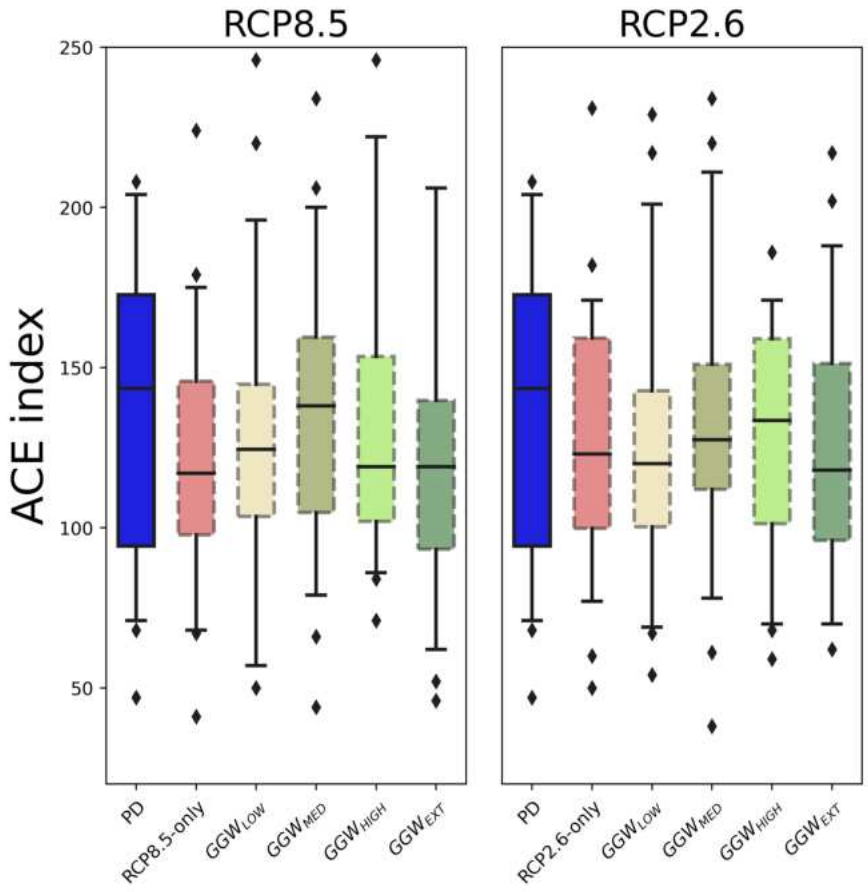

Figure C.10: Accumulated cyclone energy (ACE) boxplots. Left). Seasonal ACE comparison among the Present-Day experiment (blue), the RCP-only (red), GGW_{LOW} (yellow), GGW_{MED} (olive green), GGW_{HIGH} (light green) and GGW_{EXT} (dark green) experiments between June and November for the period 1990-2019. RCP8.5 experiments are in the left panel, while RCP2.6 are in the right panel. Boxplots show the median (black line), the quartiles (the box), the 5-95-th percentiles (the wiskers) and outliers (dots). Dotted boxes show not significantly differencies at 5% significance level.

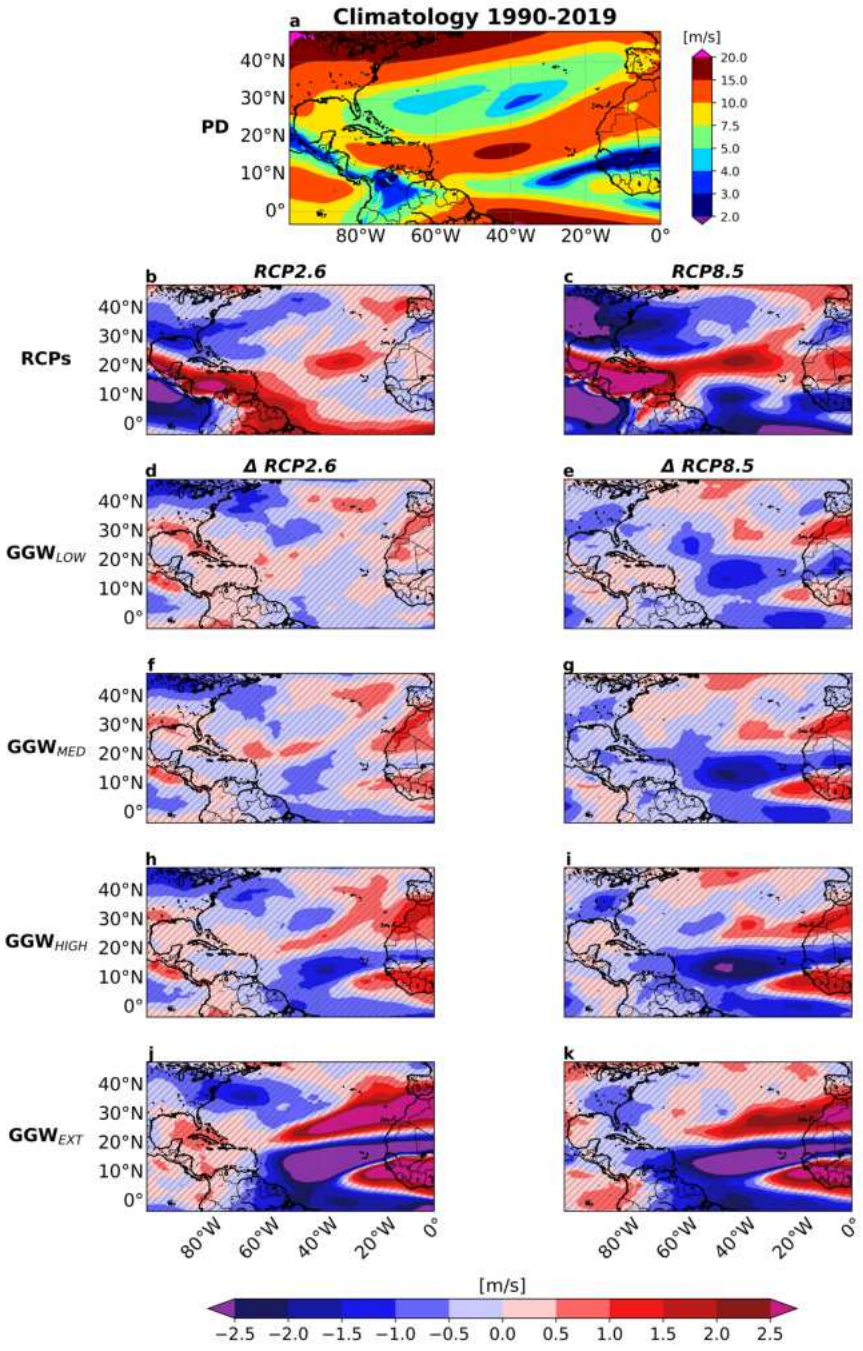

Figure C.11: Wind shear. a) 200-750 hPa wind shear climatology for the PD experiment between June and November for the period 1990-2019. Change in mean wind shear for RCP2.6-only (b) and RCP8.5-only (c) relatively to PD. Change in mean potential intensity for GGW_{LOW} (d-e), GGW_{MED} (f-g) GGW_{HIGH} (h,i) and GGW_{EXT} (j,k) relatively to RCP2.6-only and RCP8.5-only experiments. Hatches indicate values that are not significantly different at the 5% significance level using a local (grid-point) Wilcoxon signed-rank test.

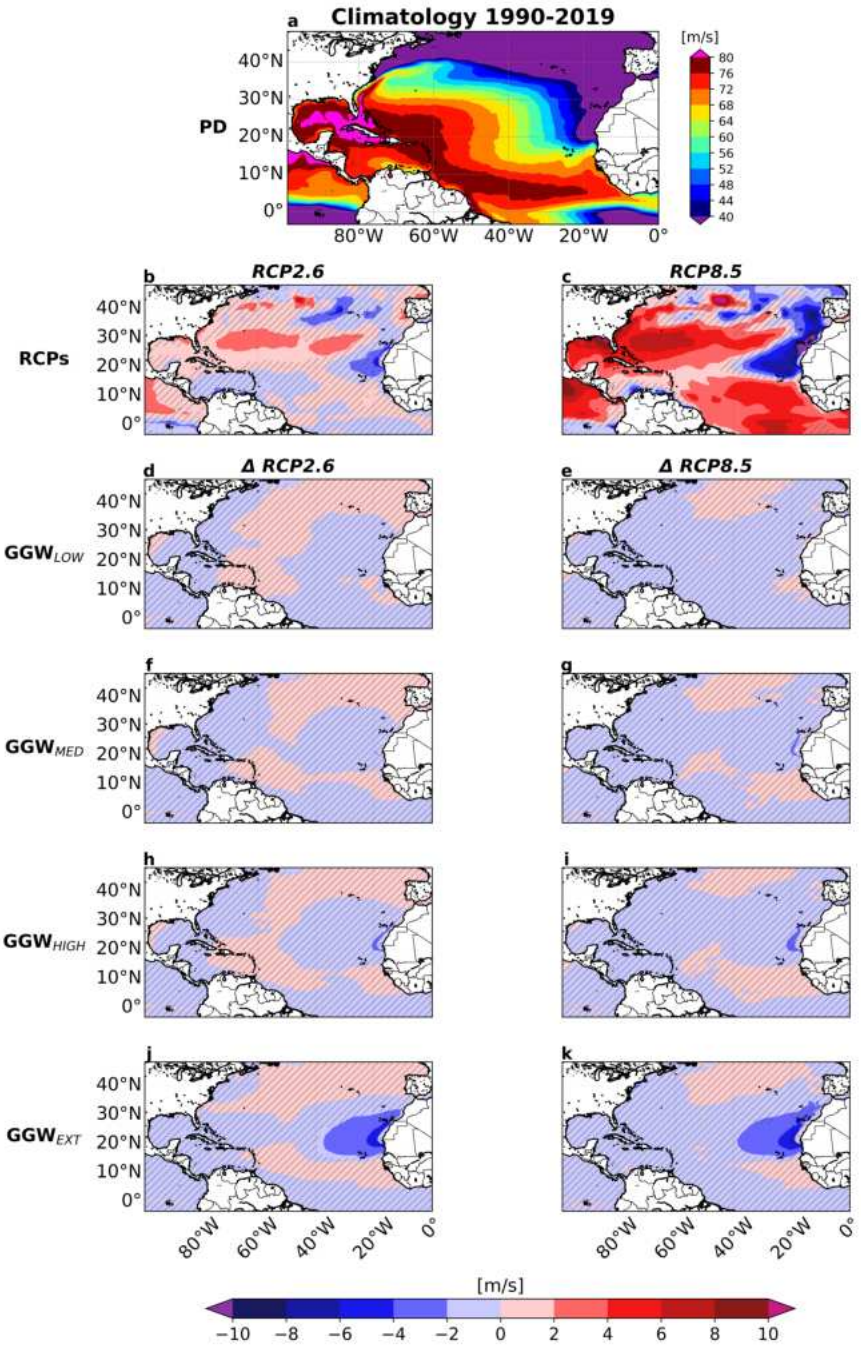

Figure C.12: Potential intensity. a) Potential intensity climatology for the PD experiment between June and November for the period 1990-2019. Change in mean potential intensity for RCP2.6-only (b) and RCP8.5-only (c) relatively to PD. Change in mean potential intensity for GGW_{LOW} (d-e), GGW_{MED} (f-g) GGW_{HIGH} (h,i) and GGW_{EXT} (j,k) relatively to RCP2.6-only and RCP8.5-only experiments. Hatches indicate values that are not significantly different at the 5% significance level using a local (grid-point) Wilcoxon signed-rank test.

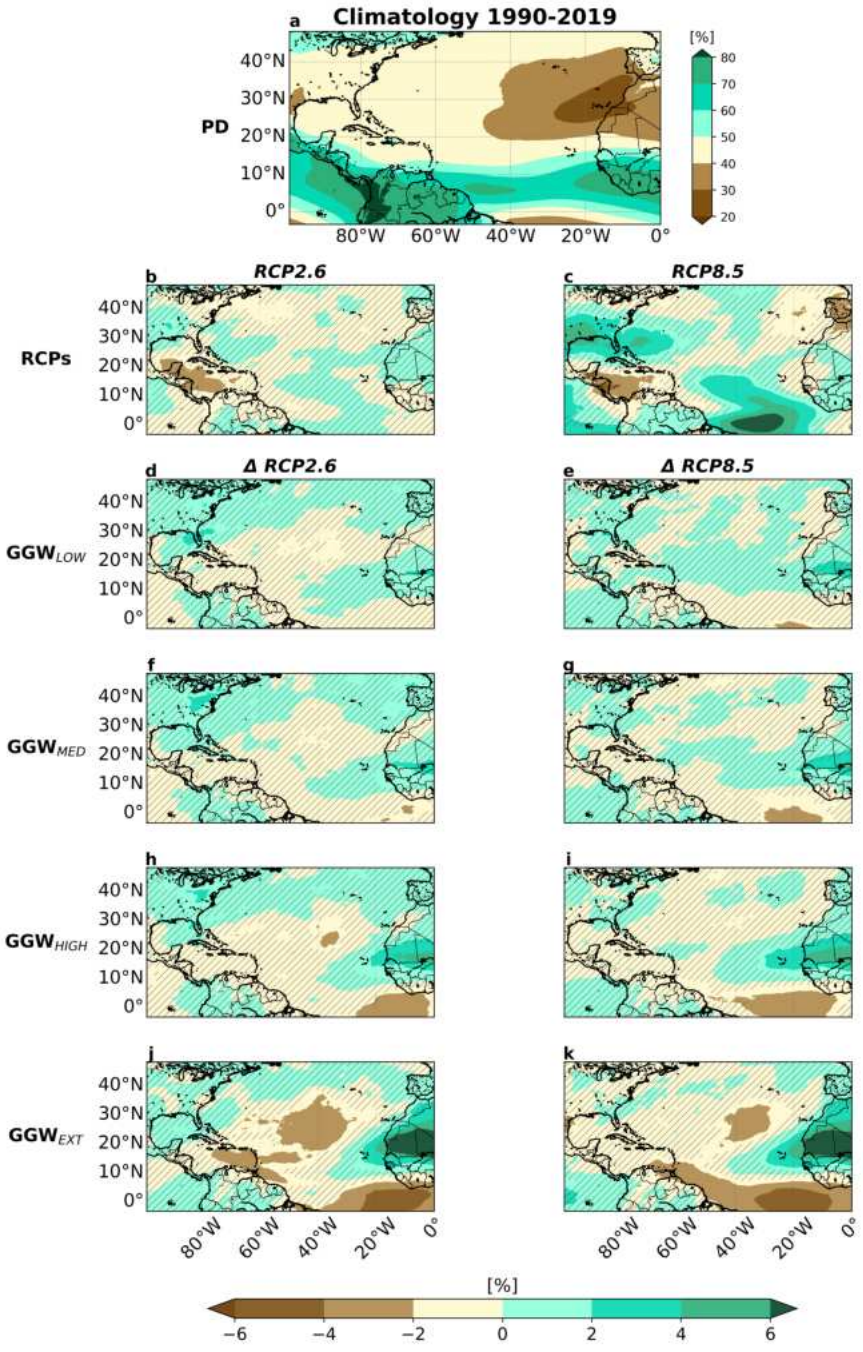

Figure C.13: Relative humidity. a) Relative humidity at 700hPa climatology for the PD experiment between June and November for the period 1990-2019. Change in mean relative humidity for RCP2.6-only (b) and RCP8.5-only (c) relatively to PD. Change in mean potential intensity for GGW_{LOW} (d-e), GGW_{MED} (f-g) GGW_{HIGH} (h,i) and GGW_{EXT} (j,k) relatively to RCP2.6-only and RCP8.5-only experiments. Hatches indicate values that are not significantly different at the 5% significance level using a local (grid-point) Wilcoxon signed-rank test.

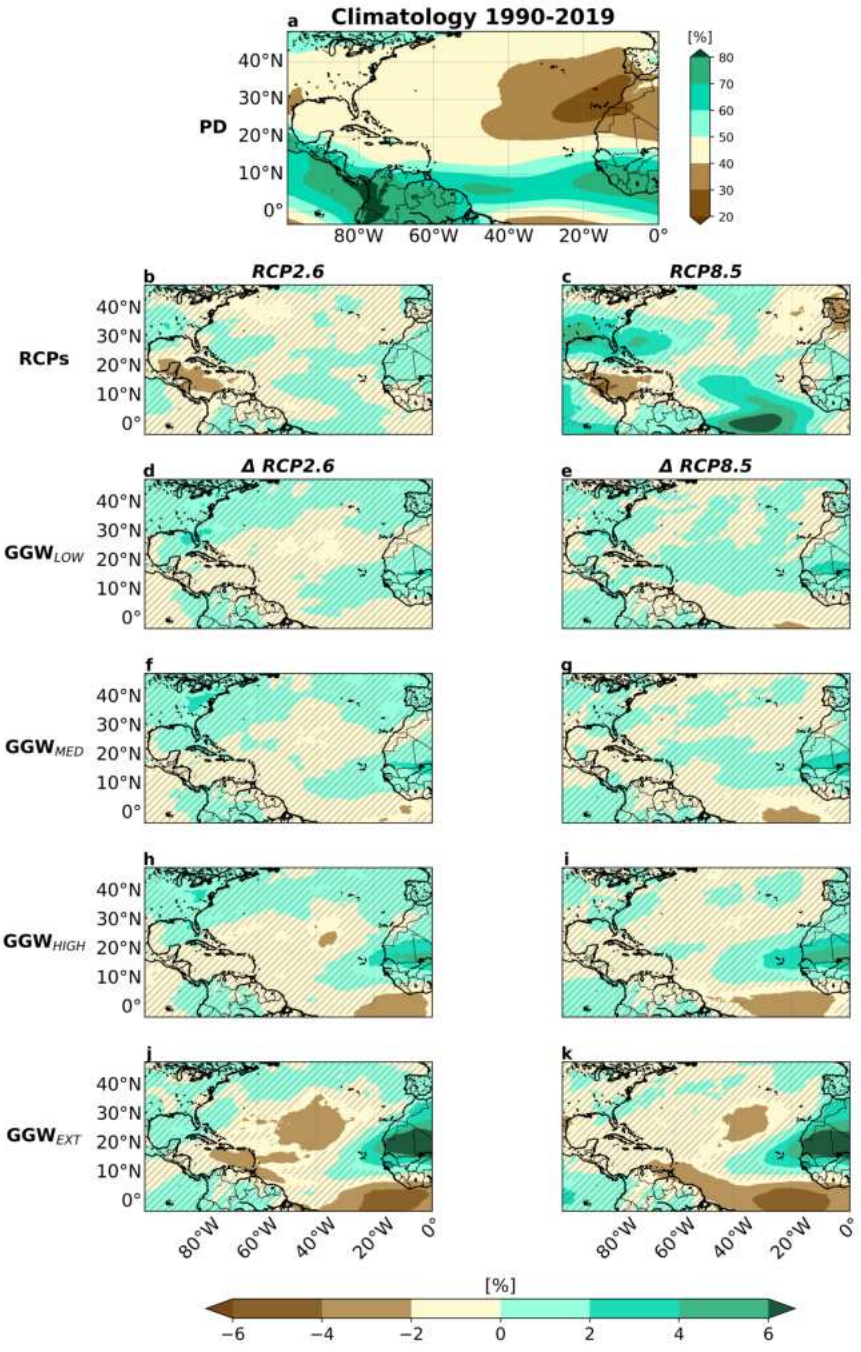

Figure C.14: Absolute vorticity. a) Absolute vorticity at 850hPa climatology for the PD experiment between June and November for the period 1990-2019. Change in mean absolute vorticity for RCP2.6-only (b) and RCP8.5-only (c) relatively to PD. Change in mean potential intensity for GGW_{LOW} (d-e), GGW_{MED} (f-g) GGW_{HIGH} (h,i) and GGW_{EXT} (j,k) relatively to RCP2.6-only and RCP8.5-only experiments. Hatches indicate values that are not significantly different at the 5% significance level using a local (grid-point) Wilcoxon signed-rank test.

APPENDIX D

SUPPLEMENTARY MATERIAL CHAPTER 4

D.1 Analysis of residuals: initial displacements

The initial displacement model uses only steering winds and the Coriolis parameter as predictors. The correlation between the residuals of the North Atlantic initial zonal and meridional displacements is close to zero (-0.009, Fig.D.2, bottom) confirming no significant correlation between those two components. No correlations are found between the residuals of the initial displacements and latitude/longitude values except for a significant negative correlation between longitude and the zonal displacement residuals (-0.219) (Fig.D.2 top and middle). These relationships show greater variance in the distributions compared to those involving all residuals of zonal and meridional displacements. This is expected as the initial displacement modules are trained on only two predictors based on much smaller samples.

No notable spatial patterns are found in either basins (Fig.D.3). The bias is larger compared to the other observed biases reaching 0.4-0.5 in absolute value. As previously mentioned, similar performances of the initial displacement modules are expected, given the limitations of the model due to the missing previous displacements.

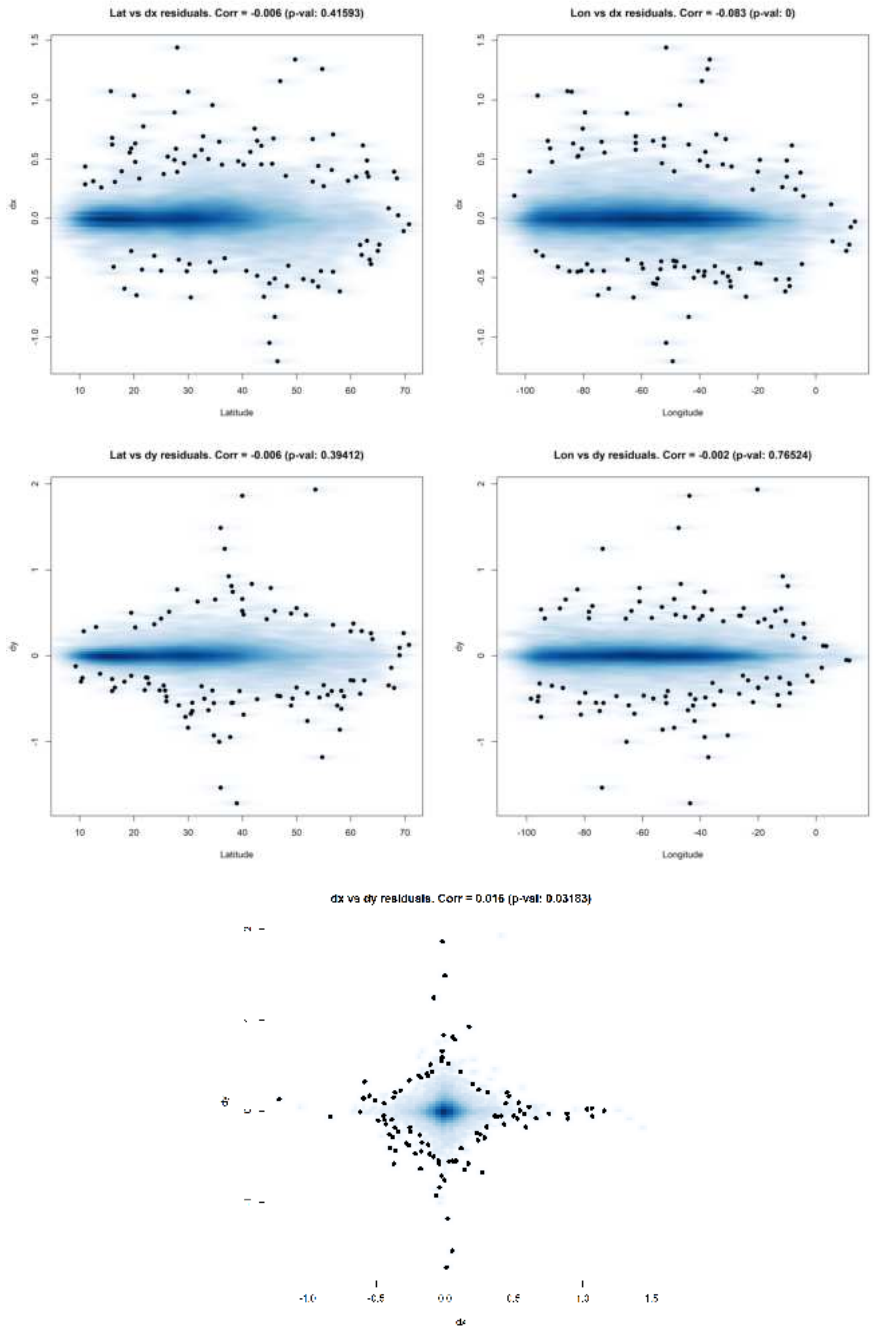

Figure D.1: Residuals of zonal and meridional displacements over North Atlantic. Scatterplots of top) zonal displacement residuals vs latitude and longitude values, middle) meridional displacement residuals vs latitude and longitude values and bottom) zonal vs meridional displacements residuals with their relative correlations and associated p-values for North Atlantic. p-values of each correlation are shown in brackets.

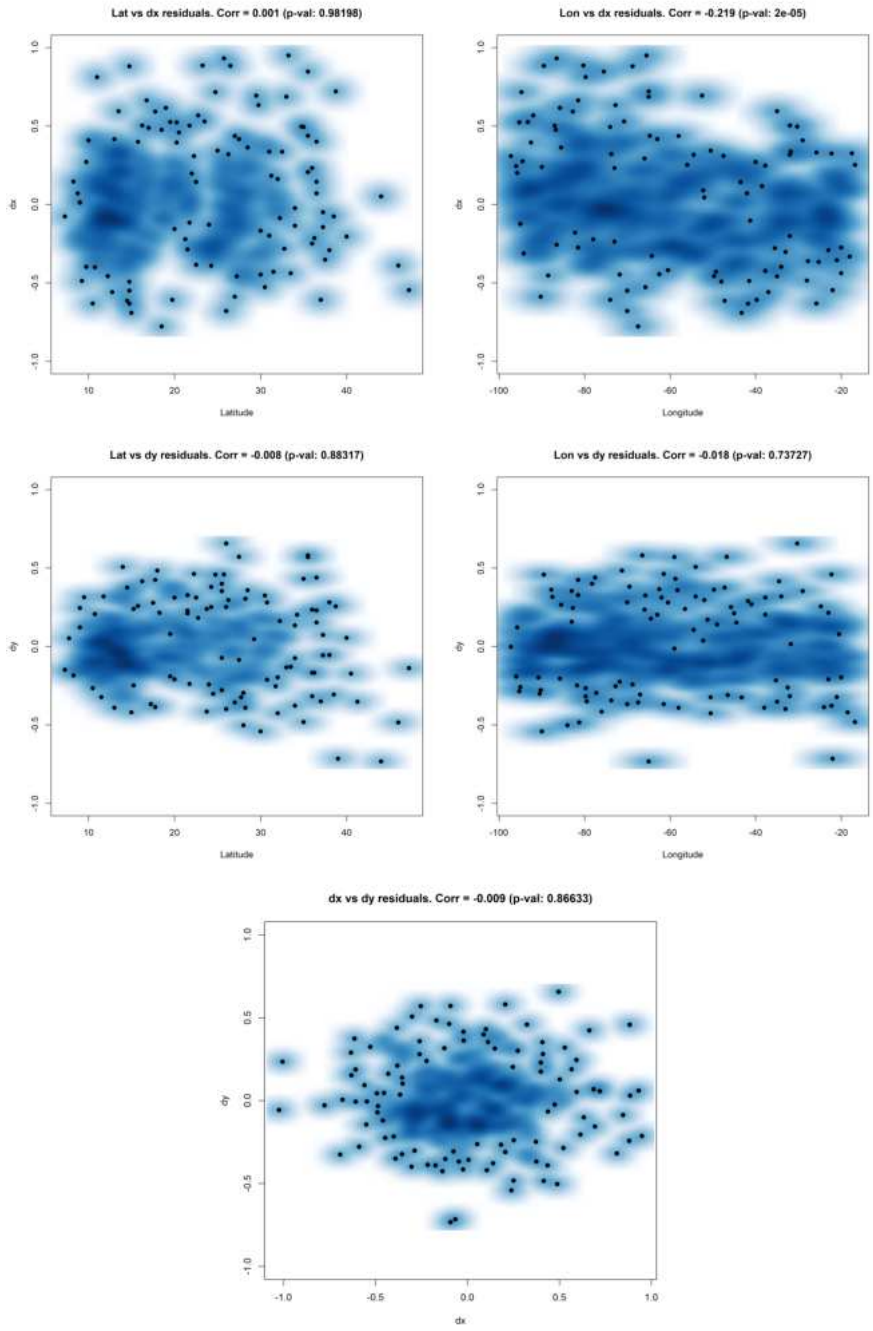

Figure D.2: Residuals of zonal and meridional initial displacements over North Atlantic. Scatterplots of top) zonal initial displacement residuals vs latitude and longitude values, middle) meridional initial displacement residuals vs latitude and longitude values and bottom) zonal vs meridional initial displacements residuals with their relative correlations and associated p-values for North Atlantic. p-values of each correlation are shown in brackets.

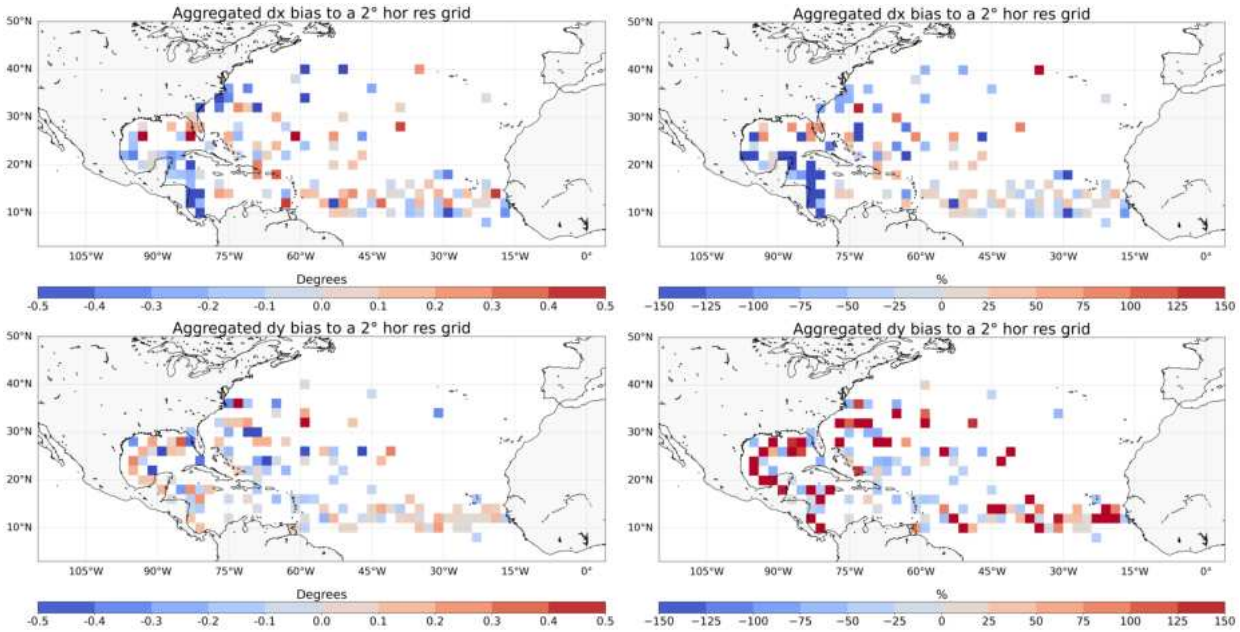

Figure D.3: Maps of zonal and meridional initial displacement residuals over North Atlantic. Maps of North Atlantic zonal (top) and meridional (bottom) initial displacements residuals in degrees (left) and percentage (right).

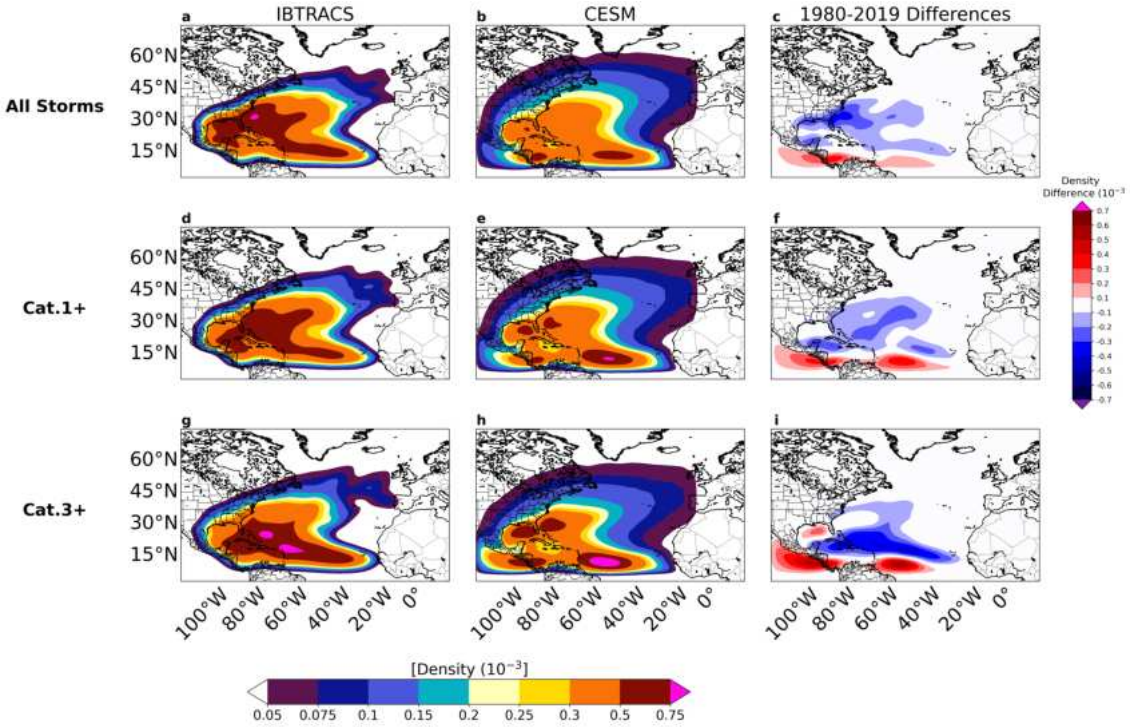

Figure D.4: Difference in North Atlantic TC density between observations and RV-CESM. JJASON TC density for the period 1980-2019 for a,d,g) IBTrACS and b,e,h) RV-CESM model and c,f,i) and difference in TC density for the RV-CESM version relatively to observations. Top row) all storms, Middle row) Cat1+ and Bottom row) major storms.

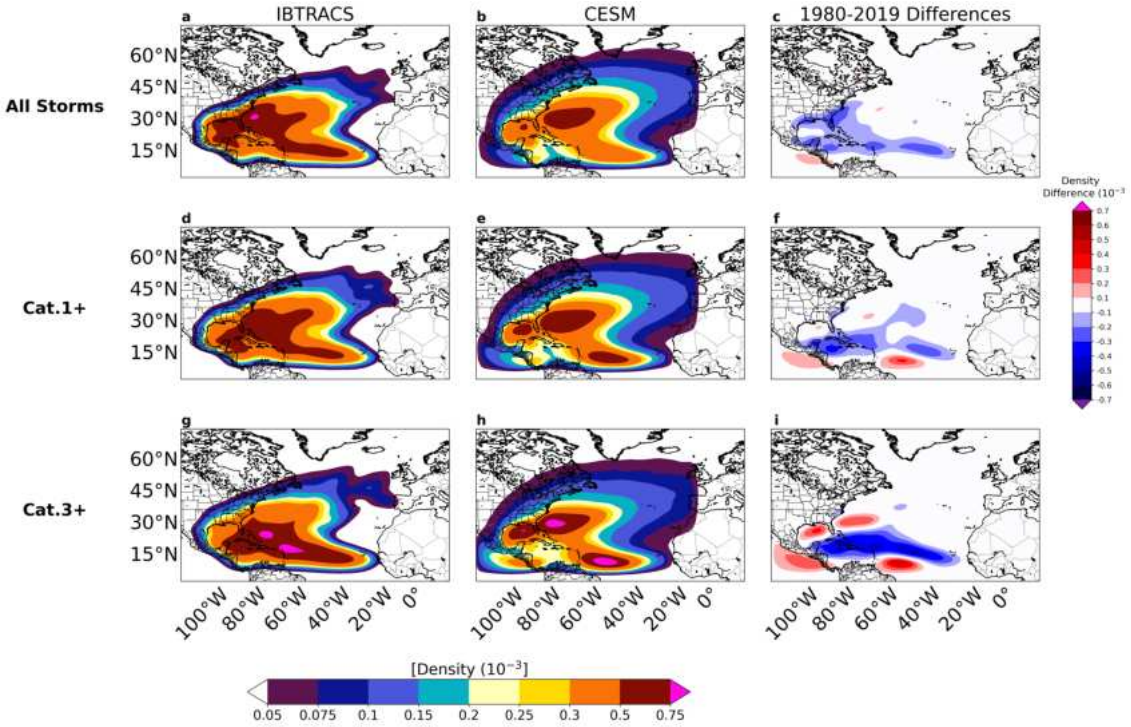

Figure D.5: Difference in North Atlantic TC density between observations and AV-CESM. JJASON TC density for the period 1980-2019 for a,d,g) IBTrACS and b,e,h) AV-CESM model and c,f,i) and difference in TC density for the AV-CESM version relatively to observations. Top row) all storms, Middle row) Cat1+ and Bottom row) major storms.

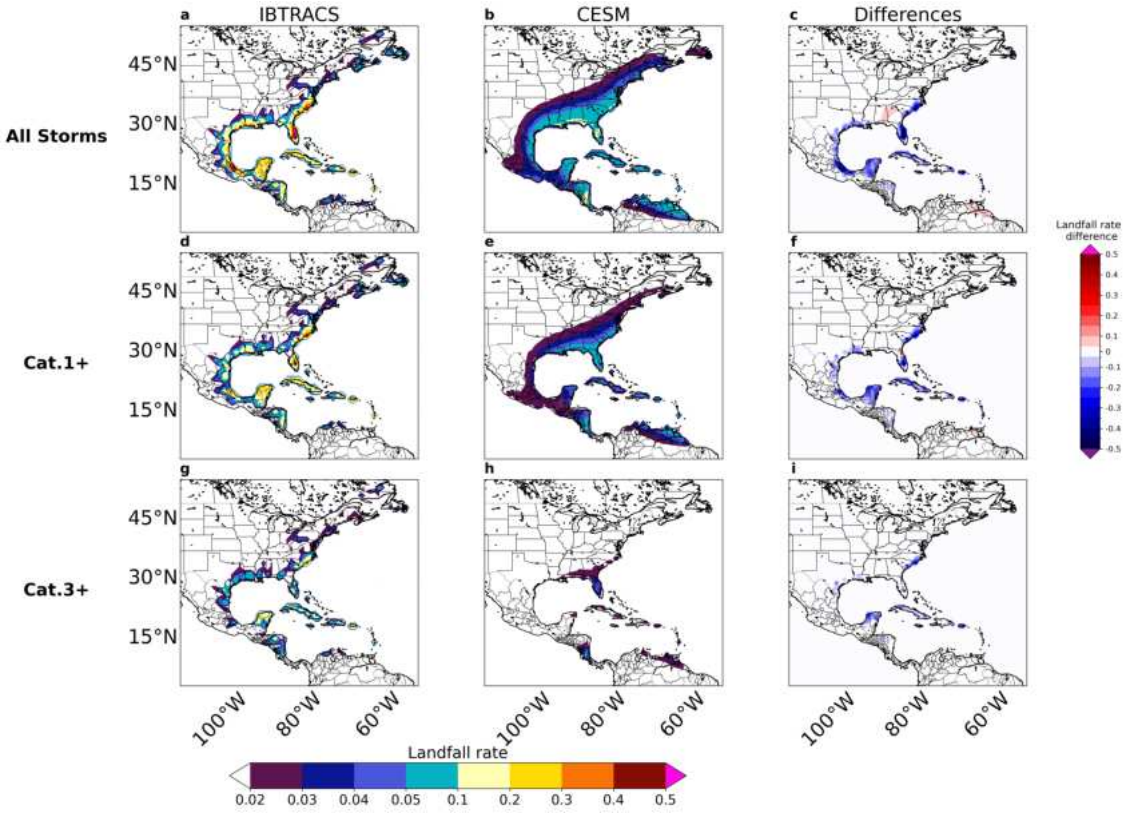

Figure D.6: Difference in North Atlantic TC landfall rates between observations and RV-CESM. JJASON TC landfall rates for the period 1980-2019 for a,d,g) IBTrACS and b,e,h) RV-CESM model and c,f,i) and difference in TC landfall rates for the RV-CESM version relatively to observations. Top row) all storms, Middle row) Cat.1+ and Bottom row) major storms.

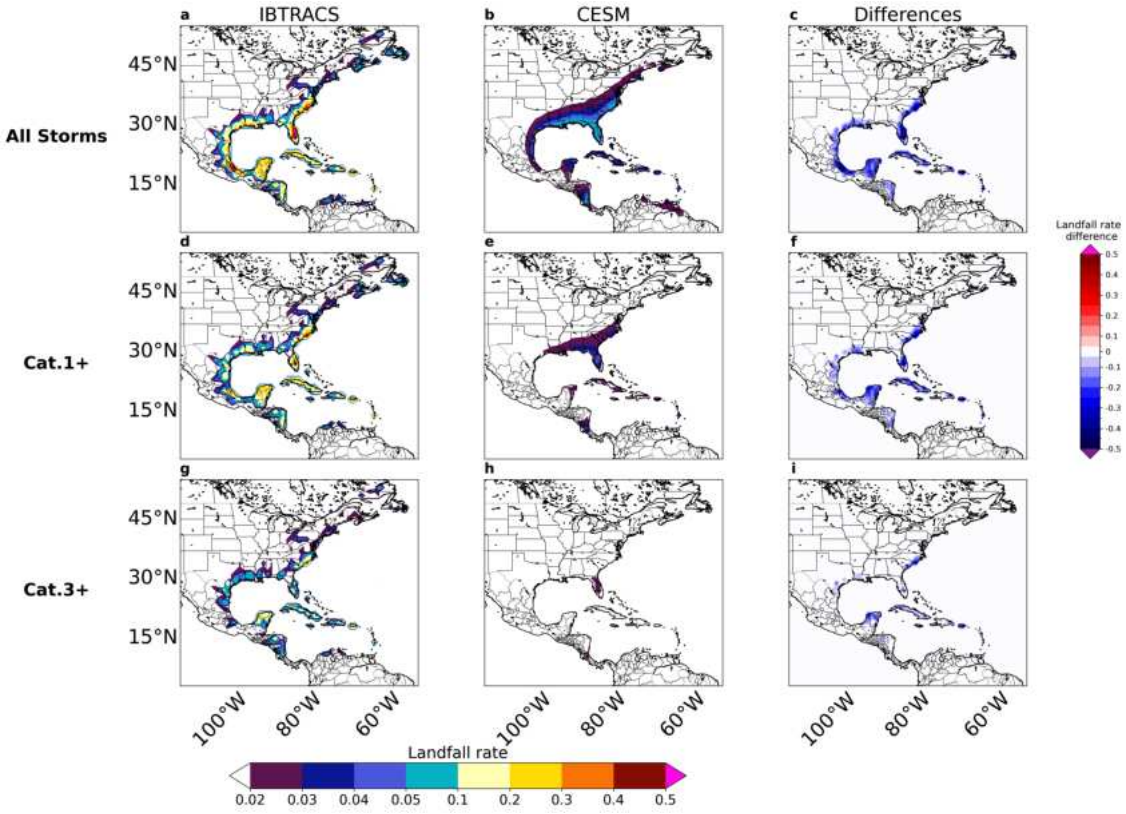

Figure D.7: Difference in North Atlantic TC landfall rates between observations and AV-CESM. JJASON TC landfall rates for the period 1980-2019 for a,d,g) IBTrACS and b,e,h) AV-CESM model and c,f,i) and difference in TC landfall rates for the AV-CESM version relatively to observations. Top row) all storms, Middle row) Cat.1+ and Bottom row) major storms.

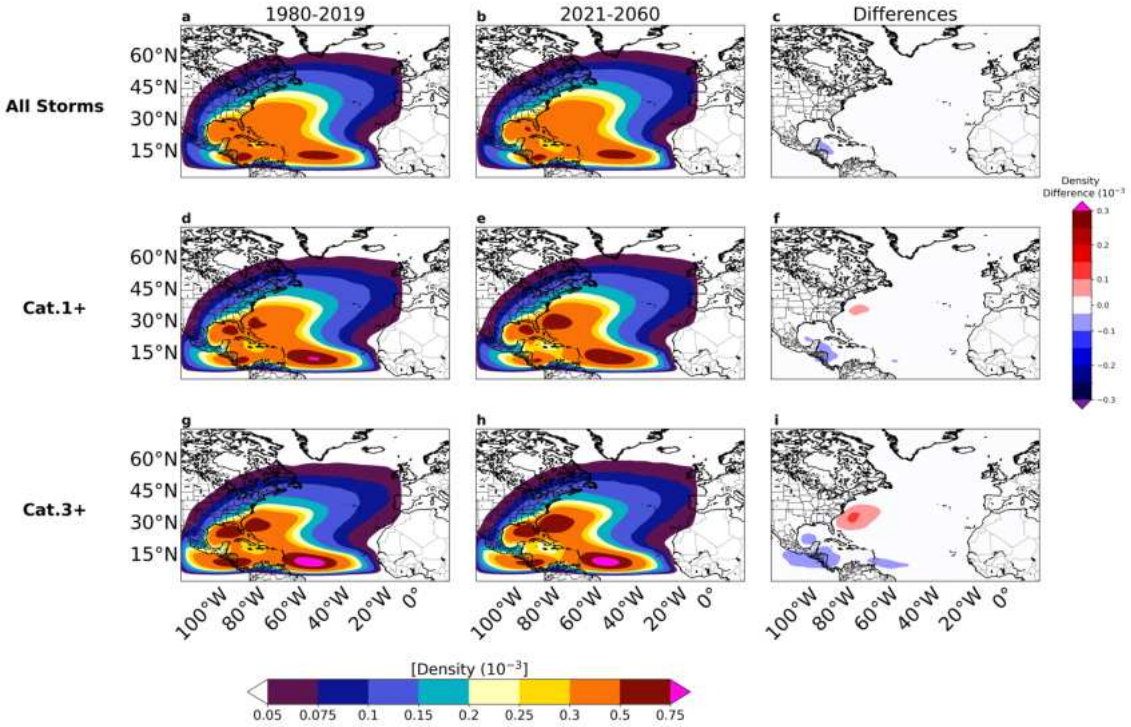

Figure D.8: Future change in North Atlantic JJASON TC density. TC density for the period a,d,g) 1980-2019 and b,e,h) 2021-2060 and c,f,i) change in TC density for the RV-CESM version relative to observations. Top row) all storms, Middle row) Cat.1+ and Bottom row) major storms.

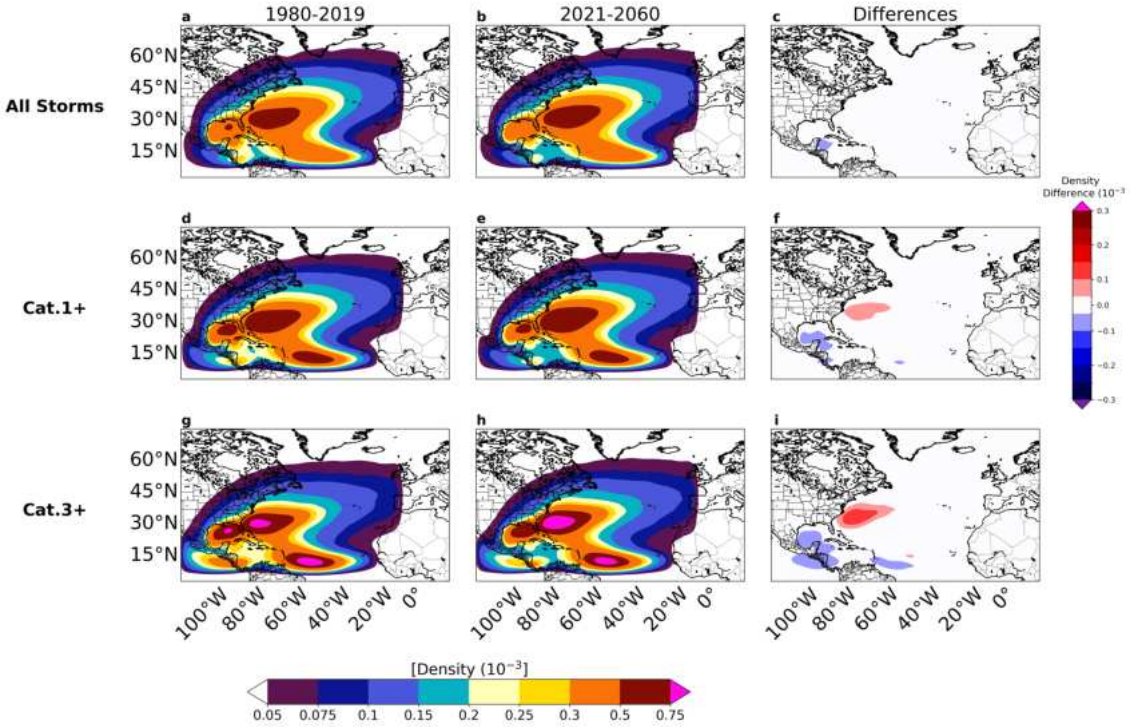

Figure D.9: Future change in North Atlantic JJASON TC density. TC density for the period a,d,g) 1980-2019 and b,e,h) 2021-2060 and c,f,i) change in TC density for the AV-CESM version relative to observations. Top row) all storms, Middle row) Cat.1+ and Bottom row) major storms.

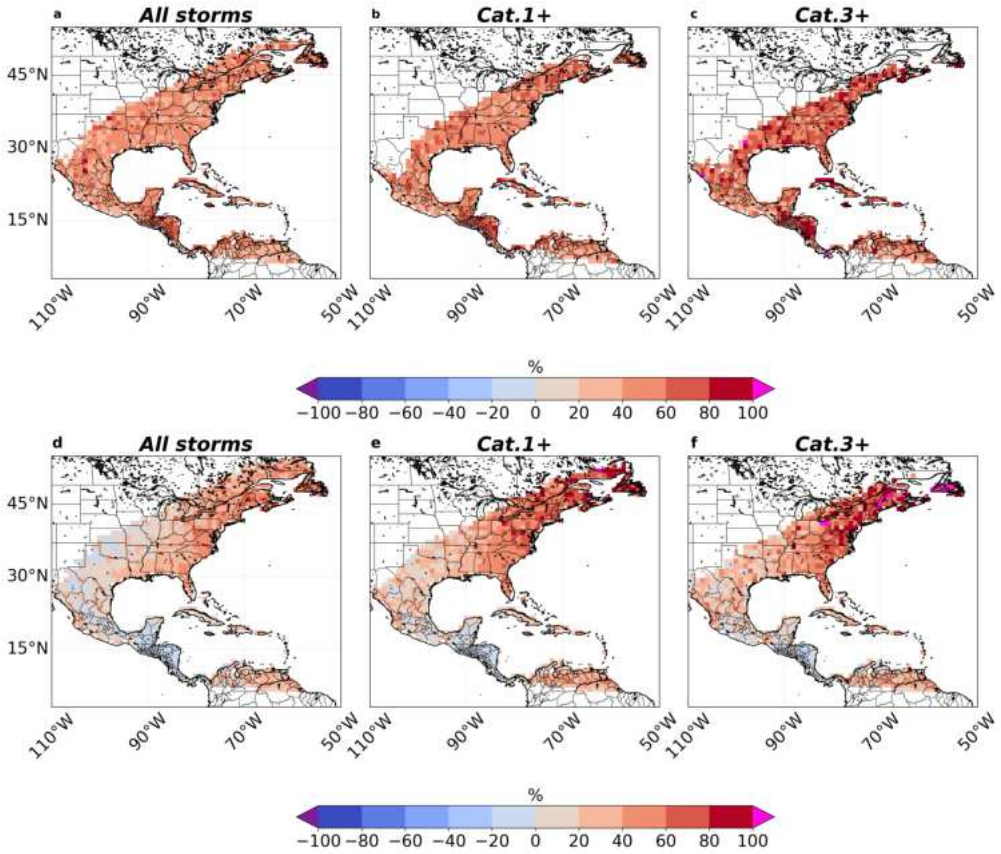

Figure D.10: Change in North Atlantic landfall rates. a-c) Change (%) in landfall rates over in North Atlantic for the period 2010-2030 relatively to 1980-2000 for a) all storms, b) Cat.1+ and c) major storms in RV-CESM. d-f) Same as a-c but for 2041-2060 relatively to 2011-2030.

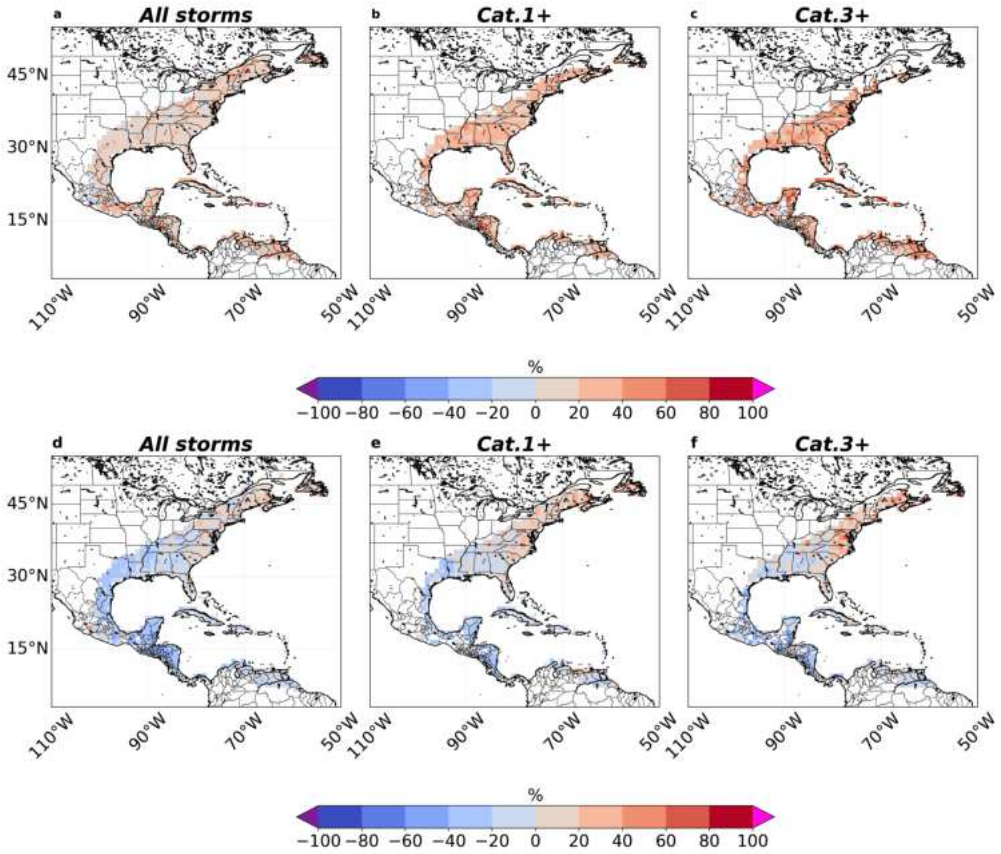

Figure D.11: Change in North Atlantic landfall rates. a-c) Change (%) in landfall rates over in North Atlantic for the period 2010-2030 relatively to 1980-2000 for a) all storms, b) Cat.1+ and c) major storms in AV-CESM. d-f) Same as a-c but for 2041-2060 relatively to 2011-2030.

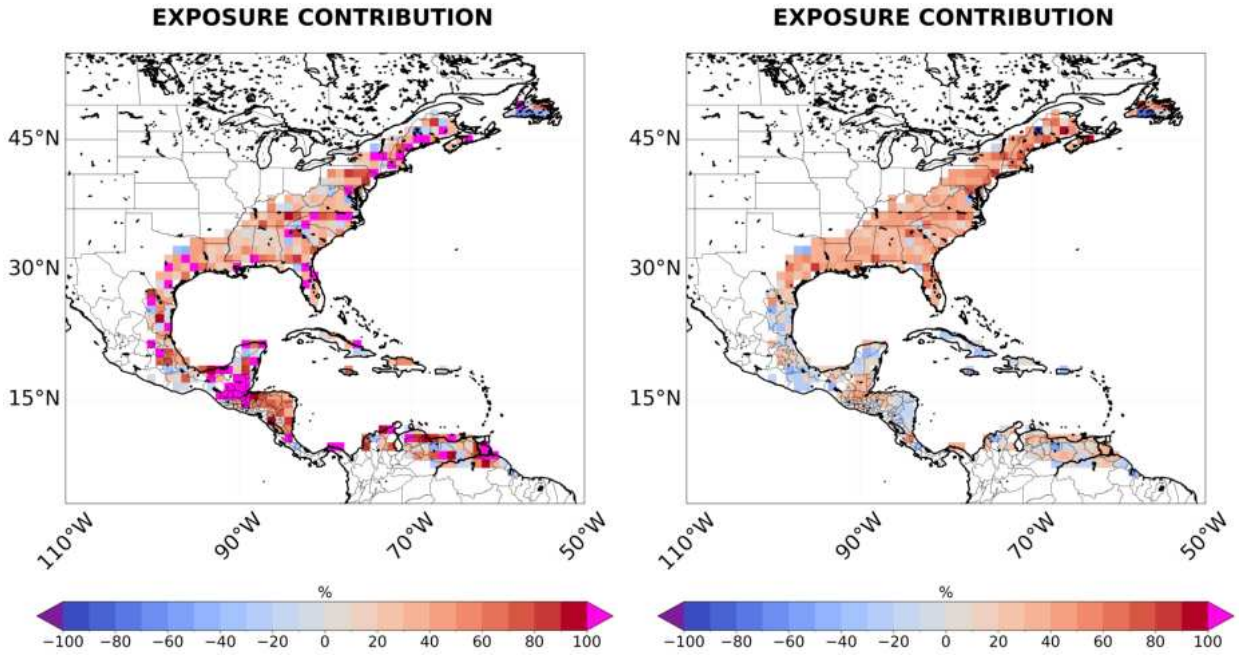

Figure D.12: Change in North Atlantic population. Left panel) Change (%) in population in North Atlantic for the period 2010-2030 relatively to 1980-2000. Right panel) same as right panel but for 2041-2060 relatively to 2011-2030.

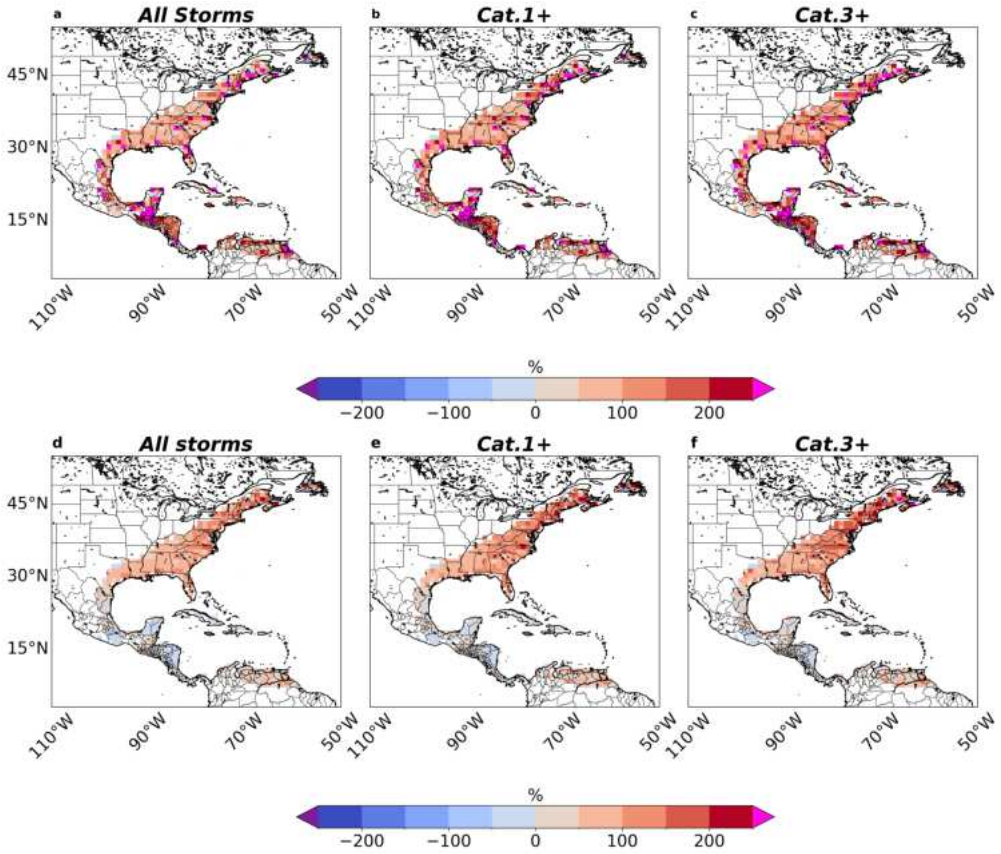

Figure D.13: Change in North Atlantic total risk. a-c) Change (%) in total risk over North Atlantic for the period 2010-2030 relatively to 1980-2000 for a) all storms, b) Cat.1+ and c) major storms in RV-CESM. d-f) same as a-c but for 2041-2060 relatively to 2011-2030.

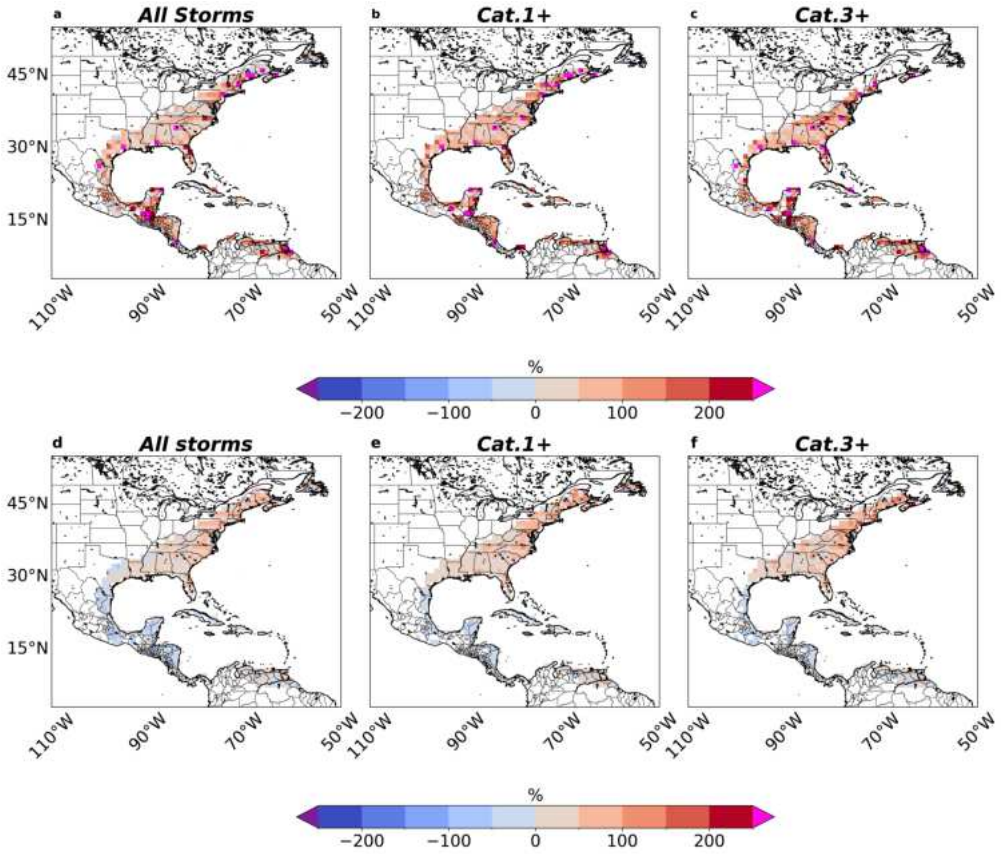

Figure D.14: Change in North Atlantic total risk. a-c) Change (%) in total risk over North Atlantic for the period 2010-2030 relatively to 1980-2000 for a) all storms, b) Cat.1+ and c) major storms in AV-CESM. d-f) same as a-c but for 2041-2060 relatively to 2011-2030.

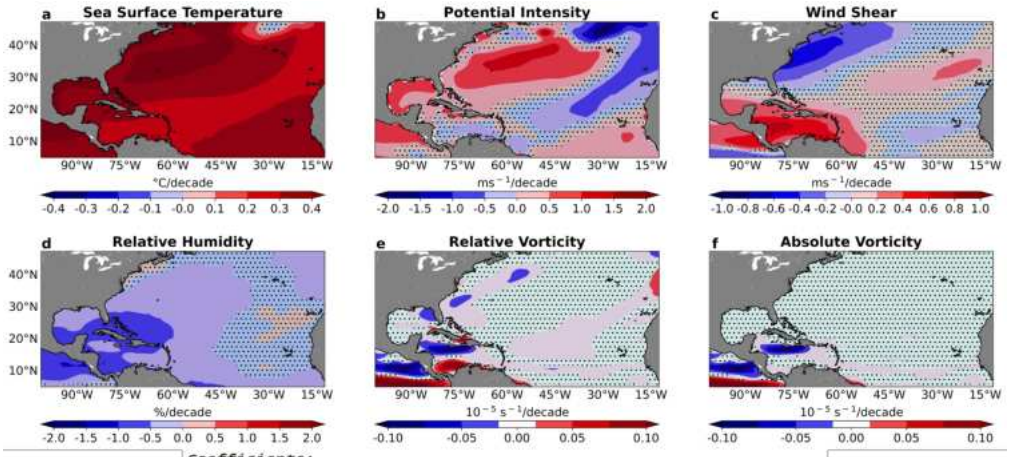


```
Coefficients:
             Estimate Std. Error z value Pr(>|z|)
(Intercept) -1.284e+01  1.284e+00  -9.998  < 2e-16 ***
SST          4.422e-01  5.040e-02   8.775  < 2e-16 ***
WS          -7.718e-02  1.384e-02  -5.578 2.43e-08 ***
RH          -1.431e-02  7.428e-03  -1.926   0.0541 .
RV           1.143e+05  8.577e+03  13.332  < 2e-16 ***
```

RV

```
Coefficients:
             Estimate Std. Error z value Pr(>|z|)
(Intercept) -2.037e+01  1.537e+00 -13.254  < 2e-16 ***
SST          2.162e-01  4.054e-02   5.332 9.72e-08 ***
WS          -5.489e-02  1.419e-02  -3.867  0.00011 ***
RH           8.240e-02  8.067e-03  10.214  < 2e-16 ***
AV           2.246e+05  2.515e+04   8.930  < 2e-16 ***
```

AV

```
Coefficients:
             Estimate Std. Error z value Pr(>|z|)
(Intercept) -1.824e+01  1.242e+00 -14.684  < 2e-16 ***
PI           3.709e-02  5.627e-03   6.591 4.37e-11 ***
WS          -6.342e-02  1.314e-02  -4.825 1.40e-06 ***
RH           8.442e-02  7.517e-03  11.231  < 2e-16 ***
AV           2.571e+05  2.516e+04  10.222  < 2e-16 ***
---
Signif. codes:  0 '***' 0.001 '**' 0.01 '*' 0.05 '.' 0.1 ' ' 1
```

PI

Figure D.15: Trend map of all model's predictors across the North Atlantic and their coefficients and statistics in the cyclogenesis module Top) Trend map for all model's predictors. Slopes and significance are calculated by using a Theil-Sen's Slope Estimator and a Mann-kendall test. Bottom) Statistics and coefficients for all the predictors in the cyclogenesis module of the three versions of UQAM-TCW2

D.2 North-West Pacific

D.2.1 The cyclogenesis component

D.2.1.1 Model performances

AUC values equals to 0.81 for the RV version (Fig.D.16a) and 0.84 and 0.85 for the AV and PI versions, respectively (Fig.D.16b-c).

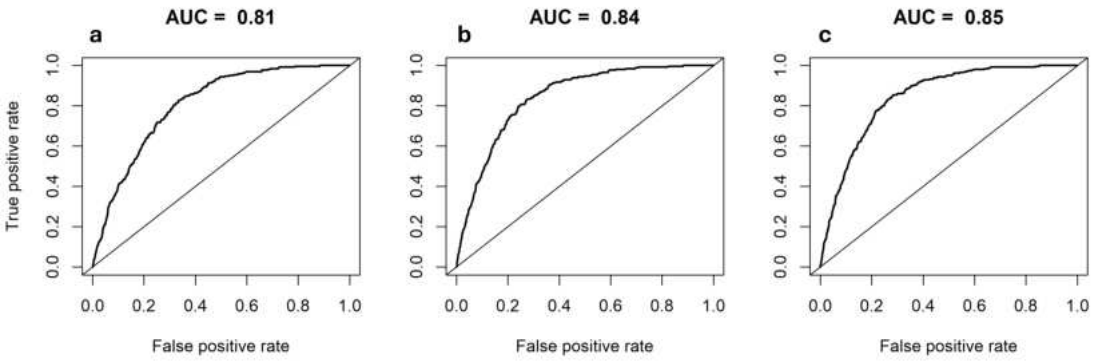

Figure D.16: ROC curves and AUC values. ROC curves and AUC values for a) RV, b) AV, and c) PI versions for the North-West Pacific basin.

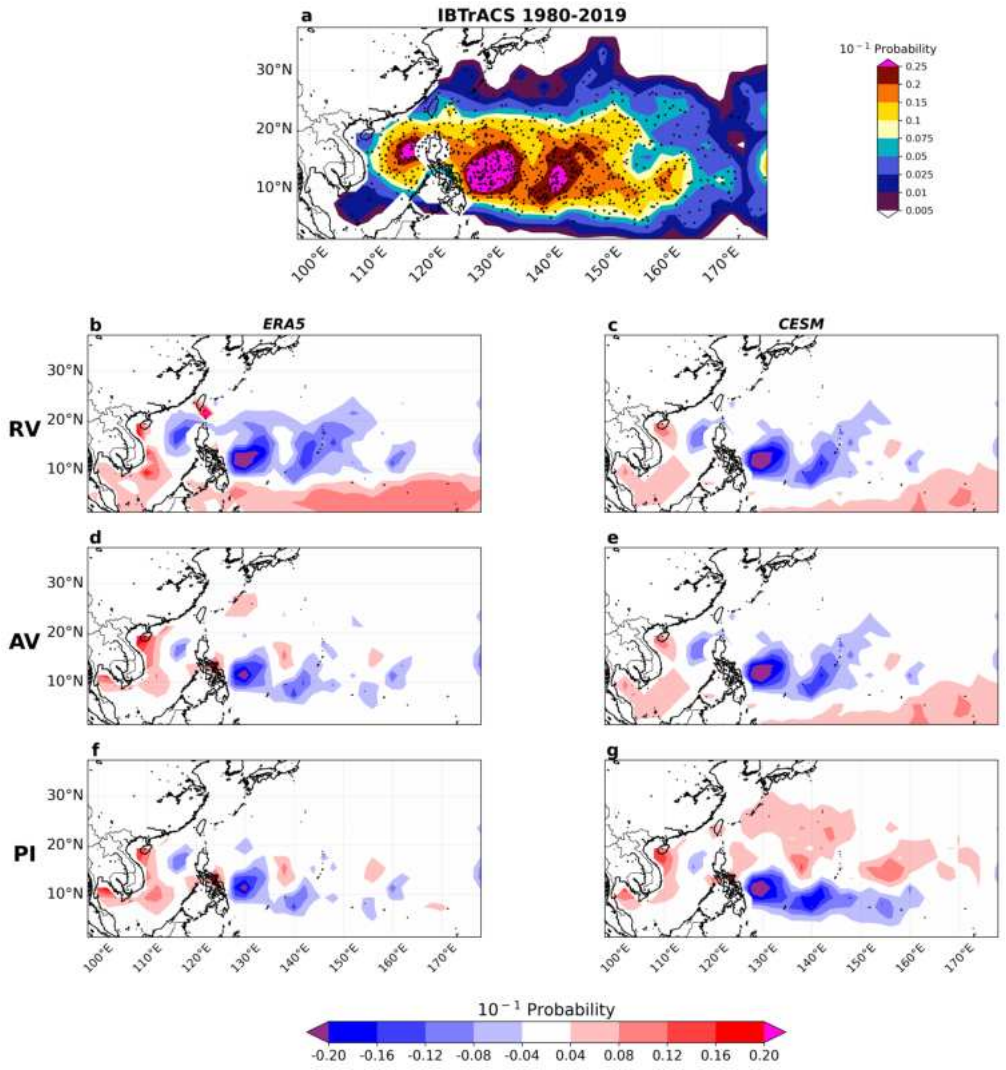

Figure D.17: Difference in North-West Pacific TC genesis probability between observations and model versions. JJASON TC genesis probability for the period 1980-2019 for a) IBTrACS (black dots represent historical cyclogenesis) and difference in TC genesis probability for b-c) the RV-ERA5 and RV-CESM versions, d-e) the AV-ERA5 and AV-CESM versions, f-g) the PI-ERA5 and PI-CESM versions relative to IBTrACS.

In the North-West Pacific, the ERA5-forced versions mainly reproduce the observed TC genesis probability (Fig.D.17). All versions, whether driven by ERA5 or CESM1-LE, exhibit a strong local underestimation off the eastern coast of the Philippines. Additionally, all versions show a slight to moderate overestimation over the South China Sea. This overestimation is more pronounced in the ERA5-driven versions and in PI-CESM. RV-CESM shows a moderate overestimation of TC genesis over the southern North-West Pacific basin. A smaller overestimation in the same area is also observed in the RV-CESM and AV-CESM versions.

Additionally, a slight overestimation is noted over the central part of the basin, around 15-20°N, in PI-CESM.

Although the ERA5-driven versions perform well in capturing the spatial distributions of TC genesis, they struggle to reproduce observed inter-annual variability and past trends. All versions show a significant upward trend of 1.43 (RV-ERA5), 3.72 (AV-ERA5) and 3.37 (PI-ERA5) TCs per decade, contrary to the slightly decreasing but not significant trend in observations (Fig.D.18,a). The correlation is positive and equal to 0.25 for RV-ERA5, whereas it is negative for AV-ERA5 and PI-ERA5 with correlations of -0.16 and -0.21, respectively.

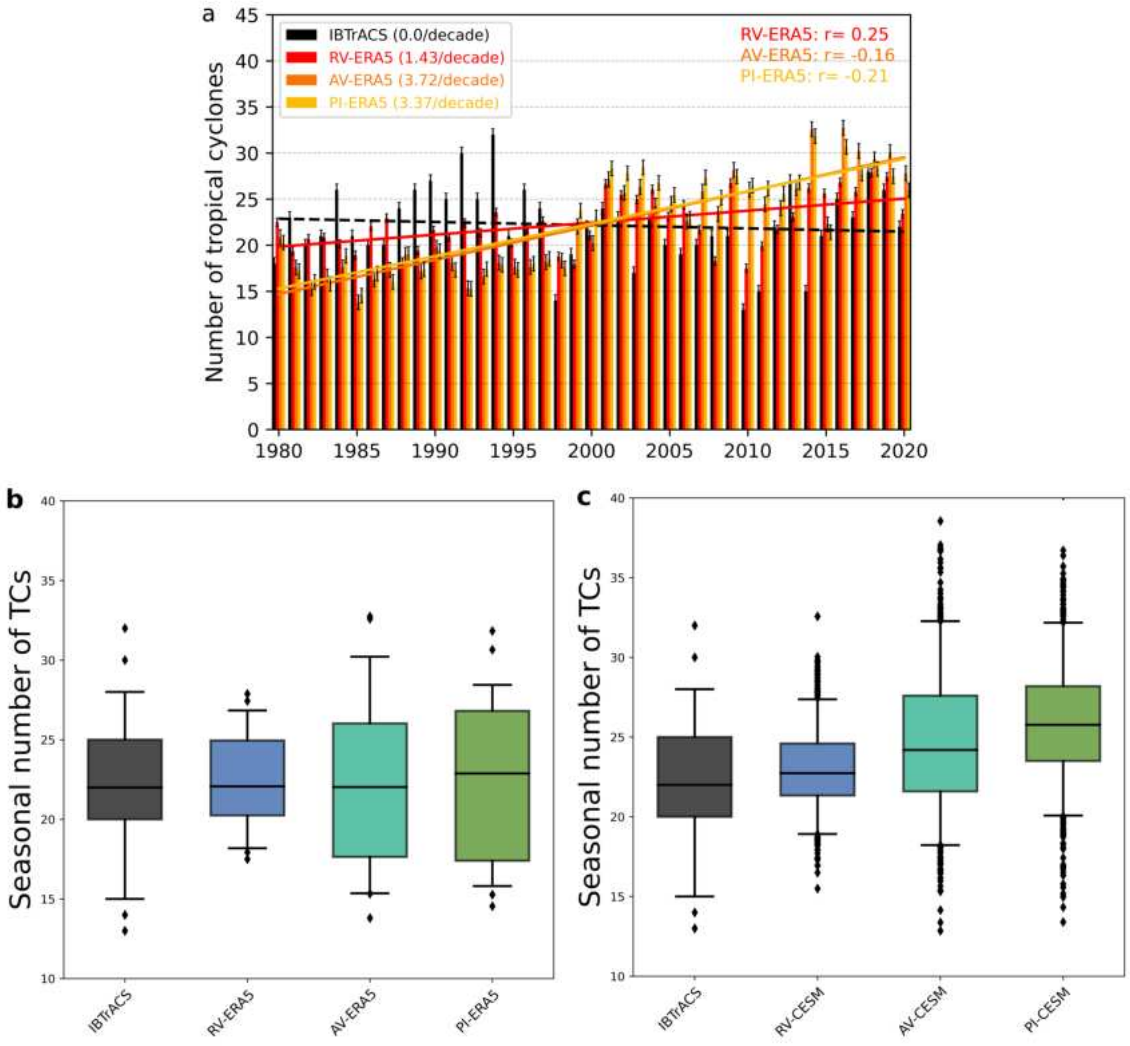

Figure D.18: Seasonal number of TCs over North-West Pacific and their distributions for the period 1990-2019. a) Seasonal (JJASON) number of tropical cyclones across North-West Pacific during the period 1980-2019 for observations (black bars), RV-ERA5 (red bars), AV-ERA5 (orange bars), PI-ERA5 (yellow bars). Continuous trend lines indicate significant values at 5% significance level. Trend values are shown in brackets at the top-left. Correlation values are shown at the top-right with values in bold indicating statistical significance. b) Seasonal number of TCs among IBTrACS (black) and the RV-CESM (blue), AV-CESM (green-blue) and PI-CESM (grassy green) versions. Boxplots show the median (black line), the quartiles (the box), the 5-95th percentiles (the whisker) and outliers (dots). c) Same as right but for versions forced by CESM1-LE.

D.2.2 The displacement component

D.2.2.1 Analysis of residuals

North-West Pacific dx and dy displacements residuals show no correlation (Fig.D.20). Really small correlation values are observed between the residuals and geographical coordinates although some of them present a statistical significance as shown by the correlation between longitude and dx (negative) and dy (positive) displacements residuals. Similar results to North Atlantic are found in the spatial patterns of the model bias (Fig.D.19). Again, no particular patterns are found over the North-West Pacific with higher relative change for dy compared to dx mainly due to the small values of the meridional bias. For initial displacements, similar results to North-Atlantic are found in the North-West Pacific with a significant negative correlation between longitude and dx residuals (-0.147) (Fig.D.21). No notable spatial patterns are found over the basin D.22).

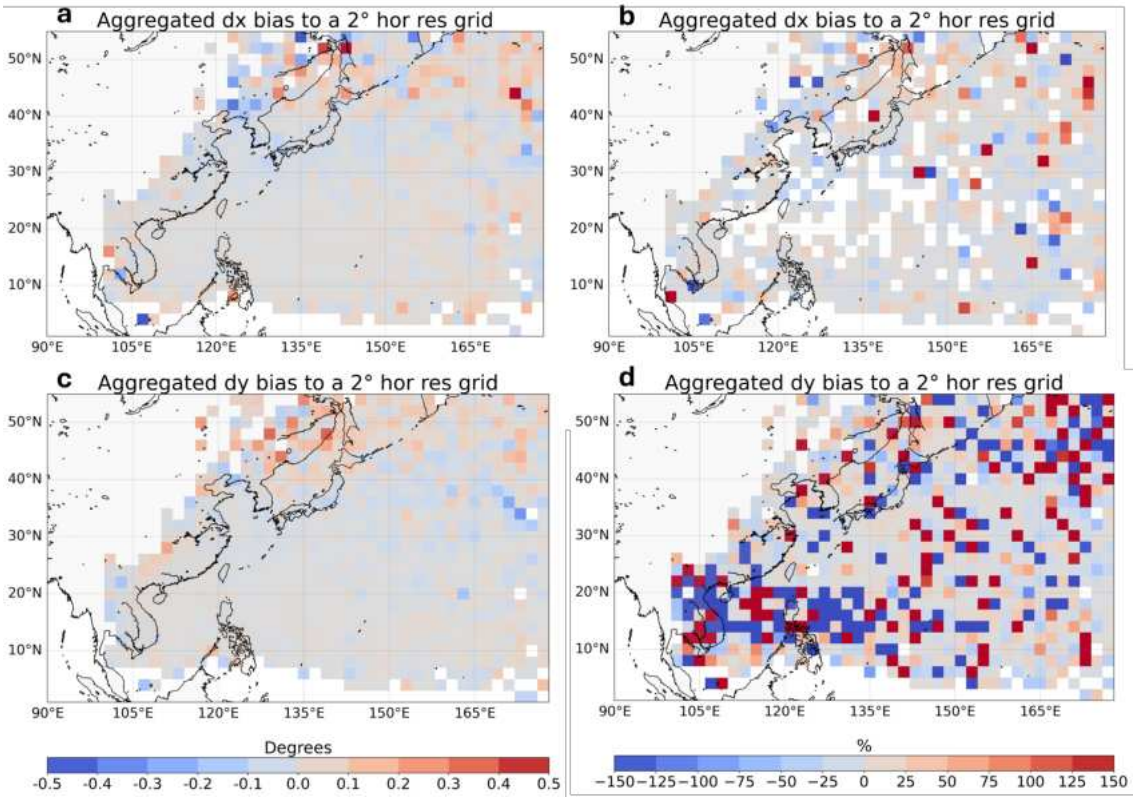

Figure D.19: Maps of zonal and meridional displacement residuals over North-West Pacific. Maps of North-West Pacific of zonal (a,b) and meridional (c,d) displacements residuals in degrees (a,c) and percentage (b,d).

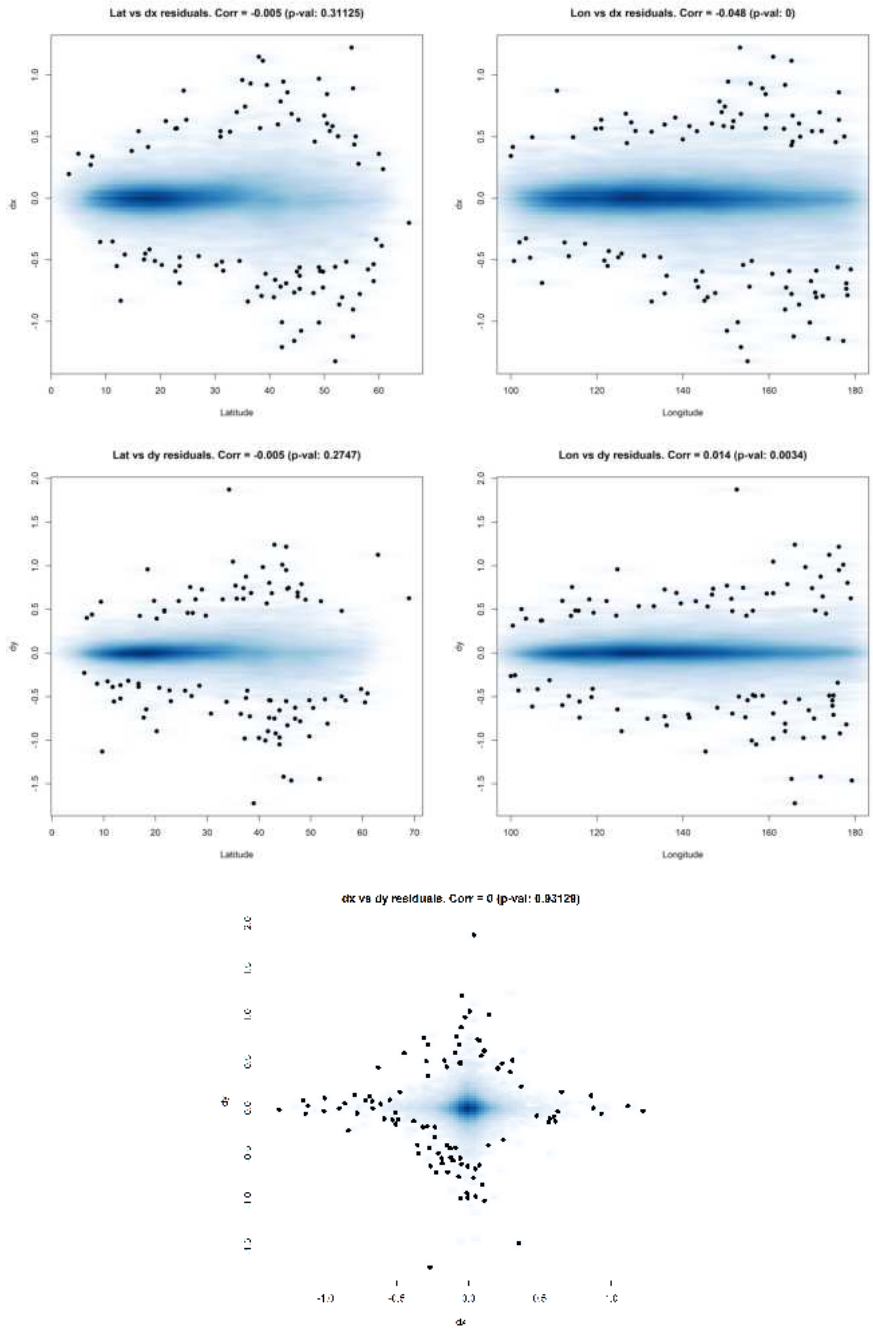

Figure D.20: Residuals of zonal and meridional displacements over North-West Pacific. Scatterplots of top) zonal displacement residuals vs latitude and longitude values, middle) meridional displacement residuals vs latitude and longitude values and bottom) zonal vs meridional displacements residuals with their relative correlations and associated p-values for North-West Pacific. p-values of each correlation are shown in brackets.

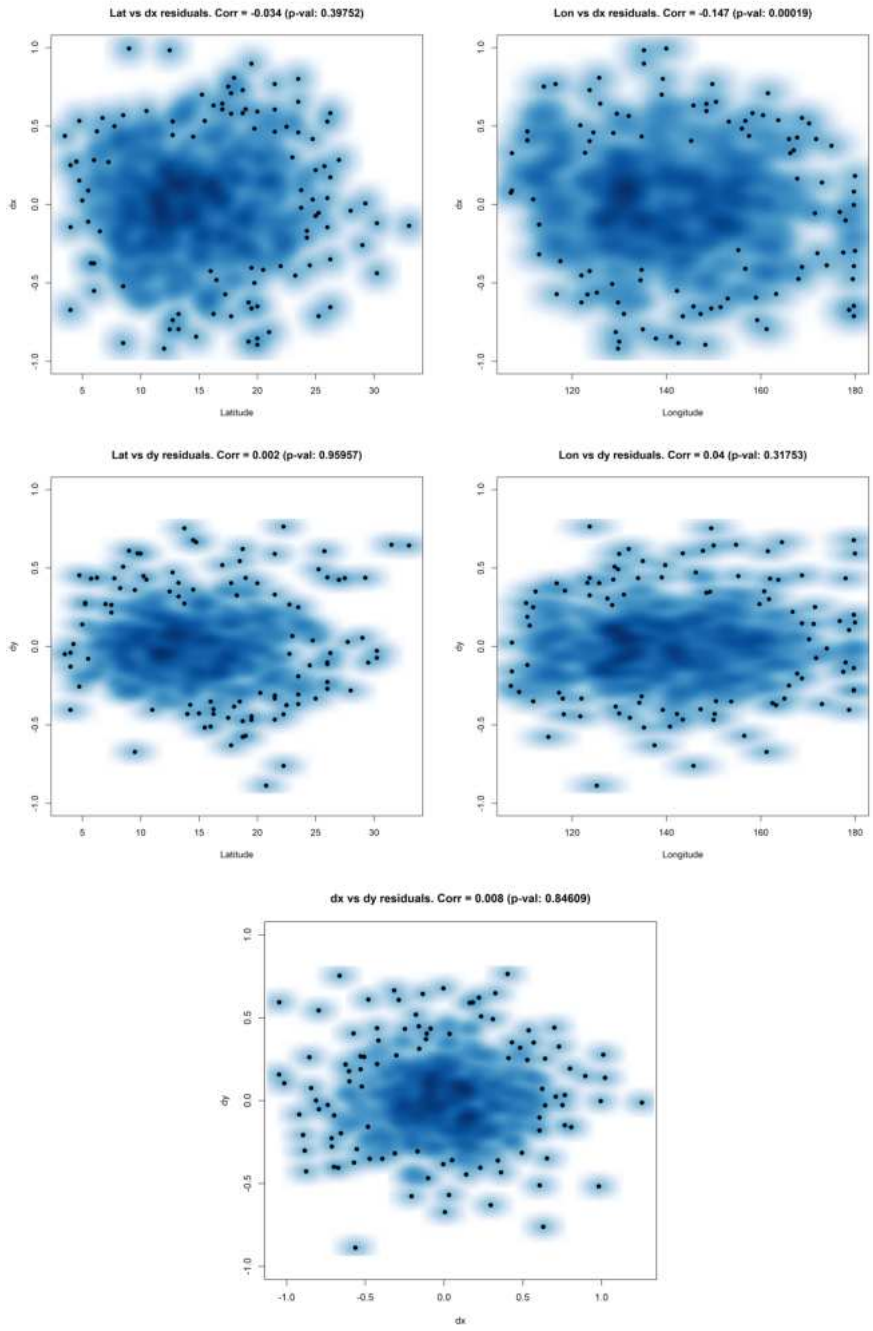

Figure D.21: Residuals of zonal and meridional initial displacements over North-West Pacific. Scatterplots of top) zonal initial displacement residuals vs latitude and longitude values, middle) meridional initial displacement residuals vs latitude and longitude values and bottom) zonal vs meridional initial displacements residuals with their relative correlations and associated p-values for North-West Pacific. p-values of each correlation are shown in brackets.

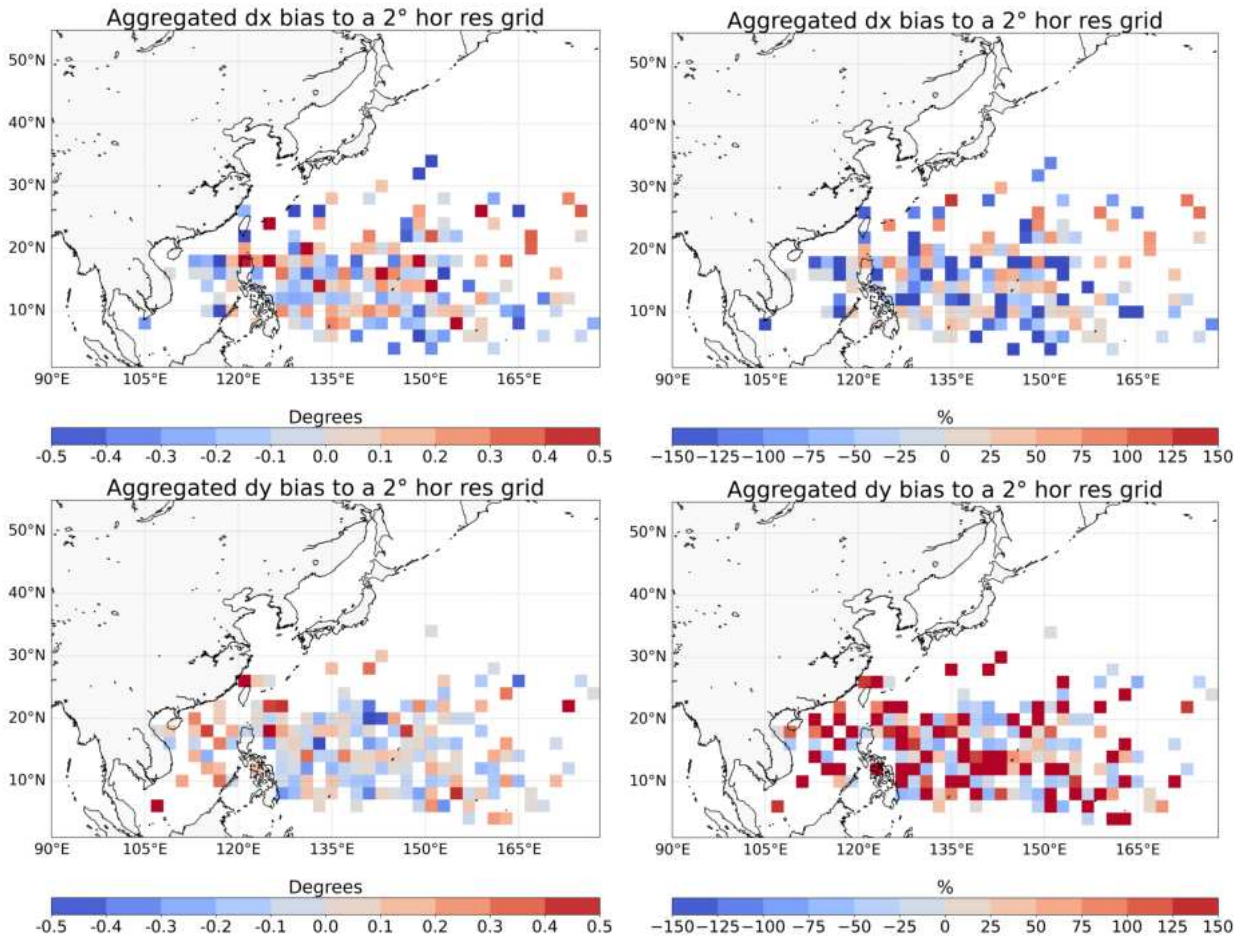

Figure D.22: Maps of zonal and meridional initial displacement residuals over North-West Pacific. Maps of North-West Pacific zonal (top) and meridional (bottom) initial displacements residuals in degrees (left) and percentage (right).

D.2.3 TC activity and landfalls

D.2.3.1 TC intensity distribution.

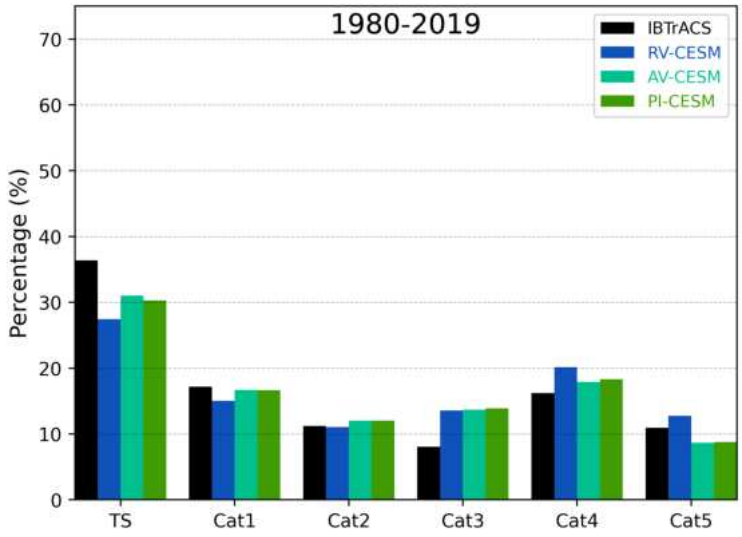

Figure D.23: Percentage of Tropical Cyclones for each category over North-West Pacific Comparison for the North-West Pacific seasonal (JJASON) percentage of tropical cyclones between observations (black bars), RV-CESM (blue bar), AV-CESM (green-blue bars) and PI-CESM (grassy green bars) during the period 1980-2019.

The model underestimates the percentage of tropical storms compared to observations with RV-CESM, AV-CESM, and PI-CESM showing 27%, 31%, and 30% tropical storms, respectively, compared to 36% in the observations (Fig.D.23). Unlike the North Atlantic basin, here the model accurately reproduces major storms without needing post-processing adjustments. However, the model tends to overestimate Cat.3 storms with 13% of model storms classified as Cat.3 compared to only 8% in the observations. A slight overestimation occurs for Cat.4 storms with RV-CESM reaching 20% of Cat.4 storms, roughly 4% more than observations. Observed Cat.5 storms proportions reach about 11% of all storms, which is slightly overestimated by the RV-CESM version (13%) and underestimated by AV-CESM and PI-CESM (9%).

D.2.3.2 TC spatial density

The model tends to underestimate TC density of all storms over the western part of the basin compared to observations (Fig.D.24c, Fig.D.35c and Fig.D.36c). There are two primary peaks in the western part of the

basin: the largest is located over the South China Sea, while the other peak is situated over the Philippine Sea. The model indicates increased tropical cyclone density in the central-eastern part of the basin, with AV-CESM and PI-CESM showing the most pronounced positive differences. In contrast, RV-CESM slightly underestimates TC density in the southern region of the North-West Pacific. A similar pattern is observed for Cat.1 and higher storms, but with slightly smaller peaks in all versions (Fig.D.24f, Fig.D.35f and Fig.D.36f). When focusing solely on major storms, the model eliminates the negative bias over the South China Sea and reduce it over the Philippine Sea (Fig.D.24i, Fig.D.35i and Fig.D.36i). Furthermore, the negative bias extends to southern Japan. A higher TC density is always seen by the model compared to observations across the central-eastern part of the basin but these differences are smaller compared to all storms and Cat1+ cases.

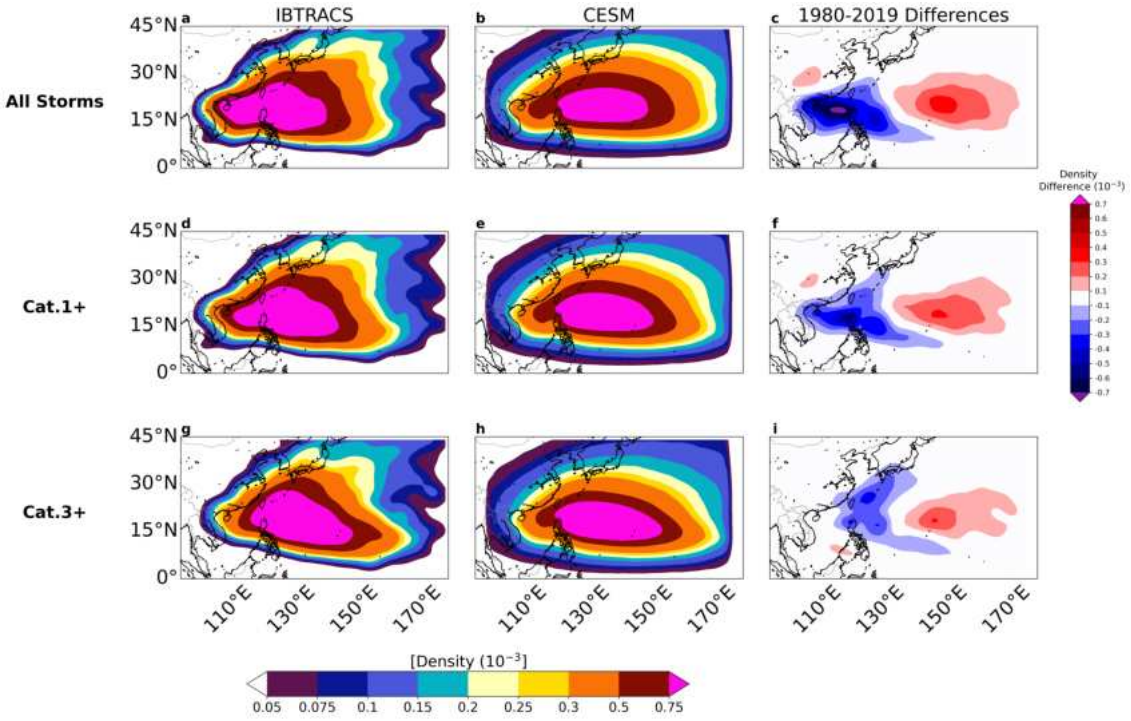

Figure D.24: North-West Pacific TC density. JJASON North-West Pacific TC density for the period 1980-2019 for a,d,g) IBTrACS and b,e,h) PI-CESM model and c,f,i) and difference in TC density for PI-CESM relatively to observations. Top row) all storms, Middle row) Cat.1+ and Bottom row) major storms.

D.2.3.3 TC metrics.

UQAM-TCW2 tends to slightly overestimate LMI but they still accurately reproduce the overall shape of the distributions (Fig.D.25). The observed mean LMI is 41.2 ms^{-1} with 5th and 95th percentiles of 18 and 72 ms^{-1}, respectively. RV-CESM present the highest median with 47.8 ms^{-1} and 5th and 95the percentiles of 20 and

76.4 ms^{-1}, whereas AV-CESM and PI-CESM medians are equal to 44.3 and 45.8 ms^{-1}, respectively with 5th and 95the percentiles of 19.8 and 73.6 ms^{-1}

The observed median of the normalized ACE is 11 with 5th and 95th percentiles equal to 6.4 and 16.8, respectively (Fig.D.26). Similar to the North Atlantic basin, the model is characterized by an underestimation of the normalized ACE medians and distributions. Medians of 9.1, 8.4 and 8.5 are observed for RV-CESM, AV-CESM and PI-CESM, respectively. The 5th and 95th percentiles are 6.8 and 10.9 in RV-CESM, while values equal to 6.8-6.9 and 10 are found in AV-CESM and PI-CESM. Again, extreme values in the right tail of the model distributions are close (RV-CESM) or below (AV-CESM and PI-CESM) the median of the observations.

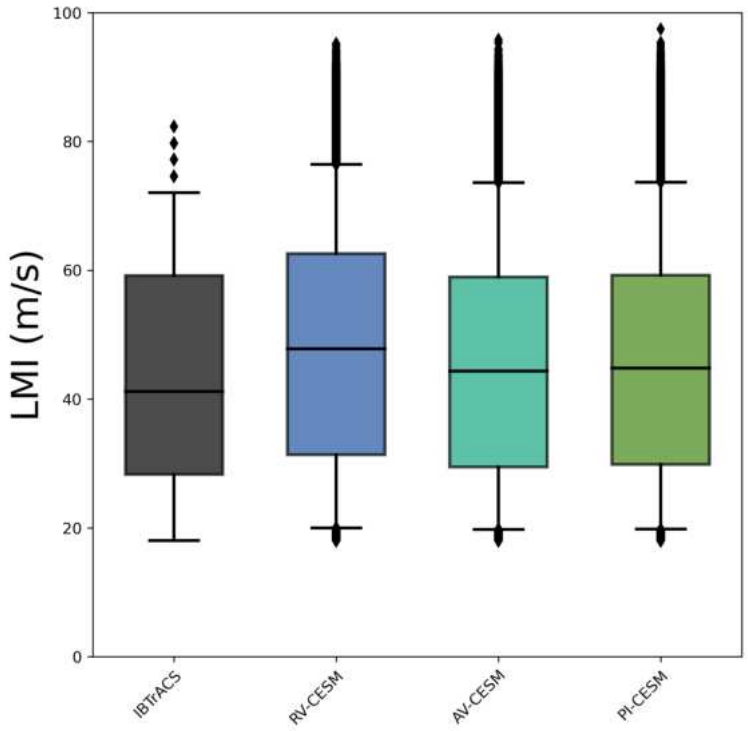

Figure D.25: LMI boxplots over North-West Pacific for the period 1990-2019. Boxplots of Nort-West Pacific LMI for IBTrACS (black) and the RV-CESM (blue), AV-CESM (green-blue) and PI-CESM (grassy green) versions. Boxplots show the median (black line), the quartiles (the box), the 5th-95th percentiles (the whiskers) and outliers (dots). Post-processing is not applied here.

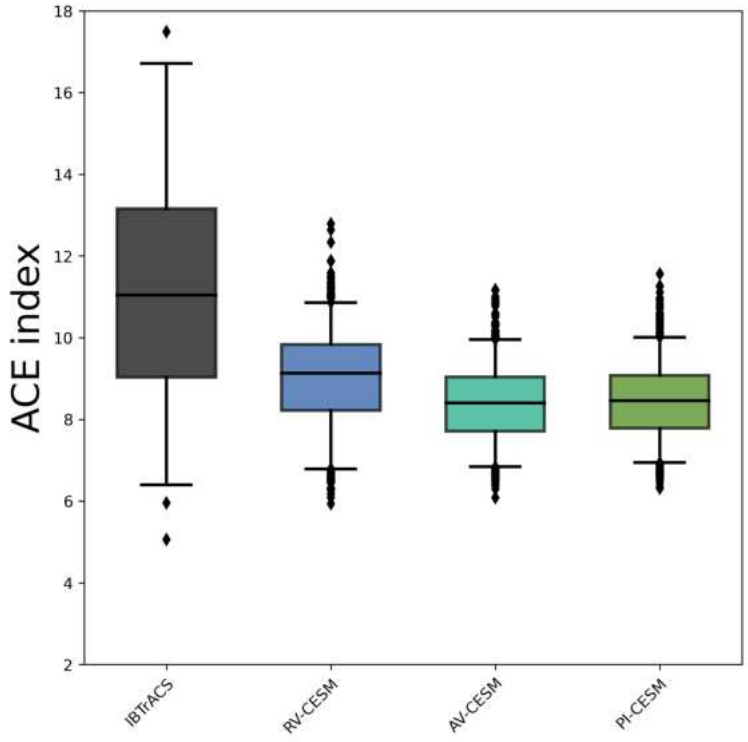

Figure D.26: normalized ACE boxplots over North-West Pacific for the period 1990-2019. Boxplots of normalized North-West Pacific ACE for IBTrACS (black) and the RV-CESM (blue), AV-CESM (green-blue) and PI-CESM (grassy green) versions. Boxplots show the median (black line), the quartiles (the box), the 5th-95th percentiles (the whiskers) and outliers (dots).

D.2.3.4 Landfall rates.

Observations reveal TC landfall peaks over Luzon Island (northern Philippines), Kyushu Island (South-West Japan), Taiwan, the Fujian and Hainan regions in China and northern Vietnam (Fig.D.27a,d,h), Fig.D.37a,d,h and Fig.D.38a,d,h) While all versions capture these peaks, they generally underestimate the overall landfalls in the North-West Pacific. The largest discrepancy is generally observed over northern Philippine and Taiwan across all categories of storms. An exception is found along the eastern coasts of Asia where the model accurately reproduces observed landfall rates for major storms, except for the Fujian region and the southern parts of the Guangxi and Guangdong regions in China (Fig.D.27i, Fig.D.37i and Fig.D.38i).

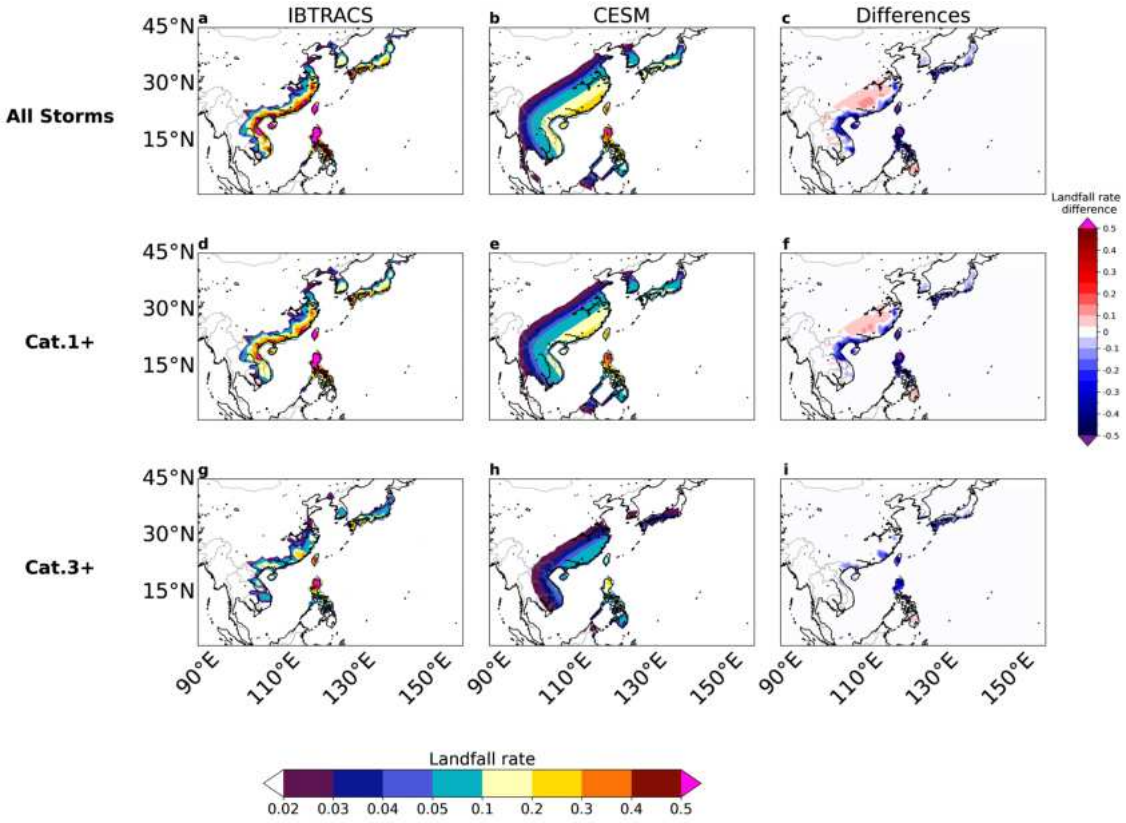

Figure D.27: Difference in North-West Pacific TC landfall rates between observations and PI-CESM. JJASON TC landfall rates for the period 1980-2019 for a,d,g) IBTrACS and b,e,h) PI-CESM and c,f,i) and difference in TC landfall rates for PI-CESM relatively to observations. Top row) all storms, Middle row) Cat.1+ and Bottom row) major storms.

D.2.4 Projected Future Change in TC activity

D.2.4.1 Change in frequency and density

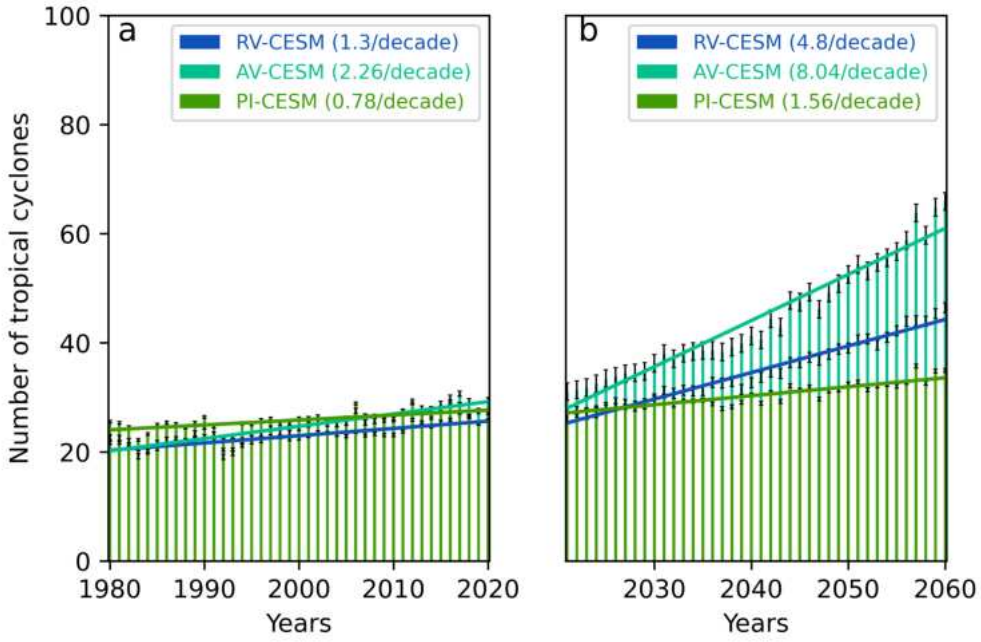

Figure D.28: Past and future North-West Pacific Seasonal tropical cyclones frequency. Seasonal (JJASON) number of tropical cyclones across North-West Pacific during the period a) 1980-2019 and b) 2021-2060 for RV-CESM (blue bar), AV-CESM (green-blue bars) and PI-CESM (grassy green bars). Continuous trend lines indicate significant values at 5% significance level. Trend values are shown in brackets at the top-left.

Past trends (1980-2020) in the CESM1-LE-driven versions show significant increases, with values of 1.3, 2.3, and 0.8 tropical cyclones per decade (Fig.D.28,a). Increasing trends are also observed in the future with RV-CESM and AV-CESM showing increases more than three times greater than their past trends, reaching 4.8 and 8 tropical cyclones per decade, respectively (Fig.D.28,b). The trend in PI-CESM also doubles, rising to 1.6 tropical cyclones per decade.

Cat.4 storms are projected to increase by 52% in RV-CESM, 83% in AV-CESM and 21% in PI-CESM. For Cat.5 cyclones, the projected increases are 73%, 106% and 36% for RV-CESM, AV-CESM and PI-CESM, respectively. When combining Cat.4 and Cat.5 storms, the projected increases are 60%, 91% and 26% for RV-CESM, AV-CESM and PI-CESM, respectively. All model versions project a slight decrease of approximately 1% in tropical storms compared to the past (Fig.D.29). However, there is a projected increase in Category 5 storms of a

similar magnitude across all versions. No notable changes are observed in the other storm categories.

A small decrease in TC density is observed across the western part of the Philippine Sea and the northern part of the South China Sea, including Luzon Island in North Philippines for all categories, except for RV-CESM (Fig.D.30, Fig.D.39, Fig.D.40).

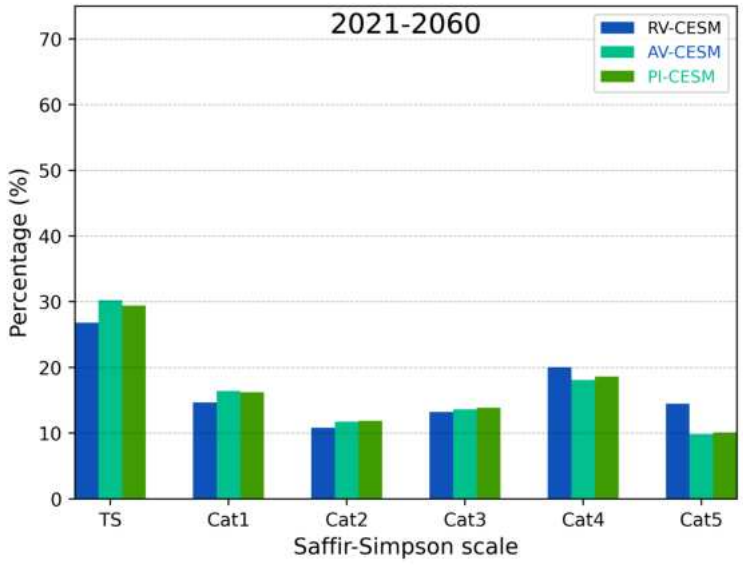

Figure D.29: Percentage of future North-West Pacific tropical cyclones for each category Comparison for the seasonal (JJASON) percentage of North-West Pacific tropical cyclones between RV-CESM (blue bar), AV-CESM (green-blue bars) and PI-CESM (grassy green bars) during the period 2021-2060.

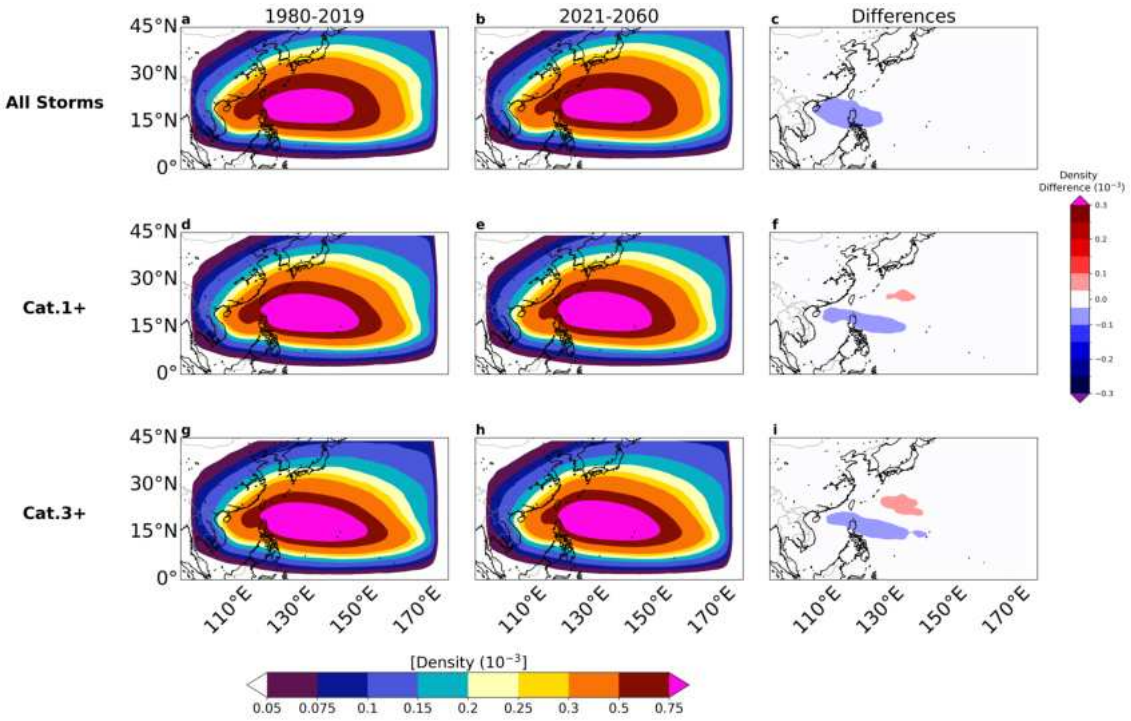

Figure D.30: Future change in North-West Pacific JJASON TC density. TC density for the period a,d,g) 1980-2019 and b,e,h) 2021-2060 and c,f,i) change in TC density for the PI-CESM relative to observations. Top row) all storms, Middle row) Cat.1+ and Bottom row) major storms.

D.2.4.2 Change in TC metrics

Similarly to what was observed in the North Atlantic, a small but significant increase in LMI medians and 95th percentiles is detected in all versions for the future period compared to the past (Fig.D.31). The LMI median for RV-CESM increases from 47.8 ms^{-1} to 48.7 ms^{-1} and its 95th percentile from 76.4 ms^{-1} to 77.7 ms^{-1}. The increase in AV-CESM shows its medians rising from 44.3 ms^{-1} in the past to 45.1 ms^{-1} and 95th percentile from 73.6 ms^{-1} to 74.7 ms^{-1}. Medians in PI-CESM increase from 44.8 ms^{-1} to 45.8 ms^{-1} and 95th percentile from 73.7 ms^{-1} to 74.8 ms^{-1}.

The normalized ACE also shows a significant increase in all model versions, similar to what was observed in the North Atlantic. The medians shift from 9.14, 8.41 and 8.46 to 9.4, 8.7 and 8.8 for RV-CESM, AV-CESM and PI-CESM, respectively (Fig.D.32). The extreme values also show an increase with 5th percentile move from 6.8 to 7 in RV-CESM and AV-CESM and from 6.9 to 7.2 in PI-CESM. 95th percentiles increase from 10.9 to 11.4 in RV-CESM and from 9.9 and 10 to 10.5 and 10.6 in AV-CESM and PI-CESM, respectively.

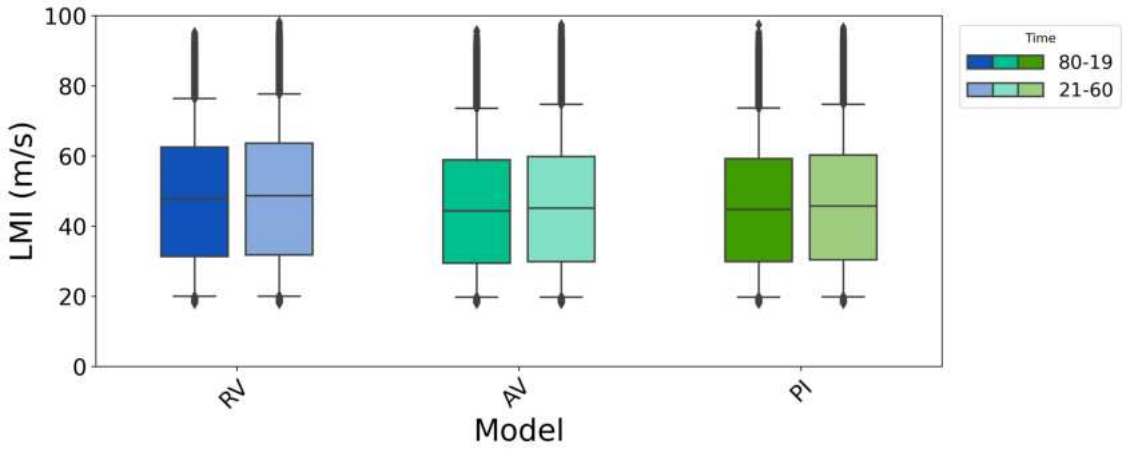

Figure D.31: Comparison in LMI boxplots over North-West Pacific for the periods 1980-2019 vs 2021-2060. Boxplots of North-West Pacific LMI for IBTrACS (black) and RV-CESM (blue), AV-CESM (green-blue) and PI-CESM (grassy green) for the period 1980-2019 (left in each version) and 2021-2060 (right in each version). Boxplots show the median (black line), the quartiles (the box), the 5th-95th percentiles (the whiskers) and outliers (dots).

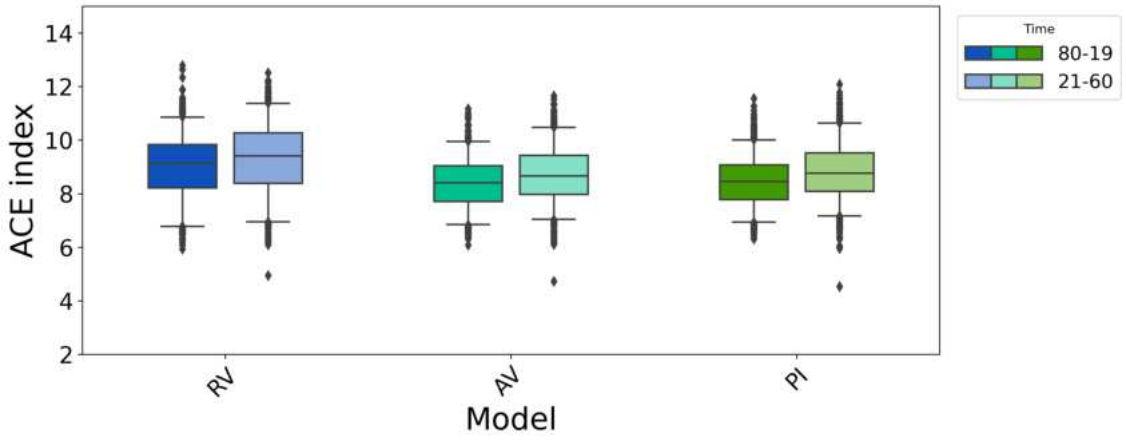

Figure D.32: Comparison in normalized ACE boxplots over North-West Pacific for the periods 1980-2019 vs 2021-2060. Boxplots of North-West Pacific normalized ACE for IBTrACS (black) and RV-CESM (blue), AV-CESM (green-blue) and PI-CESM (grassy green) for the period 1980-2019 (left in each version) and 2021-2060 (right in each version). Boxplots show the median (black line), the quartiles (the box), the 5th-95th percentiles (the whiskers) and outliers (dots).

D.2.5 Past and future change in landfall rates and risk

D.2.5.1 Change in landfall rates

The reference-period change compared to the past in landfall rates over the North-West Pacific is positive across all versions and shows similar trends for different categories of storms. RV-CESM presents an increase in landfall rates between +20% and +40% overall (Fig.D.41). In AV-CESM, this increase is higher compared to RV-CESM, especially in the northern part of the basin, with values between +20% and +60% (Fig.D.42). On the contrary, PI-CESM shows smaller changes mainly between 0 and +20% with few peaks between +20% and +40% (Fig.D.33). The future increase in landfall rates is higher across all versions and remains consistent across different categories of storms. Relative changes between +40% and +60% with some peaks above +60% are observed in RV-CESM. AV-CESM shows values that are even higher than those of RV-CESM over Japan, Korea and the north-western coasts of China, generally between +80% and +100% and above +100%. In PI-CESM, the areas mentioned for AV-CESM—such as Japan, Korea, and the north-western coasts of China—show higher changes compared to the present day, with values ranging from 40% to 80% over North-West China and Korea.

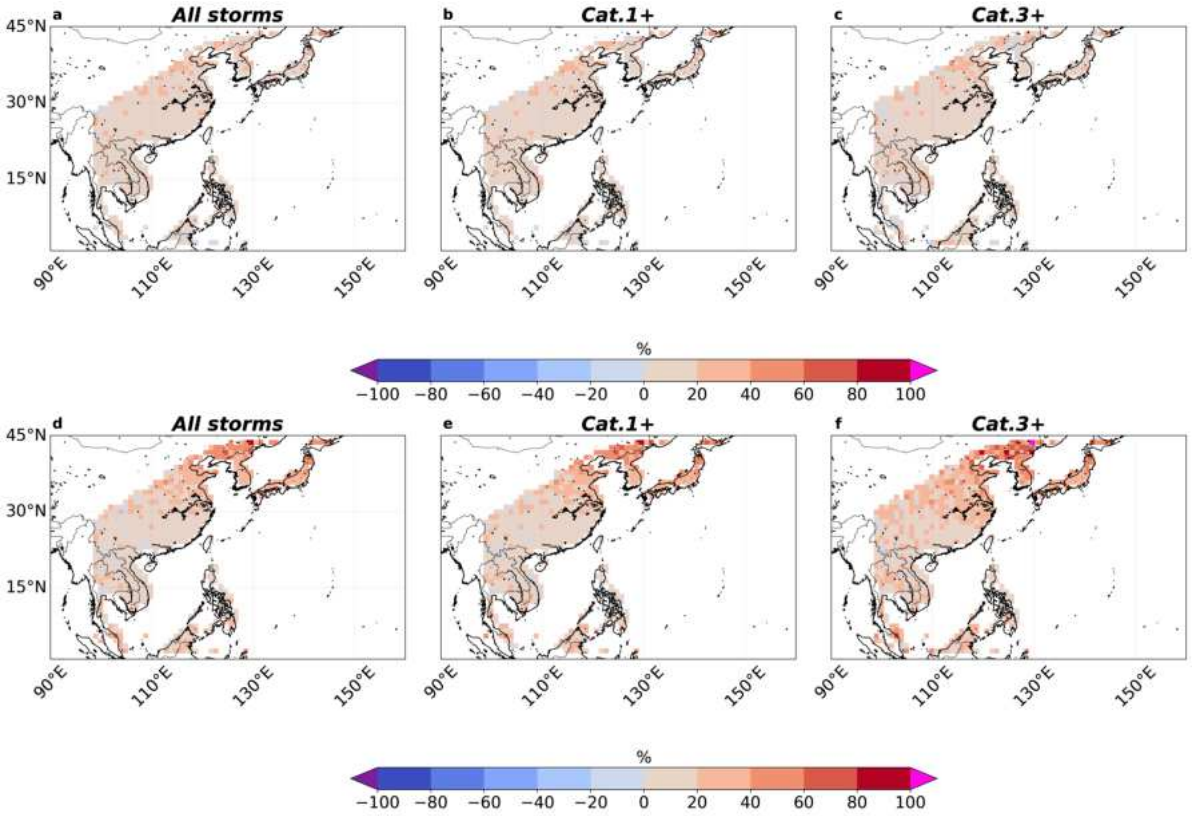

Figure D.33: Change in North-West Pacific landfall rates. a-c) Change (%) in landfall rates over in North-West Pacific for the period 2010-2030 relatively to 1980-2000 for a) all storms, b) Cat.1+ and c) major storms in PI-CESM. d-f) Same as a-c but for 2041-2060 relatively to 2011-2030.

D.2.5.2 Change in Risk

An increase in total risk for the reference-period relative changes is also observed across all model versions and storm categories. RV-CESM and AV-CESM present a similar pattern, with total risk values ranging from +20% to over +100% (Fig.D.44a-c and Fig.D.45a-c). AV-CESM generally shows higher changes compared to RV-CESM, consistent with its higher past and future trends.(Fig.D.28). The parts which are characterized by major changes include northern Philippines, Vietnam, northern China, Korea and China. PI-CESM shows lower relative changes (Fig.D.34a-c) but the areas experiencing the highest changes are the same as those in RV-CESM and AV-CESM. The high variability in risk changes across the basin can be attributed to high fluctuations in exposure (Fig.D.43, left) which exhibit significant variability in both values and signs across different areas of the same region. On the contrary, changes in landfall rates show less variance and are

more homogeneous. As a result, the contribution from landfall rates to the total risk change can range from less than +20% to more than +100%. In RV-CESM, the contribution from landfall rates generally falls between +20% and +40%. Over the area with the highest changes in risk (from +80% to above +100%) the landfall rate contribution typically accounts for about one-sixth to one-quarter of the total risk change. In other regions, the landfall rate contribution varies widely, influenced by the high variability in exposure. Similar results are obtained in AV-CESM, although in the northern part of the basin, the contribution from landfall rates (ranging from +40% to +60%) is higher than in RV-CESM. Here, the landfall rate contribution constitutes about one-quarter to one-half of the total risk change. In PI-CESM, the contribution from landfall rates is relatively small, ranging from 0% to one-fifth of the total risk in areas with the highest changes.

UQAM-TCW2 shows varying results for the projected changes, consistent with the trends shown in Fig.D.28. Both RV-CESM and AV-CESM indicate a future increase in total risk, independently of the intensity of the storms (Fig.D.44d-f and Fig.D.45d-f). In RV-CESM, a relative increase ranging between 40% and 80% with some peaks above 100% is observed over South East Asia and between 40% to above 100% over Japan, Korea and north-western China. Values above +80% are present over the Philippine. Similar results are obtained in AV-CESM, although the changes in risk are generally higher than in RV-CESM. PI-CESM shows a smaller increase in risk over the northern part of the basin and Southeast Asia, with changes generally ranging between 20% and 60% for all categories of storms (Fig.D.34d-f). Contrary to the other versions, PI-CESM also shows a slight decrease between 0% and 40% over the south-central China, except for a small increase along the coasts. Future exposure changes indicate a decrease in population across most areas, with exceptions including parts of Korea, northern China, Laos, Thailand, Cambodia and the Philippine (Fig.D.43, right). In RV-CESM and AV-CESM, the increase in total risk is solely attributable to the increase in landfall rates. In contrast, in PI-CESM, landfall rates are the primary driver of the increase in total risk over the northern part of the basin, with exposure contributing minimally (about one-fifth of the total). In South Asia, the contributions from landfall rates and exposure are nearly equal. In south-central China, the contribution from exposure exceeds that from landfall rates, except along the coasts, where both contributions are comparable.

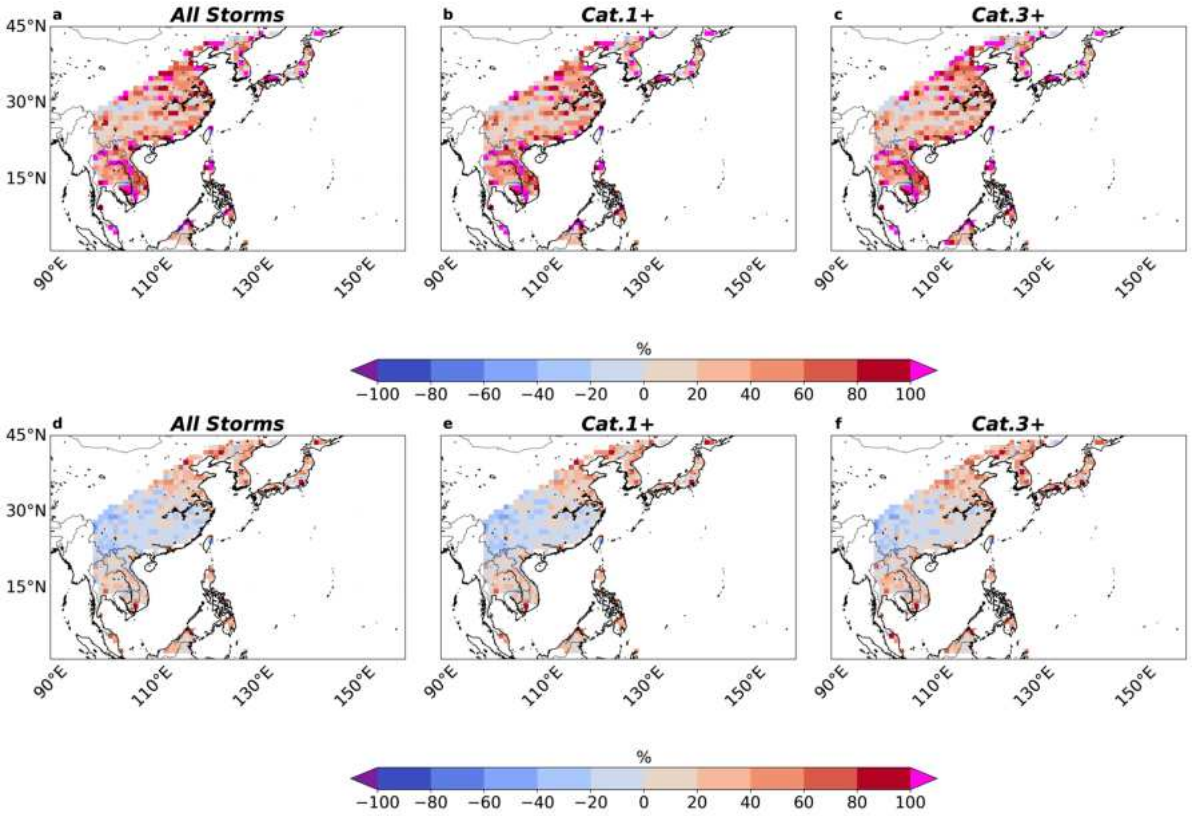

Figure D.34: Change in North-West Pacific total risk. a-c) Change (%) in total risk over North-West Pacific for the period 2010-2030 relatively to 1980-2000 for a) all storms, b) Cat.1+ and c) major storms in PI-CESM. d-f) same as a-c but for 2041-2060 relatively to 2011-2030.

D.2.5.3 Validation

The model reproduces the spatial pattern of the observed TC genesis probabilities (Fig.D.17), but contrary to the case of North Atlantic, a notable underestimation is present occurring off the eastern coast of the Philippine in the North-West Pacific basin. In terms of inter-annual variability, some issues persist for the North-West Pacific. In this region, the correlations between the model versions and observations for the seasonal number of tropical cyclones are low (around 0.2 in absolute values) and negative for AV-ERA5 and PI-ERA5 (Fig.D.18a). These results are in part due to the inability of the model to properly reproduce the inter-annual variability of the first two decades. When focusing solely on the last two decades, the correlations improve, with the correlation between observations and RV-ERA5 reaching 0.5. Moreover, the correlations for the other two versions, AV-ERA5 and PI-ERA5, change sign during this period.

There was no necessity to apply any post-processing for the North-Pacific as the proportions among different TC categories according to the Saffir-Simpson scale are adequately replicated in the model results (Fig.D.23).

A notable underestimation of TC density characterized by two main peaks over South China (except for major storms) and the Philippine seas is present in the western part of the North-West Pacific basin (Fig.D.24, Fig.D.35 and Fig.D.36). A positive bias is also observed in the central-eastern part of the basin, especially in AV-CESM and PI-CESM.

In terms of landfall rates, there is an overall underestimation along the coasts of the North-West Pacific, except for major storms along the eastern Asia coasts (Fig.D.27, Fig.D.37 and Fig.D.38).

D.2.5.4 Future Changes

All our model versions show an increase in TCs over North-West Pacific, of about 46%, 74% and 17% for RV-CESM, AV-CESM and PI-CESM, respectively. RV-CESM and AV-CESM are clear outliers compared to the climate models considered in Knutson et al. (2020), whereas PI-CESM is close to the 95^{th}. This suggests a potential overestimation of the future positive change in TC frequency over the North-West Pacific.

The CHAZ model used in Lee et al. (2020) showed an upward trends of 1.2 TCs per decade, which corresponds to an increase of 50% in the North-West Pacific by the end of the century, which is similar to what we found in this study by 2060.

In North-West Pacific, the relative changes associated with the RV-CESM (+64%) and AV-CESM (+95%) versions are outliers in Knutson et al. (2020)'s results, while PI-CESM changes (32%) are between the 75^{th} and the 95^{th} percentiles. Bloemendaal et al. (2022) found positive changes ranging between 37% and 82%, similar to what we obtain in our versions (between 26% and 91%).All increases in the relative changes for Cat.4-5 storms are associated with upward trends.

AV-CESM and PI-CESM show a small decrease in storm density between the western part of the Philippine Sea and the northern part of the South China Sea across all categories of storms(Fig.D.30, Fig.D.40).

The LMI relative change in the North-West Pacific is more modest, approximately +1%, below the 5^{th} percentile of relative change values reported by Knutson et al. (2020).

An opposite result to our increase in ACE is instead obtained in the North-West Pacific by Roberts et al. (2020) probably due to a decrease in TC frequency observed in low resolution models.

In the North-Pacific, RV-CESM indicates an increase in landfall rates ranging from 20% to 40%, while AV-CESM shows a more substantial increase, ranging from 40% to over 100%. This increase is almost uniform with higher values compared to the rest of the basin over north-western China, Korea and Japan. PI-CESM exhibits a similar pattern to AV-CESM, but with smaller values, ranging from 0% to 60%.

In North-West Pacific, an increase in total risk is found all over the basin in all versions, except for central-southern China in PI-CESM (Fig.D.34, Fig.D.44, Fig.D.45). Changes in risk for AV-CESM are higher compared to the other versions. The increase in risk can be attributed to the positive change in landfall rates for RV-CESM and AV-CESM. PI-CESM indicates more complex results with landfall rates being the main contribution in the increase in total risk over the northern part of the basin. Landfall rates and exposure have the same impact on the increasing risk over South Asia whereas exposure becomes the main factor over south-central China, except for the coasts where landfall rate changes play a similar role.

D.3 North-West Pacific (Supplementary figures)

Regarding the initial displacement residuals, similar results are found in the North-West Pacific with a significant negative correlation between longitude and dx residuals (-0.147) (Fig.D.21). As well as in the North Atlantic, no notable spatial patterns are found across the basin (Fig.D.22).

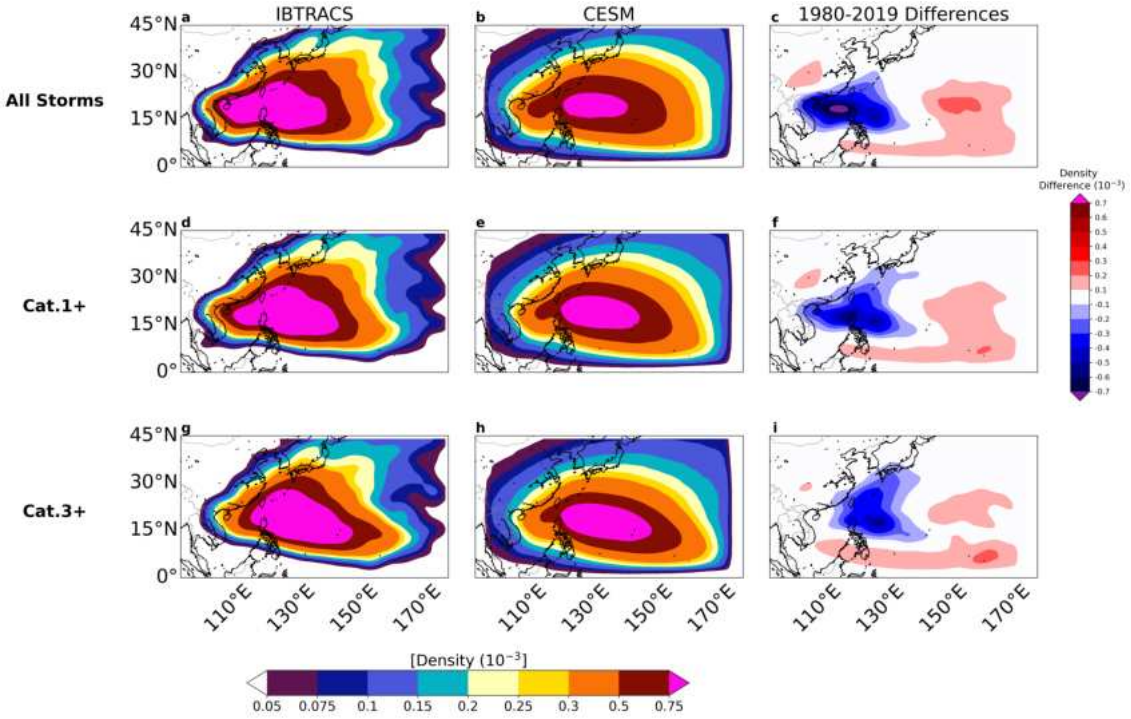

Figure D.35: Difference in North-West Pacific TC density between observations and RV-CESM. JJASON North-West Pacific TC density for the period 1980-2019 for a,d,g) IBTrACS and b,e,h) RV-CESM model and c,f,i) and difference in TC density for RV-CESM relatively to observations. Top row) all storms, Middle row) Cat.1+ and Bottom row) major storms.

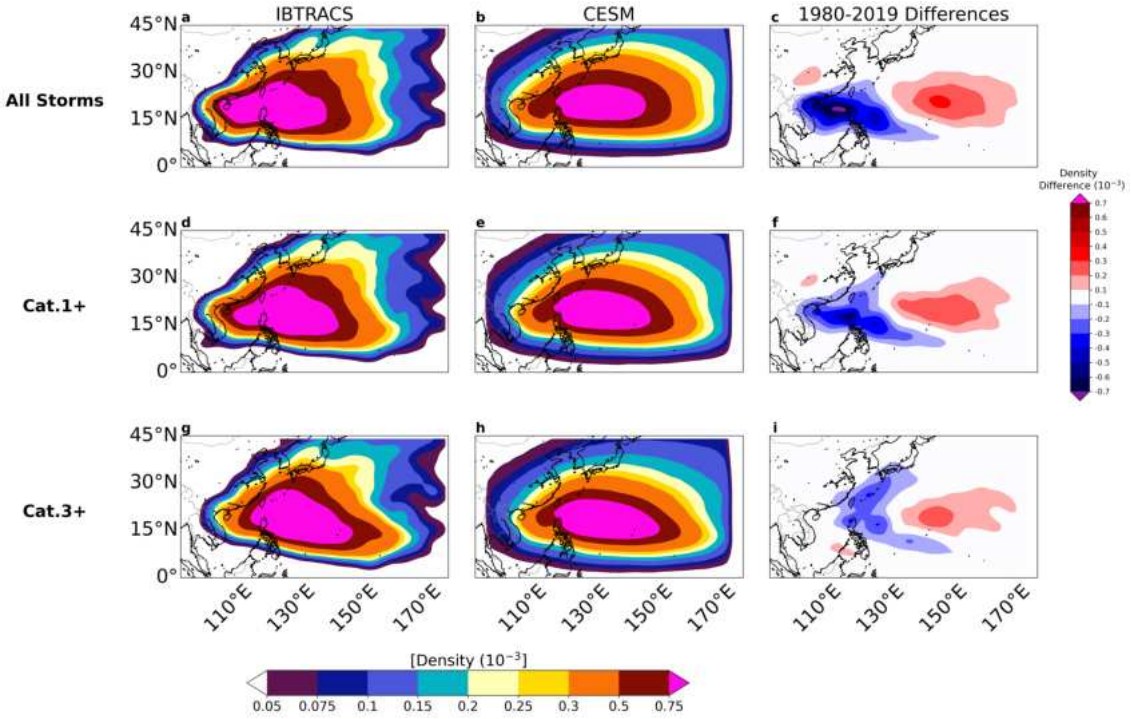

Figure D.36: Difference in North-West Pacific TC density between observations and AV-CESM. JJASON North-West Pacific TC density for the period 1980-2019 for a,d,g) IBTrACS and b,e,h) AV-CESM model and c,f,i) and difference in TC density for AV-CESM relatively to observations. Top row) all storms, Middle row) Cat.1+ and Bottom row) major storms.

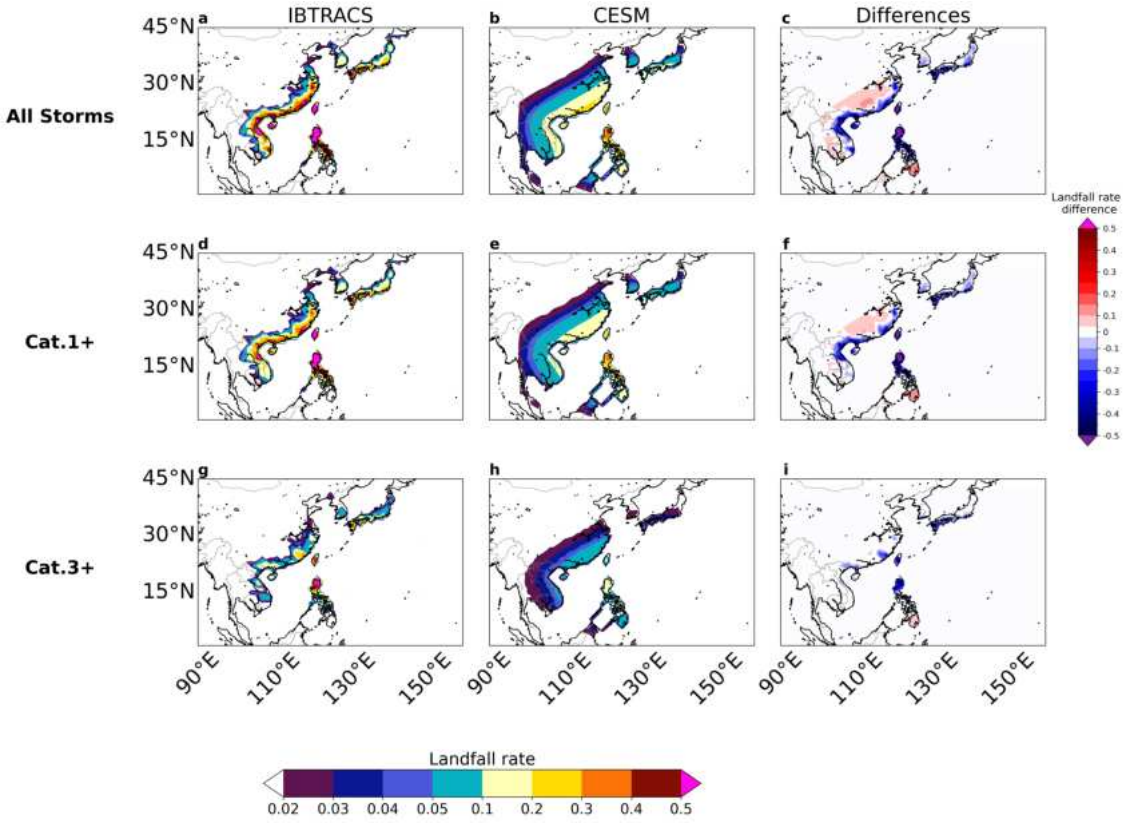

Figure D.37: Difference in North Atlantic TC landfall rates between observations and RV-CESM. JJASON TC landfall rates for the period 1980-2019 for a,d,g) IBTrACS and b,e,h) RV-CESM model and c,f,i) and difference in TC landfall rates for the RV-CESM model relatively to observations. Top row) all storms, Middle row) Cat.1+ and Bottom row) major storms.

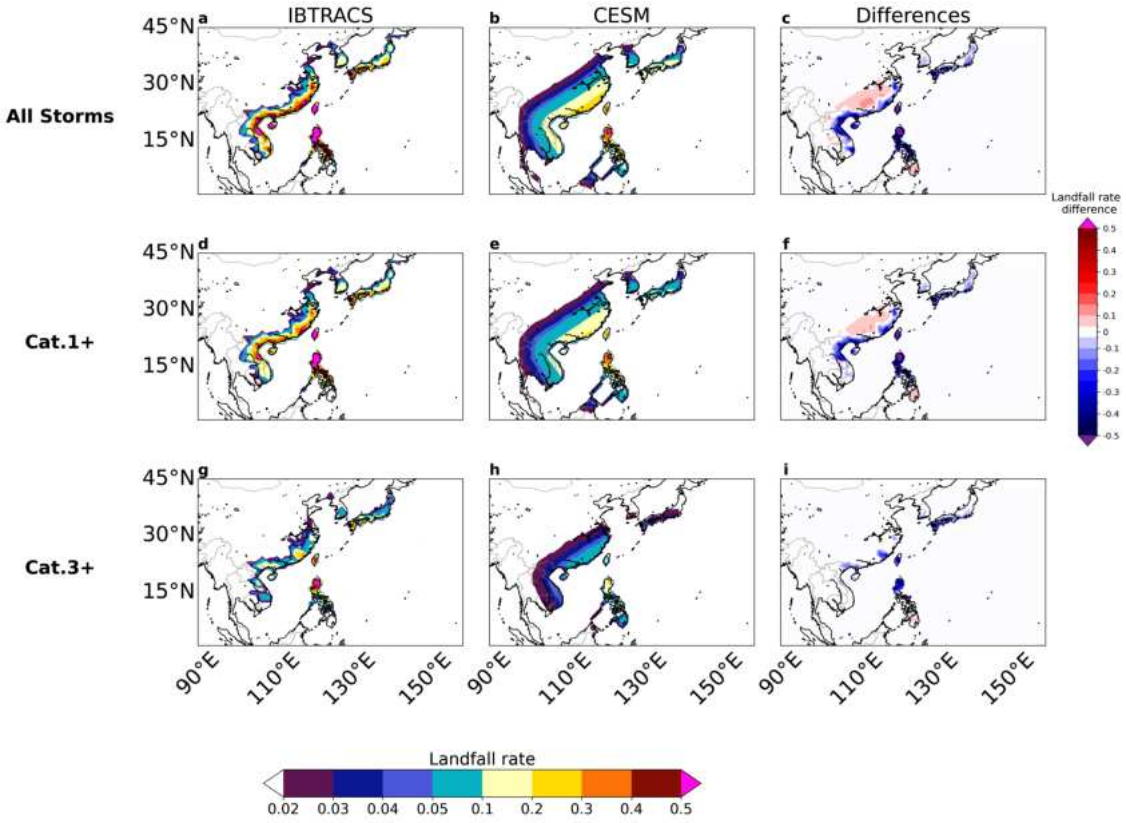

Figure D.38: Difference in North Atlantic TC landfall rates between observations and AV-CESM. JJASON TC landfall rates for the period 1980-2019 for a,d,g) IBTrACS and b,e,h) AV-CESM model and c,f,i) and difference in TC landfall rates for the AV-CESM model relatively to observations. Top row) all storms, Middle row) Cat.1+ and Bottom row) major storms.

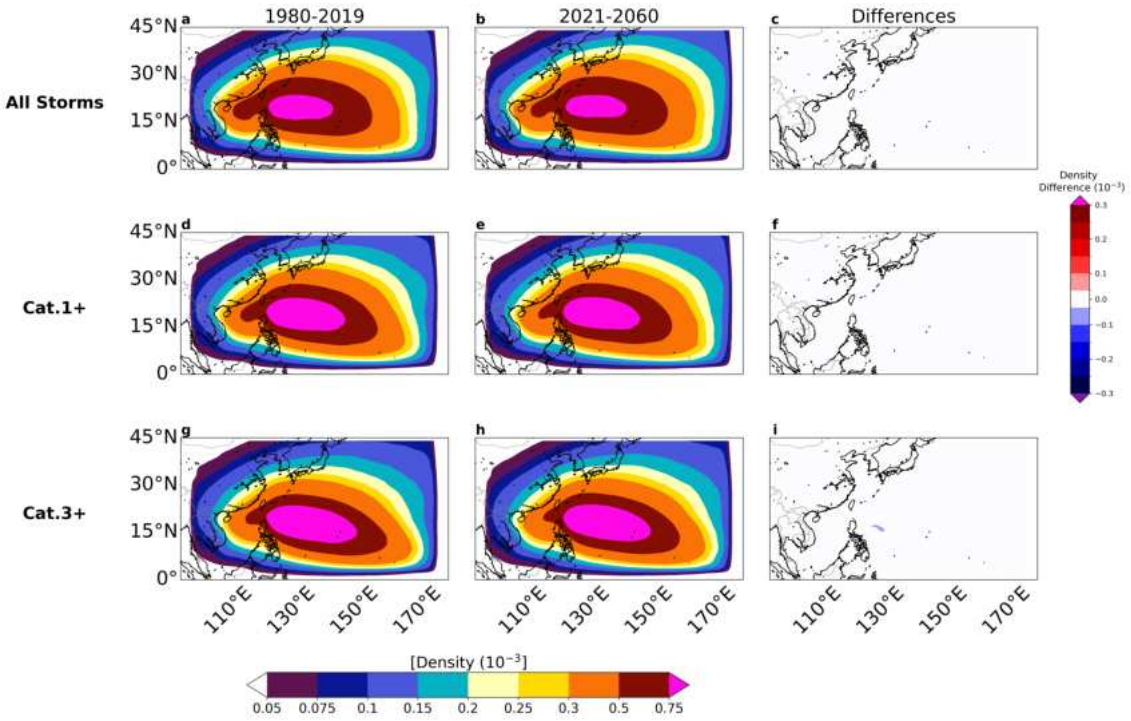

Figure D.39: Future change in North-West Pacific JJASON TC density. TC density for the period a,d,g) 1980-2019 and b,e,h) 2021-2060 and c,f,i) change in TC density for the RV-CESM relative to observations. Top row) all storms, Middle row) Cat.1+ and Bottom row) major storms.

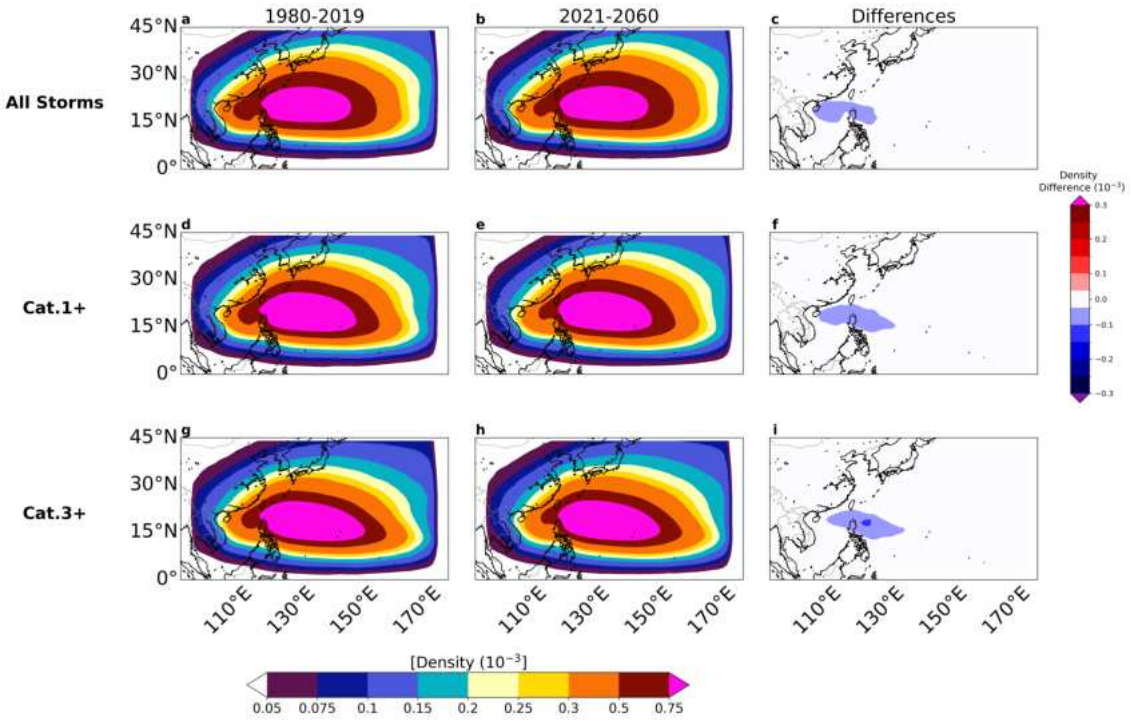

Figure D.40: Future change in North-West Pacific JJASON TC density. TC density for the period a,d,g) 1980-2019 and b,e,h) 2021-2060 and c,f,i) change in TC density for the AV-CESM relative to observations. Top row) all storms, Middle row) Cat.1+ and Bottom row) major storms.

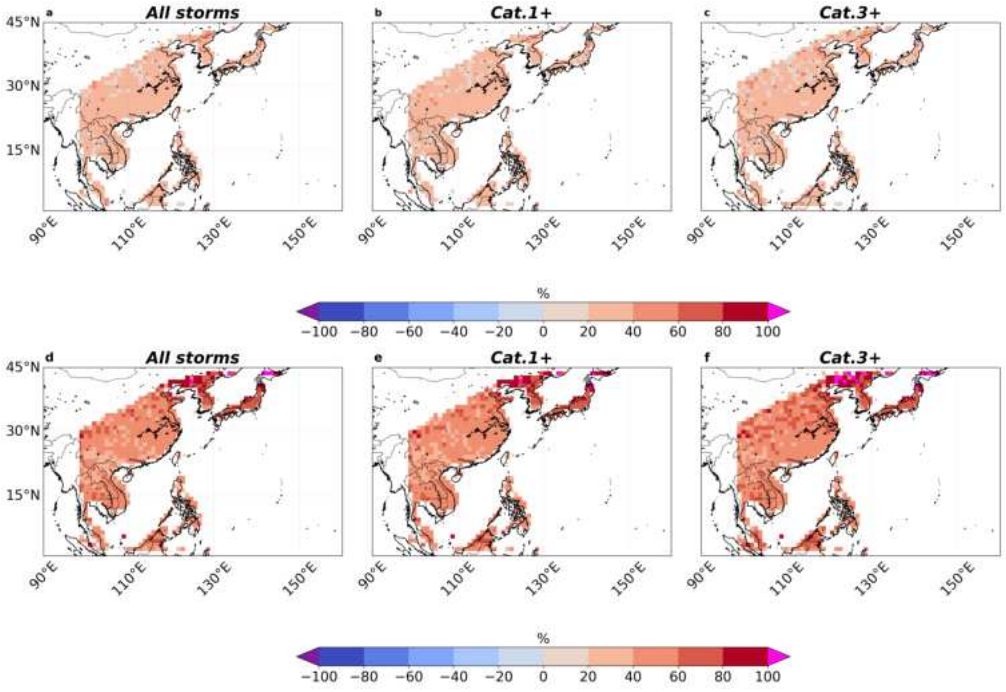

Figure D.41: Change in North-West Pacific landfall rates. a-c) Change (%) in landfall rates over in North-West Pacific for the period 2010-2030 relatively to 1980-2000 for a) all storms, b) Cat.1+ and c) major storms in RV-CESM. d-f) Same as a-c but for 2041-2060 relatively to 2011-2030.

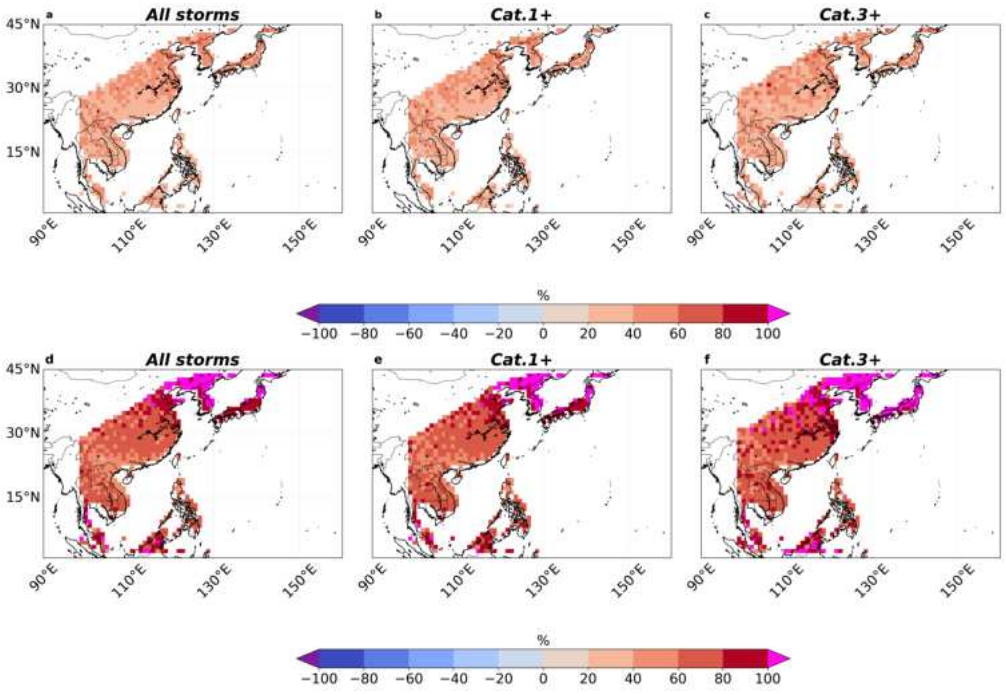

Figure D.42: Change in North-West Pacific landfall rates. a-c) Change (%) in landfall rates over in North-West Pacific for the period 2010-2030 relatively to 1980-2000 for a) all storms, b) Cat.1+ and c) major storms in AV-CESM. d-f) Same as a-c but for 2041-2060 relatively to 2011-2030.

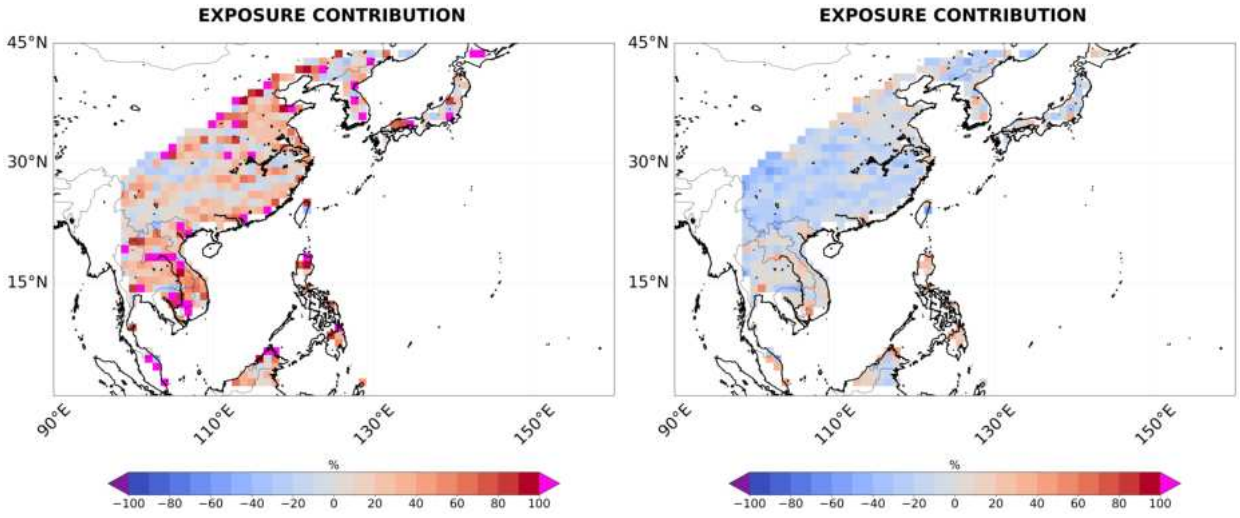

Figure D.43: Change in North-West Pacific population. Left panel) Change (%) in population in North-West Pacific for the period 2010-2030 relatively to 1980-2000. Right panel) same as right panel but for 2041-2060 relatively to 2011-2030.

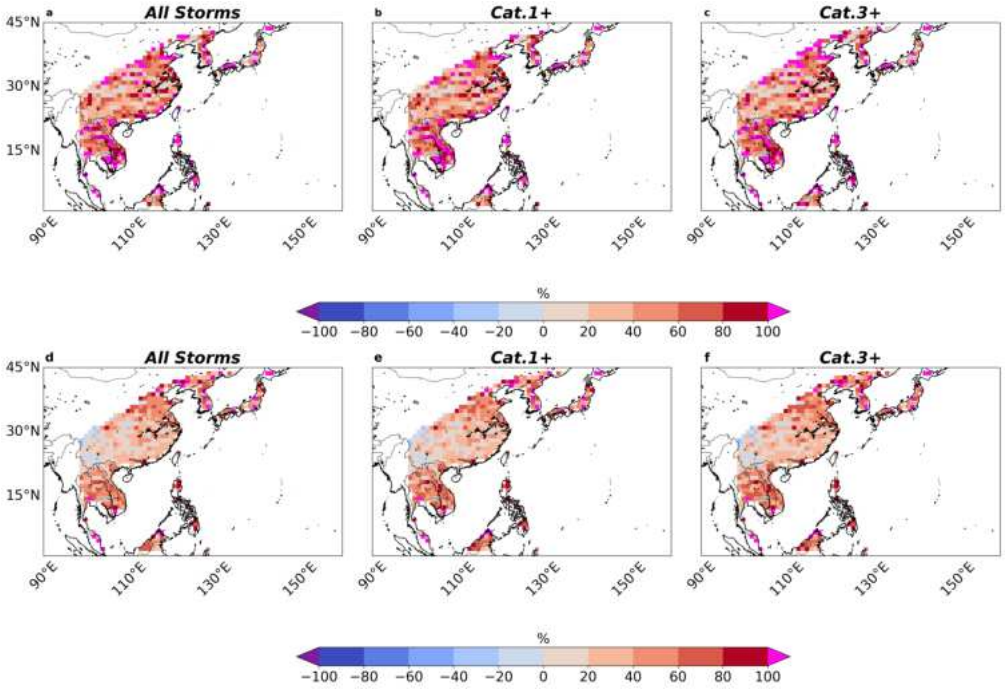

Figure D.44: Change in North-West Pacific total risk. a-c) Change (%) in total risk over North-West Pacific for the period 2010-2030 relatively to 1980-2000 for a) all storms, b) Cat.1+ and c) major storms in RV-CESM. d-f) same as a-c but for 2041-2060 relatively to 2011-2030.

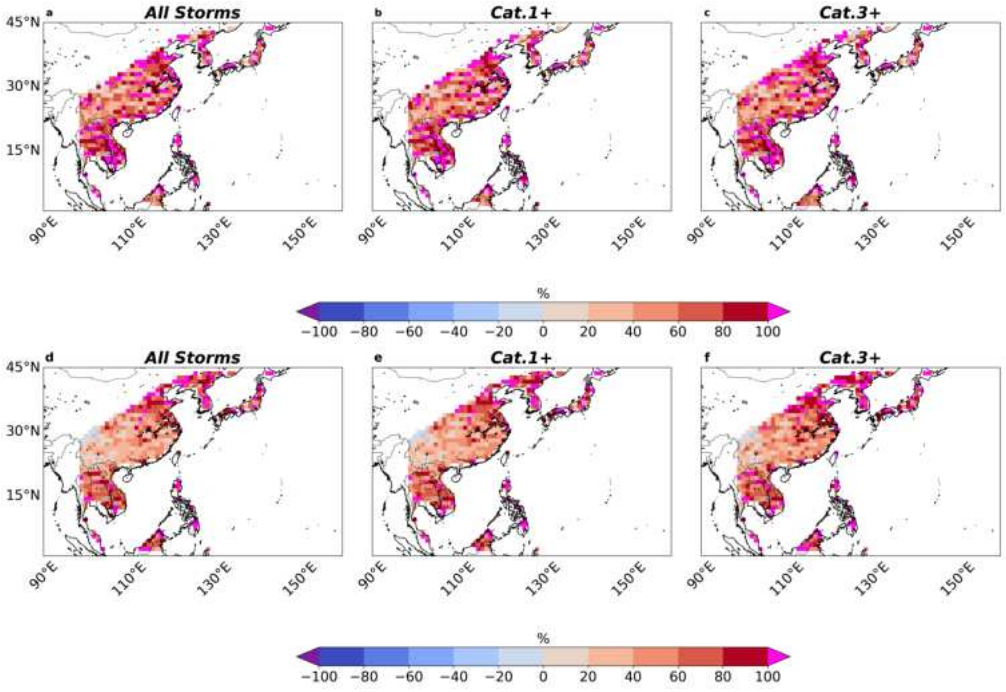

Figure D.45: Change in North-West Pacific total risk. a-c) Change (%) in total risk over North-West Pacific for the period 2010-2030 relatively to 1980-2000 for a) all storms, b) Cat.1+ and c) major storms in AV-CESM. d-f) same as a-c but for 2041-2060 relatively to 2011-2030.

BIBLIOGRAPHY

Abiodun, B. J., Adeyewa, Z. D., Oguntunde, P. G., Salami, A. T., and Ajayi, V. O. (2012). Modeling the impacts of reforestation on future climate in West Africa. *Theoretical and Applied Climatology*, 110:77–96.

Agwe, J. N., Arnold, M., Buys, P., Chen, R. S., Deichmann, U. K., Dilley, M., Kjevstad, O., Lerner-Lam, A. L., Lyon, B., and Yetman, G. (2005). Natural disaster hotspots: A global risk analysis.

Aiyyer, A. and Thorncroft, C. (2011). Interannual-to-multidecadal variability of vertical shear and tropical cyclone activity. *Journal of Climate*, 24.

Ali, A. and Lebel, T. (2009). The Sahelian standardized rainfall index revisited. *International Journal of Climatology*, 29.

Andersson, E., Brogaard, S., and Olsson, L. (2011). The political ecology of land degradation.

Arthur, W. C. (2021). A statistical-parametric model of tropical cyclones for hazard assessment. *Natural Hazards and Earth System Sciences*, 21:893–916.

Ascenso, G., Cavicchia, L., Scoccimarro, E., and Castelletti, A. (2023). Optimisation-based refinement of genesis indices for tropical cyclones. *Environmental Research Communications*, 5:021001.

Audu, E., Dixon, R., and Diallo, I. (2024). Understanding the zonal variability in projections of Sahel precipitation. *Geophysical Research Letters*, 51:e2024GL110177.

Avila, L. A., Pasch, R. J., and Jiing, J. G. (2000). Atlantic tropical systems of 1996 and 1997: Years of contrasts. *Monthly Weather Review*, 128.

Aznar-Siguan, G. and Bresch, D. N. (2019). CLIMADA v1: A global weather and climate risk assessment platform. *Geoscientific Model Development*, 12.

Bacmeister, J. T., Reed, K. A., Hannay, C., Lawrence, P., Bates, S., Truesdale, J. E., Rosenbloom, N., and Levy, M. (2018). Projected changes in tropical cyclone activity under future warming scenarios using a high-resolution climate model. *Climatic Change*, 146:547–560.

Bamba, A., Diallo, I., Touré, N. D., Kouadio, K., Konaré, A., Dramé, M. S., Diedhiou, A., Silué, S., Doumbia, M., and Tall, M. (2019). Effect of the African greenbelt position on West African summer climate: a regional climate modeling study. *Theoretical and Applied Climatology*, 137:309–322.

Behnke, R. and Mortimore, M. (2016). *Introduction: The End of Desertification?* Springer.

Bell, G. D., Halpert, M. S., Schnell, R. C., Higgins, R. W., Lawrimore, J., Kousky, V. E., Tinker, R., Thiaw, W., Chelliah, M., and Artusa, A. (2000). Climate assessment for 1999. *Bulletin of the American Meteorological Society*, 81.

Beobide-Arsuaga, G., Bayr, T., Reintges, A., and Latif, M. (2021). Uncertainty of ENSO-amplitude projections in CMIP5 and CMIP6 models. *Climate Dynamics*, 56:3875–3888.

Bercos-Hickey, E. and Patricola, C. M. (2021). Anthropogenic influences on the African Easterly Jet–African Easterly Wave system. *Climate Dynamics*, 57:2779–2792.

Berkson, J. (1944). Application of the logistic function to bio-assay. *Journal of the American Statistical Association*, 39:357–365.

Biasutti, M. (2013). Forced Sahel rainfall trends in the CMIP5 archive. *Journal of Geophysical Research Atmospheres*, 118.

Biasutti, M. (2019). Rainfall trends in the African Sahel: Characteristics, processes, and causes.

Biasutti, M., Held, I. M., Sobel, A. H., and Giannini, A. (2008). SST Forcings and Sahel rainfall variability in simulations of the twentieth and twenty-first centuries. *Journal of Climate*, 21:3471–3486.

Bister, M. and Emanuel, K. A. (1998). Dissipative heating and hurricane intensity. *Meteorology and Atmospheric Physics*, 65.

Bloemendaal, N., de Moel, H., Martinez, A. B., Muis, S., Haigh, I. D., van der Wiel, K., Haarsma, R. J., Ward, P. J., Roberts, M. J., Dullaart, J. C., and Aerts, J. C. (2022). A globally consistent local-scale assessment of future tropical cyclone risk. *Science Advances*, 8:8438.

Bloemendaal, N., Haigh, I. D., de Moel, H., Muis, S., Haarsma, R. J., and Aerts, J. C. (2020). Generation of a global synthetic tropical cyclone hazard dataset using STORM. *Scientific Data 2020 7:1*, 7:1–12.

Bourdin, S., Fromang, S., Dulac, W., Cattiaux, J., and Chauvin, F. (2022). Intercomparison of four algorithms for detecting tropical cyclones using ERA5. *Geoscientific Model Development*, 15:6759–6786.

Bove, M. C., Elsner, J. B., Landsea, C. W., Niu, X., and O'Brien, J. J. (1998). Effect of El Niño on U.S. landfalling hurricanes, revisited. *Bulletin of the American Meteorological Society*, 79.

Bruyère, C. L., Holland, G. J., and Towler, E. (2012). Investigating the use of a genesis potential index for tropical cyclones in the North Atlantic basin. *Journal of Climate*, 25:8611–8626.

Burpee, R. W. (1972). The origin and structure of easterly waves in the lower troposphere of North Africa. *Journal of the Atmospheric Sciences*, 29.

Burpee, R. W. (1974). Characteristics of North African easterly waves during the summers of 1968 and 1969. *Journal of the Atmospheric Sciences*, 31.

Bye, J. and Keay, K. (2008). A new hurricane index for the Caribbean. *Interciencia*, 33:556–560.

Byrne, M. P. and O'Gorman, P. A. (2013). Link between land-ocean warming contrast and surface relative humidities in simulations with coupled climate models. *Geophysical Research Letters*, 40.

Byrne, M. P. and O'Gorman, P. A. (2018). Trends in continental temperature and humidity directly linked to ocean warming. *Proceedings of the National Academy of Sciences of the United States of America*, 115.

Camargo, S. J. (2013). Global and regional aspects of tropical cyclone activity in the CMIP5 models. *Journal of Climate*, 26:9880–9902.

Camargo, S. J., Giulivi, C. F., Sobel, A. H., Wing, A. A., Kim, D., Moon, Y., Strong, J. D., Genio, A. D. D., Kelley, M., Murakami, H., Reed, K. A., Scoccimarro, E., Vecchi, G. A., Wehner, M. F., Zarzycki, C., and Zhao, M. (2020). Characteristics of model tropical cyclone climatology and the large-scale environment. *Journal of Climate*, 33:4463–4487.

Camargo, S. J., Murakami, H., Bloemendaal, N., Chand, S. S., Deshpande, M. S., Dominguez-Sarmiento, C., González-Alemán, J. J., Knutson, T. R., Lin, I. I., Moon, I. J., Patricola, C. M., Reed, K. A., Roberts, M. J., Scoccimarro, E., Tam, C. Y. F., Wallace, E. J., Wu, L., Yamada, Y., Zhang, W., and Zhao, H. (2023). An update on the influence of natural climate variability and anthropogenic climate change on tropical cyclones. *Tropical Cyclone Research and Review*, 12:216–239.

Camargo, S. J., Sobel, A. H., Barnston, A. G., and Emanuel, K. A. (2007). Tropical cyclone genesis potential index in climate models. *Tellus A*, 59:428–443.

Camargo, S. J., Sobel, A. H., Barnston, A. G., and Klotzbach, P. J. (2010). The influence of natural climate variability on tropical cyclones, and seasonal forecasts of tropical cyclone activity. *Global Perspectives On Tropical Cyclones: From Science To Mitigation*, pages 325–360.

Camargo, S. J., Tippett, M. K., Sobel, A. H., Vecchi, G. A., and Zhao, M. (2014). Testing the performance of tropical cyclone genesis indices in future climates using the HiRAM model. *Journal of Climate*, 27:9171–9196.

Camargo, S. J. and Wing, A. A. (2016). Tropical cyclones in climate models. *Wiley Interdisciplinary Reviews: Climate Change*, 7:211–237.

Camargo, S. J. and Zebiak, S. E. (2002). Improving the detection and tracking of tropical cyclones in atmospheric general circulation models. *Weather and Forecasting*, 17.

Carlson, T. N. (1969). Some remarks on african disturbances and their progress over the tropical atlantic. *Monthly Weather Review*, 97.

Caron, L. P. and Jones, C. G. (2012). Understanding and simulating the link between African easterly waves and Atlantic tropical cyclones using a regional climate model: The role of domain size and lateral boundary conditions. *Climate Dynamics*, 39:113–135.

Caron, L. P., Jones, C. G., and Winger, K. (2011). Impact of resolution and downscaling technique in simulating recent Atlantic tropical cylone activity. *Climate Dynamics*, 37:869–892.

Carozza, D. A., Boudreault, M., Grenier, M., and Caron, L. P. (2024). UQAM-TCW: A global hybrid tropical cyclone wind model based upon statistical and coupled climate models. *Journal of Advances in Modeling Earth Systems*, 16:e2023MS003799.

Chan, J. C. and Gray, W. M. (1982). Tropical cyclone movement and surrounding flow relationships. *Monthly Weather Review*, 110.

Chand, S. S., Mcbride, J. L., Tory, K. J., Wheeler, M. C., and Walsh, K. J. (2013). Impact of different ENSO regimes on southwest pacific tropical cyclones. *Journal of Climate*, 26:600–608.

Charney, J., Stone, P. H., and Quirk, W. J. (1975). Drought in the Sahara: A biogeophysical feedback mechanism. *Science*, 187.

Chauvin, F., Pilon, R., Palany, P., and Belmadani, A. (2020). Future changes in Atlantic hurricanes with the rotated-stretched ARPEGE-Climat at very high resolution. *Climate Dynamics*, 54:947–972.

Chauvin, F., Royer, J. F., and Déqué, M. (2006). Response of hurricane-type vortices to global warming as simulated by ARPEGE-Climat at high resolution. *Climate Dynamics*, 27:377–399.

Chen, T. C., Wang, S. Y., and Clark, A. J. (2008). North Atlantic hurricanes contributed by african esterly waves north and south of the African easterly jet. *Journal of Climate*, 21.

Chou, C. and Neelin, J. D. (2003). Mechanisms limiting the northward extent of the northern summer monsoons over North America, Asia, and Africa. *Journal of Climate*, 16.

Coats, S. and Karnauskas, K. B. (2017). Are simulated and observed twentieth century tropical Pacific sea surface temperature trends significant relative to internal variability? *Geophysical Research Letters*, 44:9928–9937.

Collins, M., il An, S., Cai, W., Ganachaud, A., Guilyardi, E., Jin, F.-F., Jochum, M., Lengaigne, M., Power, S., Timmermann, A., Vecchi, G., and Wittenberg, A. (2010). The impact of global warming on the tropical pacific ocean and El Niño. *Nature Geoscience*, 3.

Conover, W. J. (1999). Chapter 6 nonparametric methods. *Chapter 5*, II:126–200.

Corder, G. W. and Foreman, D. I. (2011). Nonparametric statistics for non-statisticians: A step-by-step approach. *Nonparametric Statistics for Non-Statisticians: A Step-by-Step Approach*, pages 1–536.

Côté, J., Gravel, S., Mé, A., Thot, , Patoine, A., Roch, M., and Staniforth, A. (1998). The operational cmc–mrb global environmental multiscale (gem) model. part i: Design considerations and formulation. *Monthly Weather Review*, 126:1373–1395.

Dandoy, S., Pausata, F. S., Camargo, S. J., Laprise, R., Winger, K., and Emanuel, K. (2021). Atlantic hurricane response to Saharan greening and reduced dust emissions during the mid-holocene. *Climate of the Past*, 17:675–701.

Danso, D. K., Patricola, C. M., and Bercos-Hickey, E. (2022). Influence of African Easterly Wave Suppression on Atlantic Tropical Cyclone Activity in a Convection-Permitting Model. *Geophysical Research Letters*, 49:e2022GL100590.

Dardel, C., Kergoat, L., Hiernaux, P., Mougin, E., Grippa, M., and Tucker, C. J. (2014). Re-greening Sahel: 30 years of remote sensing data and field observations (Mali, Niger). *Remote Sensing of Environment*, 140.

Dare, R. A. and Mcbride, J. L. (2011). The threshold sea surface temperature condition for tropical cyclogenesis. *Journal of Climate*, 24:4570–4576.

Davin, E. L., Rechid, D., Breil, M., Cardoso, R. M., Coppola, E., Hoffmann, P., Jach, L. L., Katragkou, E., Noblet-Ducoudré, N. D., Radtke, K., Raffa, M., Soares, P. M., Sofiadis, G., Strada, S., Strandberg, G., Tölle, M. H., Warrach-Sagi, K., and Wulfmeyer, V. (2020). Biogeophysical impacts of forestation in Europe: First results from the LUCAS (Land Use and Climate across Scales) regional climate model intercomparison. *Earth System Dynamics*, 11.

Davis, C. A. (2018). Resolving tropical cyclone intensity in models. *Geophysical Research Letters*, 45:2082–2087.

Dee, D. P., Uppala, S. M., Simmons, A. J., Berrisford, P., Poli, P., Kobayashi, S., Andrae, U., Balmaseda, M. A., Balsamo, G., Bauer, P., Bechtold, P., Beljaars, A. C., van de Berg, L., Bidlot, J., Bormann, N., Delsol, C., Dragani, R., Fuentes, M., Geer, A. J., Haimberger, L., Healy, S. B., Hersbach, H., Hólm, E. V., Isaksen, L., Kållberg, P., Köhler, M., Matricardi, M., Mcnally, A. P., Monge-Sanz, B. M., Morcrette, J. J., Park, B. K., Peubey, C., de Rosnay, P., Tavolato, C., Thépaut, J. N., and Vitart, F. (2011). The ERA-Interim reanalysis: configuration and performance of the data assimilation system. *Quarterly Journal of the Royal Meteorological Society*, 137:553–597.

DeMaria, M., Knaff, J. A., and Connell, B. H. (2001). A tropical cyclone genesis parameter for the tropical Atlantic. *Weather and Forecasting*, 16.

Diba, I., Camara, M., and Sarr, A. B. (2016). Impacts of the Sahel-Sahara interface reforestation on West African climate: Intraseasonal variability and extreme precipitation events. *Advances in Meteorology*, 2016:3262451.

Diedhiou, A., Bichet, A., Wartenburger, R., Seneviratne, S. I., Rowell, D. P., Sylla, M. B., Diallo, I., Todzo, S., Touré, N. E., Camara, M., Ngatchah, B. N., Kane, N. A., Tall, L., and Affholder, F. (2018). Changes in climate extremes over West and central Africa at 1.5°c and 2°c global warming. *Environmental Research Letters*, 13:065020.

Diedhiou, A., Janicot, S., Viltard, A., Felice, P. D., and Laurent, H. (1999). Easterly wave regimes and associated convection over West Africa and tropical Atlantic: Results from the NCEP/NCAR and ECMWF reanalyses. *Climate Dynamics*, 15:795–822.

Dieng, A. L., Sall, S. M., Eymard, L., Leduc-Leballeur, M., and Lazar, A. (2017). Trains of African Easterly Waves and their relationship to tropical cyclone genesis in the eastern Atlantic. *Monthly Weather Review*, 145:599–616.

Diffenbaugh, N. S. and Giorgi, F. (2012). Climate change hotspots in the CMIP5 global climate model ensemble. *Climatic Change*, 114:813–822.

Donohoe, A., Marshall, J., Ferreira, D., and Mcgee, D. (2013). The relationship between ITCZ location and cross-equatorial atmospheric heat transport: From the seasonal cycle to the last glacial maximum. *Journal of Climate*, 26.

Dosio, A., Jury, M. W., Almazroui, M., Ashfaq, M., Diallo, I., Engelbrecht, F. A., Klutse, N. A., Lennard, C., Pinto, I., Sylla, M. B., and Tamoffo, A. T. (2021). Projected future daily characteristics of African precipitation based on global (CMIP5, CMIP6) and regional (CORDEX, CORDEX-CORE) climate models. *Climate Dynamics*, 57:3135–3158.

Dosio, A., Lennard, C., and Spinoni, J. (2022). Projections of indices of daily temperature and precipitation based on bias-adjusted CORDEX-Africa regional climate model simulations. *Climatic Change 2022 170:1*, 170:1–24.

Douris, J., Kim, G., Abrahams, J., Moreno, J. L., Shumake-Guillemot, J., Green, H., and Murray, V. (2021). *WMO Atlas of Mortality and Economic Losses from Weather, Climate and Water Extremes (1970–2019) (WMO-No. 1267)*, volume 1267. WMO.

Elagib, N. A., Khalifa, M., Babker, Z., Musa, A. A., and Fink, A. H. (2021). Demarcating the rainfed unproductive zones in the African Sahel and Great Green Wall regions. *Land Degradation and Development*, 32:1400–1411.

Elsner, J. B., Kossin, J. P., and Jagger, T. H. (2008). The increasing intensity of the strongest tropical cyclones. *Nature 2008 455:7209*, 455:92–95.

Emanuel, K. (2003). Tropical cyclones. *Annual Review of Earth and Planetary Sciences*, 31:75–104.

Emanuel, K. (2005). Increasing destructiveness of tropical cyclones over the past 30 years. *Nature*, 436.

Emanuel, K. (2010). Tropical cyclone activity downscaled from NOAA-CIRES reanalysis, 1908–1958. *Journal of Advances in Modeling Earth Systems*, 2.

Emanuel, K. (2017). A fast intensity simulator for tropical cyclone risk analysis. *Natural Hazards*, 88:779–796.

Emanuel, K. (2022). Tropical cyclone seeds, transition probabilities, and genesis. *Journal of Climate*, 35:3557–3566.

Emanuel, K. and Jagger, T. (2010). On estimating hurricane return periods. *Journal of Applied Meteorology and Climatology*, 49:837–844.

Emanuel, K. and Nolan, D. S. (2004). Tropical cyclone activity and the global climate system. In Soc., A. M., editor, *26th Conference on Hurricanes and Tropical Meteorology*.

Emanuel, K., Ravela, S., Vivant, E., and Risi, C. (2006). A statistical deterministic approach to hurricane risk assessment. *Bulletin of the American Meteorological Society*, 87:299–314.

Emanuel, K. and Sobel, A. (2013). Response of tropical sea surface temperature, precipitation, and tropical cyclone-related variables to changes in global and local forcing. *Journal of Advances in Modeling Earth Systems*, 5.

Emanuel, K., Sundararajan, R., and Williams, J. (2008). Hurricanes and global warming: Results from downscaling IPCC AR4 simulations. *Bulletin of the American Meteorological Society*, 89.

Emanuel, K. A. (1986). An air-sea interaction theory for tropical cyclones. Part i: steady-state maintenance. *Journal of the Atmospheric Sciences*, 43.

Emanuel, K. A. (1987). The dependence of hurricane intensity on climate. *Nature*, 326.

ESA (2015). Land cover CCI product user guide version 2.0.

Findell, K. L., Pitman, A. J., England, M. H., and Pegion, P. J. (2009). Regional and global impacts of land cover change and sea surface temperature anomalies. *Journal of Climate*, 22.

Folland, C. K., Palmer, T. N., and Parker, D. E. (1986). Sahel rainfall and worldwide sea temperatures, 1901–85. *Nature 1986 320:6063*, 320:602–607.

Fosu, B., Sobel, A., Camargo, S., Tippett, M., Hemmati, M., Bowen, S., and Bloemendaal, N. (2024). Assessing future tropical cyclone risk using downscaled 1 CMIP6 projections. *Journal of Catastrophe Risk and Resilience*, 2.

Frank, N. L. (1970). Atlantic tropical systems of 1969. *Monthly Weather Review*, 98.

Frich, P., Alexander, L. V., Della-Marta, P., Gleason, B., Haylock, M., Klein, A. M. T., and Peterson, T. (2002). Observed coherent changes in climatic extremes during the second half of the twentieth century. *Climate Research*, 19:193–212.

Gebremichael, M. and Hossain, F. (2010). Satellite rainfall applications for surface hydrology. *Satellite Rainfall Applications for Surface Hydrology*, pages 1–327.

Giambelluca, T. W., Hölscher, D., Bastos, T. X., Frazão, R. R., Nullet, M. A., and Ziegler, A. D. (1997). Observations of albedo and radiation balance over postforest land surfaces in the eastern Amazon Basin. *Journal of Climate*, 10.

Giannini, A. and Kaplan, A. (2019). The role of aerosols and greenhouse gases in Sahel drought and recovery. *Climatic Change*, 152:449–466.

Giannini, A., Salack, S., Lodoun, T., Ali, A., Gaye, A. T., and Ndiaye, O. (2013). A unifying view of climate change in the Sahel linking intra-seasonal, interannual and longer time scales. *Environmental Research Letters*, 8:024010.

Giannini, A., Saravanan, R., and Chang, P. (2003). Oceanic forcing of Sahel rainfall on interannual to interdecadal time scales. *Science*, 302:1027–1030.

Gilford, D. M. (2021). PyPI (v1.3): Tropical cyclone potential intensity calculations in Python. *Geoscientific Model Development*, 14:2351–2369.

Giorgi, F. (2006). Climate change hot-spots. *Geophysical Research Letters*, 33.

Giorgi, F., Jones, C., and Asrar, G. (2009). Addressing climate information needs at the regional level: the CORDEX framework. ... *Organization (WMO) Bulletin*.

Girard, C., Plante, A., Desgagné, M., Mctaggart-Cowan, R., Côté, J., Charron, M., Gravel, S., Lee, V., Patoine, A., Qaddouri, A., Roch, M., Spacek, L., Tanguay, M., Vaillancourt, P. A., and Zadra, A. (2014). Staggered vertical discretization of the Canadian Environmental Multiscale (GEM) model using a coordinate of the log-hydrostatic-pressure type. *Monthly Weather Review*, 142:1183–1196.

Goffner, D., Sinare, H., and Gordon, L. J. (2019). The Great Green Wall for the Sahara and the Sahel initiative as an opportunity to enhance resilience in Sahelian landscapes and livelihoods. *Regional Environmental Change*, 19:1417–1428.

Goldenberg, S. B., Landsea, C. W., Mestas-Nuñez, A. M., and Gray, W. M. (2001). The recent increase in Atlantic hurricane activity: Causes and implications. *Science*, 293.

Goldenberg, S. B. and Shapiro, L. J. (1996). Physical mechanisms for the association of El Niño and west African rainfall with Atlantic major hurricane activity. *Journal of Climate*, 9.

Govaerts, Y. and Lattanzio, A. (2008). Estimation of surface albedo increase during the eighties Sahel drought from Meteosat observations. *Global and Planetary Change*, 64.

Gray, W. M. (1979). Hurricanes : Their formation, structure and likely role in the general circulation. *Meteorology over the Tropical Oceans*, 87.

Gray, W. M. (1990). Strong association between West African rainfall and U.S. landfall of intense hurricanes. *Science*, 249:1251–1256.

Grist, J. P. and Nicholson, E. (2001). A study of the dynamic factors influencing the rainfall variability in the West African Sahel. *Journal of Climate*, 14.

Gu, G. and Adler, R. F. (2004). Seasonal evolution and variability associated with the West African monsoon system. *Journal of Climate*, 17.

Guenedal, T. L., Drobinski, P., and Tankov, P. (2022). Cyclone generation Algorithm including a THERmodynamic module for Integrated National damage Assessment (CATHERINA 1.0) compatible with Coupled Model Intercomparison Project (CMIP) climate data. *Geoscientific Model Development*, 15:8001–8039.

Guha-Sapir, D., Below, R., and Hoyois, P. (2017). EM-DAT - The international disaster database.

Hamilton, R. A., Archbold, J. W., and Douglas, C. K. (1945). Meteorology of Nigeria and adjacent territory. *Quarterly Journal of the Royal Meteorological Society*, 71.

Hardy, T. A., McConochie, J. D., and Mason, L. B. (2003). Modeling tropical cyclone wave population of the great barrier reef. *Journal of Waterway, Port, Coastal, and Ocean Engineering*, 129:104–113.

Harris, I., Osborn, T. J., Jones, P., and Lister, D. (2020). Version 4 of the CRU TS monthly high-resolution gridded multivariate climate dataset. *Scientific Data*, 7.

Hastenrath, S. and Lamb, P. (1977). Some aspects of circulation and climate over the eastern equatorial Atlantic. *Monthly Weather Review*, 105.

Hastie, T., Tibshirani, R., James, G., and Witten, D. (2021). An introduction to statistical learning with applications in R (2nd edition). *Springer texts*, 102.

Hausfather, Z. and Peters, G. P. (2020). Emissions – the 'business as usual' story is misleading. *Nature 2021 577:7792*, 577:618–620.

He, F. and Posselt, D. J. (2015). Impact of parameterized physical processes on simulated tropical cyclone characteristics in the community atmosphere model. *Journal of Climate*, 28:9857–9872.

Hernández-Díaz, L., Laprise, R., Sushama, L., Martynov, A., Winger, K., and Dugas, B. (2013). Climate simulation over CORDEX Africa domain using the fifth-generation Canadian Regional Climate Model (CRCM5). *Climate Dynamics*, 40:1415–1433.

Hernández-Díaz, L., Nikiéma, O., Laprise, R., Winger, K., and Dandoy, S. (2019). Effect of empirical correction of sea-surface temperature biases on the CRCM5-simulated climate and projected climate changes over North America. *Climate Dynamics*, 53:453–476.

Herrmann, S. M., Anyamba, A., and Tucker, C. J. (2005). Recent trends in vegetation dynamics in the African Sahel and their relationship to climate. *Global Environmental Change*, 15.

Hersbach, H., Bell, B., Berrisford, P., Hirahara, S., Horányi, A., Muñoz-Sabater, J., Nicolas, J., Peubey, C., Radu, R., Schepers, D., Simmons, A., Soci, C., Abdalla, S., Abellan, X., Balsamo, G., Bechtold, P., Biavati, G., Bidlot, J., Bonavita, M., Chiara, G. D., Dahlgren, P., Dee, D., Diamantakis, M., Dragani, R., Flemming, J., Forbes, R., Fuentes, M., Geer, A., Haimberger, L., Healy, S., Hogan, R. J., Hólm, E., Janisková, M., Keeley, S., Laloyaux, P., Lopez, P., Lupu, C., Radnoti, G., de Rosnay, P., Rozum, I., Vamborg, F., Villaume, S., and Thépaut, J. N. (2020). The ERA5 global reanalysis. *Quarterly Journal of the Royal Meteorological Society*, 146:1999–2049.

Hohenegger, C., Brockhaus, P., Bretherton, C. S., and Schär, C. (2009). The soil moisture–precipitation feedback in simulations with explicit and parameterized convection. *Journal of Climate*, 22:5003–5020.

Holl, K. D. and Brancalion, P. H. (2020). Tree planting is not a simple solution.

Holland, G. J. (1997). The maximum potential intensity of tropical cyclones. *Journal of the Atmospheric Sciences*, 54.

Holland, M. M., Hannay, C., Fasullo, J., Jahn, A., Kay, J. E., Mills, M., Simpson, I. R., Wieder, W., Lawrence, P., Kluzek, E., and Bailey, D. (2024). New model ensemble reveals how forcing uncertainty and model structure alter climate simulated across CMIP generations of the Community Earth system Model. *Geoscientific Model Development*, 17:1585–1602.

Hoogewind, K. A., Chavas, D. R., Schenkel, B. A., and O'Neill, M. E. (2020). Exploring controls on tropical cyclone count through the geography of environmental favorability. *Journal of Climate*, 33.

Horn, M., Walsh, K., Zhao, M., Camargo, S. J., Scoccimarro, E., Murakami, H., Wang, H., Ballinger, A., Kumar, A., Shaevitz, D. A., Jonas, J. A., and Oouchi, K. (2014). Tracking scheme dependence of simulated tropical cyclone response to idealized climate simulations. *Journal of Climate*, 27:9197–9213.

Hosmer, D. W., Lemeshow, S., and Sturdivant, R. X. (2013). *Applied Logistic Regression: Third Edition*. Wiley.

Hsieh, T. L., Vecchi, G. A., Yang, W., Held, I. M., and Garner, S. T. (2020). Large-scale control on the frequency of tropical cyclones and seeds: a consistent relationship across a hierarchy of global atmospheric models. *Climate Dynamics*, 55:3177–3196.

Hsieh, T. L., Yang, W., Vecchi, G. A., and Zhao, M. (2022). Model spread in the tropical cyclone frequency and seed propensity index across global warming and ENSO-like perturbations. *Geophysical Research Letters*, 49:e2021GL097157.

Ingrosso, R. and Pausata, F. S. (2024). Contrasting consequences of the Great Green Wall: Easing aridity while increasing heat extremes. *One Earth*, 7:455–472.

IPCC (2001). Climate change 2001: The scientific basis. in contribution of working group i to the third assessment report of the IPCC. *Cambridge University Press, Cambridge*.

IPCC (2023). Weather and climate extreme events in a changing climate. *Climate Change 2021 – The Physical Science Basis*, pages 1513–1766.

Izumo, T., Vialard, J., Lengaigne, M., and Suresh, I. (2020). Relevance of relative sea surface temperature for tropical rainfall interannual variability. *Geophysical Research Letters*, 47:e2019GL086182.

James, M. K. and Mason, L. B. (2006). Closure to "synthetic tropical cyclone database" by M. K. James and L. B. Mason. *Journal of Waterway, Port, Coastal, and Ocean Engineering*, 132:502–503.

Janicot, S., Moron, V., and Fontaine, B. (1996). Sahel droughts and ENSO dynamics. *Geophysical Research Letters*, 23:515–518.

Jing, R. and Lin, N. (2020). An environment-dependent probabilistic tropical cyclone model. *Journal of Advances in Modeling Earth Systems*, 12:e2019MS001975.

Jungandreas, L., Hohenegger, C., and Claussen, M. (2023). How does the explicit treatment of convection alter the precipitation-soil hydrology interaction in the mid-Holocene African humid period? *Climate of the Past*, 19:637–664.

Kachitvichyanukul, V. and Schmeiser, B. W. (1988). Binomial random variate generation. *Communications of the ACM*, 31:216–222.

Kalnay, E., Kanamitsu, M., Kistler, R., Collins, W., Deaven, D., Gandin, L., Iredell, M., Saha, S., White, G., Woollen, J., Zhu, Y., Chelliah, M., Ebisuzaki, W., Higgins, W., Janowiak, J., Mo, K. C., Ropelewski, C., Wang, J., Leetmaa, A., Reynolds, R., Jenne, R., and Joseph, D. (1996). The NCEP/NCAR 40-year reanalysis project. *Bulletin of the American Meteorological Society*, 77.

Kang, S. M., Held, I. M., Frierson, D. M., and Zhao, M. (2008). The response of the ITCZ to extratropical thermal forcing: Idealized slab-ocean experiments with a GCM. *Journal of Climate*, 21.

Kay, J. E., Deser, C., Phillips, A., Mai, A., Hannay, C., Strand, G., Arblaster, J. M., Bates, S. C., Danabasoglu, G., Edwards, J., Holland, M., Kushner, P., Lamarque, J. F., Lawrence, D., Lindsay, K., Middleton, A., Munoz, E., Neale, R., Oleson, K., Polvani, L., and Vertenstein, M. (2015). The community earth system model (CESM) large ensemble project: A community resource for studying climate change in the presence of internal climate variability. *Bulletin of the American Meteorological Society*, 96:1333–1349.

Kemena, T. P., Matthes, K., Martin, T., Wahl, S., and Oschlies, A. (2018). Atmospheric feedbacks in North Africa from an irrigated, afforested Sahara. *Climate Dynamics*, 50:4561–4581.

Kendon, E. J., Stratton, R. A., Tucker, S., Marsham, J. H., Berthou, S., Rowell, D. P., and Senior, C. A. (2019). Enhanced future changes in wet and dry extremes over Africa at convection-permitting scale. *Nature Communications 2019 10:1*, 10:1–14.

Kim, D., Moon, Y., Camargo, S. J., Wing, A. A., Sobel, A. H., Murakami, H., Vecchi, G. A., Zhao, M., and Page, E. (2018). Process-oriented diagnosis of tropical cyclones in high-resolution GCMs. *Journal of Climate*, 31:1685–1702.

Klutse, N. A. B., Ajayi, V. O., Gbobaniyi, E. O., Egbebiyi, T. S., Kouadio, K., Nkrumah, F., Quagraine, K. A., Olusegun, C., Diasso, U., Abiodun, B. J., Lawal, K., Nikulin, G., Lennard, C., and Dosio, A. (2018). Potential impact of 1.5°c and 2°c global warming on consecutive dry and wet days over West Africa. *Environmental Research Letters*, 13:055013.

Knapp, K. R. and Kruk, M. C. (2010). Quantifying interagency differences in tropical cyclone best-track wind speed estimates. *Monthly Weather Review*, 138:1459–1473.

Knapp, K. R., Kruk, M. C., Levinson, D. H., and Gibney, E. J. (2009). Archive compiles new resource for global tropical cyclone research. *Eos, Transactions American Geophysical Union*, 90:46–46.

Knutson, T., Camargo, S. J., Chan, J. C., Emanuel, K., Ho, C. H., Kossin, J., Mohapatra, M., Satoh, M., Sugi, M., Walsh, K., and Wu, L. (2020). Tropical cyclones and climate change assessment: Part ii: Projected response to anthropogenic warming. *Bulletin of the American Meteorological Society*, 101:E303–E322.

Knutson, T. R., Sirutis, J. J., Garner, S. T., Vecchi, G. A., and Held, I. M. (2008). Simulated reduction in Atlantic hurricane frequency under twenty-first-century warming conditions. *Nature Geoscience*, 1.

Kossin, J. P., Knapp, K. R., Olander, T. L., and Velden, C. S. (2020). Global increase in major tropical cyclone exceedance probability over the past four decades. *Proceedings of the National Academy of Sciences of the United States of America*, 117:11975–11980.

Kucharski, F., Zeng, N., and Kalnay, E. (2013). A further assessment of vegetation feedback on decadal Sahel rainfall variability. *Climate Dynamics*, 40.

Kutzbach, J., Bonan, G., Foley, J., and Harrison, S. P. (1996). Vegetation and soil feedbacks on the response of the African monsoon to orbital forcing in the early to middle Holocene. *Nature 1996 384:6610*, 384:623–626.

Lafore, J. P., Flamant, C., Guichard, F., Parker, D. J., Bouniol, D., Fink, A. H., Giraud, V., Gosset, M., Hall, N., Höller, H., Jones, S. C., Protat, A., Roca, R., Roux, F., Saïd, F., and Thorncroft, C. (2011). Progress in understanding of weather systems in West Africa. *Atmospheric Science Letters*, 12.

Landman, W. A., Seth, A., and Camargo, S. J. (2005). The effect of regional climate model domain choice on the simulation of tropical cyclone–like vortices in the southwestern Indian Ocean. *Journal of Climate*, 18:1263–1274.

Landsea, C. W. (1993). A climatology of intense (or major) Atlantic hurricanes. *Monthly Weather Review*, 121.

Landsea, C. W., Bell, G. D., Gray, W. M., and Goldenberg, S. B. (1998). The extremely active 1995 Atlantic hurricane season: Environmental conditions and verification of seasonal forecasts. *Monthly Weather Review*, 126.

Landsea, C. W. and Gray, W. M. (1992). The strong association between western Sahelian monsoon rainfall and intense Atlantic hurricanes. *Journal of Climate*, 5.

Lavauden, L. (1927). Les forêts du sahara. *Revue des Eaux et Forêts*, 65:265–277.

Lebel, T., Diedhiou, A., and Laurent, H. (2003). Seasonal cycle and interannual variability of the Sahelian rainfall at hydrological scales. *Journal of Geophysical Research: Atmospheres*, 108:8389.

Lee, C. Y., Camargo, S. J., Sobel, A. H., and Tippett, M. K. (2020). Statistical–dynamical downscaling projections of tropical cyclone activity in a warming climate: Two diverging genesis scenarios. *Journal of Climate*, 33:4815–4834.

Lee, C. Y., Tippett, M. K., Sobel, A. H., and Camargo, S. J. (2018). An environmentally forced tropical cyclone hazard model. *Journal of Advances in Modeling Earth Systems*, 10:223–241.

Lee, S., L'Heureux, M., Wittenberg, A. T., Seager, R., O'Gorman, P. A., and Johnson, N. C. (2022). On the future zonal contrasts of equatorial Pacific climate: Perspectives from observations, simulations, and theories. *npj Climate and Atmospheric Science 2022 5:1*, 5:1–15.

Leipper, D. F. and Volgenau, D. (1972). Hurricane heat potential of the Gulf of Mexico. *Journal of Physical Oceanography*, 2.

Li, X. and Wang, B. (1994). Barotropic dynamics of the beta gyres and beta drift. *Journal of the Atmospheric Sciences*, 51.

Lin, I. I., Camargo, S. J., Patricola, C. M., Boucharel, J., Chand, S., Klotzbach, P., Chan, J. C., Wang, B., Chang, P., Li, T., and Jin, F. F. (2020). ENSO and tropical cyclones. *Geophysical Monograph Series*, 253:377–408.

Lin, J., Rousseau-Rizzi, R., Lee, C. Y., and Sobel, A. (2023). An open-source, physics-based, tropical cyclone downscaling model with intensity-dependent steering. *Journal of Advances in Modeling Earth Systems*, 15:e2023MS003686.

Lin, Y., Zhao, M., and Zhang, M. (2015). Tropical cyclone rainfall area controlled by relative sea surface temperature. *Nature Communications 2015 6:1*, 6:1–7.

Lofgren, B. M. (1995). Surface albedo-climate feedback simulated using two-way coupling. *Journal of Climate*, 8.

Lu, J. and Delworth, T. L. (2005). Oceanic forcing of the late 20th century Sahel drought. *Geophysical Research Letters*, 32.

Ma, Z., Xie, Y., Jiao, J., li, L., and Wang, X. (2011). The construction and application of an aledo-NDVI based desertification monitoring model. *Procedia Environmental Sciences*, 10.

Manganello, J. V., Hodges, K. I., Kinter, J. L., Cash, B. A., Marx, L., Jung, T., Achuthavarier, D., Adams, J. M., Altshuler, E. L., Huang, B., Jin, E. K., Stan, C., Towers, P., and Wedi, N. (2012). Tropical cyclone climatology in a 10-km global atmospheric GCM: Toward weather-resolving climate modeling. *Journal of Climate*, 25:3867–3893.

Marks, D. G. (1992). The Beta and advection model for hurricane track forecasting.

Martonne, E. D. (1926). Em. de Martonne, aréisme et indice d'aridité. *Geographical Review of Japan*, 2.

Mathon, V., Laurent, H., and Lebel, T. (2002). Mesoscale convective system rainfall in the Sahel. *Journal of Applied Meteorology*, 41.

McGauley, M. G. and Nolan, D. S. (2011). Measuring environmental favorability for tropical cyclogenesis by statistical analysis of threshold parameters. *Journal of Climate*, 24.

McTaggart-Cowan, R., Davies, E. L., Fairman, J. G., Galarneau, T. J., and Schultz, D. M. (2015). Revisiting the 26.5°c sea surface temperature threshold for tropical cyclone development. *Bulletin of the American Meteorological Society*, 96:1929–1943.

McTaggart-Cowan, R., Vaillancourt, P. A., Zadra, A., Chamberland, S., Charron, M., Corvec, S., Milbrandt, J. A., Paquin-Ricard, D., Patoine, A., Roch, M., Separovic, L., and Yang, J. (2019). Modernization of Atmospheric Physics Parameterization in Canadian NWP. *Journal of Advances in Modeling Earth Systems*, 11:3593–3635.

Meehl, G. A. (1994). Influence of the land surface in the Asian summer monsoon: external conditions versus internal feedbacks. *Journal of Climate*, 7.

Mei, W., Pasquero, C., and Primeau, F. (2012). The effect of translation speed upon the intensity of tropical cyclones over the tropical ocean. *Geophysical Research Letters*, 39.

Meiler, S., Vogt, T., Bloemendaal, N., Ciullo, A., Lee, C. Y., Camargo, S. J., Emanuel, K., and Bresch, D. N. (2022). Intercomparison of regional loss estimates from global synthetic tropical cyclone models. *Nature Communications*, 13.

Messori, G., Gaetani, M., Zhang, Q., Zhang, Q., and Pausata, F. S. (2019). The water cycle of the mid-holocene West African monsoon: The role of vegetation and dust emission changes. *International Journal of Climatology*, 39:1927–1939.

Mironov, D., Heise, E., Kourzeneva, E., Ritter, B., Schneider, N., and Terzhevik, A. (2010). Implementation of the lake parameterisation scheme FLake into the numerical weather prediction model COSMO. *Boreal Environment Research*.

Morrison, J. (2016). The “Great Green Wall” didn’t stop desertification, but it evolved into something that might.

Moss, R. H., Edmonds, J. A., Hibbard, K. A., Manning, M. R., Rose, S. K., Vuuren, D. P. V., Carter, T. R., Emori, S., Kainuma, M., Kram, T., Meehl, G. A., Mitchell, J. F., Nakicenovic, N., Riahi, K., Smith, S. J., Stouffer, R. J., Thomson, A. M., Weyant, J. P., and Wilbanks, T. J. (2010). The next generation of scenarios for climate change research and assessment. *Nature 2010 463:7282*, 463:747–756.

Murakami, H. (2014). Tropical cyclones in reanalysis data sets. *Geophysical Research Letters*, 41:2133–2141.

Murakami, H., Delworth, T. L., Cooke, W. F., Zhao, M., Xiang, B., and Hsu, P. C. (2020). Detected climatic change in global distribution of tropical cyclones. *Proceedings of the National Academy of Sciences of the United States of America*, 117:10706–10714.

Murakami, H., Vecchi, G. A., Underwood, S., Delworth, T. L., Wittenberg, A. T., Anderson, W. G., Chen, J. H., Gudgel, R. G., Harris, L. M., Lin, S. J., and Zeng, F. (2015). Simulation and prediction of category 4 and 5 hurricanes in the high-resolution GFDL HiFLOR coupled climate model. *Journal of Climate*, 28:9058–9079.

Murakami, H. and Wang, B. (2022). Patterns and frequency of projected future tropical cyclone genesis are governed by dynamic effects. *Communications Earth and Environment 2022 3:1*, 3:1–10.

Nakicenovic, N., Alcamo, J., Grubler, A., Riahi, K., Roehrl, R., Rogner, H.-H., and Victor, N. (2000). Special Report on Emissions Scenarios (SRES), a special report of working group 3 of the intergovernmental panel on climate change.

Nationalgeographic (2024). The Great Green Wall. *NatGeo*.

Nature (2020). Get Africa’s Great Green Wall back on track. *Nature*, 587:8.

Nature (2022). How to make Africa’s ‘Great Green Wall’ a success. *Nature*, 605:8.

Newell, R. E. and Kidson, J. W. (1984). African mean wind changes between Sahelian wet and dry periods. *Journal of Climatology*, 4:27–33.

Nicholson, S. E. (2009). A revised picture of the structure of the "monsoon" and land ITCZ over West Africa.

Nicholson, S. E., Acs, F., Bordi, I., and Wang, D.-Y. (2013). The West African Sahel: A review of recent studies on the rainfall regime and its interannual variability. *International Scholarly Research Notices*, 2013:453521.

Nicholson, S. E., Barcilon, A. I., Challa, M., and Baum, J. (2007). Wave activity on the tropical easterly jet. *Journal of the Atmospheric Sciences*, 64:2756–2763.

NOAA (2024). Costliest U.S. tropical cyclones.

Ogata, T., Mizuta, R., Adachi, Y., Murakami, H., and Ose, T. (2016). Atmosphere-ocean coupling effect on intense tropical cyclone distribution and its future change with 60 km-AOGCM. *Scientific Reports*, 6.

O'Neill, B. C., Tebaldi, C., Vuuren, D. P. V., Eyring, V., Friedlingstein, P., Hurtt, G., Knutti, R., Kriegler, E., Lamarque, J. F., Lowe, J., Meehl, G. A., Moss, R., Riahi, K., and Sanderson, B. M. (2016). The Scenario Model Intercomparison Project (ScenarioMIP) for CMIP6. *Geoscientific Model Development*, 9:3461–3482.

OnePlanetSummit (2025). Great Green Wall accelerator.

Ornstein, L., Aleinov, I., and Rind, D. (2009). Irrigated afforestation of the Sahara and Australian outback to end global warming. *Climatic Change*, 97:409–437.

PAGGW (2018). Initiative de la grande muraille verte : Realisations 2011-2017 et defis sur la trajectoire 2030. *LES ECHOS DE LA GMV*.

Pal, J. S., Giorgi, F., Bi, X., Elguindi, N., Solmon, F., Gao, X., Rauscher, S. A., Francisco, R., Zakey, A., Winter, J., Ashfaq, M., Syed, F. S., Bell, J. L., Differbaugh, N. S., Karmacharya, J., Konari, A., Martinez, D., Rocha, R. P. D., Sloan, L. C., and Steiner, A. L. (2007). Regional climate modeling for the developing world: The ICTP RegCM3 and RegCNET. *Bulletin of the American Meteorological Society*, 88:1395–1410.

Palmer, T. N. (1986). Influence of the Atlantic, Pacific and Indian Oceans on Sahel rainfall. *Nature*, 322.

Paniagua, L. L., García-Martín, A., Moral, F. J., and Rebollo, F. J. (2019). Aridity in the Iberian Peninsula (1960–2017): distribution, tendencies, and changes. *Theoretical and Applied Climatology*, 138:811–830.

Paradis, D., Lafore, J. P., Redelsperger, J. L., and Balaji, V. (1995). African easterly waves and convection. Part i: linear simulations. *Journal of the Atmospheric Sciences*, 52.

Parker, D. J. and Diop-Kane, M. (2016). *Meteorology of tropical West Africa: The forecasters' handbook*. WILEY Blackwell.

Patricola, C. M., Saravanan, R., and Chang, P. (2018). The response of atlantic tropical cyclones to suppression of African Easterly waves. *Geophysical Research Letters*, 45:471–479.

Pausata, F. S., Emanuel, K. A., Chiacchio, M., Diro, G. T., Zhang, Q., Sushama, L., Stager, J. C., and Donnelly, J. P. (2017a). Tropical cyclone activity enhanced by Sahara greening and reduced dust emissions during the African Humid Period. *Proceedings of the National Academy of Sciences of the United States of America*, 114:6221–6226.

Pausata, F. S., Gaetani, M., Messori, G., Berg, A., de Souza, D. M., Sage, R. F., and deMenocal, P. B. (2020). The greening of the Sahara: Past changes and future implications. *One Earth*, 2:235–250.

Pausata, F. S., Messori, G., and Zhang, Q. (2016). Impacts of dust reduction on the northward expansion of the African monsoon during the Green Sahara period. *Earth and Planetary Science Letters*, 434:298–307.

Pausata, F. S., Zhang, Q., Muschitiello, F., Lu, Z., Chafik, L., Niedermeyer, E. M., Stager, J. C., Cobb, K. M., and Liu, Z. (2017b). Greening of the Sahara suppressed ENSO activity during the mid-Holocene. *Nature Communications 2017 8:1*, 8:1–12.

PielkeJr., R. A., Gratz, J., Landsea, C. W., Collins, D., Saunders, M. A., and Musulin, R. (2008). Normalized hurricane damage in the United States: 1900–2005. *Natural Hazards Review*, 9:29–42.

Prince, S. D., Colstoun, E. B. D., and Kravitz, L. L. (1998). Evidence from rain-use efficiencies does not indicate extensive Sahelian desertification. *Global Change Biology*, 4.

Ramsay, H. A. and Sobel, A. H. (2011). Effects of relative and absolute sea surface temperature on tropical cyclone potential intensity using a single-column model. *Journal of Climate*, 24.

Reed, K. A. and Jablonowski, C. (2011). An analytic vortex initialization technique for idealized tropical cyclone studies in AGCMs. *Monthly Weather Review*, 139:689–710.

Reenberg, A. (2012). Insistent dryland narratives: Portraits of knowledge about human-environmental interactions in sahelian environment policy documents. *West African Journal of Applied Ecology*, 20.

Reij, C., Scoones, I., and Toulmin, C. (1996). *Sustaining the soil: indigenous soil and water conservation in Africa*. Routledge.

Roberts, M. J., Camp, J., Seddon, J., Vidale, P. L., Hodges, K., Vannière, B., Mecking, J., Haarsma, R., Bellucci, A., Scoccimarro, E., Caron, L. P., Chauvin, F., Terray, L., Valcke, S., Moine, M. P., Putrasahan, D., Roberts, C. D., Senan, R., Zarzycki, C., Ullrich, P., Yamada, Y., Mizuta, R., Kodama, C., Fu, D., Zhang, Q., Danabasoglu, G., Rosenbloom, N., Wang, H., and Wu, L. (2020). Projected future changes in tropical cyclones using the CMIP6 HighResMIP multimodel ensemble. *Geophysical Research Letters*, 47:e2020GL088662.

Rodríguez-Fonseca, B., Mohino, E., Mechoso, C. R., Caminade, C., Biasutti, M., Gaetani, M., Garcia-Serrano, J., Vizy, E. K., Cook, K., Xue, Y., Polo, I., Losada, T., Druyan, L., Fontaine, B., Bader, J., Doblas-Reyes, F. J., Goddard, L., Janicot, S., Arribas, A., Lau, W., Colman, A., Vellinga, M., Rowell, D. P., Kucharski, F., and Voldoire, A. (2015). Variability and predictability of West African droughts: A review on the role of sea surface temperature anomalies. *Journal of Climate*, 28:4034–4060.

Royer, J. F., Chauvin, F., Timbal, B., Araspin, P., and Grimal, D. (1998). A GCM study of the impact of greenhouse gas increase on the frequency of occurrence of tropical cyclones. *Climatic Change*, 38.

Russell, J. O., Aiyyer, A., White, J. D., and Hannah, W. (2017). Revisiting the connection between African Easterly Waves and Atlantic tropical cyclogenesis. *Geophysical Research Letters*, 44:587–595.

Ruti, P. M. and Dell'Aquila, A. (2010). The twentieth century african easterly waves in reanalysis systems and IPCC simulations, from intra-seasonal to inter-annual variability. *Climate Dynamics*, 35:1099–1117.

Ryan, B. F., Watterson, I. G., and Evans, J. L. (1992). Tropical cyclone frequencies inferred from Gray's yearly genesis parameter: Validation of GCM tropical climates. *Geophysical Research Letters*, 19:1831–1834.

Saerens, M., Latinne, P., and Decaestecker, C. (2002). Adjusting the outputs of a classifier to new a Priori probabilities: A simple procedure. *Neural Computation*, 14:21–41.

Saley, I. A., Salack, S., Sanda, I. S., Moussa, M. S., Bonkaney, A. L., Ly, M., and Fodé, M. (2019). The possible role of the Sahel greenbelt on the occurrence of climate extremes over the West African Sahel. *Atmospheric Science Letters*, 20:e927.

Saunders, M. A., Klotzbach, P. J., and Lea, A. S. (2017). Replicating annual North Atlantic hurricane activity 1878–2012 from environmental variables. *Journal of Geophysical Research: Atmospheres*, 122:6284–6297.

Schreck, C. J., Knapp, K. R., and Kossin, J. P. (2014). The impact of best track discrepancies on global tropical cyclone climatologies using IBTrACS. *Monthly Weather Review*, 142.

Schwalm, C. R., Glendon, S., and Duffy, P. B. (2020). RCP8.5 tracks cumulative CO2 emissions. *Proceedings of the National Academy of Sciences of the United States of America*, 117:19656–19657.

Science (2020). New funds could help grow Africa's Great Green Wall. But can the massive forestry effort learn from past mistakes? *Science*.

Scoones, I. (2018). Review of the end of desertification? Disputing environmental change in the drylands by Roy H. Behnke and Michael Mortimore. *Pastoralism*, 8.

Seager, R., Cane, M., Henderson, N., Lee, D. E., Abernathey, R., and Zhang, H. (2019). Strengthening tropical pacific zonal sea surface temperature gradient consistent with rising greenhouse gases. *Nature Climate Change 2019 9:7*, 9:517–522.

Seager, R., Henderson, N., and Cane, M. (2022). Persistent discrepancies between observed and modeled trends in the tropical Pacific Ocean. *Journal of Climate*, 35:4571–4584.

Sendzimir, J., Reij, C. P., and Magnuszewski, P. (2011). Rebuilding resilience in the Sahel: Regreening in the Maradi and Zinder regions of Niger. *Ecology and Society*, 16.

Seneviratne, S., Zhang, X., Adnan, M., Badi, W., Dereczynski, C., Luca, A. D., Ghosh, S., Iskandar, I., Kossin, J., Lewis, S., Otto, F., Pinto, I., Satoh, M., Vicente-Serrano, S., Wehner, M., and Zhou, B. (2021). *Weather and Climate Extreme Events in a Changing Climate*. Cambridge University Press.

Shanahan, T. M., Overpeck, J. T., Anchukaitis, K. J., Beck, J. W., Cole, J. E., Dettman, D. L., Peck, J. A., Scholz, C. A., and King, J. W. (2009). Atlantic forcing of persistent drought in West Africa. *Science*, 324.

Shekhar, R. and Boos, W. R. (2017). Weakening and shifting of the Saharan shallow meridional circulation during wet years of the West African monsoon. *Journal of Climate*, 30:7399–7422.

Simpson, R. H. (1974). The hurricane disaster—potential scale. *Weatherwise*, 27:169–186.

Simpson, R. H., Frank, N., Shideler, D., and Johnson, H. M. (1969). Atlantic tropical disturbances of 1968. *Monthly Weather Review*, 97.

Sinclair, A. R. and Fryxell, J. M. (1985). The Sahel of Africa: ecology of a disaster. *Canadian Journal of Zoology*, 63.

Skinner, C. B. and Diffenbaugh, N. S. (2014). Projected changes in African easterly wave intensity and track in response to greenhouse forcing. *Proceedings of the National Academy of Sciences of the United States of America*, 111:6882–6887.

Sobel, A. H., Camargo, S. J., Barnston, A. G., and Tippett, M. K. (2016). Northern hemisphere tropical cyclones during the quasi-El Niño of late 2014. *Natural Hazards*, 83:1717–1729.

Sobel, A. H., Lee, C. Y., Bowen, S. G., Camargo, S. J., Cane, M. A., Clement, A., Fosu, B., Hart, M., Reed, K. A., Seager, R., and Tippett, M. K. (2023). Near-Term tropical cyclone risk and coupled Earth system model biases. *Proceedings of the National Academy of Sciences of the United States of America*, 120.

Sobel, A. H., Wing, A. A., Camargo, S. J., Patricola, C. M., Vecchi, G. A., Lee, C. Y., and Tippett, M. K. (2021). Tropical cyclone frequency. *Earth's Future*, 9:e2021EF002275.

Sohoulande, C. D., Awoye, H., Nouwakpo, K. S., Dogan, S., Szogi, A. A., Stone, K. C., and Martin, J. H. (2022). A global-scale assessment of water resources and vegetation cover dynamics in relation with the earth climate gradient. *Remote Sensing in Earth Systems Sciences*, 5:193–206.

Sparks, N. and Toumi, R. (2024). The Imperial College Storm Model (IRIS) dataset. *Scientific Data 2024 11:1*, 11:1–12.

Stebbing, E. P. (1935). The Encroaching Sahara: The threat to the West African Colonies. *The Geographical Journal*, 85.

Stevenson, S. L. (2012). Significant changes to ENSO strength and impacts in the twenty-first century: Results from CMIP5. *Geophysical Research Letters*, 39.

Strachan, J., Vidale, P. L., Hodges, K., Roberts, M., and Demory, M. E. (2013). Investigating global tropical cyclone activity with a hierarchy of AGCMs: The role of model resolution. *Journal of Climate*, 26:133–152.

Sugi, M., Yamada, Y., Yoshida, K., Mizuta, R., Nakano, M., Kodama, C., and Satoh, M. (2020). Future changes in the global frequency of tropical cyclone seeds. *SOLA*, 16:70–74.

Sultan, B. and Janicot, S. (2003). The West African monsoon dynamics. Part ii: The "preonset" and "onset" of the summer monsoon. *Journal of Climate*, 16.

Swanson, K. L. (2008). Nonlocality of Atlantic tropical cyclone intensities. *Geochemistry, Geophysics, Geosystems*, 9.

Tang, B. and Emanuel, K. (2012). A ventilation index for tropical cyclones. *Bulletin of the American Meteorological Society*, 93:1901–1912.

Taylor, C. M., Birch, C. E., Parker, D. J., Dixon, N., Guichard, F., Nikulin, G., and Lister, G. M. (2013). Modeling soil moisture-precipitation feedback in the Sahel: Importance of spatial scale versus convective parameterization. *Geophysical Research Letters*, 40:6213–6218.

Taylor, C. M., Lambin, E. F., Stephenne, N., Harding, R. J., and Essery, R. L. (2002). The influence of land use change on climate in the Sahel. *Journal of Climate*, 15.

Thorncroft, C. and Hodges, K. (2001). African easterly wave variability and its relationship to Atlantic tropical cyclone activity. *Journal of Climate*, 14.

Thorncroft, C. D. and Blackburn, M. (1999). Maintenance of the African easterly jet. *Quarterly Journal of the Royal Meteorological Society*, 125:763–786.

Thorncroft, C. D., Hall, N. M., and Kiladis, G. N. (2008). Three-dimensional structure and dynamics of african easterly waves. Part iii: Genesis. *Journal of the Atmospheric Sciences*, 65:3596–3607.

Timm, O., Köhler, P., Timmermann, A., and Menviel, L. (2010). Mechanisms for the onset of the African Humid Period and Sahara greening 14.5–11 ka BP. *Journal of Climate*, 23:2612–2633.

Timmermann, A., An, S. I., Kug, J. S., Jin, F. F., Cai, W., Capotondi, A., Cobb, K., Lengaigne, M., McPhaden, M. J., Stuecker, M. F., Stein, K., Wittenberg, A. T., Yun, K. S., Bayr, T., Chen, H. C., Chikamoto, Y., Dewitte, B., Dommenget, D., Grothe, P., Guilyardi, E., Ham, Y. G., Hayashi, M., Ineson, S., Kang, D., Kim, S., Kim, W. M., Lee, J. Y., Li, T., Luo, J. J., McGregor, S., Planton, Y., Power, S., Rashid, H., Ren, H. L., Santoso, A., Takahashi, K., Todd, A., Wang, G., Wang, G., Xie, R., Yang, W. H., Yeh, S. W., Yoon, J., Zeller, E., and Zhang, X. (2018). El Niño–Southern Oscillation complexity. *Nature 2018 559:7715*, 559:535–545.

Tippett, M. K., Camargo, S. J., and Sobel, A. H. (2011). A poisson regression index for tropical cyclone genesis and the role of large-scale vorticity in genesis. *Journal of Climate*, 24:2335–2357.

Tory, K. J., Chand, S. S., Dare, R. A., and Mcbride, J. L. (2013). An assessment of a model-, grid-, and basin-independent tropical cyclone detection scheme in selected CMIP3 global climate models. *Journal of Climate*, 26:5508–5522.

Toulmin, C. and Brock, K. (2016). *Desertification in the Sahel: Local Practice Meets Global Narrative*, chapter 2, pages 37–66. Springer.

Tucker, C. J., Dregne, H. E., and Newcomb, W. W. (1991). Expansion and contraction of the Sahara desert from 1980 to 1990. *Science*, 253.

Turco, M., Palazzi, E., Hardenberg, J. V., and Provenzale, A. (2015). Observed climate change hotspots. *Geophysical Research Letters*, 42:3521–3528.

Turner, M. D., Carney, T., Lawler, L., Reynolds, J., Kelly, L., Teague, M. S., and Brottem, L. (2021). Environmental rehabilitation and the vulnerability of the poor: The case of the Great Green Wall. *Land Use Policy*, 111:105750.

Turner, M. D., Davis, D. K., Yeh, E. T., Hiernaux, P., Loizeaux, E. R., Fornof, E. M., Rice, A. M., and Suiter, A. K. (2023). Great green walls: Hype, myth, and science. *Annual Review of Environment and Resources*, 48:263–287.

Tölgyesi, C., Török, P., Hábenczyus, A. A., Bátori, Z., Valkó, O., Deák, B., Tóthmérész, B., Erdős, L., and Kelemen, A. (2020). Underground deserts below fertility islands? Woody species desiccate lower soil layers in sandy drylands. *Ecography*, 43.

Vecchi, G. A. and Soden, B. J. (2007a). Effect of remote sea surface temperature change on tropical cyclone potential intensity. *Nature*, 450.

Vecchi, G. A. and Soden, B. J. (2007b). Increased tropical Atlantic wind shear in model projections of global warming. *Geophysical Research Letters*, 34.

Vecchi, G. A., Swanson, K. L., and Soden, B. J. (2008). Whither hurricane activity? *Science*, 322.

Verseghy, D. L. (2000). The canadian land surface scheme (CLASS): Its history and future. *Atmosphere-Ocean*, 38:1–13.

Vickery, P. J., Skerlj, P. F., and Twisdale, L. A. (2000). Simulation of hurricane risk in the U.S. using empirical track model. *Journal of Structural Engineering*, 126:1222–1237.

Vidale, P. L., Hodges, K., Vannière, B., Davini, P., Roberts, M. J., Strommen, K., Weisheimer, A., Plesca, E., and Corti, S. (2021). Impact of stochastic physics and model resolution on the simulation of tropical cyclones in climate GCMs. *Journal of Climate*, 34:4315–4341.

Vitart, F. and Anderson, J. L. (2001). Sensitivity of Atlantic tropical storm frequency to enso and interdecadal variability of SSTs in an ensemble of AGCM integrations. *Journal of Climate*, 14.

Walsh, K. J., Fiorino, M., Landsea, C. W., and McInnes, K. L. (2007). Objectively determined resolution-dependent threshold criteria for the detection of tropical cyclones in climate models and reanalyses. *Journal of Climate*, 20:2307–2314.

Waters, J. J., Evans, J. L., and Forest, C. E. (2012). Large-scale diagnostics of tropical cyclogenesis potential using environment variability metrics and logistic regression models. *Journal of Climate*, 25:6092–6107.

Webster, P. J. (1987). The elementary monsoon.

Wehner, M., Prabhat, Reed, K. A., Stone, D., Collins, W. D., and Bacmeister, J. (2015). Resolution dependence of future tropical cyclone projections of CAM5.1 in the U.S. CLIVAR hurricane working group idealized configurations. *Journal of Climate*, 28:3905–3925.

Weinkle, J., Maue, R., and Pielke, R. (2012). Historical global tropical cyclone landfalls. *Journal of Climate*, 25:4729–4735.

West, C. T., Somé, A., and Nebié, E. K. (2014). Famines are a thing of the past: Food security trends in northern Burkina Faso. *Human Organization*, 73.

Wilcoxon, F. (1945). Individual comparisons by ranking methods. *Biometrics Bulletin*, 1:80.

Wilkinson, G. N. and Rogers, C. E. (1973). Symbolic description of factorial models for analysis of variance. *Journal of Applied Statistics*, 22:392–399.

Willoughby, H. E., Darling, R. W., and Rahn, M. E. (2006). Parametric representation of the primary hurricane vortex. Part ii: A new family of sectionally continuous profiles. *Monthly Weather Review*, 134.

Xu, W., Balaguru, K., August, A., Lalo, N., Hodas, N., DeMaria, M., and Judi, D. (2021). Deep learning experiments for tropical cyclone intensity forecasts. *Weather and Forecasting*, 36:1453–1470.

Xu, W., Balaguru, K., Judi, D. R., Rice, J., Leung, L. R., and Lipari, S. (2024). A North Atlantic synthetic tropical cyclone track, intensity, and rainfall dataset. *Scientific Data 2024 11:1*, 11:1–12.

Xue, Y. and Shukla, J. (1993). The influence of land surface properties on Sahel climate. Part i: desertification. *Journal of Climate*, 6.

Yamada, Y., Kodama, C., Satoh, M., Sugi, M., Roberts, M. J., Mizuta, R., Noda, A. T., Nasuno, T., Nakano, M., and Vidale, P. L. (2021). Evaluation of the contribution of tropical cyclone seeds to changes in tropical cyclone frequency due to global warming in high-resolution multi-model ensemble simulations. *Progress in Earth and Planetary Science*, 8:1–17.

Yanai, M., Esbensen, S., and Chu, J.-H. (1973). Determination of bulk properties of tropical cloud clusters from large-scale heat and moisture budgets. *Journal of the Atmospheric Sciences*, 30.

Yang, W., Hsieh, T. L., and Vecchi, G. A. (2021). Hurricane annual cycle controlled by both seeds and genesis probability. *Proceedings of the National Academy of Sciences of the United States of America*, 118:e2108397118.

Yokoi, S., Takayabu, Y. N., and Chan, J. C. (2009). Tropical cyclone genesis frequency over the western North Pacific simulated in medium-resolution coupled general circulation models. *Climate Dynamics*, 33.

Yuan, J. (2020). Investigation of spatial and temporal changes in the land surface albedo for the entire Chinese territory. *Geosciences 2020, Vol. 10, Page 362*, 10:362.

Yuen, K. K. and Dixon, W. J. (1973). The approximate behaviour and performance of the two sample trimmed t. *Biometrika*, 60.

Zarzycki, C. M. and Ullrich, P. A. (2017). Assessing sensitivities in algorithmic detection of tropical cyclones in climate data. *Geophysical Research Letters*, 44:1141–1149.

Zeng, N. (2003). Drought in the sahel. *Science*, 302:999–1000.

Zeng, N., Neelin, J. D., Lau, K. M., and Tucker, C. J. (1999). Enhancement of interdecadal climate variability in the Sahel by vegetation interaction. *Science*, 286:1537–1540.

Zhang, G. and Cook, K. H. (2014). West African monsoon demise: Climatology, interannual variations, and relationship to seasonal rainfall. *Journal of Geophysical Research: Atmospheres*, 119:10,175–10,193.

Zhang, X., Alexander, L., Hegerl, G. C., Jones, P., Tank, A. K., Peterson, T. C., Trewin, B., and Zwiers, F. W. (2011). Indices for monitoring changes in extremes based on daily temperature and precipitation data. *Wiley Interdisciplinary Reviews: Climate Change*, 2:851–870.

Zhao, M., Held, I. M., and Lin, S. J. (2012). Some counterintuitive dependencies of tropical cyclone frequency on parameters in a GCM. *Journal of the Atmospheric Sciences*, 69:2272–2283.

Zolfaghari, F., Azarnivand, H., Khosravi, H., Zehtabian, G., and Sigaroudi, S. K. (2022). Monitoring the severity of degradation and desertification by remote sensing (case study: Hamoun International Wetland). *Frontiers in Environmental Science*, 10:902687.

Ángel F. Adames Corraliza and Mayta, V. C. (2023). On the accuracy of the moist static energy budget when applied to large-scale tropical motions. *Journal of the Atmospheric Sciences*, 80.